



**Strål  
säkerhets  
myndigheten**

Swedish Radiation Safety Authority

**Redaktörer:** Ninos Garis, Strålsäkerhetsmyndigheten (SSM)  
Lennart Agrenius, Agrenius Ingenjörsbyrå AB

Forskning

**2018:16**

APRI 9 – Accident Phenomena of  
Risk Importance

En lägesrapport om forskningen inom området  
svåra haverier under åren 2015-2017



## **SSM perspektiv**

### **Bakgrund**

Strålsäkerhetsmyndigheten (SSM) och kraftbolagen FKA, OKG och RAB har gemensamt under lång tid finansierat och hanterat ett forskningsprogram inom svåra haverier kallat Accident Phenomena of Risk Importance (APRI). Senaste programmet har löpt som tre-årsprojekt och avslutades i slutet av år 2017.

Ramarna för APRI-programmet har varit att studera riskdominerande haverifonen under ett svårt haveri. Den svenska hanteringen med ett vattenfyllt nedre primärutrymme i kokvattenreaktorerna i samband med ett svårt haveri, är i det närmaste unik och finns inte representerad i den internationella forskningen. Även haverihanteringen av de svenska tryckvattenreaktorerna, med en avsiktlig vattenfyllning av reaktorgropen i samband med ett svårt haveri, är ovanlig i den internationella forskningen och innebär liknande frågeställningar.

Syftet med APRI-programmet har varit att skapa en gemensam plattform och kunskapsbas gällande fenomen och händelseförlopp av betydelse vid svåra haverier i en kärnkraftsreaktor. Den av APRI finansierade forskningen bedrivs i huvudsak av KTH och Chalmers.

### **Resultat**

En kort historisk återblick avseende utfallet från föregående APRI-program är att resultaten hittills

- har verifierat den nuvarande strategin för hantering av svåra haverier och att anläggningsmodiferingar inte har varit nödvändiga,
- har bidragit till nationell kompetensförsörjning inom området, och
- har utgjort ett forum för teknisk/vetenskaplig samverkan mellan myndighet och tillståndshavare.

KTH:s forskning har under APRI-programmen fokuserat på att kvantifiera de osäkerheter som är förknippade med den svenska strategin att hantera en härdsmälta. Tillämpningen av verktyget ROAAM (Risk Oriented Accident Analysis Method) och utvecklingen av ROAAM+ vid KTH har bidragit till en ökad förståelse och ökade möjligheter att analysera fenomenen och förloppen under ett svårt haveri. Metoden anses vara ett adekvat verktyg för att hantera frågor där både osäkerheter avseende scenarion och osäkerheter i den deterministiska modelleringen är stora. ROAAM+ har även gett kunskap om vilka experiment som behöver prioriteras i syfte att minska osäkerheterna i den svenska haverihanteringsstrategin.

APRI-stödet till Chalmers har fokuserat på att öka förståelsen för hur kemiska reaktioner påverkar det radioaktiva utsläppet till omgivningen vid en härdsmälta. Forskningen under APRI-9 har resulterat i ökade kunskaper om tellurs och ruteniums kemi i haverisammanhang.

Uppföljningen av internationell forskning har ökat kunskapen om svåra haverier i olika avseenden. Genom tillförsel av medel till KTH och Chalmers från SSM och industrin har kontinuiteten avseende forskning om svåra haverier kunnat säkras.

### **Relevans**

Det finns kvarvarande osäkerheter förknippade med den svenska haverihanteringsstrategin som behöver belysas ytterligare genom forskning. Genom den svenska strategin undviks troligen en stor inledande interaktion mellan betong och smälta. Å andra sidan kan ångexplosioner inträffa när smältan faller i djupt vatten. Den forskning som bedrivs inom APRI-programmet är relevant för den svenska haverihanteringsstrategi eftersom det finns obetydlig mycket lite internationell forskning som direkt belyser denna. Dock bedrivs internationell forskning om fenomen och haverihanteringsstrategin som är av relevans även för svenska förhållanden och som kan inkorporeras i den specifikt svenska strategin.

### **Behov av vidare forskning**

Det finns fortfarande behov av fortsatt forskning inom området svåra haverier. Det gäller bland annat fortsatt deltagande i internationella projekt och fortsatt stöd till forskargrupper på KTH och Chalmers för vidare studier av haverifenomen och haverikemi.

### **Projekt information**

Kontaktperson SSM: Ninos Garis och Patrick Isaksson.

Referens: SSM 2015-2033 / 2037012 - 94



**Strål  
säkerhets  
myndigheten**

Swedish Radiation Safety Authority

**Redaktörer:** Ninos Garis, Strålsäkerhetsmyndigheten (SSM)  
Lennart Agrenius, Agrenius Ingenjörsbyrå AB

# 2018:16

## APRI 9 – Accident Phenomena of Risk Importance

En lägesrapport om forskningen inom området  
svåra haverier under åren 2015-2017

Datum: Juni 2018

Rapportnummer: 2018:16 ISSN: 2000-0456

Tillgänglig på [www.stralsakerhetsmyndigheten.se](http://www.stralsakerhetsmyndigheten.se)

Denna rapport har tagits fram på uppdrag av Strålsäkerhetsmyndigheten, SSM. De slutsatser och synpunkter som presenteras i rapporten är författarens/författarnas och överensstämmer inte nödvändigtvis med SSM:s.

Forskningsprojektet APRI-9 har genomförts i samarbete mellan följande organisationer:

Strålsäkerhetsmyndigheten (SSM)  
Ringhals AB (RAB)  
OKG Aktiebolag (OKG)  
Forsmarks Kraftgrupp AB (FKA)

Projektet har varit underställd en styrgrupp med representanter från SSM och kraftbolagen enligt följande:

Mauritz Gårdinge, OKG (ordförande)  
Ninos Garis, SSM  
Patrick Isaksson, SSM  
Anders Henoch, RAB  
Staffan Dittmer, RAB  
Margareta Tanse Larsson, FKA  
Lennart Agrenius, Agrenius Ingenjörsbyrå AB (projektledare)

Arbetet har genomförts i projektform med deltagande från parterna och andra svenska och utländska uppdragstagare och samarbetspartners.

Redaktörer:

Ninos Garis, SSM  
Lennart Agrenius, Agrenius Ingenjörsbyrå AB

Personer som har bidragit till olika avsnitt i rapporten:

Patrick Isaksson, SSM  
Oddbjörn Sandervåg, Oddsan Consult  
Christian Linde, SSM  
Johan Ljung, RAB  
Pavel Kudinov, KTH  
Weimin Ma, KTH  
Sevostian Bechta, KTH  
Dmitry Grishchenko, KTH  
Sergey Galushin, KTH  
Sergey Yakush, IPM RAS  
Mikhail Davydov, EREC  
Alexander Konovalenko, KTH  
Simone Basso, KTH  
Sachin Thakre, KTH  
Mohsen Hoseyni, KTH  
Walter Villanueva, KTH  
Peng Yu, KTH  
Louis Manickam, KTH  
Christian Ekberg, Chalmers  
Fredrik Espegren, Chalmers  
Ivan Kajan, Chalmers  
Mark Foreman, Chalmers



# SAMMANFATTNING

Kunskap om de fenomen som kan uppträda vid svåra haverier i en kärnkraftsanläggning är en viktig förutsättning för att kunna förutse anläggningens beteende, för att kunna utforma rutiner och instruktioner för haverihantering, för beredskapsplanningen samt för att få god kvalitet på haverianalyser och riskstudier.

Sedan början på 80-talet har kärnkraftföretagen och myndigheten i Sverige samarbetat inom forskningsområdet svåra reaktorhaverier. Samarbetet i början var framför allt knutet till att förstärka skyddet mot omgivningskonsekvenser efter ett svårt reaktorhaveri genom att bl.a. ta fram system för filtrerad tryckavlastning av reaktorinneslutningen. Sedan början på 90-talet har samarbetet delvis ändrat karaktär och inriktats mer på fenomenologiska frågor av riskdominerande betydelse.

Under åren 2015-2017 har samarbetet fortsatt inom forskningsprogrammet APRI-9. Syftet har varit att visa om de lösningar som har valts i den svenska strategin för haverihantering ger ett tillräckligt skydd för omgivningen. Detta sker genom att få fördjupad kunskap om dels viktiga fenomen vid härdsmälteförlopp, dels mängden radioaktivitet som kan släppas ut till omgivningen vid ett svårt haveri.

För att nå syftet har forskningsprogrammet omfattat dels uppföljning av den internationella forskningen inom svåra haverier och utvärdering av resultaten, dels fortsatt stöd till forskningen på KTH och Chalmers om svåra haverier.

Uppföljningen av den internationella forskningen har främjat utbyte av kunskap och erfarenheter samt har gett tillgång till en mängd information om olika fenomen av betydelse för händelseförlopp vid svåra haverier. Detta är viktigt för att erhålla en god bedömningsgrund av de utsläppsbepränsande åtgärderna i svenska kärnkraftsaktörer.

Det fortsatta stödet till KTH har gett ökade kunskaper om möjligheterna och förutsättningarna för att kyla härdrester i reaktortanken och om de identifierade processerna i samband med tankgenomsmältnings samt kylbarheten av härdrester i inneslutningen. Utvecklingen av ROAAM+ har resulterat i ett ramverk med en uppsättning beräkningsverktyg och gränssnitt i MATLAB. ROAAM+ innehåller olika beräkningsmodeller som kan identifiera stora bidrag till osäkerheter i riskbedömningar i samband med svåra härdhaverier. Resultaten har visats kunna användas för att förfina och förbättra PSA-analyser på flera sätt. Studier med en storskalig PSA-modell visar att integration av ROAAM+ -resultatet med PSA-modellen inte bara är möjlig utan kan också leda till en ändring av den beräknade frekvensen för inneslutningsbrott.

Stödet till Chalmers har resulterat i ökade kunskaper om hur rutenium och tellur interagerar med olika färger och andra material i inneslutningen. Forskningen av tellur har givit kunskaper om dess aerosolkemi. Mer specifikt hur tellur i aerosolform beter sig vid kontakt med olika ytor som finns i reaktorinneslutningen. Vidare har den potentiella användningen av havsvatten som en nödlösning vid total förlust av kylmedel utvärderats, med ett fokus på fissionsprodukter. Ruteniumstudierna inkluderade effekter av temperatur, radiolysprodukter i luft och cesiumjodidaerosoler på de kemiska formerna av rutenium som kan transporteras i reaktorinneslutningen vid ett svårt reaktorhaveri.



# INNEHÅLLSFÖRTECKNING

<b>1. Inledning .....</b>	<b>7</b>
1.1 Kort historik .....	7
1.2 Projektets syfte .....	8
1.3 Organisation och arbetsformer .....	9
1.4 Erfarenhetsutbyte och seminarier .....	10
1.5 Ekonomi och rapportering .....	10
<b>2. Internationell Forskning inom svåra haverier.....</b>	<b>11</b>
2.1 CSARP – NRC:s Forskningsforum .....	11
2.2 STEM - Source Term Evaluation and Mitigation .....	12
2.3 THAI 3 - Thermal-hydraulics, Hydrogen, Aerosols and Iodine project .....	16
2.4 BIP - Behaviour of Iodine Project.....	20
2.5 CSNI/NEA-rapporter inom svåra haverier under perioden 2015-2017 .....	23
<b>3. KTH:s forskning inom svåra haverier .....</b>	<b>24</b>
3.1 Inledning på svenska .....	24
3.2 Motivation, Goals and Approach.....	34
3.3 Risk Evaluation and Synthesis (RES) .....	35
3.4 Melt Ejection Mode (MEM) .....	45
3.5 Debris Coolability Map (DECO) .....	74
3.6 Steam Explosion Impact Map (SEIM).....	104
3.7 Results of Risk Analysis using ROAAM+ Framework .....	108
3.8 Improvements in PSA Modelling using Integration with ROAAM+.....	115
3.9 Summary of the ROAAM+ Development and Risk Analysis Results .....	120
3.10 Infrastructure development for high-temperature melt experiments .....	123
3.11 References.....	130
<b>4. Chalmers forskning inom svåra haverier.....</b>	<b>141</b>
4.1 Inledning på svenska .....	141
4.2 Tellurium Chemistry.....	144
4.3 Tellurium, behavior and interaction in the containment of an NPP .....	144
4.4 Investigation of the effects of seawater on the tellurium source term .....	154
4.5 Ruthenium chemistry in severe accident conditions .....	158
4.6 Tellurium, niobium and ruthenium interaction with iodine .....	177
4.7 References.....	180
<b>5. Uppföljning av kärnkraftsolyckan i Fukushima Daiichi .....</b>	<b>182</b>
5.1 Status för kärnkraftsreaktorerna i Fukushima Daiichi 1-3 .....	182
5.2 Status för reaktorhårdarna i Fukushima Daiichi 1-3.....	189
5.3 Status för bränslebassängerna i Fukushima Daiichi .....	197
5.4 Referenser .....	205
<b>6. Sammanfattning, slutsatser och rekommendationer .....</b>	<b>208</b>
6.1 Sammanfattning av projektet .....	208
6.2 Slutsatser .....	211
6.3 Rekommendationer.....	211
<b>7. Förkortningslista.....</b>	<b>213</b>



# 1. INLEDNING

Kunskap om de fenomen som kan uppträda vid svåra haverier i en kärnkraftsanläggning är en viktig förutsättning för att kunna förutse anläggningens beteende, för att kunna utforma rutiner och instruktioner för haverihantering, för beredskapsplanningen samt för att få god kvalitet på haverianalyser och riskstudier.

De svenska deltagarna, SSM och kärnkraftföretagen i Sverige har under en följd av år samarbetat inom forskningsområdet svåra reaktorhaverier. Detta har skett inom projekten FILTRA, RAMA, RAMA II, RAMA III, HAFOS, APRI, APRI-2, APRI-3, APRI-4, APRI-5, APRI-6, APRI-7 och APRI-8.

FILTRA- och RAMA-projekten var knutna till processen att utforma, genomföra och verifiera de haveriförebyggande och konsekvenslindrande åtgärder som 1989 införts vid samtliga kärnkraftverk.

I projektet HAFOS, APRI, APRI-2, APRI-3, APRI-4, APRI-5, APRI-6, APRI-7 och APRI-8 var en viktig uppgift att följa internationell forskning rörande svåra härdhaverier. En annan uppgift var att stödja eget arbete inom Sverige där forskningen på härdsmälteförlopp genomförts vid KTH och kemiska förhållanden i inneslutningen har undersökts vid Chalmers.

APRI 9-projektet har i stora drag haft samma inriktning som tidigare APRI-projekt.

## 1.1 Kort historik

Sedan början på 1980-talet har kärnkraftföretagen i Sverige och myndigheten samarbetat inom forskningsområdet svåra reaktorhaverier. Samarbetet var i början framför allt knutet till att förstärka skyddet mot omgivningskonsekvenser efter ett svårt reaktorhaveri genom att bl.a. ta fram system för filtrerad tryckavlastning av reaktorinnehållet. Sedan början på 1990-talet har samarbetet delvis ändrat karaktär och inriktats mer på fenomenologiska frågor av riskdominerande betydelse.

I början av 1986 beslutade regeringen att som villkor för fortsatt drift skulle utsläpps begränsande åtgärder vidtas vid reaktorerna i Forsmark, Oskarshamn och Ringhals. Åtgärderna skulle vara genomfördas senast vid utgången av 1988. I anslutning till dessa regeringsbeslut<sup>1</sup> uppdrog regeringen åt dåvarande Statens kärnkraftinspektion (SKI) att utöver redovisning av beslut som myndigheten fattat med anledning av regeringens nya driftsvillkor även redovisa en bedömning av behovet av fortsatta insatser inom området svåra haveriförlopp.

Efter myndighetens granskning av de åtgärder som vidtagits vid berörda anläggningar konstaterades i ett beslut<sup>2</sup> av den 19 december 1988 att de mål som regeringen angivit som villkor för fortsatt drift hade uppfyllts. I myndighetens beslut pekades emellertid också på att tillståndshavarna även fortsättningsvis behövde följa de forsknings- och utvecklingsinsatser som bedrevs och dra slutsatser om vilka ytterligare säkerhetshöjande åtgärder som bör komma ifråga vid de egna anläggningarna.

---

<sup>1</sup> Regeringsbeslut 14 ”Uppdrag att redovisa det fortsatta arbetet att begränsa utsläpp vid svåra reaktorhaverier”. Industridepartementet 1986-02-27.

<sup>2</sup> SKI-beslut ”Utsläppsbepränsande åtgärder vid kärnkraftverken i Forsmark, Oskarshamn och Ringhals”. SKI 1988-12-19.

I slutet av 1990-talet förtydligades myndighetens allmänna krav på utsläpps begränsande åtgärder genom föreskrifterna SSMFS 2008:1 om säkerhet i kärntekniska anläggningar. I föreskrifterna ställdes krav på att radiologiska olyckor skall förebyggas genom en för varje anläggning anpassad grundkonstruktion med flera barriärer och ett anpassat djupförsvar. Bestämmelserna om djupförsvar innehåller bl.a. krav på att utsläpp av radioaktiva ämnen till omgivningen skall förhindras och begränsas genom anordningar och förberedda åtgärder. I föreskrifterna infördes även krav på att säkerheten vid en anläggning fortlöpande skall analyseras och bedömas på ett systematiskt sätt, och i allmänna råd pekades på att bl.a. forskningsresultat särskilt bör beaktas vid sådan fortlöpande analys och bedömning.

Genom föreskrifterna SSMFS 2008:17 om konstruktion och utförande av kärnkraftsreaktorer har myndigheten sedan ytterligare förtydligat och skärpt kraven i vissa avseenden. Även svåra haverier med större härdskador skall beaktas när det gäller konstruktionen av inneslutningsfunktionen, instrumentering för övervakning av anläggningens tillstånd, samt för att kunna uppnå ett stabilt sluttillstånd med reaktorn så att den inte utgör ett hot mot omgivningen på lång sikt. I konsekvensutredningen<sup>3</sup> av föreskrifterna konstaterades att dessa krav, som inte fanns då reaktorerna konstruerades, tillkom i viss omfattning genom regeringsbeslutet om utsläpps begränsande åtgärder 1986.

Den svenska strategin för haverihantering innebär att inneslutningarna försetts med förstärkt inneslutningskyllning, tryckavlastning och filtrering av utsläpp. Den svenska strategin för att hantera en härdsmälta-att låta en härdsmälta falla i djupt vatten i inneslutningen – har visat sig vara ovanlig. Endast i ett fåtal andra reaktorer i världen tillämpas denna strategi aktivt. Eftersom den svenska strategin är ovanlig, finns det mycket lite internationell forskning som direkt belyser denna. Dock bedrivs internationell forskning om fenomen som även kan inträffa under ett svårt haveri i ett svenskt verk.

Det finns kvarvarande osäkerheter förknippade med den svenska strategin som behöver belysas ytterligare genom forskning. Genom den svenska strategin undviks troligen en stor inledande interaktion mellan betong och smälta. Å andra sidan kan ångexplosioner inträffa när smältan faller i djupt vatten. Forskningen på svåra haverier inriktas nu på att visa om de lösningar som har valts ger ett tillräckligt skydd för omgivningen, vilket vi idag håller för troligt med vissa osäkerheter som nämnts ovan.

Utgående från regeringens och myndighetens beslut i slutet av 1980-talet har myndigheten och tillståndshavarna tillsammans fortsatt att bedriva forskning om svåra haverier samt följa upp internationell forskning.

## 1.2 Projektets syfte

Projektet syftar till att visa om de lösningar som har valts i den svenska strategin för haverihantering ger ett tillräckligt skydd för omgivningen. Detta sker genom att få fördjupad kunskap om dels viktiga fenomen vid härdsmälteförlopp, dels mängden radioaktivitet som kan släppas ut till omgivningen vid ett svårt haveri.

---

<sup>3</sup> Konsekvensutredning av Statens kärnkraftinspektion förslag till föreskrifter (SKIFS 2004:2) om konstruktion och utförande av kärnkraftsreaktorer, Statens kärnkraftinspektion 2004-10-07.

För att nå syftet och i enlighet med rekommendationerna från APRI-8 (SSM rapport 2015:27) har projektet arbetat med följande uppgifter:

- att följa den internationella forskningen inom svåra haverier och utvärdera resultaten för att erhålla en god bedömningsgrund av de utsläppsbepränsande åtgärderna i svenska kärnkraftsreaktorer.
- att fortsätta att stödja forskningen på KTH och Chalmers om svåra haverier.
- att speciellt studera vissa fenomen som t ex smältans kylbarhet i reaktortanken och i reaktorinneslutningen samt haverikemi.
- att utveckla metodik (ROAAM+) för att beskriva och kvantifiera beroenden mellan haverifenomen.

### **1.3 Organisation och arbetsformer**

Projektet har bedrivits under åren 2015 - 2017 med en total kostnadsram på 21,6 MSEK. SSM och kärnkraftföretagen har bidragit med ungefärligen hälften var till denna budget. Under projektperioden har styrgruppen hållit 19 möten utöver de två uppföljningsmöten per år som har hållits på KTH (MSWI). De årliga Chalmersmötena ingår i de 19.

Arbetet inom projektet har varit uppdelat i 7 delprojekt med var sin delprojektledare.

#### **Deltagande i CSARP - NRC:s forskningsprogram**

Delprojektledare har varit Patrick Isaksson, SSM. En redogörelse för denna verksamhet ges i avsnitt 2.1

#### **Deltagande i STEM 2 – Source Term Evaluation and Mitigation**

Delprojektledare har varit Christian Linde SSM. En redogörelse för denna verksamhet ges i avsnitt 2.3.

#### **Deltagande i THAI 3 – Thermal-hydraulics, Hydrogen, Aerosols and Iodine project**

Delprojektledare har varit Johan Ljung Ringhals AB . En redogörelse för denna verksamhet ges i avsnitt 2.4.

#### **Deltagande i BIP 3 – Behaviour of Iodine Project**

Delprojektledare har varit Christian Linde SSM. En redogörelse för denna verksamhet ges i avsnitt 2.5.

#### **KTH:s forskning inom svåra haverier**

Forskningen vid KTH beskrivs i kap. 3 och har följts upp av styrgruppen genom två möten per år.

Under tidigare APRI-projekt har betydande framsteg av förståelse av de fysikaliska fenomen som inträffar i samband med svårt härdhaveri gjorts. Dessa insikter har resulterat i bedömmningen att endast deterministisk analys av fenomen såsom kylbarhet och ångexplosioner ej är tillräckligt för att få adekvat kunskap om hur fenomenen påverkar haveriförloppet. Därför började inom APRI 8 en så kallad Risk Oriented Accident Analysis Methodology (ROAAM) utvecklas som kombinerar probabilistiska metoder med deterministiska. I APRI 9 har denna utveckling resulterat i ett ramverk med en uppsättning beräkningsverktyg och gränssnitt i MATLAB. ROAAM+

innehåller olika beräkningsmodeller som kan identifiera stora bidrag till osäkerheter i riskbedömningar i samband med svåra härdhaverier. Detta ramverk kan användas i nivå 2-delen i PSA-analyser.

### **Chalmers forskning inom svåra haverier**

Forskningen vid Chalmers beskrivs i kap. 4 och har följs upp av styrgruppen genom ett möte per år. Forskningen under perioden har behandlat tellur- och ruteniumkemi.

Forskningen av fissionsprodukten tellur vid svåra kärnkraftshaverier har givit kunskaper om tellurs aerosolkemi. Denna forskning redovisas i avsnitt 4.2 – 4.4.

Ruteniumstudierna inkluderade effekter av temperatur, radiolysprodukter i luft och cesiumjodidaerosoler på de kemiska formerna av rutenium som kan transporteras i reaktorinneslutningen vid ett svårt reaktorhaveri. Denna forskning redovisas i avsnitt 4.5.

I forskningen rörande oxyhalider har jods interagerande med niobium, rutenium och tellur vid höga temperaturer undersökts. Denna forskning redovisas i avsnitt 4.6.

### **Uppföljning av kärnkraftsolyckan i Fukushima Daiichi**

Delprojektledare har varit Oddbjörn Sandervåg. En redogörelse för denna verksamhet ges i kapitel 5.

## **1.4 Erfarenhetsutbyte och seminarier**

Ett slutseminarium med ca 60 deltagare arrangerades i APRI:s regi den 7 - 8 mars 2018 på Johannesbergs Slott, Rimbo. Seminariets syfte var att presentera det arbete som utförts och de resultat som erhållits inom projektet APRI-9. Ett annat syfte med seminariet var också att ge möjlighet till diskussioner mellan representanter för kraftverken och de som deltagit i APRI:s arbete.

## **1.5 Ekonomi och rapportering**

Ekonomiskt har en viss omfördelning skett mellan olika delprojekt och några nya delprojekt har tillkommit men den totala budgetramen har innehållits.

De olika delprojekten har genererat publicerade artiklar, reserapporter och dylikt vilket framgår av referenslistan i varje kapitel.

## 2. INTERNATIONELL FORSKNING INOM SVÅRA HAVERIER

### 2.1 CSARP – NRC:s Forskningsforum

CSARP står för ”Cooperative Severe Accident Research Programme” och var från början den amerikanska kärnsäkerhetsmyndigheten NRC:s (Nuclear Regulatory Commission) forskningsprogram om svåra haverier. CSARP startade i början på 1990-talet. Numera deltar de flesta kärnkraftsländerna, inklusive Sverige och Finland, i CSARP-programmet där man utbyter forskningsresultat och erfarenheter samt gemensamt diskuterar inriktning och prioriteringar av fortsatt forskning inom området svåra haverier. Länder som har valt att delta på senare år är exempelvis Kina och Polen (där det senare landet har planer på att utveckla kärnkraft i landet). CSARP-mötena hålls årligen i USA och arrangeras av NRC. Mötesplatsen är främst i Washington, men ibland arrangeras CSARP även i Albuquerque, New Mexico, där Sandia National Labs (SNL) har sin placering. Forskning bedrivs inte inom CSARP-ramen i sig, utan CSARP är ett forum för erfarenhetsutbyte och förmedling av resultat inom området.

Ett viktigt inslag i CSARP är utvecklingen och tillämpningen av Melcor-koden. NRC:s huvudsakliga satsningar inom svåra haverier består av dels deltagande i internationella OECD/NEA-projekt samt att finansiellt stötta utvecklingen av Melcor som bedrivs av SNL. SNL har börjat skissa på en stor upgradering av haverikoden Melcor till något de kallar Melcor version 3. Ambitionen är att strukturera om koden så att de mekanistiska modellerna som beskriver haverifonenomenen skiljs från de numeriska beräkningarna. En modell som exempelvis behöver en ”solver” för differentialekvationer anropar denna i det kommande beräkningspaketet i Melcor. Idag är modellerna och de numeriska beräkningsmetoderna sammanlänkade vilket kan göra koden tämligen rörig. Ansatsen är ambitiös och forskningschefen på NRC bekymrade sig över finansieringen. Mer modesta uppdateringar av Melcor har gjorts inom nuvarande version 2.2, där bland annat ett paket som heter ”Lower Head Containment” (LHC) har introducerats i Melcor. Med det nya paketet kan tex. en core catcher simuleras. Utvecklingen av LHC har drivits av behoven från företaget NuScale som är en reaktorkonstruktör av ”Small Modular Reactors” (SMR).

Japan och Frankrike rapporterade under CSARP 2017 om kommande experiment kring sprinkling av bränslebassänger, där Japan (via JAEA) studerar sprinkling av BWR-bränsle och Frankrike (via IRSN) studerar sprinkling av PWR-bränsle. NRC har etablerat bilaterala avtal med Japan och Frankrike för att stödja och följa denna forskning. Syftet är att studera hur effektiv sprinkling av bränslebassängerna är som konsekvenslindrande system vid en överhettning av bränslelement i bränslebasängen. Ett viktigt fenomen i detta sammanhang är motströmsflödet (counter current flow) som begränsar sprinklings effektivitet.

I USA bedrivs ett arbete med att gå igenom gamla experimentella data och att använda dessa data för att vidareutveckla koder som Melcor mot dessa data. Koder som Melcor och MAAP börjar nu bli så pass välutvecklade att de börjar användas för exempelvis haverihantering, medan koderna tidigare har haft en mer begränsad användning för att riskinformera. En annan observation är att mycket arbete läggs på beaktande och hantering av osäkerheter som stöd till ett riskinformerat beslutsfattande. Här är KTH:s utveckling av ROAAM+ ett exempel på detta arbete som har sin motsvarighet inom andra forskningsgrupper i USA och Europa.

## 2.2 STEM - Source Term Evaluation and Mitigation

STEM-projektet startade år 2011 i syfte att skaffa bättre kunskap om komplexa fenomen som påverkar den s.k. källtermen vid en radiologisk olycka, dvs. de radioaktiva ämnen som förväntas släppas ut till omgivningen i samband ett haveri. Projektet motiverades av ett behov att öka allmänhetens förtroende av det faktum att många äldre reaktorer planerade för förlängd drifttid. Det handlade bl.a. om att förse beredskapsorganisationen med bättre metoder för att förutsäga och hantera fenomenen i samband med haveriet, för att på så sätt minska konsekvenserna för omgivningen. Projektets huvudsakliga fokus ligger på förståelse för fenomen kopplade till radioaktiv jod och dess interaktion med andra ämnen, samt också transportfenomen kopplade till rutinium som är en annan viktig fissionsprodukt.

### 2.2.1. STEM-1

STEM-1 genomfördes under åren 2011-2015 och hade en budget på 3,5 M EUR. Projektet leddes av IRSN i Frankrike med deltagande organisationer från Kanada, Tjeckien, Finland, Tyskland, Korea och U.S.A. Sverige deltog inte i STEM-1, men har genom deltagande i det pågående fortsättningsprojektet STEM-2 även tillgång till resultaten från det första projektet.

I STEM-1 behandlades följande frågor:

- Frigörande av jod i det medellånga perspektivet, speciellt med fokus på stabiliteten hos jodaerosoler och partiklar under bestrålning (sönderfall inducerat genom bestrålning som leder till bildande av gasformig jod).
- Interaktion mellan jod och målade ytor under bestrålning i ett kort och ett medellångt perspektiv.
- Kemin för transport av rutinium i primärsystemet med fokus på karakterisering av olika former av rutinium, i synnerhet fördelningen mellan gas och kondenserade former.

Försök har utförts för att studera jods frigörelse då en målad yta med deponerad elementär jod bestrålas. Resultaten visar att omvandling till organisk jod och dess frigörelse motverkas om den relativa fuktigheten stiger i atmosfären, exempelvis leder en ökning av den relativa fuktigheten från 20 till 60 % att frigörelsehastigheten reduceras med en faktor tre. Detta kan förklaras med att ökad fuktighet gör att joden diffunderar djupare in i färglagret. Frigörelsen av elementär jod minskar också något vid ökad fuktighet, men temperatur och dosrat spelar större roll. Höjning av dessa parametrar kan antas leda till att interaktionen med färgen ökar vilket leder till starkare bindning av jod.

Motsvarande försök med deponerad cesiumjodid visar att målade ytor har en förmåga att binda denna, men att denna förmåga saknas hos kvarts- eller stålytor. Detta kan förklaras med att cesiumjodids interaktionen med färgytan förbättras genom bestrålning eller att omvandling av cesiumjodiden till elementär jod leder till att joden återadsorberas på färgytan på samma sätt som i försöken där man utgår från deponerad elementär jod. Jodoxider sönderfaller till viss del vid bestrålning, vilket visas av frigörelseförsöken där man utgår från deponerade jodoxider.

Resultaten från det första STEM-projektet har gett ökad förståelse av nyckelfenomenen inom jodkemin och har lett till förbättrade modeller, t.ex. för ASTEC där förbättringar har skett avseende i) interaktion mellan elementär jod och metyljodid under bestrålning, ii) bildande och radiolytiskt sönderfall av jodoxider i gas- och i aerosolform,

iii) radiolytisk omvandling av gasformig elementär jod till metyljodid, iv) interaktion mellan elementär jod och stål eller aerosoler.

Interaktionen mellan jod och målade ytor har kartlagts i en litteraturstudie som sammanfattar status i frågan om hur färgens förmåga att interagera påverkas av temperatur, strålning, fuktighet och åldrande. Slutsatserna utgör utgångspunkt för de försök som senare föreslogs för fortsättningsprojektet STEM-2 (se nästa avsnitt).

När det gäller rutenium så är det visat att oxidativa betingelser under ett haveri kan leda till frigörelse och transport bl.a. genom bildandet av den flyktiga formen ruteniumtetroxid. Förståelsen för ruteniums uppträdande är emellertid begränsad. Frigörelse- och transport försök har utförts i den rörugn (START) där rutenium kan förångas och transporteras med hjälp av ett gasflöde. Uppställningen har stora likheter med den rörugn som har använts i samarbetet emellan Chalmers och VTT för ruteniumförsök som genomfördes tidigare än försöken vid IRSN.

Ruteniumresultaten har lett till implementering i ASTEC av en preliminär modell för ruteniumtransport i primärsystemet. Detta har gett en första möjlighet att implementera en källterm för rutenium i verktyget för PSA nivå 2, vilket ledde till slutsatsen att de radiologiska konsekvenserna av rutenium kan vara signifikanta.

Resultaten från det första STEM-projektet bidrog tillsammans med slutsatserna från den workshop som hölls inom OECD-NEA/NUGENIA-SARNET i mars 2015 till identifiering av fortsatta frågeställningar bl.a. om jods uppförande. Detta ledde till fortsättningsprojektet STEM-2 där SSM deltar för APRI:s räkning.

## 2.2.2. STEM-2

STEM-2 har en budget på 2,48 M EUR för de fyra åren 2016-2020, varav Sverige totalt bidrar med 24 800 EUR, vilket motsvarar 1 % av projektets budget. Deltagande länder: Frankrike, Finland, Japan, Kanada, Korea, Storbritannien, Sverige, Tyskland och USA. Spanien har för avsikt att ansluta men har ännu inte tecknat avtal.

I den analytiska arbetsgruppen ingår följande organisationer med olika koder: GRS (COCOSYS V3), IRSN (ASTEC V2.1.1.1), KINS (RAIM V1.5), NNL (INSPAIR) och VTT (ASTEC V2.1.1.0).

Centrala frågor rör åldringseffekter på målade ytor vid höga stråldoser ( $>100$ - $1000$  kGy), jodoxiders sönderfall till flyktiga jodformer och ruteniumtransport i primärsystemet. Det experimentella arbetet utförs av IRSN (*L'Institut de Radioprotection et de Sécurité Nucléaire*) i Cadarache, Frankrike.

STEM-2 har följande fokusområden inom jod- och ruteniumkemi:

- *Åldringseffekter på målade ytor* - Åldringens påverkan på målade ytors interaktion med jod studeras även inom BIP-3 (Behaviour of Iodine Project 3). Denna testserie i STEM-2 innehåller kompletterande experiment för att undersöka åldringseffekter vid höga stråldoser ( $>100$ - $1000$  kGy), vilket motsvarar den förväntade dosen vid en LOCA-transient. Vid försöken ska kinetiken för frigörande från epoxifärg av både elementär jod och metyljodid mätas och jämförelser göras med frigörelser från normalbestrålade ytor.
- *Radiolytiskt inducerat sönderfall av jodoxider* - Sönderfall av jodoxider ( $I_xO_y$ ) har tidigare uppmärksammats av STEM-1 som en källa till bildning av elementär jod ( $I_2$ ). I testserien ska kinetiken för frigörelse av elementär jod och metyljodid

mäts ”on-line” vid bestrålning av jodoxid på ett färgprov. Ytterligare några tester ska genomföras under icke-radiolytiska betingelser, exempelvis hydrolysis av deponerat material på ytor.

- *Kemiskt inducerat sönderfall av jodoxider* - I denna serie ska de potentiella reaktionerna mellan jodoxider och kolmonoxid (CO), vätgas ( $H_2$ ), samt metangas ( $CH_4$ ) undersökas. Samtliga dessa reaktioner förväntas påverka jods flyktighet genom omvandling av jodoxiderna till elementär jod eller till methyljodid.
- *Radiolytisk oxidation av jodaerosoler i multikomponentblandning* - Liksom övriga testserier under söks här hur källtermen för flyktiga jodformer påverkas av radiolytisk oxidation av jod i aerosolform som förväntas transporteras från primärsystemet till inneslutningen vid ett haveri. Försöken innehåller både torra och våta ytor.
- *Rutenium* - I syfte att komplettera observationer från det första STEM-projektet gällande ruteniumtransport från primärsystemet genomförs en ny testserie under ytterligare variation av betingelser. Det har tidigare konstaterats att fördelningen mellan olika former av rutenium är avgörande för flyktigheten där rutenium-tetroxid ( $RuO_4$ ) är en identifierad form med hög flyktighet. Även graden av återförgasning av deponerat material är en viktig parameter. I de nya testerna ska en mer representativ yta av rostfritt stål användas för deponeringen. Inverkan av ånga ska också studeras. Förhöjda oxidativa betingelser ska användas för att mer efterlikna de betingelser som uppstår genom radiolysis av luft vid ett haveri. Avslutningsvis ska även representativa gaser och/eller aerosoler användas som kan inverka på ruteniumtetraoxidens uppförande.

#### *Åldringseffekter på målade ytor*

Försöken AP1 och AP2 syftade till att studera ytor som har åldrats genom långvarig bestrålning med höga doser. I AP1 utsattes ytan för 1 MGy/timme i 30 timmar. I AP2 åldrades ytan först med 0.1 MGy/timme och sedan med 1 MGy/timme vid 80 °C i sammanlagt 30 timmar. På ytorna applicerades sedan jod som fick interagera med färgytan under bestrålning (ca 2 kGy/timme i 30 timmar), under vilken frigörelse av organisk jod (RI) och elementär jod ( $I_2$ ) studerades. Resultaten från AP1 visar att båda jodformernas flyktighet reducerades signifikant som en följd av åldrandet. Detta kan förstås som att den höga stråldosen degraderar färgstrukturen på ett sådant sätt att den ger ökade bindningsmöjligheter för elementär jod. Samtidigt reduceras möjligheterna till bildande av organiska radikaler vilket leder till minskad frigörelse av organisk jod. Genom åldringsbehandlingen i AP2 påverkades flyktigheten av organisk jod i mindre utsträckning och flyktigheten för elementär jod inte alls.

Strålnings- och temperaturförhållandena för olika färgytor kan se olika ut i olika delar av inneslutningen under ett svårt haveri och ytornas egenskaper kan därigenom också skilja sig i ett verkligt fall. Liksom i BIP-3 är den generella slutsatsen i STEM-2 att flyktigheten för deponerad jod är lägre från åldrade ytor. Flera tester med varierad bestrålning för åldringssteget kommer utföras för att studera effekten av dos.

#### *Radiolytiskt inducerat sönderfall av jodoxider till flyktiga jodformer*

Försök har genomförts för utvärdering av jodoxiders kemiska sönderfall till andra jodformer, dels genom värmbehandling och dels genom gammabestrålning. Jodoxiderna framställdes i försöken genom oxidation av elementär jod med ozon som sedan

tilläts deponera på provkuponger av kvarts. Det deponerade materialet har karakteriseras med Ramanspektroskopi som visar på olika oxiderade jodformer ( $I_2O_4$ ,  $I_4O_9$ ,  $HIO_3$ ).

Termiska försök utfördes sedan vid temperaturer mellan 80 och 120 °C vid varierande relativ fuktighet mellan 50 och 80 %. Försöken visar att elementär jod bildades både genom termiskt sönderfall av jodoxiderna samt vid fortsatt hydrolysk i närvaro av ånga. Försöken visar också att gammabestrålning är en viktigare orsak till jodoxiders sönderfall än värmeförhöjning, men att instabiliteten är påtaglig vid temperaturer kring 120 °C.

#### *Kemiskt inducerat sönderfall av jodoxider till flyktiga jodformer*

Försök har utförts som syftar till att studera jodoxiders ( $I_xO_y$ ) kemiska sönderfall genom gammabestrålning under reduktiva betingelser i närvaro av kolmonoxid (CO). Kolmonoxid skulle kunna bildas under ett haveri då borkarbid frigörs från degradrade styrstavar eller genom interaktioner mellan smälta och betong. Frågan gäller här om de betingelserna kan göra att jodoxiderna förflyktigas genom reduktion till elementär jod ( $I_2$ ).

En jämförelse med referensförsöket som utfördes utan tillsats av kolmonoxid visar att de jodformer ( $I_2O_4$ ,  $I_4O_9$ ,  $HIO_3$ ) som bildades i närvaro av kolmonoxid, producerades i liknande mängder, men att kinetiken för bildandet varierade. Resultaten visar på en fördröjning av frigörelsen av elementär jod i närvaro av kolmonoxid.

Flera tester kommer utföras i serien, dels med förhöjd relativ fuktighet (80 %) och dels med lägre syrgashalt (3 %). Ytterligare försök under reduktiva betingelser med vätgas i atmosfären kommer att genomföras.

#### *Ruteniumtransport i primärsystemet*

Försök har påbörjats i en testmatris och utgår från ruteniumdioxid ( $RuO_2$ ) eller rutenium-tetraoxid ( $RuO_4$ ). Temperaturen varieras mellan 900 och 1200 °C och den relativ luft-fuktigheten från 0 till 100 %. Försöken utförs antingen i kvartsrör eller i rör av rostfritt stål för ruteniumtransporten samt med eller utan tillsats av kvävedioxid ( $NO_2$ ). Försöksmatrisen avseende ruteniumtransport i primärsystemet ska ses som kompletterande till den studie som genomfördes under tidigare samarbete mellan VTT och Chalmers, som finansierades av APRI och NKS.

Kinetiken för ruteniumtransporten har uppmäts och visar att förångningshastigheten är oberoende av den mängd rutenium som finns att förångas utan beror snarare av hur stor yta som materialet är utbredd över. Den totala mängden transporterad rutenium uppgick som högst till ca 6 %. Kinetiken för förångning är densamma för upprepade försök med samma material, vilket tyder på att materialet är tämligen kemiskt stabilt.

Bland försöken kan nämnas att IRSN inte har observerat samma effekt som Chalmers/VTT när det gäller kvävedioxids ( $NO_2$ ) påverkan på flyktigheten hos ruteniumdioxid ( $RuO_2$ ). Sökning pågår för att finna en förklaring till detta.

#### *Multi-komponent aerosoltester*

Studier planeras nästa år avseende termiskt sönderfall av aerosoler av multikomponent-blandningar bestående av bl.a. silverjodid ( $AgI$ ), cesiumjodid ( $CsI$ ), cesiummolybdat ( $Cs_2MoO_4$ ) och tenndioxid ( $SnO_2$ ).

## **2.3 THAI 3 - Thermal-hydraulics, Hydrogen, Aerosols and Iodine project**

### **2.3.1. Bakgrund och syfte**

Det övergripande målet med THAI-projektet är att ta itu med öppna frågor om fenomen kopplade till vätgas, jod och aerosoler i inneslutningen vid svåra haverier i lättvattenreaktorer. Förståelsen för de processer som äger rum under sådana händelser är avgörande för möjligheten att kunna utvärdera vilka utmaningar som kan uppstå mot inneslutningens integritet (vätgas), samt för att bestämma storleken på mängden luftburen radioaktivitet (jod och aerosoler) i inneslutningen vid svåra haverier.

THAI-projektets olika faser har genom åren bidragit med värdefulla data för utveckling av förståelsen för hur och under vilka betingelser som vätgas defligrerar. Ytterligare data har genererats som har använts för att bättre beskriva hur passiva autokatalytiska rekombinatorers (PARs) prestanda påverkas under olika försvårande betingelser och hur de bäst kan användas för att effektivt minska vätgashalten under ett haveri. Beträffande fissionsprodukter har projektet kartlagt samspelet mellan gasformig jod och olika typer av aerosoler, samt undersökt huruvida PAR kan integrera jod och därigenom påverka källtermen.

Parallellt med det experimentella programmet har ett omfattande analytiskt arbete utförts, som har innehållat kodberäkningar för att bedöma förberedande försök och stödja utformning av nya tester, samt för att utvärdera resultaten och extrapolera dessa till reaktorbetingelser. Projektet har bidragit till validering och vidareutveckling av avancerade LP- och CFD-koder som används för reaktortillämpningar, t.ex. genom att tillhandahålla experimentella data för ”benchmark”-beräkningar med olika koder. Liksom många andra OECD/NEA-projekt bidrar THAI också till att upprätthålla kompetens inom reaktorsäkerhet och till att främja internationellt samarbete.

### **2.3.2. OECD-THAI**

En första etapp av projektet, OECD-THAI, pågick under åren 2007–2009. Totalt genomfördes över 70 försök. Nedan redovisas projektets olika testområden med huvudsakliga slutsatser för respektive område (1):

- *Helium/hydrogen Material scaling (HM1-5):*  
Testerna bekräftade att helium kan användas istället för vätgas vid undersökningar av flödeskemiska fenomen i inneslutningsatmosfären. Beräkningar med olika beräkningskoder (både av LP- och CFD-typ) visade att stora framsteg skett i modelleringen av stratifiering och omblandning.
- *Hydrogen Deflagration (HD1-29):*  
Genom att variera olika parametrar såsom initialtryck och -temperatur, ånghalt, förbränningssriktning och gasernas spatiala fördelning kunde deras inflytande på tryck- och temperaturförlopp, flamfrontspridning och förbränningens fullständighet bestämmas.
- *Hydrogen Recombiner (HR1-30):*  
Kunskapsbasen kring olika PAR-typers prestanda under typiska svåra haveriförhållanden ökade markant som ett resultat av HR-testerna. Detta gäller både PAR-eheternas förmåga att komma igång, deras rekombineringshastighet och potentialen för PAR-inducerad antändning. En särskiltiktig slutsats var att PAR-

inducerad antändning bara är möjlig i ett relativt begränsat område i Shapirodia-grammet.

- *Interaction of metal iodides with passive autocatalytic recombiner (HR-31):* Testet visade att cesiumjodid kan brytas ner och omvandlas till gasformig jod i en omfattning som kan påverka källtermen till inneslutningen.
- *Passive autocatalytic recombiner poisoning (HR-32):* Testet visade att förgiftning av PAR-enheterna i form av aerosoler och jod inte förefaller påverka prestandan i någon större utsträckning.
- *Aerosol wash-down (scoping test):* Testet visade att svagt lutande ytor utsätts för nedtvättning av CsI-partiklar med en tidskala som varierar från minuter till timmar. Tidsskalan och även omfattningen/effektiviteten beror på vattenflödet och ytans egenskaper.

Det experimentella arbetet kompletterades med analysverksamhet genom att en analytisk arbetsgrupp etablerades med målsättningen att utvärdera testresultaten för att validera och vidareutveckla modeller och analysverktyg.

### 2.3.3. OECD-THAI2

En andra etapp av projektet, OECD-THAI2, pågick under åren 2011–2014 då totalt 16 försök genomfördes. Nedan redovisas projektets olika testområden med huvudsakliga slutsatser för respektive område (2):

- *Release of gaseous iodine from a flashing jet (Iod29):* Försöket syftade till att undersöka hur gasformig jod kan frigöras vid flashning i samband med ett ånggeneratortubbrott. Testet misslyckades då man trots ansträngningar med förberedande analyser inte fick rätt kemiska förhållanden för att kunna dra relevanta slutsatser. Ingen gasformig jod detekterades i THAI-behållaren (halterna hamnade under detektionsgränsen för instrumenteringen) då injicerad molekylär jod snabbt reagerade medstålet i förvaringsbehållarens vägg under uppvärmning innan försöket påbörjades.
- *Deposition of molecular iodine on aerosol particles (Iod25-26):* Experimenten visade tydligt skillnaden mellan reaktiva (Ag) och icke-reaktiva ( $\text{SnO}_2$ ) aerosolers förmåga att påverka inventariet av gasformig jod. Minskningen av gasformig jod var betydligt effektivare (ca 25 gånger snabbare) med Ag-aerosoler, som möjliggör s.k. kemisorption, jämfört med  $\text{SnO}_2$ , som endast tillåter svagare s.k. fysisorption.
- *Hydrogen combustion during spray operation (HD33-35):* Försöken har gett kunskap om sprinklingens inverkan på deflagrationsförfloppet. Med något enstaka undantag visar försöken att sprinklingen har en dämpande effekt på det resulterande, maximala trycket. Sprinklingens nedkyllning av reaktionszonen är den dominerande effekten, men maximala tryck och temperaturer reduceras även pga. att den ånga som produceras via förångning av vattendroparna fungerar som en värmesänka.
- *PAR operation in case of low oxygen content (HR33-42):* Försöken har utökat databasen för rekombinatorernas prestanda med nya förhållanden. Testerna visar att rekombineringen startar vid mycket låga  $\text{O}_2$ -koncentrationer ( $\Phi \ll 1$ ) där  $\Phi = 2 c(\text{O}_2)/c(\text{H}_2)$  är ett mått på tillgången på syrgas och

är = 1 för en stökiometrisk blandning, <1 vid syrgasunderskott och >1 vid syrgasöverskott. För  $\Phi \leq 1$  styrs rekombineringshastigheten främst av syrgasdiffusjon genom katalysatorns yta, dvs. av tillgången på syrgas. För  $1 < \Phi \leq 2$  styrs rekombineringshastigheten av tillgången på både syrgas och vätgas. För  $\Phi > 2$  blir tillgången på vätgas styrande och ökningen i effektivitet ( $\gamma$ , förbrukningsgrad av vätgas) blir väldigt liten för ökande syrgashalt. Förbrukningsgraden  $\gamma$  stannar på runt 50-70 %.

Även i THAI2 etablerades en analytisk arbetsgrupp för att samla den analytiska verksamhet som bedrivits av deltagarna för bl.a. utveckling och validering av både beräkningskoder och modeller.

Projektet redovisades dels i en öppen slutrapport (2), dels i en mer omfattande slutrapport (3) som är endast öppen för projektets deltagare.

#### 2.3.4. OECD-THAI3

Projektets tredje etapp, OECD-THAI3, löper under perioden februari 2016 – juli 2019 med en sammanlagd budget på 4.75 miljoner euro. Projektet kan nu dra fördel av den utökade anläggningsutförningen THAI+ med en ny behållare (PAD) kopplad till den ursprungliga, se Figur 2.3.1.

Deltagande länder i THAI3:

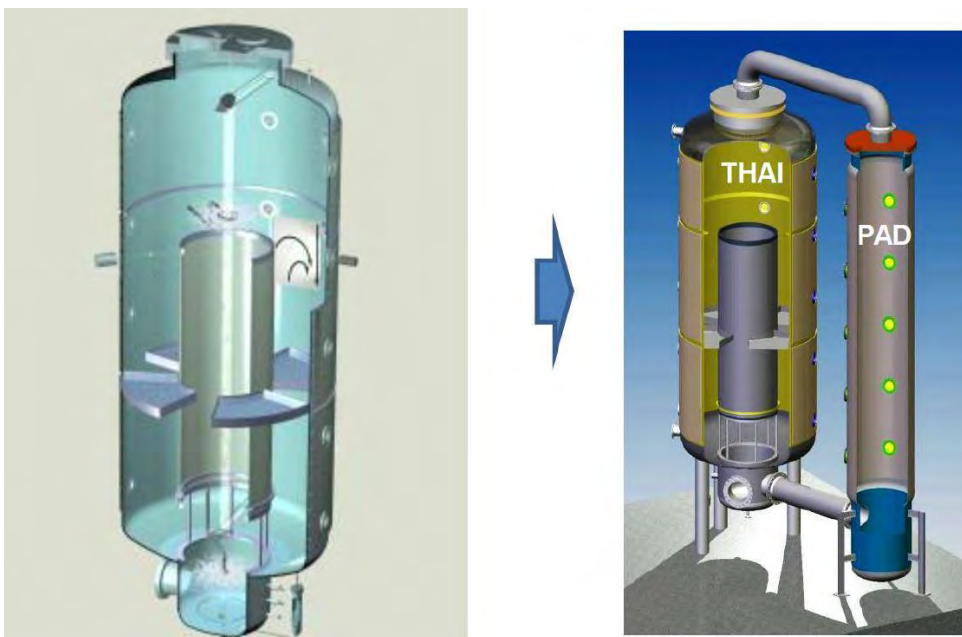
Tyskland (Becker Technologies (OA – ”operating agent”), GRS, Areva, RWTH-Aachen), Belgien (BelV, VKI), Canada (CNL), Finland (STUK, VTT), Frankrike (IRSN, EDF), Indien (BARC, AERB, NPCIL), Japan (NRA, JAEA), Kina (SNPSDC, SNPTC, SPIC), Luxemburg (MESR), Schweiz (PSI), Slovakien (UJD), Storbritannien (ONR), Sverige (SSM/APRI), Sydkorea (KAERI, KINS, KHNP), Tjeckien (UJV, NRI) och Ungern (MVM Paks, NUBIKI)

Det pågående projektet undersöker följande fyra huvudsakliga frågeställningar (4):

- *PAR operation under counter-current flow conditions:*  
Syftet är att kartlägga hur PAR-enheternas uppstartsbehörighet och prestanda påverkas av motströmsflöde, samt hur prestandan påverkas av PAR-enhetens utformning såsom skorstenshöjd. Samtliga försök (totalt 5 st) har redan genomförts. Bland slutsatserna hittills kan nämnas att kapaciteten hos Areva:s PAR inte påverkas nämnvärt av motströmsflöde. Effekterna av motströmsflöde är samma vid högre som vid lägre omgivningstryck, medan PAR-inducerad antändning sker något tidigare vid ett högre omgivningstryck. Utformningen av skorstenen i Areva:s PAR-enheter (den är inte öppen rakt uppåt) förhindrar effektivt inträngning av motströmflödet in i PAR-enheten. Motströmflöde uppstår endast vid väldigt låga vätgaskoncentrationer.
- *Hydrogen combustion in connected two compartment system:*  
Försöken ska undersöka hur förbränningens förloppet (såsom flamfrontsprage-ring) påverkas av dels strömningsförhållanden under konvektiva förhållanden, dels stratifierade förhållanden med en vätgaskoncentrationsgradient genom att utnyttja THAI+-anläggningen med separata utrymmen som står i förbindelse med varandra. Totalt 6 försök planeras.
- *Fission product re-entrainment from water pool at elevated temperature:*

Försöksserien syftar till kartläggning av hur fissionsprodukter (både aerosoler och flyktig jod) kan återföras (via s.k. ”re-entrainment”) till inneslutningsatmosfären vid förhöjda temperaturer i kondensationsbassäng/sump antingen genom kontinuerlig uppvärmning till kokning eller genom trycksänkningsinducerad kokning (såsom vid filtrerad tryckavlastning). Inverkan av olika hydrodynamiska förhållanden, olika kemiska förhållanden (såsom pH och tillsatser) samt egenskaper hos gasflödet till vattenbassängen (t.ex. massflöde, andel icke-kondenserbara gaser m.m.) kommer att undersökas. Hittills har två av tre planerade försök genomförts. Bland slutsatserna hittills kan lyftas fram att överföringen av aerosoler till gasfasen ökar (inte oväntat) medökande temperatur. Överföringen är mindre då flödet i nedblåsningsrören består av ren luft än för en blandning av luft och ånga. Man uppnådde en stabil stratifiering av I<sub>2</sub> i gasfasen med högre koncentrationer av gasformig I<sub>2</sub> högre upp i behållaren. I<sub>2</sub> deponerade troligtvis på stålväggarna i gasfasen, vilket ger en källa till re-suspension i en senare fas. Den ökade överföringen av I<sub>2</sub> från sump till gasfas vid kokning gav ett gasförmigt jodinventarium som var ca 100 gånger högre än utan kokning.

- *Aerosol and iodine re-suspension from deposits by hydrogen deflagration:*  
Syftet är att undersöka frigörelse av fördeponerade aerosoler och olika former av jod från ytor i samband med vätgasdeflagration samt hur målade ytor kan påverkas av förbränningen. Ett integralt test med två separata testfaser planeras.



Figur 2.3.1. Den ursprungliga anläggningen THAI (vänster) och den nyligen utökade THAI+ (höger)

### 2.3.5. Referenser

- (1). OECD/NEA THAI Project – Hydrogen and Fission Product Issues Relevant for Containment Safety Assessment under Severe Accident Conditions, Final Report, NEA/CSNI/R(2010)3, <https://www.oecd-nea.org/nsd/docs/2010/csni-r2010-3.pdf>.
- (2). Aerosol and Iodine Issues, and Hydrogen Mitigation under Accidental Conditions in Watercooled Reactors, Thermal-hydraulics, Hydrogen, Aerosols and Iodine (THAI-2) Project, Final Report, <http://www.oecd-nea.org/nsd/docs/2016/csni-r2016-8.pdf>

(3). OECD-NEA THAI-2 Project, Final Report, Aerosol and Iodine Issues and Hydrogen Mitigation under Accidental Conditions in Water Cooled Reactors (Restricted Version), Becker Technologies GmbH, Report No. 1501420-FR-1, May 2015

(4). AGREEMENT ON THE OECD NUCLEAR ENERGY AGENCY (NEA) THAI-3 PROJECT

## 2.4 BIP - Behaviour of Iodine Project

BIP-3 är en fortsättning på OECD/NEA-projekten BIP och BIP-2, och syftar till att undersöka frågeställningar kring jods uppförande under svåra haveriförhållanden. Detta tredje program har följande huvudmål:

- *att förbättra möjligheten att simulera jods adsorption och desorption på ytor i reaktorinneslutningen,*
- *att förutsäga metyljodids uppförande (bildande och sönderfall) under haveriförhållanden,*
- *att undersöka hur åldring av målade ytor inverkar på dessa processer,*
- *att undersöka inverkan från föroreningar som klor ( $Cl_2$ ) och nitrösa gaser ( $NO_x$ ).*

Det experimentella arbetet utförs av Canadian Nuclear Laboratories (CNL) i Chalk River, ca 18 mil nordväst om Ottawa i Kanada. Detta är samma anläggning som i de tidigare BIP-programmen, men som vid denna period organiserade under Atomic Energy of Canada Limited (AECL).

BIP-3 genomförs under år 2016-2018 och har en budget på totalt 1 M EUR, varav Sverige totalt bidrar med 10 000 EUR, vilket motsvarar 1 % av projektets budget.

Deltagande länder: Kanada (CNL - *operating agent*), Belgien (GdF Suez – Tractebel S.A.), Finland (STUK, VTT), Frankrike (IRSN, EDF), Japan (NRA, NSR, JAEA), Korea (KAERI, KINS), Schweiz (PSI), Spanien (CIEMAT), Storbritannien (NNL & EDF), Sverige (SSM/APRI), Tyskland (GRS, Areva) och USA (NRC)

I den analytiska arbetsgruppen ingår följande organisationer med olika koder: CNL (LIRIC V3.3), GRS (COCOSYS V3), IRSN (ASTEC V2.1.1.1), NNL (INSPAIR), Tractebel (ASTEC V2.1.1.1) och VTT (ASTEC V2.1.1.0).

### *Åldringseffekter på målade ytor - bildandet av metyljodid*

Termisk, kemisk och strålningsinducerade förändringar av målade ytor förväntas påverka jods interaktioner med dessa ytor. För försöken används färgprover, s.k. ”kuponger” som har förbehandlats med olika grad av strålning eller som har åldrats naturligt eller med andra simulerade metoder.

Försöksserien är uppdelad i studier av adsorption och desorption (upptag och frigörande) av jod, frigörande av lösningsmedel eller andra organiska kolföreningar från de olika ytorna, samt studier av hur bildandet av metyljodid påverkas av dessa åldringsmetoder.

Försök har även genomförts för att undersöka bildandet av metyljodid vid gammastrålning av deponerad jod på målade ytor. Åldrade färgprover preparerade med jod bestrålades med ca 0,75 Gy/h i 2,5 timmar. Resultaten visar att färgprover som har åldrats naturligt ger en produktion av metyljodid som är jämförbar med produktionen från en nymålad yta. Färgprover som har åldrats genom värmeförädling eller

gammabestrålning uppvisar däremot en minskad produktion av metyljodid med stigande grad av åldring. Detta kan tolkas som att åldring leder till en minskning av mängden flyktigt organiskt material som kan omvandlas till metyljodid vid gammabestrålning i närvaro av jod.

Färgtjockleken är ytterligare en parameter som har inverkan på resultaten. En jämförelse av försök med prover från samma batch men med varierande färgtjocklek visar att ett tjockare färglager ger en högre produktion av metyljodid.

Sammanfattningsvis ger färsk färgytor den största produktionen av metyljodid vid gammabestrålning. Denna förmåga minskar med provets ålder. Förändringen är dock måttlig med en observerad variation på som mest en faktor fyra.

#### *Åldringseffekter på målade ytor - Lakning av organiska föreningar (TOC)*

Lakningsförsök av åldrade prover har genomförts för att studera frigörelse av organiska föreningar vid förhöjd temperatur. Proverna värmdes i vattenbad vid 65 °C under 300 timmar varefter vattnet analyserades med avseende på organiska och oorganiska kolföreningar. Försöken visar på en högre grad av frigörelse från äldre prover oavsett åldringsmetod, vilket alltså även gäller naturligt åldrade prover. Ökad frigörelse erhålls också från prover försedda med ett tjockare färglager. Resultaten kan tolkas som att åldring förstör den polymera färgstrukturen, vilket leder till en fragmentering som underlättar urlakning. Graden av urlakning varierar dock endast med upp till en faktor tre jämfört med nya färgprover.

#### *Åldringseffekter på målade ytor - Adsorptions/desorptionskapacitet*

Under tidigare BIP-projekt har det observerats att desorption av jod från målade ytor kan ske även utan att ytan utsätts för strålning. Fenomenet observeras framför allt då stora mängder jod har applicerats på ytan. Detta tolkas som att det finns en begränsad mängd aktiva "sites" per ytenehet, som kan binda jod irreversibelt och att den resterande mängden endast binds reversibelt och därigenom kan frigöras även i frånvaro av strålning.

En testserie har utförts där man varierar jodkoncentrationen i gasfas med flera storleksordningar för att man på så sätt ska kunna studera om det finns en övre mättnadsgräns för mängden jod som kan adsorberas på ytan. För serien används ytor med epoxibaserad (Amerlock) och alkydbaserad färg (Ripolin).

De tidigare försöken i serien har utförts med färgprover av epoxifärgen "Amerlock Paint". Dessa hade åldrats med tre olika metoder; naturlig åldring (0, 1, 3 och 7 år), gammabestrålning (100 kGy och 1000 kGy) och termiskt (upphettning till 130 °C i torr respektive ångmättad atmosfär under 96 timmar).

Försöken gällande adsorption av jod på de åldrade färgproverna visar att adsorptionshastigheten sjunker med stigande grad av åldring oavsett vilken av de tre åldringsmetoderna som hade använts. Förhöjd ånghalt förstärker trenden ytterligare. Dessa resultat skiljer sig från de effekter som noterades under BIP-1, där naturligt åldrade prover gav en ökad deponeringshastighet av jod. Det spekuleras i möjligheten att färgtjockleken är ytterligare en parameter som kan ha en inverkan på deponeringshastigheten. Detta skulle komplikera modellering av deponeringsprocessen och även försvåra analys av specifika fall där färgtjockleken är okänd. Det kan ändå konstateras att trenderna är desamma oavsett val av åldringsmetod och att variationerna i deponeringshastigheter inte är större än upp till en faktor två mellan de olika försöken.

Desorptionsförsöken visar att färgprovernas förmåga att kvarhålla jod sjunker vid ökning av den mängd som inledningsvis har applicerats på ytan. Det tycks alltså uppstå en gradvis mättnad då mängden deponerad jod ökar på ytan. Desorptionshastigheten är också beroende av koncentrationen av jod i gasfas, vilket är förväntat vid en jämviktsprocess mellan adsorption och desorption.

Försök med åldrade Ripolinprover (100 och 250 KGy) visar att de har samma förmåga att kvarhålla deponerad jod som icke åldrade prover av Amerlock. En jämförelse mellan desorptionshastigheter visar att de är likvärdiga, jod binds lika bra på båda ytorna.

Sammanfattningsvis är trenden att adsorptionshastigheten är oberoende av hur proverna har åldrats, men att åldring gör att adsorptionshastigheten sjunker något, som mest med en faktor 2 mellan de olika försöken. Förhöjd ånghalt förstärker trenden ytterligare. Åldrade prover har också en god kvarhållande förmåga där desorptionsgraden inte är mer än som mest 6 % av den deponerade joden. En viss mättnad visar sig dock när det gäller färgprovets förmåga att binda jod, då desorptionsgraden är högre i försök med tjockare ytlager av jod. Ytans förmåga att kvarhålla joden avtar alltså med tjockleken på jodlagret.

#### *Påverkan av reaktiva gaser i inneslutningen*

Det finns farhågor att de reaktiva gaser som bildas under haveriförhållanden skulle kunna påverka målade ytors förmåga att binda jod, exempelvis genom att ockupera de "sites" som annars skulle fyllas av jod.

I en testserie görs kompetitiva adsorptionsexperiment mellan jod och klorgas ( $\text{Cl}_2$ ) respektive nitrösa gaser ( $\text{NO}_x$ ) vid varierande koncentrationer. Klorgas förväntas från pyrolys av klorerat kabelmaterial vid ett svårt haveri och nitrösa gaser förväntas från radiolys av luft. Luftfuktighetens inverkan ska också varieras, vilket ska simulera inverkan från sprayning av atmosfären i inneslutningen. Planering pågår för försök i närväro av klorgas ( $\text{Cl}_2$ ) eller nitrösa gaser ( $\text{NO}_x$ ) som ska genomföras under år 2018.

#### *Bildande av methyljodid i gasfas*

I syfte att bekräfta om det är möjligt att bilda methyljodid i gasfas, genomförs en testserie där bestrålning sker av gasblandningar innehållande metan och jod av olika koncentrationer. Att detta är möjligt hävdas i flera referenser, men från andra håll bedöms betydelsen av denna process som ringa. Anledningen till detta är att den intermediära methylradikalen som erhålls från radiolys av metan är mycket reaktiv och därför i första hand skulle reagera med syrgas i atmosfären istället för med jod. I testserien varieras förutom syrgashalten även blandningens fukthalt.

Analyser från försöken visar att metan delvis degraderas vid gammabestrålning men att motsvarande mängd methyljodid inte återfinns vid analys. Metan och jod har även möjlighet att reagera med radiolysprodukter av luft eller fukt. Det konstateras att oavsett om gasfasreaktion mellan metan och gas inträffar, så är detta inte den mest dominerande reaktionsvägen för bildande av methyljodid.

## **2.5 CSNI/NEA-rapporter inom svåra haverier under perioden 2015-2017**

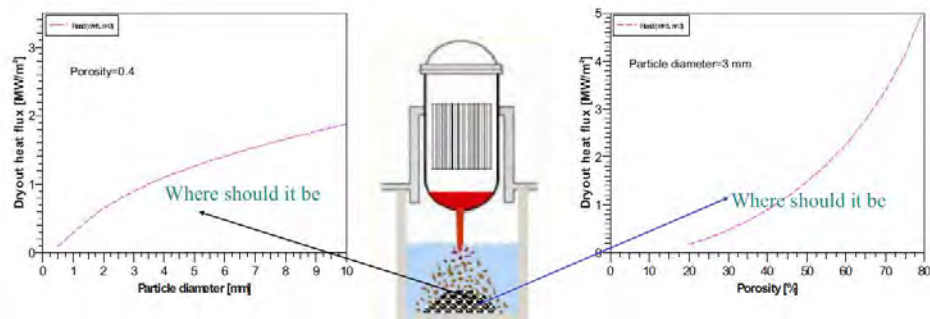
Under åren 2015-2017 som APRI 9-projektet pågått har följande rapporter utgivits inom CSNI-NEA:s regi. Rapporterna finns att hämta från NEA:s hemsida, <http://www.oecd-nea.org/nsd/docs/indexcsni.html>.

<b>Beteckning</b>	<b>Rapportens titel</b>
NEA/CSNI/R(2017)18	Phenomena Identification and Ranking Table (PIRT) on Spent Fuel Pools under Loss-of-Cooling and Loss-of-Coolant Accident Conditions WGFS Report.
NEA/CSNI/R(2017)16	Informing Severe Accident Management Guidance and Actions through Analytical Simulation report on the WGAMA WG.
NEA/CSNI/R(2017)15	Status Report on Ex-Vessel Steam Explosion: EVSE.
NEA/CSNI/R(2016)19	Safety Research Opportunities Post-Fukushima - Initial Report of the Senior Expert Group. <a href="https://www.oecd-nea.org/nsd/docs/2016/csni-r2016-19.pdf">https://www.oecd-nea.org/nsd/docs/2016/csni-r2016-19.pdf</a>
NEA/CSNI/R(2016)15	State-of-the-Art Report on Molten-Corium-Concrete interaction and Ex-Vessel Molten-Core Coolability. <a href="https://www.oecd-nea.org/nsd/docs/2016/csni-r2016-15.pdf">https://www.oecd-nea.org/nsd/docs/2016/csni-r2016-15.pdf</a>
NEA/CSNI/R(2016)8	Aerosol and Iodine Issues, and Hydrogen Mitigation under Accidental Conditions in Water Cooled Reactors - Thermal-hydraulics, Hydrogen, Aerosols and Iodine (THAI-2) Project - Final Report. <a href="https://www.oecd-nea.org/nsd/docs/2016/csni-r2016-8.pdf">https://www.oecd-nea.org/nsd/docs/2016/csni-r2016-8.pdf</a>
NEA/CSNI/R(2016)5	International Iodine Workshop Summary Report. <a href="https://www.oecd-nea.org/nsd/docs/2016/csni-r2016-5.pdf">https://www.oecd-nea.org/nsd/docs/2016/csni-r2016-5.pdf</a>
NEA/CSNI/R(2015)19	Benchmarking of Fast-running Software Tools Used to Model Releases During Nuclear Accidents. <a href="https://www.oecd-nea.org/nsd/docs/2015/csni-r2015-19.pdf">https://www.oecd-nea.org/nsd/docs/2015/csni-r2015-19.pdf</a>
NEA/CSNI/R(2015)18	Benchmark Study of the Accident at the Fukushima Daiichi Nuclear Power Plant (BSAF Project) - Phase I Summary Report, March 2015. <a href="https://www.oecd-nea.org/nsd/docs/2015/csni-r2015-18.pdf">https://www.oecd-nea.org/nsd/docs/2015/csni-r2015-18.pdf</a>
NEA/CSNI/R(2015)3	Ability of Current Advanced Codes to Predict In-Vessel Core Melt Progression and Degraded Core Coolability - Benchmark Exercise on Three Mile Island-2 Plant - Final Report. <a href="https://www.oecd-nea.org/nsd/docs/2015/csni-r2015-3.pdf">https://www.oecd-nea.org/nsd/docs/2015/csni-r2015-3.pdf</a>
NEA/CSNI/R(2015)2	Status Report on Spent Fuel Pools under Loss-of-Coolant Accident Conditions Final Report. <a href="https://www.oecd-nea.org/nsd/docs/2015/csni-r2015-2.pdf">https://www.oecd-nea.org/nsd/docs/2015/csni-r2015-2.pdf</a>

### 3. KTH:S FORSKNING INOM SVÅRA HAVERIER

#### 3.1 Inledning på svenska

KTH:s avdelning för kärnkraftssäkerhet har sedan början på 1990-talet bedrivit forskning inom svåra haverier och APRI har fortlöpande stöttat denna forskning via finansiering och förslag på inriktning. APRI:s ambition med forskningsstödet har varit att öka förståelsen samt minska osäkerheterna i beskrivningen av ett svårt haveri i en svensk kokvattenreaktor och därigenom validera den haverihantering som är utformad för svenska reaktorer. Under det första decenniet av APRI-forskning på KTH var arbetet främst inriktad på experiment, utveckling av deterministiska modeller samt kodutveckling. Ambitionen var att kartlägga och beskriva de händelseförlopp och de fenomen som uppträder under ett postulerat svårt haveri i en svensk kokvattnereaktor via en deterministisk beskrivning. Resultaten redovisades exempelvis i diagram där en framgångsrik haverihantering kunde representeras av en domän som låg på en sida av en begränsningskurva, se Figur 3.1.1.



Figur 3.1.1. Exempel på deterministiska resultat från APRI

Under Prof. Nam Dinh's ledarskap på KTH påbörjades under APRI-6 (2006-2008) och APRI-7 (2009-2011) ett mer systematiskt grepp att koppla ihop den samlade kunskapen och arbetet samt att identifiera de luckor där fortsatta insatser borde prioriteras. Frågor som ställdes var exempelvis: kan in-vessel retention etableras framgångsrikt? Kan mängden smälta begränsas vid en tankgenomsmältnings? Det konstaterades under APRI-7 att frågeställningen inte går att behandla med enbart deterministiska metoder, främst med hänsyn till komplexa beroendet mellan vad som händer under nedsmältnings av reaktorhärden (in-vessel) och de fenomen som uppträder efter tankgenomsmältnings (ex-vessel). Inför APRI-8 föreslogs därför tillämpa ROAAM (Risk Oriented Accident Analysis Methodology), som är en metodik bygger på både deterministiska och probabilistiska ansatser.

##### 3.1.1. ROAAM

ROAAM utvecklades ursprungligen i början av 1990-talet av prof. Theo Theofanous [1] med finansiellt stöd av NRC med syftet att bedöma och hantera risker med både stora osäkerheter och konsekvenser. Startskottet till ROAAM utvecklingen var problematiken kring det så kallade "Mark I liner attack" där frågeställningen gäller brott på tätplåten i en Mark I inneslutning och där ROAAM användes för att visa att vattpåfyllnad i inneslutningen innan tankgenomsmältnings var tillräcklig för att hindra

skada på tätplåten. ROAAM kom efter hanteringen av "Mark I liner attack" att tillämpas på flera svåra haverifenomen. De svåra haverifenomen som behandlades med ROAAM i ett amerikanskt sammanhang var exempelvis in-vessel ångexplosioner, där farhågan enligt Reactor Safety Study (RSS, WASH-1400 rapporten) var att reaktortanklocket skulle fungera som en missil i samband med en ångexplosion i reaktortanken (så kallad alpha-mode failure) och därigenom skada inneslutningen. Med hjälp av ROAAM kunde det visas att denna händelse var "physically unreasonable" [2]. På liknande sätt och med samma resultat hanterades DCH-fenomenet för Westinghouse Zion reaktor i USA [3].

ROAAM tillämpades även i samband med framtagandet av en haverihantering för Fortums Lovisaanläggning. Lovisa är en blandning av ett ryskt primärsystem och en Westinghouse iskondensor inneslutning (projektet fick smeknamnet "Eastinghouse"). Reaktorinneslutningen i Lovisa har ett lågt konstruktions- och brotryck och skulle omöjligen klara de trycklaster som normalt associeras med ett svårt haveris ex-vessel scenario. Lovisas inneslutning har dessutom en liten reaktorgrop som inte kan fyllas med större mängder vatten för att möjliggöra ex-vessel kylning i samband med tankgenomsmältnings. Dessa förhållanden medförde att Lovisa med prof. Harri Toumisto i spetsen utvecklade in-vessel retention (IVR) som en haverihanteringsstrategi för Lovisa. Strategin bygger på att härdsmältan stannar kvar i reaktortanken genom att kyla tanken utifrån och flera fenomen som kan utmana inneslutningen som till följd av en tankgenomsmältnings kan då undvikas, exempelvis MCCI och ångexplosioner. För att demonstrera tillämpbarheten av in-vessel retention i Lovisa användes ROAAM och både ROAAM och IVR accepterades av STUK. En viktig förutsättning för att framgångsrikt kunna demonstrera IVR i Lovisa är den förhållandevis låga effekten i reaktorerna, cirka 500 MWe. På samma sätt visades via ROAAM att IVR var tillämpligt på Westinghouse AP600 och att brott på reaktortankens nedre plenum pga. otillräcklig eller utebliven extern kylning var "physically unreasonable".

Vad är då ROAAM? Den bakomliggande filosofin till ROAAM är att på ett systematiskt sätt tillgodose kvantifierbara och hanterbara lösningar för att hantera de osäkerheter som uppträder under ett haveriförlopp. I en enkel punktlista kan ROAAM beskrivas som:

- *Metodik för att kartlägga/undersöka fenomen med låg sannolikhet och stora konsekvenser och som är behäftade med stora osäkerheter*
- *Syftet är att:*
  - *Demonstrera att förhållanden eller villkor som leder till fel eller brott på ett system (här typiskt reaktorinneslutningen) är "fysikaliskt orimligt" (physically unreasonable)*
  - *Identifera haverihanteringsåtgärder som skapar förutsättningar för att påvisa "fysikaliskt orimligt". En framgångsrik hantering av dessa haverihanteringsåtgärder kan därefter kvantificeras i vanlig PSA*
- *Bryt ner och begränsa fenomen i sub-fenomenen eller sk. "Causal Relations" (CR)*
- *Ta fram experimentellt stöd och grund för Causal Relations*
- *Utvärdera osäkerheter kopplade till Causal Relations*
- *Utveckla ett probabilistiskt ramverk för att analysera hela fenomenet, dvs alla Causal Relations inklusive osäkerheterna. För varje scenario skapas ett probabilistiskt ramverk*
- *Identifiera kriterier för fel eller brott*

- *Sist men inte minst: granskning med stöd av experter inom respektive område som fenomenen berör*

De mål, safety goals, som formuleras i ROAAM ska vara tydliga (*clear*), fullständiga (*completeness*) och förenliga (*consistency*). Målambitionen tar sig exempelvis uttryck som att i ROAAM-tillämpningen ska alla scenarion som inte kan uteslutas på fysikaliska grunder beaktas (*completeness*). Ett annat uttryck är att ROAAM-tillämpningen utgår från en ”screening frequency”, som är den lägsta frekvens för sannolikheten för en händelse som behöver beaktas och där händelser med lägre frekvens betraktas som restrisk (*consistency*). Ett klassiskt exempel på en sådan händelse är spontant reaktortankbrott.

Några centrala begrepp som återkommer i beskrivningen om ROAAM är:

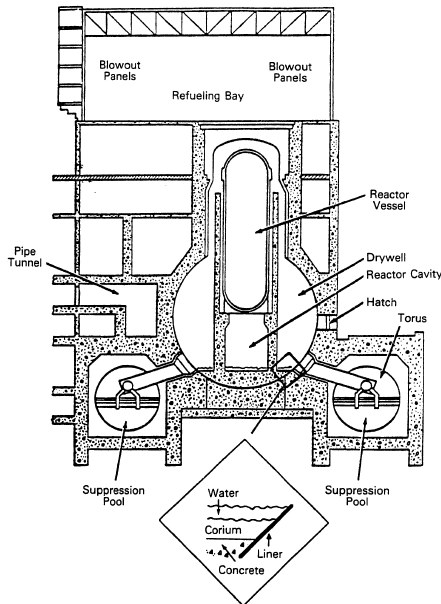
- **Causal Relations (CR)** – *Causal Relations utgör en mekanistisk koppling mellan två storheter som pga. av begränsningar i förståelse endast kan skattas summariskt (se ”intangibles”). Osäkerheterna i CR är förhållandevis små och kan hanteras med kända statistiska metoder. Varje CR kan hanteras separat och möjliggör för experter inom olika discipliner att både granska och utveckla delar av problemuppställningen oberoende av varandra.*
- **Intangibles** (”ogripbar, obestämd, vag”) – *Intangibles är parametrar vars osäkerheter endast kan skattas kvalitativt, men som samtidigt också alltid kan begränsas.*
- **Splinter** (”splittra”) – *Splinter är beteckningen av en uppdelning av ett ROAAM problem i flera scenarion, där varje separat scenario ska visas uppfulla det uppsatta målet/kriteriet.*
- **Aleatory uncertainty** (*Alea = latin ”tärning”*) – *Avser stokastisk osäkerhet som hanteras med statistiska metoder. De stokastiska osäkerheterna finns i CR enligt beskrivningen ovan.*
- **Epistemic uncertainty** (*epistēmikós = Grekiska för ”kunskap”, ”vetenskap”*) – *Avser systematisk osäkerhet och härför sig typiskt till otillräckliga kunskaper om fenomen, osäkerheter i modellbeskrivning etc. Epistemisk osäkerhet kan i princip begränsas eller elimineras, men låter sig inte göras i praktiken. De epistemiska osäkerheterna finns i intangibles.*

En annan central aspekt i ROAAM är en godtycklig sannolikhetsskala som utgör en koppling mellan sannolikheter och den fysikaliska, mekanistiska kvantifieringen, se Tabell 3.1.1. När ett ROAAM-ramverk integreras (dvs. ett slutresultat beräknas baserat på de separata CR och intangibles) görs det baserat på denna skala och med tillämpandet av konservativa värden.

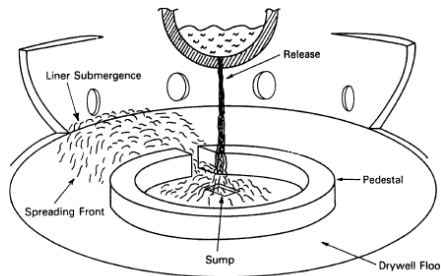
Tabell 3.1.1: Definition av sannolikhetsnivåer.

<b>Process Likelihood</b>	<b>Process Characteristics</b>
1/10	Behavior is within known trends but obtainable only at the edge-of-spectrum parameters.
1/100	Behavior cannot be positively excluded but is outside the spectrum of reason.
1/1000	Behavior is physically unreasonable and violates well-known reality. Its occurrence can be argued against positively.

I det följande görs en enkel beskrivning av en ROAAM-tillämpning baserat på beskrivningen i [5]. Frågeställningen gäller farhågan att härdrester kan angripa tätplåten som ligger an mot betongen på insidan av Mark-I inneslutningen, där tätplåten är en central del av täthetsfunktionen. Skadas tätplåten riskerar det att leda till tidigt brott på inneslutningen, så kallad Early Containment Failure, och därmed tidiga utsläpp av radioaktiva ämnen, se Figur 3.1.2 och Figur 3.1.3.



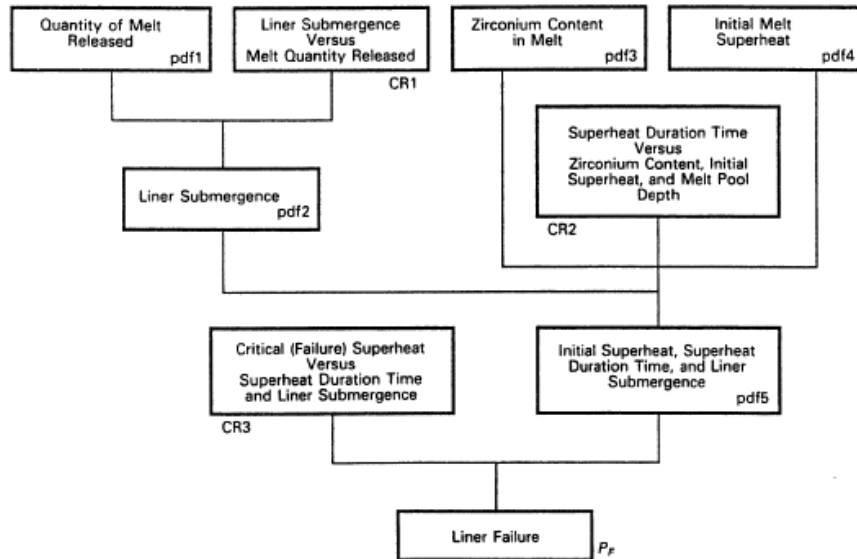
*Figur 3.1.2: Beskrivning av härdsmältans degradering av tätplåten i en Mark-I inneslutning. Hämtad ur [5].*



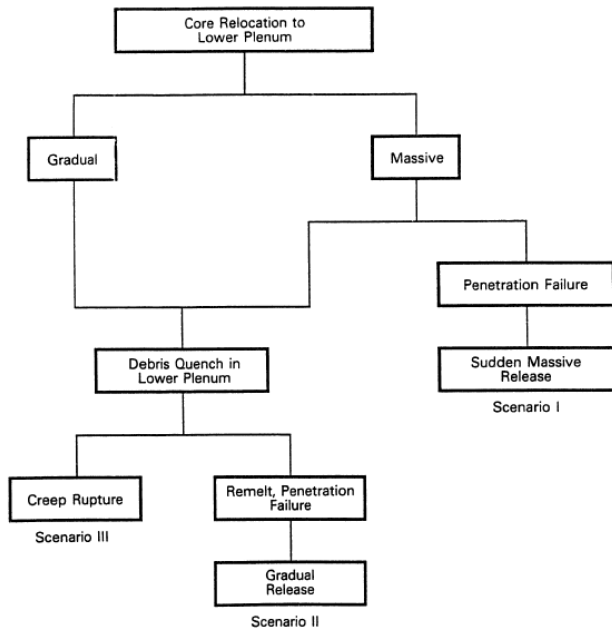
*Figur 3.1.3: Detaljbeskrivning av härdsmältans degradering av tätplåten i en Mark-I inneslutning. Hämtad ur [5].*

Syftet med ROAAM-tillämpningen i detta fall var att försöka fastställa sannolikheten för en skadad tätplåt, speciellt under förutsättningen att nedre primärutrymmet vattenfylldes innan tankgenomsmältnings. Notera att konstruktionen inte tillåter något större vattendjup i nedre primärutrymmet eftersom genomföringar leder tillfört vatten vidare till torusen och sekundärutrymmet.

Figur 3.1.4 beskriver det probabilistiska ramverket som det hanterades i ROAAM gällande tätplåten i Mark-I inneslutning. Som bilden illustrerar är framställningen uppdelad i flera delproblem.



*Figur 3.1.4: Det probabilistiska ramverket i ROAAM för att analysera "Mark-I liner attack". Hämtad ur [5].*



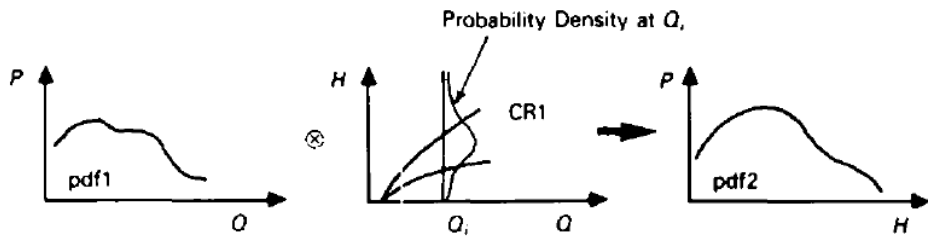
*Figur 3.1.5: "Splinter"-scenarien i ROAAM Mark-I liner attack. Hämtad ur [5].*

Benämningen *CR* representerar Causal Relations och benämningen *pdf* representerar täthetsfunktioner för parametrar behäftade med stora osäkerheter, intangibles. Valet av täthetsfunktioner sker med konservativa ansatser och expertbedömningar, eller genom att analysera utfallet av ett antal täthetsfunktioner och därefter välja funktion från konservativ ansats baserat på resultatet.

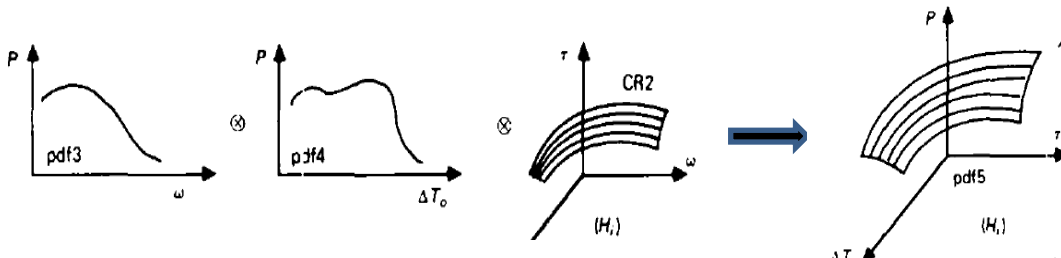
CR kopplar ihop problemframställningens olika delar. I den aktuella problemframställningen identifierades tre ”splinter”-scenarion, se Figur 3.1.5, som med expert-hjälp bedömdes vara begränsande för problemframställningen. För varje scenario finns ett tillhörande probabilistiskt ramverk, dvs. ramverket enligt Figur 3.1.4. De tre scenarierna skiljer sig åt avseende felmod för tankgenomsmältningen och där felmoden styr hur stor mängd smälta som frigörs per tidsenhet.

I det kommande görs ett försök att beskriva hanteringen och flödet i ramverket som det presenteras i Figur 3.1.4. Av de ROAAM tillämpningar som hittills har genomförts framgångsrikt så hör förmodligen ”Mark-I Liner Attack” till den kanske minst komplexa analysen och är på så sätt en bra utgångspunkt för en framställning av ROAAM. Bilderna som ingår i beskrivningen nedan är enbart schematiska. Om ramverket betraktas uppifrån och ned ges följande flöde:

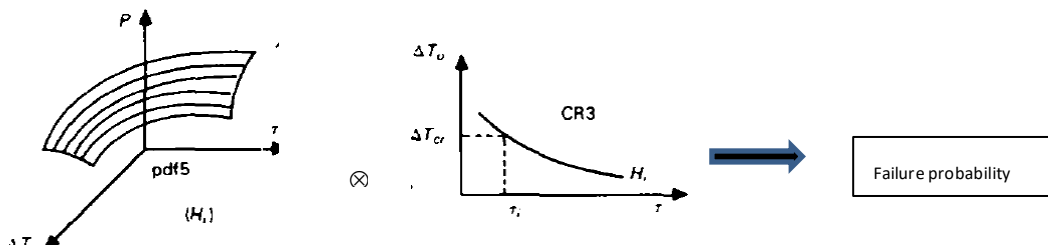
1. *För Causal Relation 1, CR1, i Figur 3.1.4 har den bakomliggande analysen gjorts med programkoden MELTSPREAD för de respektive tre scenarien som anges i Figur 3.1.5. MELTSPREAD används för att beräkna spridningen av härdrester över stål eller betong. Beräkningarna täckte en mängd kombinationer av smältvolymer, sammansättningar och överhetning. Resultaten från beräkningarna beskriver smältans höjd i anslutning till tätplåten i inneslutningen.*
2. *Parameter pdf1 är en intangible, dvs. en parameter som endast kan beskrivas kvalitativt och avser här mängden smälta som frigörs vid tankgenomsmälting.*
3. *CR1 och pdf1 ”kombineras” (via en summering) till pdf2 som beskriver en sannolikhetsfördelning över smältans djup, se Figur 3.1.6.*
4. *På motsvarande sätt ”kombineras” pdf3, pdf4 och pdf2 tillsammans CR2 med för att bilda pdf5. Parametrarna pdf3 och pdf4 avser mängden metalliskt zirkonium i smältan respektive smältans initiala överhetning, och CR2 kopplar kausalt ihop dessa parametrar via en beräkning. Beräkningen i CR2 har utförts med programkoden CORCON, se Figur 3.1.7. Vad sannolikhetsfördelningen pdf5 representerar är inte lika entydigt som pdf2 - 4, utan ses lättast som ett delresultat.*
5. *Slutligen ”kombineras” pdf5 med CR3 (via ytterligare en – i detta fall stökgsummering) för att beräkna den totala sannolikheten för brott på inneslutningen. Beräkningen i CR3 är gjord med ABAQUS och avser en strukturmekanisk beräkning vars resultat ger temperaturen i tätplåten som sedan kan jämföras med ett ”failure criterion”, dvs. felkriterie, som här har satts till 1260 °C, se Figur 3.1.8.*
6. *Resultaten från den integrerade analysen av ramverket visar att om primärutrymmet vattenfylls innan tankgenomsmältningen så är den ”slutliga konservativa uppskatningen av brott på tätplåten”  $3 \times 10^{-3}$  för felkriteriet 1260° C. Resultatet kan översättas till ”physically unreasonable event” enligt definitionen i Tabell 3.1.1.*



Figur 3.1.6: "Kombinationen" av CR1 och pdf1 som resulterar i pdf2 i ROAAM-ramverket för Mark-I liner attack. Hämtad ur [1]. Tecknet "⊗" avser en aritmetisk operation.



Figur 3.1.7: Kombinationen av pdf2 (ej med i figuren), pdf3 och pdf4 samt CR2 bildar pdf5. Hämtad ur [1].



Figur 3.1.8: Kombinationen av pdf5 samt CR3 bildar den totala sannolikheten för brott. Hämtad ur [1].

### 3.1.2. KTH:s utveckling av ROAAM till ROAAM+

De frågeställningar som hittills har hanterats framgångsrikt med ROAAM för att bemästra utmaningar kopplade till svåra haverier har haft en varierande grad av komplexitet, där möjliga tillämpningen av ROAAM för demonstrationen av in-vessel retention för Westinghouse:s reaktorsystem AP1000 har varit mest komplex. I tillämpningen av ROAAM för "Nordic BWR severe accident management", dvs. haverihanteringen vid ett svårt haveri för en generisk ABB reaktor enligt senare konstruktion, tillkommer ytterligare svårigheter. Grunden till dessa ytterligare svårigheter jämfört med tidigare tillämpningar av ROAAM härrör från den kedja av möjliga haveriförflopp som ett svårt haveri kan utvecklas till och som beror på tillstånd och åtgärder tidigt i förfloppet. Tidigare tillämpningar av ROAAM har beaktat ett fenomen, medan ambitionen i ROAAM+ är att beakta hela haveriförfloppet vilket inkluderar flera fenomen inklusive de olika uppträdanden dessa förflopp uppvisar. Med andra ord finns det ett flertal olika initiala anläggningstillstånd i samband med det

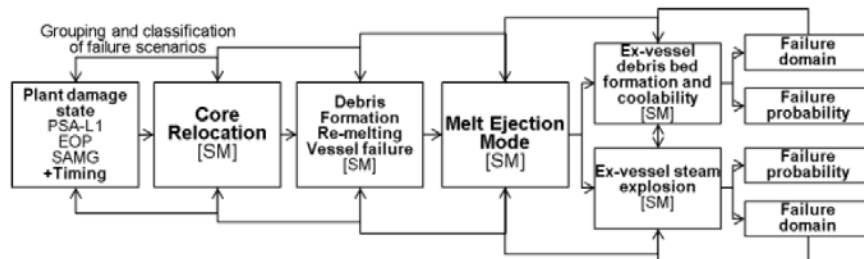
svåra haveriet som ger en stor påverkan på den last som i slutändan utmanar inneslutningen. Ett fenomen eller en fysikalisk egenskap kan även ha både positiva och negativa effekter på händelseförloppet samtidigt, vilket också påverkar möjligheterna att skapa ett robust ROAAM ramverk.

Mot bakgrund av de tillkommande svårigheter det har inneburit att tillämpa ROAAM på den svenska haverihanteringen för en svensk BWR har KTH utvecklat ROAAM till något som kallas ROAAM+. Det övergripande målet med ROAAM+ är att kunna ge tillräckligt med information för att besluta om:

- *Keep SAM-strategy; "possibility" of containment failure is low even with "conservative" treatment of uncertainty, thus current strategy is reliable.*
- *Modify SAM-strategy; "necessity" of containment failure in the course of an accident is high (i.e. "possibility that containment doesn't fail is low) even with "optimistic" treatment of uncertainty, thus the current strategy is unreliable and changes should be considered.*

Enkelt uttryckt representerar den första punktsatsen "klassisk" ROAAM, medan den andra punktsatsen representerar den modifikation som KTH har lagt till i ROAAM+. För den andra punktsatsen gäller att resultaten visar att trots en optimistisk hantering av antaganden, ansatser och indata så kommer inneslutningen att fallera, och innebär att angreppsättet att hantera frågeställningen om inneslutningen fallerar eller inte i princip är en spegelbild av den första (klassiska ROAAM) punktsatsen. Kompletteringen med frågeställningen "necessity" enligt ROAAM+ är ett uttryck för svårigheterna att hantera den svenska haverihanteringen med klassisk ROAAM. Förenklat kan man i första punktsatsen tolka resultaten som att det inte är uteslutet att inneslutningen fallerar med en viss sannolikhet, medan punktsats 2 kan tolkas som att resultaten påvisar att inneslutningen fallerar med en viss sannolikhet.

I KTH:s utveckling och tillämpning av ROAAM+ har medfört en mycket beräkningsintensiv metodik för att omhänderta beräkningar i deterministiska modeller, integrera ramverket med CR och pdf samt för att genomföra relevanta känslighets- och osäkerhetsstudier. För att effektivisera beräkningarna har KTH utgått från sk. "full model" (FM) och via datautvinnning utvecklat "surrogate model" (SM) som representerar full model, men som inte alls kräver samma beräkningskapacitet. Datautvinnning är ett verktyg för att identifiera mönster, samband eller trender ur stora datamängder. Ett exempel på full model är de modeller som ingår i svåra haverikoden Melcor. KTH har exekverat 10 000-tals Melcorberäkningar och via datautvinnning utvecklat SM som sedan har använts för miljontals beräkningar (en Melcorberäkning kan ta dagar). SM är med andra ord en förenkling av FM som har utvecklats via datautvinnning och sedan verifierats och validerats mot FM. Dessa SM har efter framtagandet utgjort stommen för CR i ROAAM+ ramverket, se Figur 3.1.9.



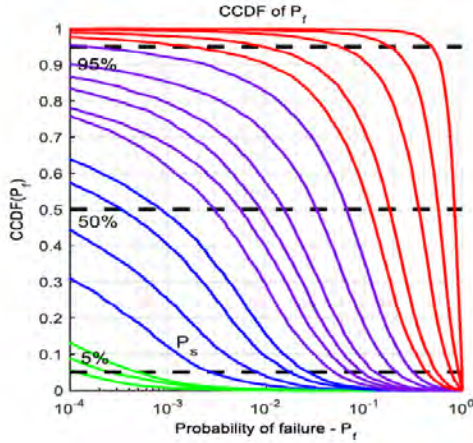
Figur 3.1.9: Ramverket i ROAAM+. Hämtad ur [6].

Som Figur 3.1.9 illustrerar kan ramverket analyseras ”framåt” (från vänster till höger), sk. ”forward analysis”, men även ”bakåt” som ”reverse analysis”, vilket representeras av pilarna som går från höger till vänster. Med forward analysis avses kopplingen mellan det initiala tillståndet och den betingade sannolikheten att inneslutningen fallerar, för varje scenario. Forward analysis följer huvuddragen i klassisk ROAAM och i forward analysis kvantifieras även de parametrar som bidrar mest till osäkerheten i resultatet. Reverse analysis används för att identifiera skadedomäner i respektive SM i syfte att identifiera kunskapsluckor och behov av exempelvis experiment för att förstärka modellerna i SM. Med skadedomän avses de scenarion och parametrar som ger ett resultat vars sannolikhet för brott på inneslutningen är större än ”physically unreasonable”, och utgående från resultaten görs en ”baklänges-analys” för att se vilka parametrar och scenarion i respektive SM som har bidragit till skadedomänen.

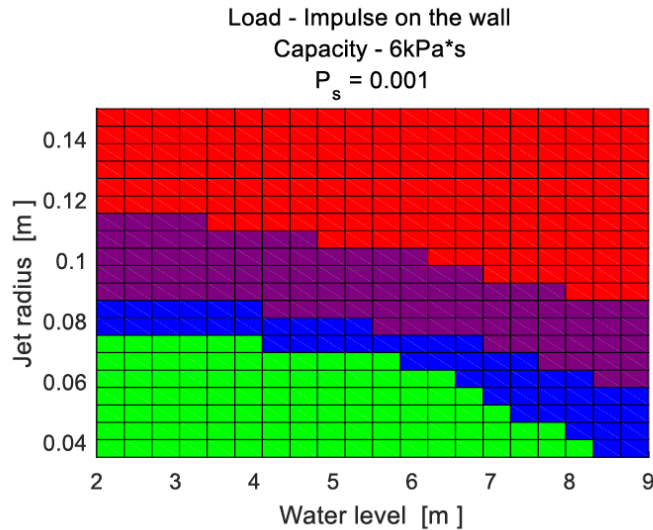
### 3.1.3. Resultatpresentation i ROAAM+

Resultaten i KTH:s ROAAM+ presenteras typiskt på flera olika sätt för att förmedla den information som analysen kan ge upphov till. Figur 3.1.10 visar en färgkodad Complementary Cumulative Density Function (CCDF) eller komplementär kumulativ fördelningsfunktion. En kumulativ fördelning för ett datamaterial anger hur stor andel av värdena som är mindre än eller lika med ett givet värde. Den komplementära kumulativa fördelningen vänder på frågan och anger hur stor del av datamaterialet som ligger över ett visst värde. I Figur 3.1.10 avser den gröna kurvan att sannolikheten att överskrida ”screening frequency  $P_s$ ” är 5%, eller med andra ord så visar resultaten med 95% konfidens att sannolikheten för brott på inneslutningen  $P_f$  understiger ”screening frequency  $P_s$ ”. Den röda kurvan avser det omvänta förhållandet: för åtminstone 95% av fallen så överskrider sannolikheten för brott på inneslutningen  $P_f$  ”screening frequency  $P_s$ ”.

Figur 3.1.11 visar ett exempel på en skadedomän som beräknats med ”reverse analysis”. Skadedomänskartan avser laster på personslussen i nedre primärutrymmet pga. ångexplosioner och ger en mer konkret illustration av risken för skada för valda scenarioparametrar. Slussen har här antagits ha en kapacitet på 6 kPas, och kartan presenterar lasten som en funktion av stråldiameter och vattendjup. Analysresultaten placeras i tre kategorier: en kategori där 95 % av de beräknade sannolikheterna är större än screeningsannolikheten (markerad som rött område), en där 95 % av beräknade sannolikheter är mindre än screeningsannolikheten (markerad som grönt område), och ett område i lila och blått som ligger mellan dessa två kategorier. Denna kategorisering utgår från hypotesen att analysresultaten inte kommer att förändras med förbättrad kunskap om aktuella sannolikhetsfördelningar av indataparametrar med osäkerheter, om dessa resultat ligger inom det röda eller det gröna området. Resultat i området mellan dessa två kategorier kan däremot förändras med förbättrade kunskaper. Ibland presenteras motsvarande karta även som en tredimensionell kub där även nedrinningshastigheten på smälten ingår som en variabel.



Figur 3.1.10: Komplementär kumulativ täthetsfunktion för brott på inneslutningen i ROAAM+. Hämtad ur [6].



Figur 3.1.11: Exempel på skadedomän i KTH:s ROAAM+. Hämtad ur [6].

### 3.1.4. Referenser

- [1] On the proper formulation of safety goals and assessment of safety margins for rare and high-consequence hazards, T.G Theofanous, Reliability Engineering and Systems Safety 54, 243-257, 1996.
- [2] The probability of alpha-mode containment failure, T.G Theofanous et al, Nuclear Engineering and Design 155, 459-473, 1995.
- [3] The probability of containment failure by direct containment heating in Zion, M.M Pilch et al, Engineering and Design 164, 1-36, 1996.
- [4] In-vessel retention of corium at the Loviisa plant, O. Kymäläinen et al, Nuclear Engineering and Design 169, 109-130, 1997.
- [5] NUREG/CR-6025 - The Probability of Mark-I Containment Failure by Melt-attack of the Liner, T.G Theofanous et al, 1993.
- [6] APRI-9, Integrated ROAAM+ Development and Analysis Results, P. Kudinov et al, 2017.

### 3.2 Motivation, Goals and Approach

Severe accident management (SAM) strategy in Nordic boiling water reactors (BWRs) employs ex-vessel core debris coolability. Molten core is released from the vessel into a deep pool of water in the lower drywell. The melt is expected to fragment, quench, and form a debris bed that is coolable by natural circulation of water. Formation of non-coolable debris bed and energetic steam explosion pose credible threats to containment integrity. Conditions of melt release from the vessel determine (i) debris bed properties and thus coolability, and (ii) steam explosion energetics. While conceptually simple, the strategy involves complex phenomena affected by the transient accident scenarios. Significant progress, that has been made in understanding and predicting physical phenomena during the last few decades, was not sufficient to make a firm conclusion on the robustness of the SAM strategy. It became apparent that the issues are intractable [52], [51] for separate probabilistic or deterministic analysis due to the uncertainty stemming from interactions between multistage accident progression scenarios (Figure 3-1) and deterministic phenomena Figure 3-2. Timing of event affects accident progression. Late recovery of core cooling affects core degradation, relocation, and formation of the debris in lower head, reheating and re-melting of multi-component corium debris, thermo-mechanical interactions between melt and vessel structures and penetrations, vessel failure, melt release mode, respective jet fragmentation in the pool, debris solidification, energetic melt-coolant interactions, two-phase flow in porous media, spreading of debris in the pool, spreading of particulate debris bed, etc. (Figure 3-2). If melt is released from the vessel later, smaller decay heat provides better chances for coolability [107]. However temperature of the melt that remained longer in the vessel can be higher, increasing the risk of debris agglomeration [63], [40], [37] that hinders coolability [114], [108]. Also higher melt temperature can increase potential energetics of steam explosion [21].

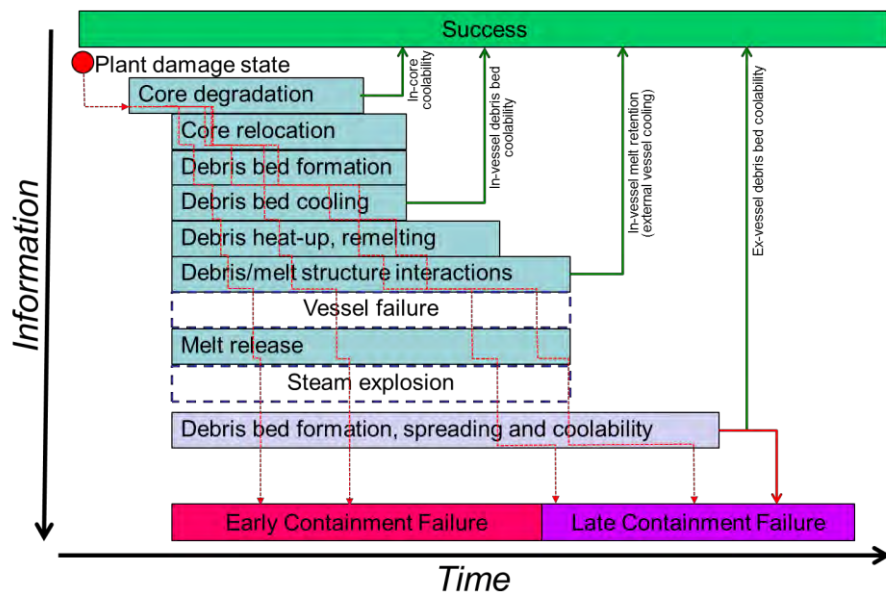


Figure 3-1: Severe accident progression in Nordic BWR.

Interdependencies between non-coolable debris and steam explosion is another source of uncertainty. If lower drywell is not flooded, then steam explosion risk can be eliminated, while hot corium melt will attack cable penetrations in the containment floor leading containment failure. Even a mild explosion might lead to degradation

of debris bed cooling function, e.g. by destroying protective covers and exposing cable penetrations to hot debris; creating a leak of coolant from the lower drywell; activating containment venting, releasing fraction of nitrogen which can potentially lead to drop of containment pressure below atmospheric level, etc.

The Risk Oriented Accident Analysis Methodology (ROAAM) marries probabilistic and deterministic approaches. ROAAM was developed and successfully applied by Professor Theofanous and co-workers to assessment and management of severe accident risks [84], [85]. It is instructive to note that Risk Management Task Force provided recommendation that NRC should implement a consistent process that includes both deterministic and probabilistic methods in risk assessments that can inform decisions about appropriate defense-in-depth measures [1].

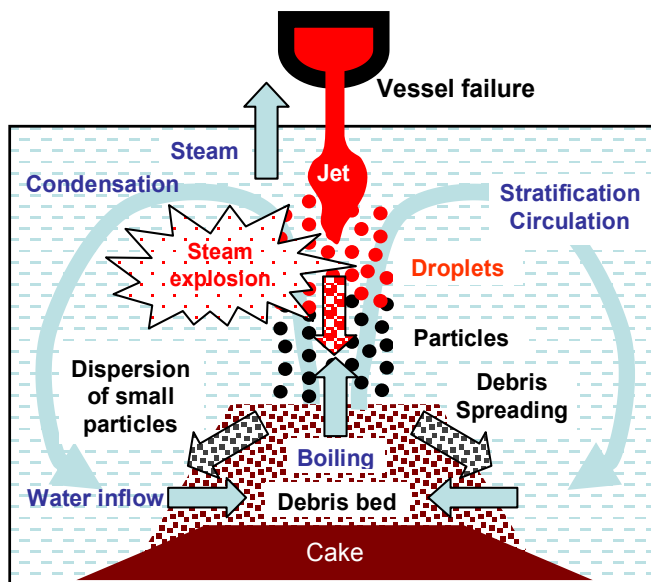


Figure 3-2: Severe accident phenomena in Nordic BWR.

The goal of this work is to develop a risk oriented accident analysis framework for quantifying conditional threats to containment integrity for a reference design of Nordic type BWR. We propose an iterative process of refining the components of the framework based on sensitivity and uncertainty analysis. The aim of the process is to achieve (i) completeness, (ii) consistency, and (iii) transparency in the review of the analysis and its results. The work is formally divided into four sub-tasks, tightly interconnected with each other: Risk Evaluation and Synthesis (RES); Melt Ejection Mode (MEM); Debris Coolability Map (DECO); Steam Explosion Impact Map (SEIM). Methodology, overall modular structure of the frameworks, and preliminary analyses results have been presented in RES papers [52], [51] and reports [58], [57]. Here we summarize main findings of the project, methodological development of ROAAM, and implications to assessment of SAM effectiveness.

### 3.3 Risk Evaluation and Synthesis (RES)

The goal of RES is to develop a robust integrated risk assessment approach for the reference Nordic type BWR plant design based on synthesis of phenomenological models, and probabilistic ROAAM+ frameworks.

### 3.3.1. Background: Quantitative Definition of Risk and ROAAM Basics

The use of Risk in ROAAM for effective management and regulation of rare, high-consequence hazards requires the simultaneous (coherent) consideration of (i) safety goal, (ii) assessment methodology, and (iii) application specifics. ROAAM provides guidelines for development of frameworks for bounding the epistemic (modeling), and aleatory (scenario) uncertainties in a transparent and verifiable manner that should enable convergence of experts' opinions in the review process. For severe accident analysis the safety goal can be defined as: "containment failure is a physically unreasonable event for any accident sequence that is not remote and speculative" [84]. ROAAM employs principal ingredients: (i) identification, separate treatment, and maintenance of separation (to the end results) of aleatory and epistemic uncertainties; (ii) identification and bounding/conservative treatment of uncertainties (in parameters and scenarios, respectively) that are beyond the reach of any reasonably verifiable quantification; and (iii) the use of external experts in a review, rather than in a primary quantification capacity.

According to quantitative definition of risk ([29] by Kaplan and Garrick), the risk  $R_i$  associated with specific scenario  $s_i$  can be characterized by its frequency  $f_i$  and consequences  $c_i$ . The degree of epistemic uncertainty in the prediction of the future course of events can be quantified as "probability"  $P_i$  or "likelihood" of  $c_i$ . Two rational beings given the identical evidence must assess the probability identically [29]. "Frequency" is the outcome of an experiment involving repeated trials. Aleatory uncertainty is expressed in terms of frequency.

$$R_i = \{s_i, f_i, P_i(c_i)\} \quad (3-1)$$

Consequences  $c_i$  of scenario  $s_i$  can be presented as joint probability density function  $\text{pdf}_{C_i L_i}(L_i, C_i)$  of loads ( $L_i$ ) on the system and its capacity ( $C_i$ ) to withstand such loads. Thus, failure probability  $P_{Fi}$  for scenario  $s_i$  can be evaluated as

$$P_{Fi} = P(L_i \geq C_i) = \iint_{L_i \geq C_i} \text{pdf}_{C_i L_i}(c, l) dc dl \quad (3-2)$$

Residual risk is judged in ROAAM with screening frequency for aleatory, and with "physically unreasonable" concept for epistemic. Plant damage states ( $D_j$ ) selected for analysis include those that have frequency higher than selected screening frequency  $f_s$  and lower than target frequency  $f_t$  achieved as the prevention goal, that is,  $f_s < f_j(D_j) < f_t$  (severe accident mitigation window). Demonstration of reaching the safety goal is successful if  $P_{Fi}$  are below "physically unreasonable" level  $P_s$ . An arbitrary scale for probability is introduced in ROAAM to define a physically unreasonable process as one involving the independent combination of an end-of-spectrum with one expected to be outside but cannot be positively excluded [84]: 1/10 - Behavior is within known trends but obtainable only at the edge-of-spectrum parameters; 1/100 - Behavior cannot be positively excluded, but it is outside the spectrum of reason; 1/1000 - Behavior is physically unreasonable and violates well-known reality. Its occurrence can be argued against positively. Separate treatment of screening frequency for aleatory, and the physically unreasonable concept for epistemic uncertainties is a must for clarity and consistency of the ROAAM result.

Conditional containment failure probability is considered in this work as an indicator of severe accident management effectiveness for Nordic BWR. It is instructive to

note that different modes of failure can potentially lead to quite different consequences in terms of fission products release. At this point we consider any failure mode as unacceptable for the sake of conservatism.

### 3.3.2. Nordic BWR challenges for ROAAM and Decision making Context

If safety margins are large, then containment failure being physically unreasonable, can be demonstrated through consistent conservative treatment of uncertainties in risk assessment and improving necessary knowledge and data. If inherent margins are small or negative, improvement of knowledge is ineffective. Risk management (through appropriate modifications of the system e.g. safety design, SAMGs, etc.) should be undertaken in order to achieve the safety goal [84].

The tight coupling between severe accident threats (steam explosion and basemat melt-through due to debris un-coolability) and highly sensitivite of the SAM effectiveness with respect to timing of the event (e.g., vessel failure) and characteristics (e.g., melt release conditions), present challenges to the ROAAM in heuristic decomposition, analysis and integration [57]. In order to address the difficulties a structured process is needed for coherent (i) development of risk assessment framework, (ii) collection of necessary data, and knowledge. This process should be guided by extensive sensitivity and uncertainty analysis and eventually result in a robust and scrutable assessment of either “possibility” or “necessity” of containment failure in order to support decision making.

### 3.3.3. ROAAM+ Probabilistic Framework for Nordic BWR

The challenges presented by Nordic BWR SAM strategy require further development of the approach. The goal of the extended (ROAAM+) approach is to provide sufficient information for a decision to:

- I. Keep the SAM strategy: “Possibility” of containment failure is low even with “conservative” treatment of uncertainty, thus current strategy is reliable.
- II. Modify the SAM strategy: “Necessity” of containment failure in the course of accident is high (i.e., “possibility” that containment doesn’t fail is low) even with “optimistic” treatment of uncertainty, thus the current strategy is unreliable and changes should be considered.

In order to achieve the goal, ROAAM+ process is developed for adaptive refinement of (i) risk assessment framework, and (ii) necessary data, and knowledge. The process is guided by extensive sensitivity and uncertainty analysis.

#### *Iterative Adaptive Process for Refinement of Risk Assessment Framework*

When system complexity limits effectiveness of heuristic approach (based on expert judgment) to identification of the key physics and system behavior, there is a need for an iterative process of identifying importance of different contributors to the risk. At each stage of the process, a framework for risk assessment provides means for sensitivity and uncertainty analysis of “possibility” and “necessity” of containment failure with respect to the uncertain factors. Such analysis shows potential impact of improvements at the next iteration of the framework development or effectiveness of risk reduction through system modifications.

### Full and Surrogate Models, “Coarse-Fine”, “Forward” and “Reverse” Analyses

Adequately complex “full models” (FMs) are implemented for each stage of the accident progression using multidimensional codes for severe accident, thermal hydraulics, and structural analysis. Application of such FMs in extensive uncertainty analysis is often unaffordable. Therefore, a two-level coarse-fine modeling approach is needed. At the bottom level, loosely coupled fine resolution FMs and experimental evidences are used in order to generate relevant data. The top layer of the ROAAM+ framework for Nordic BWR ([58], [57]) decomposes severe accident progression (Figure 3-2) into a set of causal relationships (CR) represented by respective surrogate models (SM) connected through initial conditions. SMs are developed to approximate the most important parameters of the FM solutions.

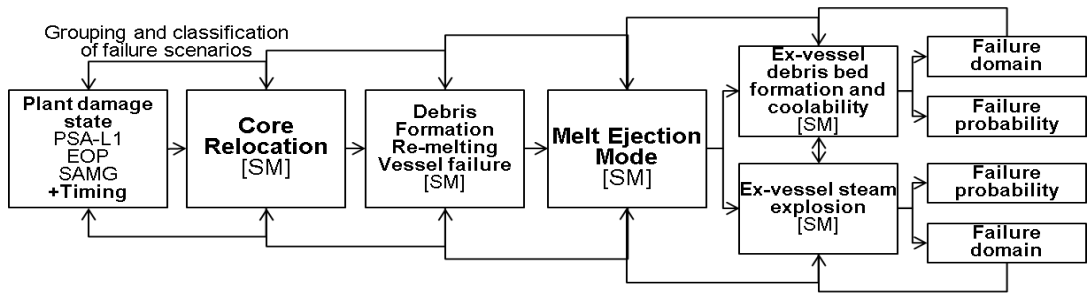


Figure 3-3: ROAAM+ framework for Nordic BWR.

Initial plant damage states  $\{D_j\}$  (determined by availability of safety systems) and their frequencies  $\{f_j\}$  are determined based on PSA L1 data [46] aiming at completeness of the analysis. For each  $\{D_j\}$  possible events which can affect further accident progression, order and timing of events create a space of scenarios  $\{s_i\}$ .

Forward analysis defines conditional containment failure probability for each scenario  $\{s_i\}$ . Reverse analysis identifies failure domains (domain where probability of containment failure is not “physically unreasonable”) in the space of scenarios  $\{s_i\}$ , and “deterministic”  $\{d_i\}$  and “intangible”  $\{i_i\}$  parameters specific to each model. Failure domain in the space of deterministic and intangible modeling parameters  $\{d_{ki}, i_{ki}\}$  help to identify the need for improvement of knowledge, modeling and data. The two-level coarse-fine approach to the development and iterative adaptive refinement of the risk assessment frameworks, details of the mathematical approaches for quantification of the failure probability and failure domains in the multistage deterministic analysis model are provided in [58], [57]. Such iterative process is designed to develop state of the art knowledge to the point when convergence of experts’ opinion on the possibility or necessity of containment failure can be achieved, which is a stopping criterion for the process.

The process of development and validation of the individual surrogate models is important for completeness, consistency, and transparency of the results. General ideas of the process is illustrated in [58], [57]. Experimental and other evidences provide a knowledge base for validation of the FMs and calibration of SMs. Full Models (FM) are implemented as detailed fine resolution (computationally expensive) simulation approach. Database of the FM transient solutions is developed in order to provide better understanding of basic physical processes and typical behavior of the target parameters. The target parameters are the input conditions for the next model in the framework. Simplified modeling approaches and data mining techniques are used in

order to develop a surrogate model. Surrogate model (SM) is an approximation of the FM model prediction of the target parameters which employ simplified (coarse resolution) physical modeling, calibratable closures, or approximations to the response surface of FM. Detailed discussion of the FM and SM development are presented in a series of publications (see Table 3-1).

### Treatment of the Intangible Uncertain Parameters

While ranges of the intangible parameters always can be (conservatively) bounded, the knowledge about distributions within the ranges is missing. In classical ROAAM, uncertainty in the intangibles can only be qualitatively approached, but it can always be bounded [84]. Such bounding approach is, in fact, similar to the interval analysis [28]. If inherent safety margins are sufficiently large, then bounding approach to the intangibles does not affect conclusions from the risk analysis. However, if failure probability  $P_f$  is sensitive not only to the ranges but also to the distributions, then uncertainty in prediction of  $P_f$  with “conservative” or “optimistic” bounding assumptions might be too large.

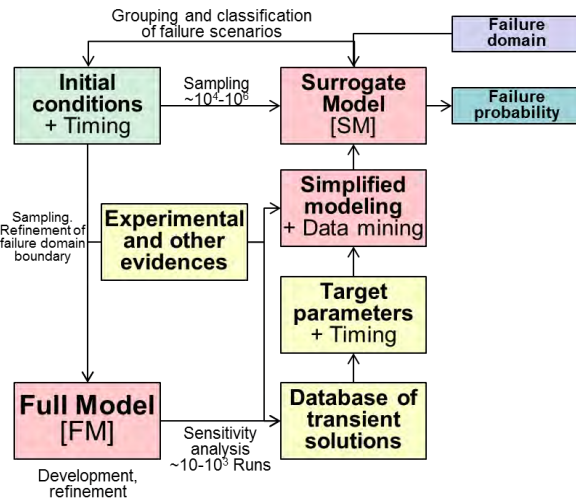


Figure 3-4: Full and Surrogate model development, integration with evidences, refinement, prediction of failure probability and failure domain identification.

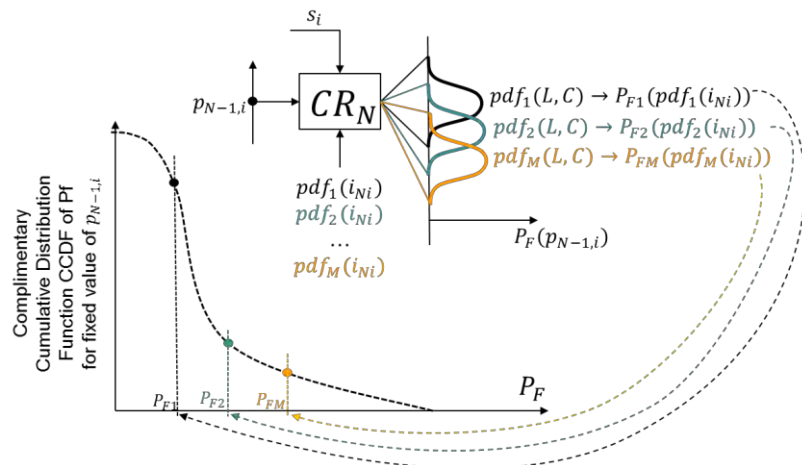


Figure 3-5: Treatment of model intangible parameters in ROAAM+ framework for Nordic BWR.

In order to assess the importance of the missing information about the distributions we consider distributions as uncertain parameters. A space of possible probability distributions of the intangible parameters is introduced. At the last stage of the framework ( $CR_N$ ), we randomly select a set of distributions of model intangible parameters  $pdf_k(i_{N,i})$  and calculate the value of  $P_{Fk}$  for selected combination of model input ( $p_{N-1,i}$ ) and scenario parameters ( $s_i$ ). Repeating this process for every possible set of distributions of  $i_{N,i}$  will yield probability distributions of  $P_F$  and  $CCDF(P_F(s_i, p_{N-1,i}))$  (Figure 3-5). Repeating the same process for each stage of the framework in the reverse analysis provides distributions of the failure probability for all possible combination of model input  $p_{ki}$  and scenario parameters  $s_i$ .

Table 3-1. Summary of full and surrogate models in ROAAM+ framework

SM	FM, experiments and SM purpose	References
CORE	FM: MELCOR model of the Nordic BWR containment. SM Type: Mapping. Given timing of ADS and ECCS activation provides time, composition and mass of core relocation and conditions in the lower drywall: pressure, pool temperature and depth. Optionally can provide time of vessel failure and release, debris properties at the onset of the release.	[46], [13], [14], [15], [16], [17], [18]
Vessel failure	FM: coupled thermo-mechanical analysis (PECM/ANSYS, DECOMSIM code) of the vessel lower head and debris. SM Type: Polynomial. Given mass and composition of the debris SM computes timings of the IGT, CRGT and vessel wall failure and corresponding mass and composition of liquid melt available for release.	[25], [26], [86], [87], [88], [89], [90], [91], [92], [93], [94], [95], [96], [97], [98], [99], [100], [114], [112], [122], [123]
Melt release	FM: parametric model of the melt release rate and vessel wall ablation. Experiment: remelting of multi-component debris and interaction with the vessel. SM Type: Physics based. Given timings and mode of lower head failure SM computes conditions of melt release, i.e. ablation of the breach, rate and duration of the release, thermal properties of the melt.	[47], [49], [55], [46], [58], [57]
SEIM	Steam Explosion Impact Map. FM: TEXAS-V code. SM Type: ANN. Given conditions of melt release and LDW characteristics SM returns a distribution of possible explosion impulses.	[21], [22], [23], [53], [24]
DECO	Debris Coolability. FMs: DECOMSIM code for coolability of the debris, debris bed spreading model, debris agglomeration models. Series of experiments on debris bed formation, agglomeration and particulate debris spreading are carried out. SMs Type: Physics based. Given conditions of melt release and pool, respective SMs return	[2], [3], [4], [5], [6], [7], [33], [34], [11], [12], [37], [38], [39], [40], [41], [42], [43], [44], [45], [48], [55], [59], [60], [61], [62], [63], [64], [65], [66], [67], [104], [106], [107], [108], [113],

	dryout heat flux and max debris bed heat flux, the effect of debris spreading and agglomerated debris are taken into account.	[114], [115], [116], [117], [118], [119], [120], [121]
--	---	--

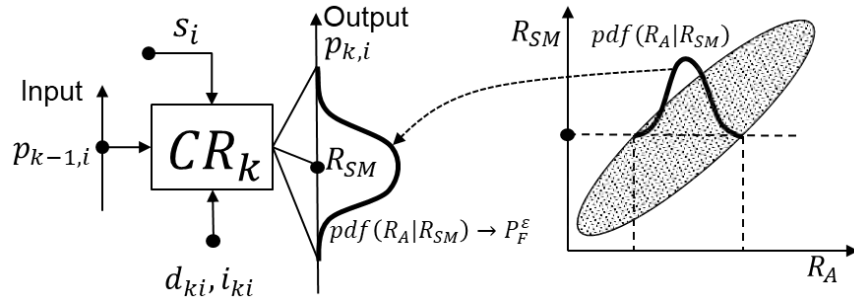


Figure 3-6: Treatment of uncertainty in SM prediction.

The uncertainty in the SM approximation of the FM can be characterized by the distribution  $pdf(R_{FM}|R_{SM})$  of possible values of full model response ( $R_{FM}$ ) given response of the SM ( $R_{SM}$ ) [57]. Respective failure probability  $P_F^\varepsilon$  which takes into account the uncertainty in the SM approximation of the FM can be calculated. The aim of the FM validation is to assess a distribution of possible values of actual system response ( $R_A$ ) given full model response ( $R_{FM}$ ), i.e.  $pdf(R_A|R_{FM})$ . Combining information about full model uncertainty with SM uncertainty one can obtain a distribution of possible actual system response given SM response  $pdf(R_A|R_{SM})$ . In this case failure probability  $P_F^\varepsilon$  will take into account uncertainty in both SM approximation of FM and uncertainty in FM prediction. It is instructive to note that data about full scale system behavior at prototypic conditions is rarely available. A challenge for validation is to develop relevant scaling approaches along with separate and integral effect test data for robust assessment of the  $pdf(R_A|R_{FM})$  (see Figure 3-6).

Figure 3-7a illustrates an example of possible CCDFs of  $P_f$  that is color-coded:

- $CCDF\{P_f(p_{N-1,i}) \geq P_s\} \leq 0.05$ : “Green” – at most 5% of the cases exceed  $P_s$ , or there is at least 95% confidence that the probability of failure  $P_f$  will not exceed selected screening probability  $P_s$ .
- $CCDF\{P_f(p_{N-1,i}) \geq P_s\} > 0.95$ : “Red” – at least 95% of the cases exceed  $P_s$ , or there at least 95% confidence the probability of failure  $P_f$  will exceed selected screening probability  $P_s$ .
- $CCDF\{P_f(p_{N-1,i}) \geq P_s\} \in (0.05 - 0.5]$ : “Blue” –  $P_f$  exceed  $P_s$  in 5-45% of the cases.
- $CCDF\{P_f(p_{N-1,i}) \geq P_s\} \in (0.5 - 0.95]$ : “Purple” –  $P_f$  exceed  $P_s$  in 50-95% of the cases. These are the cases where failure can be neither positively excluded nor assumed as imminent.

Figure 3-7b shows an example of the failure domain map calculated for the containment hatch door (with a presumed structural capacity limit 6 kPa\*s) due to steam explosion loads as a function of jet size and water level. The failure domain is constructed in the space of the input parameters. The SM is sampled in each cell to obtain a distribution of the failure probability. Each cell on the map is colored according to the  $CCDF(P_f)$  as described above.

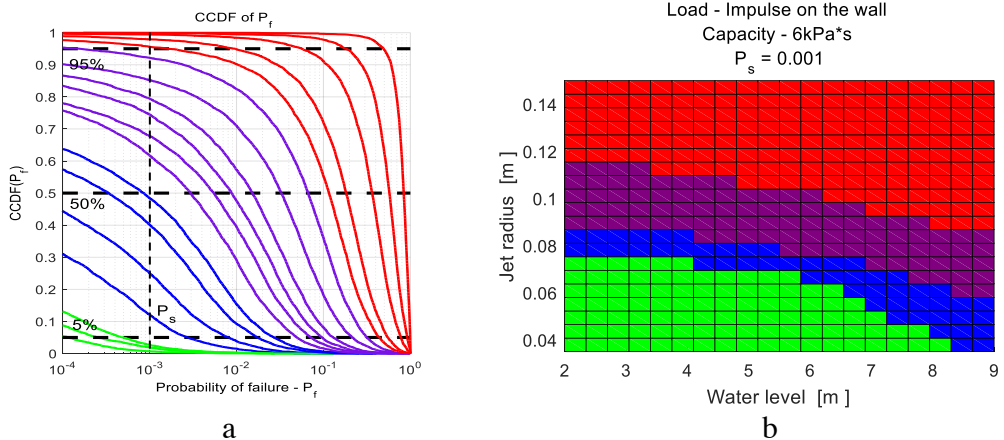


Figure 3-7. Complimentary cumulative distribution function of probability of failure  $CCDF(P_f)$  (a) and an example of the failure domain map (b).

### Implementation of ROAAM+ top Level Framework and Sampling.

Each SM in the framework is implemented as a set of functions in MATLAB, with respective I/O structure for forward and reverse analysis. Figure 3-8 illustrates implementation of PDF sampling of intangible parameters. Based on the user input in ROAAM+ configuration a set of parameters that characterize PDF for every intangible parameter in  $SM_k$  is generated. Function ‘‘PDF generator’’ generates a set of discrete PDFs (Figure 3-8 left) for every intangible parameter and then scales each PDF to ranges specific for each intangible parameter. The value of  $P_f$  is calculated for each combination of model input ( $p_{k-1,i}$ ) and selected distribution  $pdf(d_{ki}, i_{ki})$ .

### Decision Support and Connection to PSA

The aim of the ROAAM+ framework is to provide an assessment in support of the decision whether or not the risk associated with current SAM strategy is acceptable. Figure 3-9 presents decision criteria based on scenario frequency and related Conditional Probability of Unacceptable Release (CPUR), specifically, how  $pdf(P_{fi})$  (box and whiskers plots) can be used to judge the impact of uncertainty on the SAM strategy effectiveness [57]. The developed approach [50] is to (i) identify sequences from the PSA Level 1 and (ii) use ROAAM+ framework to evaluate the progress of these sequences and respective conditional containment failure probabilities for different severe accident scenarios.

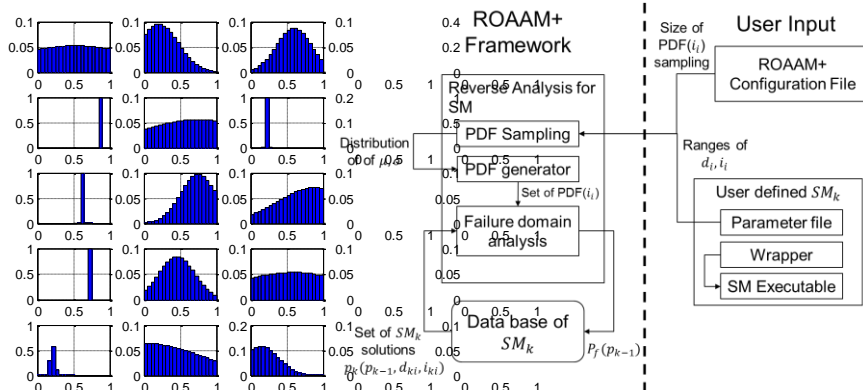


Figure 3-8: Implementation of PDF sampling in ROAAM+ framework.

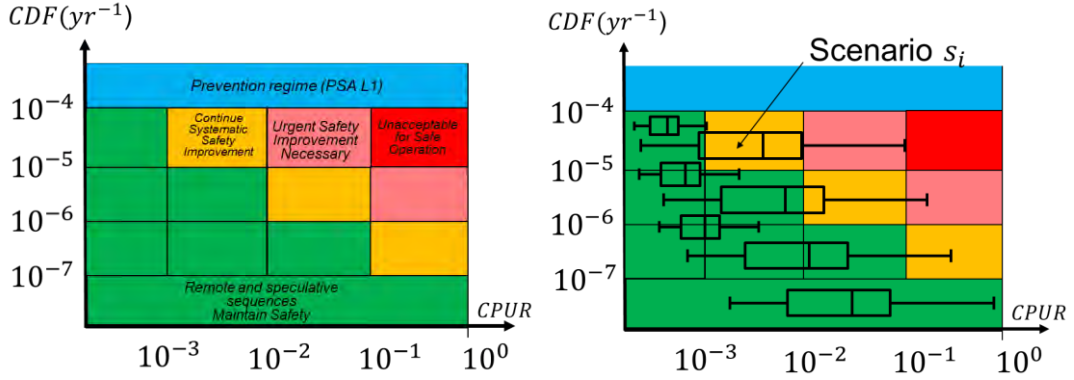


Figure 3-9: Decision support with ROAAM+.

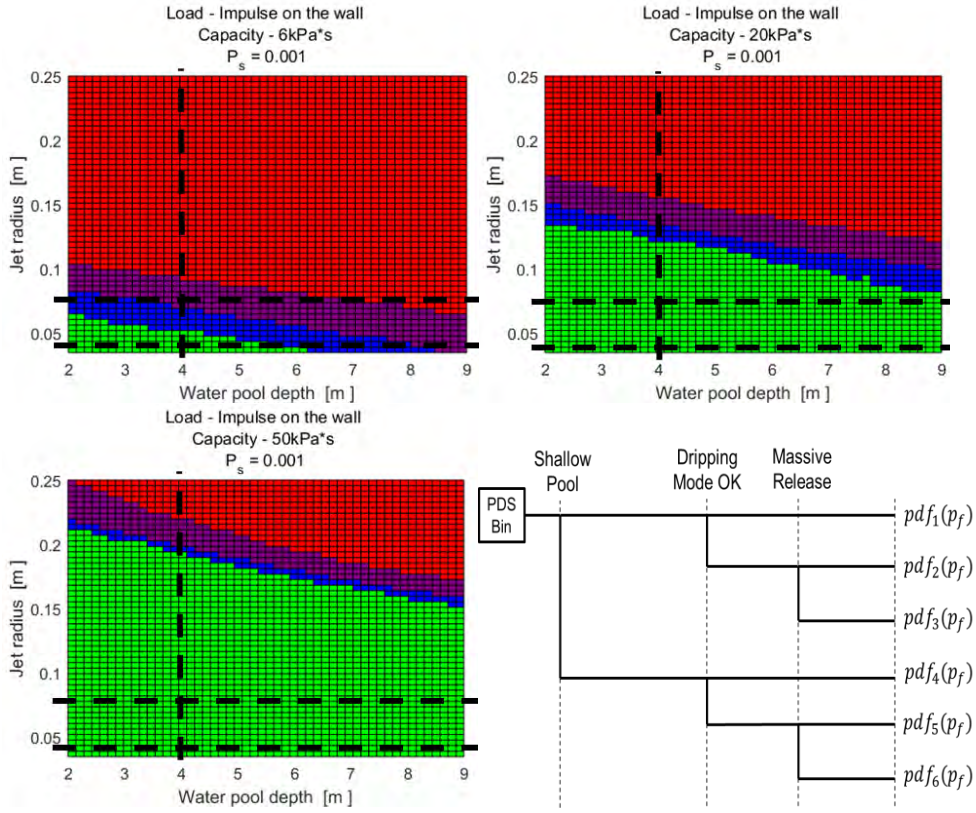


Figure 3-10: SEIM failure domain maps and refined containment event tree.

Consider failure domain maps obtained with ROAAM+ for ex-vessel steam explosion Figure 3-10. The failure domain map can be represented by 6 “modes” or “scenarios” (see the event tree in Figure 3-10). In Mode 1 (“Shallow Pool” and “Dripping Mode”), based on ROAAM+ results, maximum conditional containment failure probability is 0 for all fragility limits, meaning that containment failure due to ex-vessel steam explosion is physically unreasonable and SAM strategy is effective. In case of “deep pool” (i.e. LDW pool depth > 4m, Modes 4-6), probability of failure of non-reinforced hatch ranges from 0 to 0.729 (see Figure 3-11), depending on water pool depth and deterministic, intangible parameters used in modelling of ex-vessel steam explosion. Figure 3-11a and b show the CCDF of conditional containment failure probability (CCFP) due to ex-vessel steam explosion for Modes 1-6 in case of medium release for shallow and deep pool respectively. The results suggest that there’s significant difference in CCFP depending on the LDW water pool depth. Thus

ROAAM+ analysis can provide insights regarding under what conditions each phenomenon is relevant and if specific sequences need to be treated differently in PSA context, and result in refinement of plant damage states in PSA L1. This example is studied further in the summary of results section, including integration with the PSA.

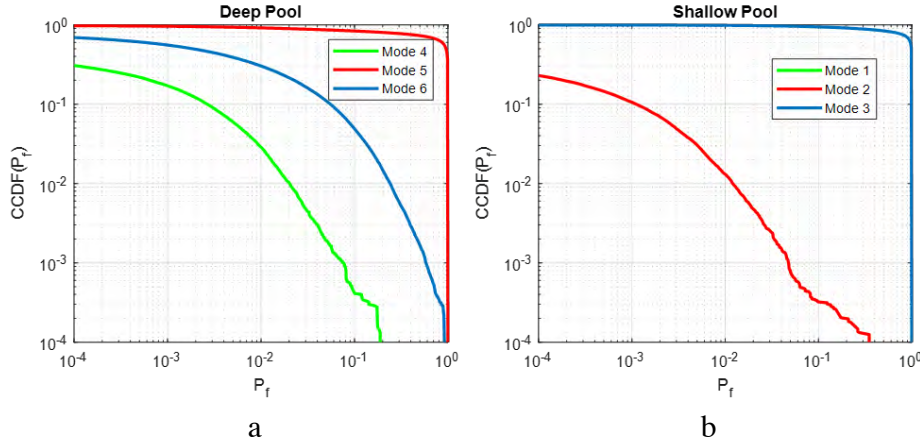


Figure 3-11: CCDF of Conditional Containment Failure Probability due to Ex-Vessel Steam Explosion with non-reinforced hatch door for deep (a) and shallow (b) pools.

### 3.3.4. RES: Summary

RES focuses on the development of theoretical background and implementation of the ROAAM+ framework. The aim is to achieve (i) completeness, (ii) consistency, and (iii) transparency in the review of the analysis and its results. A two-level coarse-fine iterative analysis approach is employed. First, fine-resolution but computationally expensive methods are used in order to (a) provide better understanding of key phenomena and their interdependencies, (b) identify transitions between qualitatively different regimes and failure modes, and (c) to generate databases of solutions. The fine-resolution codes are run independently, assuming wider possible ranges of the input parameters. Second, a set of coupled modular frameworks is developed connecting initial plant damage states with respective containment failure modes. Deterministic processes are treated using surrogate models based on the data obtained from the fine-resolution models. The surrogate models are computationally efficient and preserve the importance of scenario and timing. Analysis carried out with the complete frameworks helps to identify risk significant and unimportant regimes and scenarios, as well as ranges of the uncertain parameters where fine-resolution data is missing. This information is used in the next iteration of analysis with fine-resolution models, and then refinement of (i) overall structure of the frameworks, (ii) surrogate models, and (iii) their interconnections. Such iterative approach helps identifying areas where additional data may significantly reduce uncertainty in the fine- and coarse-resolution methods, and increase confidence and transparency in the risk assessment results. Extended treatment of the uncertain parameters including the effect of the unknown distributions is employed rendering quantification of uncertainty in the failure probability in terms of a cumulative distribution. Failure domain representation is proposed to identify “safe” and “failure” subdomains considering the confidence in whether failure probability can exceed screening probability.

The ROAAM+ framework is implemented as a general purpose modular tool in MATLAB. Different kinds of surrogate models can be easily used in the framework to carry out typical tasks of the forward and reverse analysis.

An approach for coupling between ROAAM+ and PSA is discussed. Further development can address further improvements in (i) computational efficiency of sampling using second order statistical analysis; (ii) representation of failure domains in multidimensional parameter space; (iii) further extension of connections with PSA.

### 3.4 Melt Ejection Mode (MEM)

The MEM goal is to develop deterministic models in order to establish connection between plant damage states and respective characteristics of (i) core relocation; (ii) vessel failure (timing and mode); and (iii) melt ejection (vessel breach size, melt superheat, composition, flow rate and total amount of ejected melt).

#### 3.4.1. Core Relocation

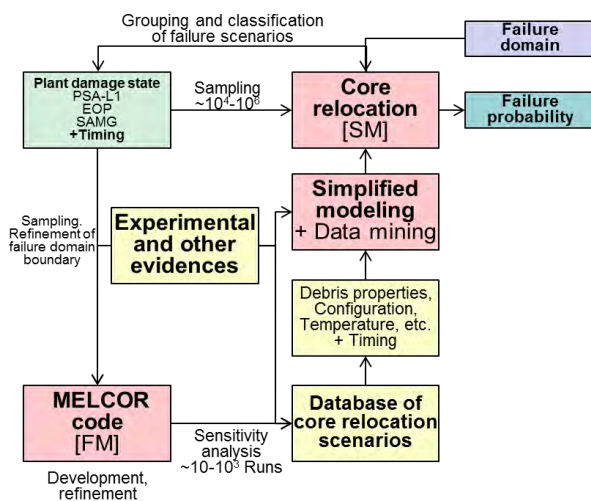


Figure 3-12: Core relocation surrogate model.

There is an apparent sensitivity of the vessel failure phenomena due to the characteristics of the debris in the lower plenum [100], [25]. The goal is to develop Core Relocation full and surrogate models that can be used in the ROAAM+ framework [49] for prediction of the effect of core degradation and relocation processes on the debris bed properties in the lower head. General approach to the development of the Core relocation SM is illustrated in Figure 3-12. In order to achieve the goal and develop the SM according to the general approach, following tasks are addressed [57]: (i) definition of the plant damage states and respective frequencies from PSA-L1; (ii) definition of the scenario space including possible timing of system recovery and operator actions; (iii) development of the database of the core degradation transients using MELCOR code with regular and GA-IDPSA adaptive sampling techniques [101], [102], [103], [68], [76], [77]; (iv) establishing connections with the other SMs in the ROAAM+ framework; (v) data mining and simplified modeling for development of the SM based on the database of the FM solutions.

#### *Definition of the plant damage states based on PSA-L1 data*

This task includes (i) grouping of initial plant damage states based on PSA-L1, EOP and SAMG; (ii) selection of representative plant damage states (based on contribution to total core damage frequency) and scenarios for MELCOR (FM) analysis. In PSA L1 for Nordic BWR reference plant design the core damage states are grouped into 4 categories: HS1 (ATWS), HS2 (core damage due to inadequate core cooling), HS3

(core damage due to inadequate residual heat removal) and HS4 (rapid overpressure of the primary system). The categories (HS1, HS2, HS4) correspond to early core damage scenarios, HS3 corresponds to late core damage. In addressing ex-vessel behavior and consequences, the following physical phenomena can challenge containment integrity: direct containment heating (DCH), ex-vessel steam explosions (EVE) and basemat penetration (BMP) by non-coolable corium debris. DCH scenario corresponds to high pressure (HP) accident scenario, steam explosion in the containment (EVE) corresponds to low pressure (LP) scenario. Both HP and LP lead to formation of ex-vessel debris bed and potential corium interaction with containment basemat.

#### *Definition of the scenario space with possible recovery and operator actions*

The station blackout (SBO) scenario occurred in Fukushima-Daiichi [19] is among the major contributors to the core damage frequency (CDF) for Nordic BWR according to PSA Level 1 analysis. In the Forsmark 2006 incident it took about 30 minutes for the plant operators to restart all diesels. In this work we consider station blackout (SBO) scenario with a delayed power recovery. We consider a simultaneous loss of the offsite power (LOOP) and backup diesel generators. This results in the simultaneous loss of all water injection systems, including crud purge flow through the control rod drive tubes. According to the considered scenario, the operator can delay activation of the depressurization system to keep coolant in the vessel. For injection of water with low pressure ECCS, depressurization has to be activated. The capacity and timing of activation of the safety systems are elements of the scenario.

#### *Core Relocation Analysis Results Using MELCOR code: The Effect of Severe Accident Scenario on the Properties of Relocated Debris in LP*

The analysis of the effect of severe accident scenario and possible recovery actions using different MELCOR code versions has been performed [14], [17]. A data base of full model solutions has been generated using MELCOR code versions 1.86 (rev2911), 2.1(rev7544) and 2.2(rev9541). Sampling, i.e. MELCOR code execution and data extraction processes, is run by a simulation driver, implemented in MATLAB, which performs: (i) sampling generation; (ii) MELCOR Input file generation; (iii) execution of the MELCOR code on distributed computing network; (iv) adaptive refinement of the maximum time step; (v) extraction of the data to the database of solutions and post-processing of the results. Summary of the results are presented in Figure 3-13 in form of maps (as functions of ADS and ECCS Timing). Post-processing of the results has been performed using pattern analysis approach [14]. The results showed that: the most common relocation pattern is a rapid relocation to LP; the major part of core materials is relocated to LP shortly after initial core support plate failure (within ~30-60mins); delay in activation of ADS can delay massive core relocation to LP, however it results in greater extent of debris oxidation; ECCS is effective in preventing massive core relocation only within relatively small time window after activation of ADS; debris composition (i.e. metallic/oxidic debris fraction) in different layers are sensitive to the accident scenario and can be classified into a limited number of groups (see Figure 3-14) (Group A – significant metallic fraction – corresponds to early ADS activation, Group B – Significant oxide fraction – corresponds to late ADS activation, Group C – corresponds to the group of scenarios with relocated debris mass within the range of 100 tons.)

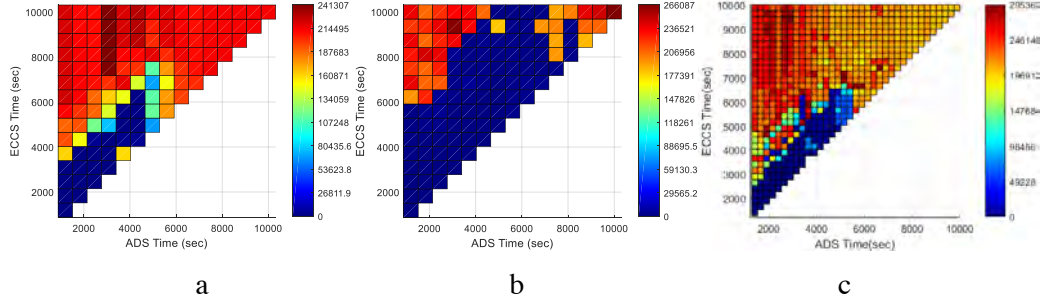


Figure 3-13: Debris Mass in Nordic BWR Lower Plenum at  $T_{ref} + 3600\text{sec}$  as a function of ADS time and ECCS time obtained with MELCOR 2.1 rev7544 (a), MELCOR 2.2 rev 9541 (b), and MELCOR 1.86 rev2911 (c).

The oxide fraction of relocated debris in LP in both groups A and B is highly correlated with the hydrogen generated during the course of accident (see Figure 3-14). Thus the scenarios can be split into 4 groups:

- Small (<10 tons) relocation domain, mostly metallic debris.
- Transition domain, total debris mass in the range from ~20 to ~100 tons (sensitive to modelling options in MELCOR (e.g. oxidized fuel rod collapse temperature)).
- Large relocation (over 100 tons) domain with small debris oxidation and relatively high metallic debris fraction (typical for early ADS activation).
- Large relocation (over 100 tons) domain with significant debris oxidation, and relatively small metallic debris fraction (typical for late ADS activation).

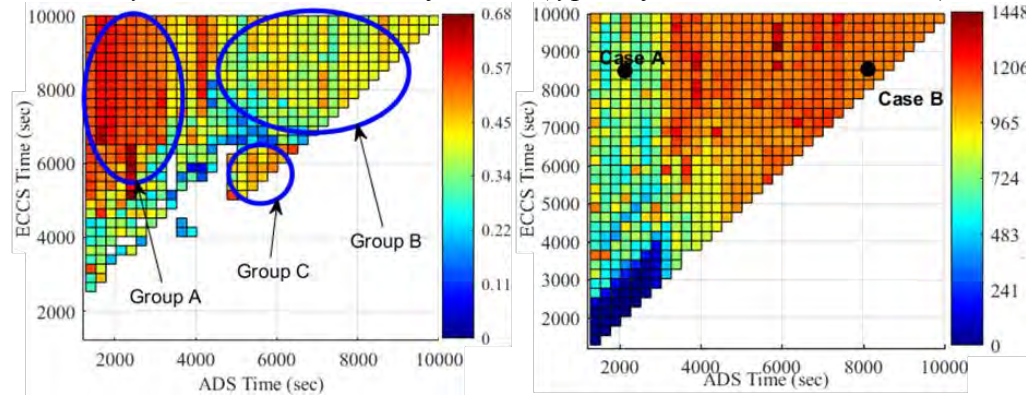


Figure 3-14: Map of metallic debris fraction in the 1<sup>st</sup> axial level (Left); Hydrogen mass in containment as a function of severe accident scenario (Right) [14].

Moreover, we found that there are some discrepancies in predictions of different code versions [17]. For example, there is a major discrepancy in prediction of the total debris mass and time of core support plate failure between MELCOR code versions 1.86/2.1 and 2.2. For scenarios with late depressurization (in the range of ~4000-7000 sec.) and reflooding MELCOR 2.2 predicts possible stop of accident progression in core region, and prevents massive core relocation to LP. One of the possible explanations is that in MELCOR 1.86/2.1(rev prior to 7864) failed canister candle to the cell below onto fuel rods leading to their earlier failure. In MELCOR 2.2 canister candle onto canisters below. This reduces rod failure when a canister fails and leads to reduced numerical variance in solutions [125], [124]. We also found other differences in prediction, which can be due to different values of default and best practices sensitivity coefficients used in the analysis.

### Sensitivity Analysis for Severe Accident Progression and LP Debris Properties

Sensitivity analysis using Morris method [75] has been performed for two representative cases with large (Case A (ADS Time – 2500sec, ECCS Time - 8500 sec) and small (Case B (ADS Time – 8000sec, ECCS Time – 8500sec) metallic debris fraction that represent typical behavior for scenarios with early and late depressurization and late water injection [14], [18]. Ranges of the parameters selected for MELCOR sensitivity study is presented in the Table 3-2. Total debris mass, hydrogen mass in containment, metallic fractions in the first and second axial levels and time of onset of massive relocation to LP were taken as response functions in this analysis. Descriptive statistics is presented in Table 3-3,

An approach for connection between Core Relocation and In-vessel Debris Bed Coolability and Vessel Failure analyses has been developed in [14] for the case when another model (not MELCOR) is used for prediction of vessel failure and melt release. Different approaches to development of the surrogate model for prediction of the properties of relocated debris and LDW pool conditions have been developed [76], [57]. The surrogate model used in this work is of a “look-up table” type. The output of the surrogate model is presented as mean and standard deviation of respective distributions of the parameters of interest [16].

Table 3-4. In Case B (see Figure 3-15a) the most important factors for hydrogen production are particulate debris porosity (PDPor) and debris falling velocity (VFALL). For the Case A, (see Figure 3-15a) the most important factors for hydrogen production are PDPor, TRDFAI. The details of results of sensitivity study are summarized in [17], [18], [57].

Table 3-2: Selected MELCOR parameters and their ranges.

Parameter name	Range	Units
<b>For 1.86</b>		
Maximum Time Step (MTS)	[0.001-2.0]	sec
Oxidized fuel rod collapse temperature (TRDFAI)	[2500-2650]	K
Particulate Debris Porosity (PDPor)	[0.3-0.5]	-
<b>For 1.86 and 2.1, 2.2</b>		
Velocity of falling debris (VFALL)	[0.01-1.0]	m/s
LP Particulate debris equivalent diameter (DHYPDLP)	[0.002-0.005]	m
<b>For 2.1, 2.2</b>		
Molten Cladding (pool) drainage rate (SC11412)	[0.1-2.0]	kg/m-s
Molten Zircaloy melt break-through temperature (SC11312)	[2100-2540]	K
Time Constant for radial (solid) debris relocation (SC10201)	[180-720]	sec
Time Constant for radial (liquid) debris relocation (SC10202)	[30-120]	sec
Heat transfer coefficient from falling debris to pool (CORCHTP)	[200-2000]	W/m <sup>2</sup> -K

Table 3-3: Descriptive statistics for the Case A and B with MELCOR 2.1.

	Mean value $\mu$ Standard deviation $\sigma$		Min Max		Skewness Kurtosis	
	A	B	A	B	A	B
<b>Debris mass (kg)</b>	209773 19220	181655 37624	137373 261324	80772 260196	-0.31 4.26	-0.06 2.54
<b>Metallic debris fraction</b>	0.43 0.03	0.36 0.05	0.36 0.5	0.26 0.5	0.01 2.60	0.13 2.29
<b>T<sub>ref</sub> (sec)</b>	5092	6882	3810	4285	-0.74	0.24

	559	905	6050	11050	2.40	5.05
<b>Hydrogen mass (kg)</b>	583	1184	344	792	0.81	0.29
	135	232	1008	1823	3.25	2.4

An approach for connection between Core Relocation and In-vessel Debris Bed Coolability and Vessel Failure analyses has been developed in [14] for the case when another model (not MELCOR) is used for prediction of vessel failure and melt release. Different approaches to development of the surrogate model for prediction of the properties of relocated debris and LDW pool conditions have been developed [76], [57]. The surrogate model used in this work is of a “look-up table” type. The output of the surrogate model is presented as mean and standard deviation of respective distributions of the parameters of interest [16].

Table 3-4: Descriptive statistics for the Case A and B with MELCOR 2.2.

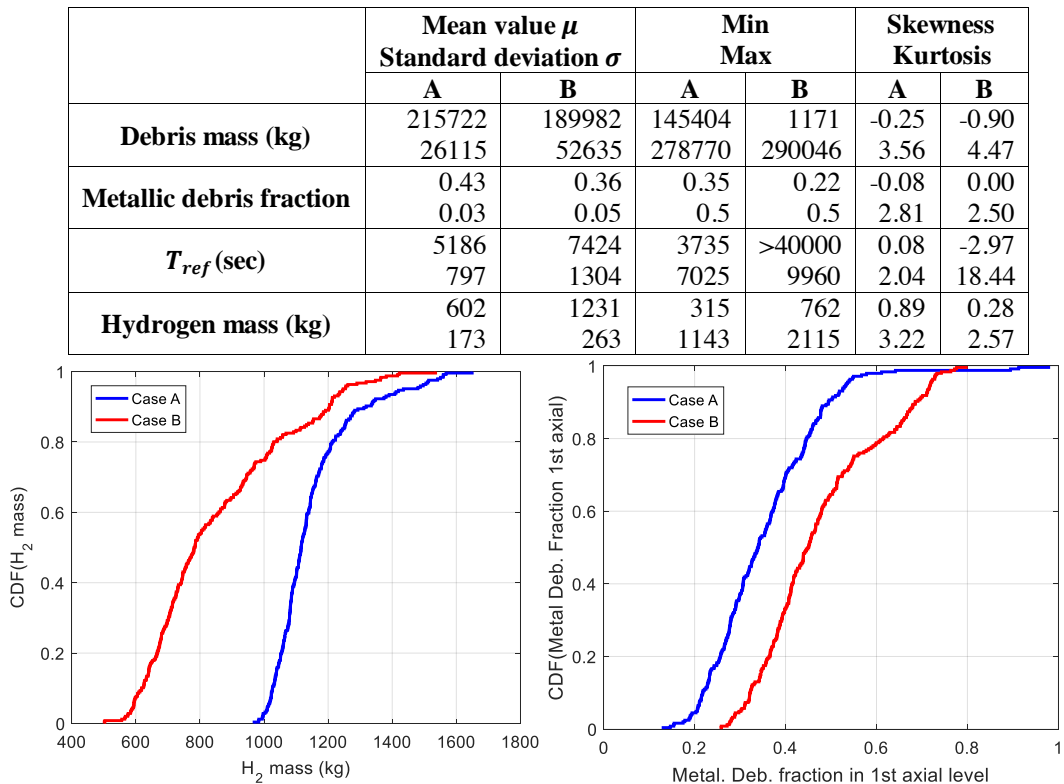


Figure 3-15: MELCOR 1.86. Cumulative distribution function of (a) Hydrogen mass generated (kg) (b) Metallic debris fraction in the first axial level.

### Summary

Full model (FM) of core relocation has been developed using MELCOR code. GA-IDPSA and MATLAB tools are used for sampling and populating the database of the FM solutions. Several thousand accident scenarios have been simulated with MELCOR. The results indicate that depending on the scenario and timing of safety systems recovery, core degradation most likely results in small (less than 10 tons) or very large (more than 200 tons) relocation of debris. The number of scenarios with intermediate (from 20 to 100 tons) mass of relocated debris is relatively small. The

domain where such scenarios are located overlaps with the domain of very large relocation, meaning that small variations in the scenario parameters can lead to significant variations of the properties of relocated debris bed in this domain. Sensitivity analysis helps to understand the effect of different modeling factors on the predictions with different MELCOR code versions.

### 3.4.2. Vessel Failure Modeling

Vessel failure mode and timing provides initial conditions and limiting factors for the melt release and ex-vessel accident progression. The ultimate goal is to develop surrogate models (Figure 3-16) for prediction of timing, amount, properties and superheat of the melt available for release in different vessel failure modes. Debris reheating, remelting, and melt-interaction with vessel wall and structures are important phenomena. The fine resolution full models based on MELCOR, DECOSIM [114], [112] and PECM/ANSYS ([88], [93], [95]) are employed for simulations.

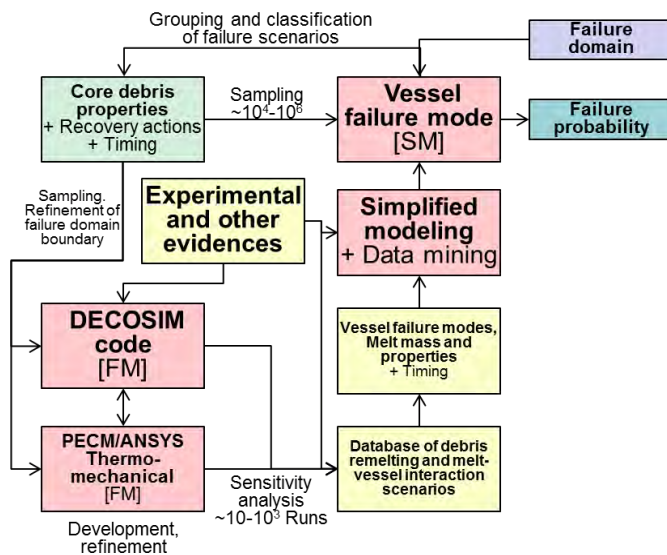


Figure 3-16: Debris re-melting Vessel failure surrogate model.

The DECOSIM and PECM/ANSYS codes are complementary approaches which describe two different classes of scenarios with initially (i) porous debris bed and (ii) “solid cake” bed, respectively. The DECOSIM code that was developed earlier for ex-vessel applications is extended to the in-vessel case by taking into account congestion of lower plenum by structural elements, heat transfer in the vapor phase, as well as remelting of the corium material. Also, the thermal hydraulics module of the code was enhanced to make simulations possible at high temperatures, characteristic of the post-dryout stage of accident progression, to determine if a porous debris bed is coolable or non-coolable. The non-coolable debris bed requires further analysis. The PECM is implemented in the commercial code FLUENT® and simulates the debris bed heatup, remelting, melt pool formation and heat transfer. A coupled thermo-mechanical creep analysis is carried out with ANSYS® code where transient heat transfer characteristics from PECM are used as boundary conditions. The deformation of the vessel wall is assumed to have negligible effect on the melt pool heat transfer, so only one way coupling between PECM and ANSYS is employed.

### Vessel Failure Analysis with MELCOR Code

The analysis of vessel breach and melt release conditions with MELCOR code was performed with MELCOR 2.1 (rev.7544). In the analysis we considered ADS and ECCS timing to be uniformly distributed within [1.e3-1.e4] (sec) (subject to ADS Timing < ECCS Timing constrain, i.e. water injection with (Low Pressure) ECCS cannot be initiated prior depressurization). The analysis was performed for 4 sets of calculations: (1) No penetration modelling, solid debris ejection: only vessel wall can failure due to creep-rupture; debris can be ejected regardless of its state. (2) No penetration modelling, no solid debris ejection: only vessel wall can failure due to creep-rupture; molten debris (plus some fraction of solid debris, based on secondary material transport model [126], [127]) can be ejected. (3) Penetration modelling, solid debris ejection: vessel can fail due to penetration failure and/or vessel wall failure (due to creep-rupture); debris can be ejected regardless of its state. (4) Penetration modelling, no solid debris ejection: vessel can fail due to penetration failure and/or vessel wall failure (due to creep-rupture); whenever any failure condition is satisfied, an opening with an initial diameter defined by the user (e.g IGT – 0.07m, CRGT – 0.14m) is established. If there are no penetrations modeled, initial diameter will take default value of 0.1m, however in case of gross failure of vessel wall, it is assumed that all debris in the bottom axial level of the corresponding ring, regardless its state, is discharged linearly over 1s time step without taking into account failure opening diameter.

Molten debris (plus some fraction of solid debris, based on secondary material transport model [126], [127]) can be ejected. The velocity of material being ejected is calculated from the pressure difference between the lower-plenum control volume and the reactor cavity control volume, the gravitational head from the debris layer itself, and a user-specified flow discharge coefficient, using the Bernoulli equation [126], [127]. Ablation of the failure opening is modeled by calculating the heat transfer to the lower head by flowing molten debris. A simplified implementation of the ablation model by Pilch and Tarbell is used [126], [127].

Figure 3-17 show the cumulative distribution of the time of vessel wall breach and release time. Penetration failure occurs earlier than vessel failure after initiating event.

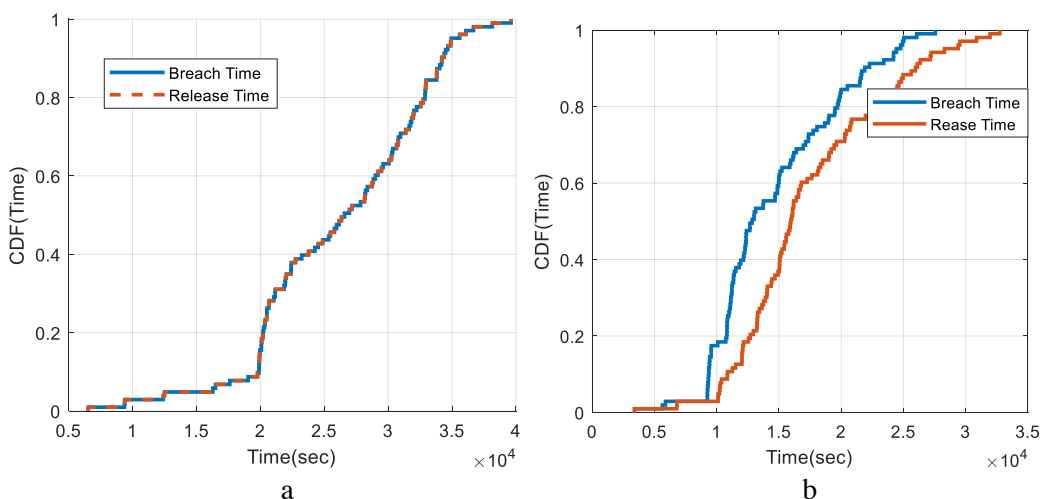


Figure 3-17: Time of Vessel Failure and Melt Release (sec) a) No penetration modelling b) With penetration modelling.

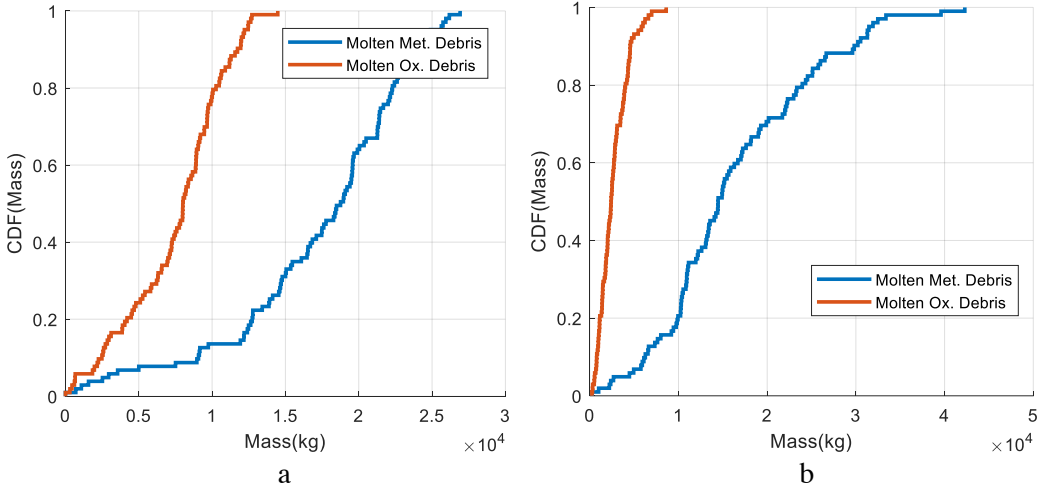


Figure 3-18: Molten Metallic and Oxidic Debris at the Time of the Release a) without and b) with penetration modelling.

In case of penetration failure, release starts with some time delay after initial vessel breach. Figure 3-18 and 3-19 show the amount of metallic and oxidic debris at the time of the release, and corresponding molten debris components superheat.

Mass of molten metallic debris can range from ~1-25 tons in case without penetration modelling (vessel wall failure, see Figure 3-18a), while in case of penetration failure (see Figure 3-18b), it ranges from ~1 to 45 tons. This difference between molten metallic debris mass, and comparable values of mass averaged superheat of metals (see Figure 3-19a,b) can be explained by water drainage from the vessel at early penetration failure, which results in rapid uncovering of the debris in scenarios where water injection is initiated after vessel breach due to penetration failure, and due to the effect of molten pool models in MELCOR code. It is assumed in MELCOR that particulate debris will sink into a molten pool, displacing the molten pool volume. Thus, once solid debris components with lower melting point (such as stainless steel) start to melt, the volume occupied by the solid debris decreases, the molten materials will occupy empty volume within the solid debris (reducing solid debris porosity). The remaining melt will form a molten pool on top of the particulate debris, which will be displaced by particulate debris to the cell located above, eventually producing a stainless steel-rich layer on top of the solid debris.

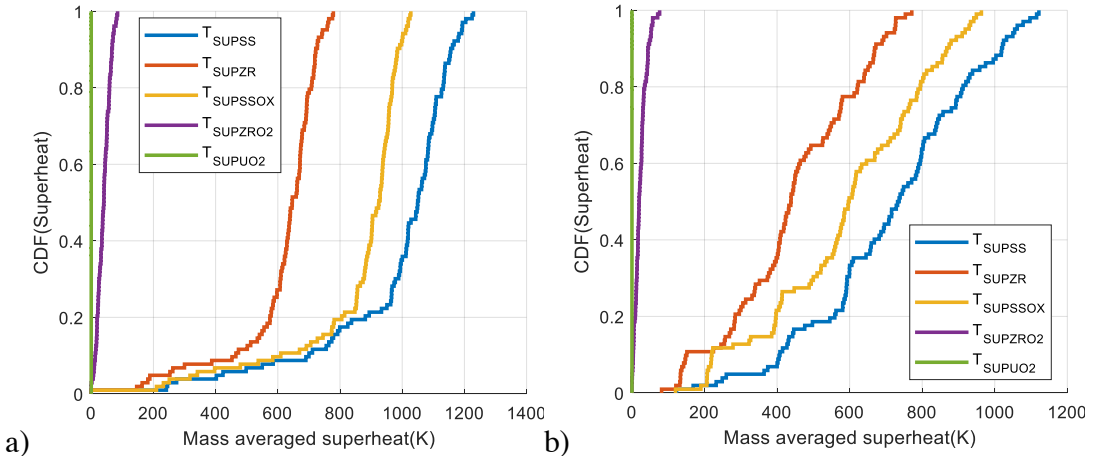


Figure 3-19: Mass Averaged Superheat of Molten Debris Components at the Time of the Release a) without and b) with penetration modelling.

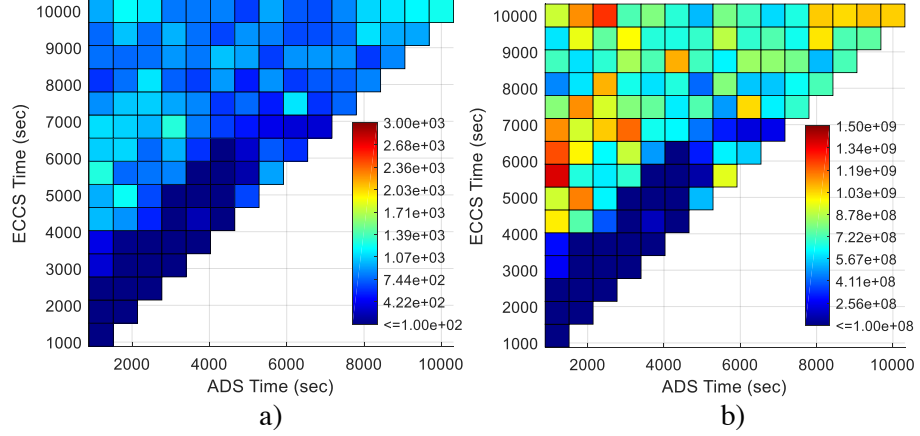


Figure 3-20: (a) Maximum debris ejection rate (kg/s) (b) Maximum enthalpy rate (J/s) with penetration modelling, solid debris ejection ON (IDEJ=0).

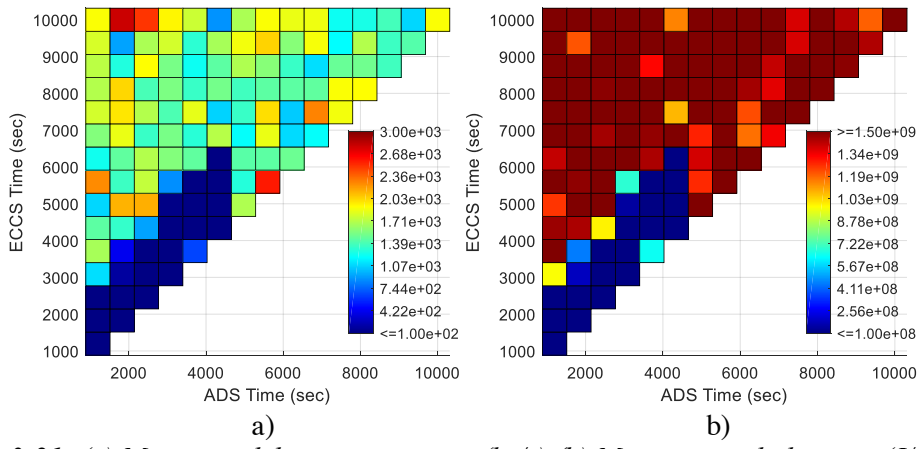


Figure 3-21: (a) Maximum debris ejection rate (kg/s) (b) Maximum enthalpy rate (J/s) without penetration modelling.

Figure 3-20 and Figure 3-21 show examples of the maps of debris ejection rate and enthalpy rate. Detailed analysis [57] show that vessel wall failure results in rapid ejection of lower plenum debris to the cavity, with initial debris ejection rates of  $\sim 2 \cdot 10^3$  (kg/s), and enthalpy rate of  $\sim 10^9$  (W), regardless of the option chosen for solid/liquid debris ejection. In case of penetration failure, debris is discharged at the rate of  $\sim 4 \cdot 10^2$  (kg/s), and enthalpy rate of  $\sim 5 \cdot 10^8$  (W), which is considerably smaller compared to the values for vessel wall failure. Furthermore, the results show that there is quite significant difference in results between solid vs. liquid debris ejection options, where the latter option results in smaller values of debris ejection and enthalpy rates [57].

#### PECM/ANSYS Thermo-Mechanical Full Model for Vessel Failure Analysis

PECM is a 3D model implemented in Fluent for prediction of melt pool convection and heat transfer (see [88], [93], [95] for more discussions) in the BWR lower plenum. ANSYS Structural under ANSYS Workbench is used to simulate deformations and thermal creep of the vessel wall and penetrations (see Figure 3-22). CRGTs can be cooled from inside by water flow; the water is assumed to be ejected from the CRGTs providing a water layer atop of the debris bed, otherwise adiabatic boundary conditions are used for CRGT surfaces. Other surfaces are subjected to Neumann boundary conditions. The vessel wall is insulated and therefore a small heat flux (20 W/m<sup>2</sup>) is allowed at the external surface. A modified time hardening (primary) creep

model is chosen in ANSYS 17. Coefficients for the model are generated using the experimental creep data for vessel steel SA533B1 from Rempe et al. [78]. See [95] for complete details along with the validation.

### *Insights from PECM-ANSYS Analysis with Homogeneous Debris*

Previous PECM-ANSYS calculations [95] were done using a 3D slice model of the lower head (see Figure 3-23b) and a 2D axisymmetric model of the vessel wall. A more detailed 3D quadrant model of the lower head has also been used but it is computationally expensive. To combine the accuracy of the 3D quadrant model and the efficiency of the 3D slice model, an effective 3D slice model was developed by preserving (i) the cooled surface to heated volume ratio, (ii) surface area (in contact with the debris bed) to volume ratio, and (iii) mechanical load to the vessel wall (due to the penetrations) as in the 3D quadrant model.

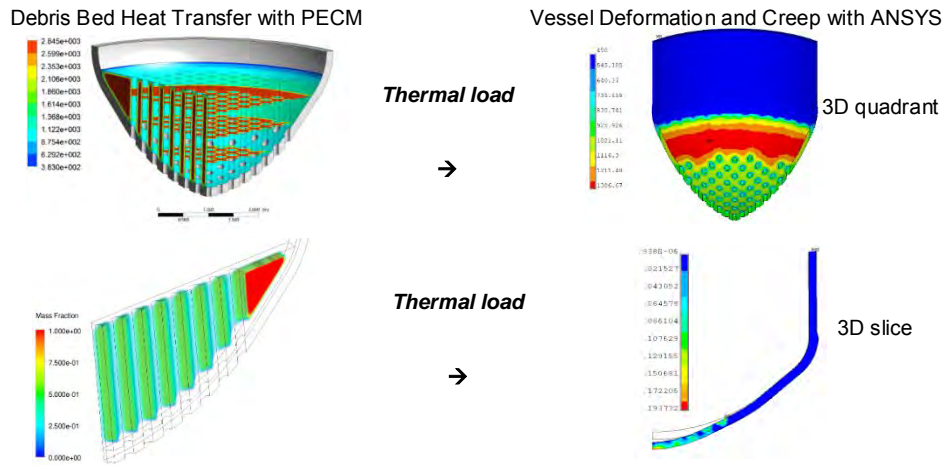


Figure 3-22: Coupled thermo-mechanical simulation flow.

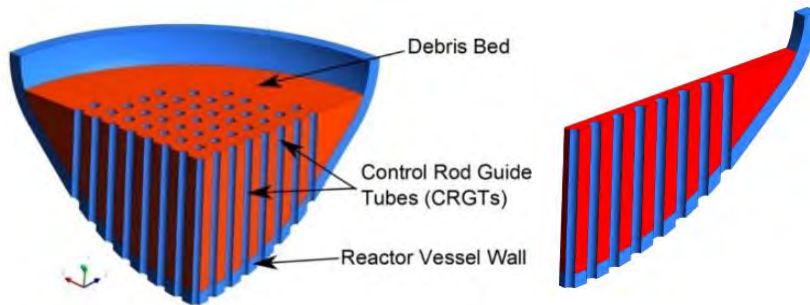


Figure 3-23: Geometry of (a) 3D quadrant and (b) 3D Slice used in PECM.

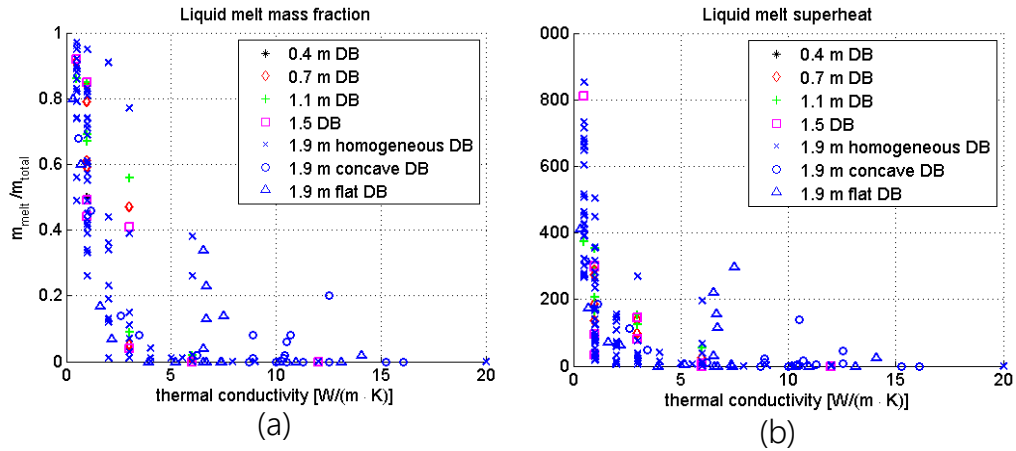
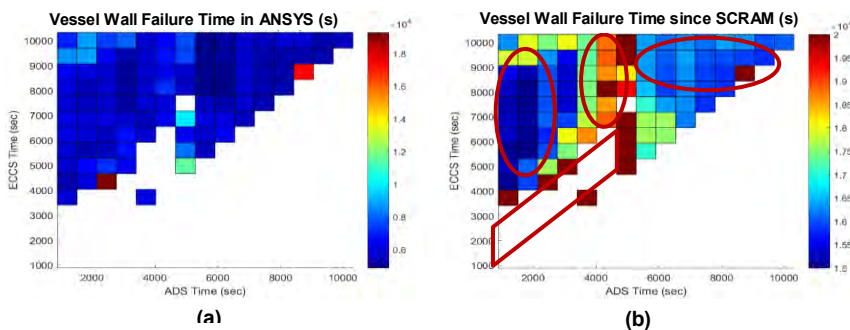


Figure 3-24: Melt mass fraction (a) melt superheat (b).

The debris averaged temperature, melt mass and displacements are in excellent agreement between quadrant and effective slice. It has been shown that higher pressure has a small effect on vessel failure timing [26]. The debris remelting starts around 2.5 hours, and it intensifies between 2.75 – 3.75 hours; during which more than 50 % (~115 tons of 230) of debris bed becomes molten in all the cases. It was also found [26] that the thermal conductivity is the most influential parameter for timing of the failure, mass and superheat of liquid melt available for release. The melt mass and melt superheat plotted with respect to the thermal conductivity of the vessel wall are shown in Figure 3-24.

#### Vessel failure analysis with debris properties provided by MELCOR

A method is developed to directly map debris bed non-homogeneity obtained in MELCOR to PECM simulations in Fluent including: non-uniform spatially-distributed temperature and physical variables; parameters are locally (mass/volume) averaged as a mixture of components (UO<sub>2</sub>/Zr/ZrO<sub>2</sub>/SS/SSOX) over each MELCOR cell; spatial and temperature dependent physical properties. A total of 120 MELCOR core relocation cases varying in ECCS/ADS activation time were used to generate a vessel failure response database. The results are analyzed regarding different vessel failure modes (vessel wall failure, CRGT failure, IGT failure) and corresponding parameters of interest (failure time, failure location, corresponding melt mass, corresponding maximum temperature or superheat). Vessel failure time is defined as the timing when maximum creep strain reaches 20%.



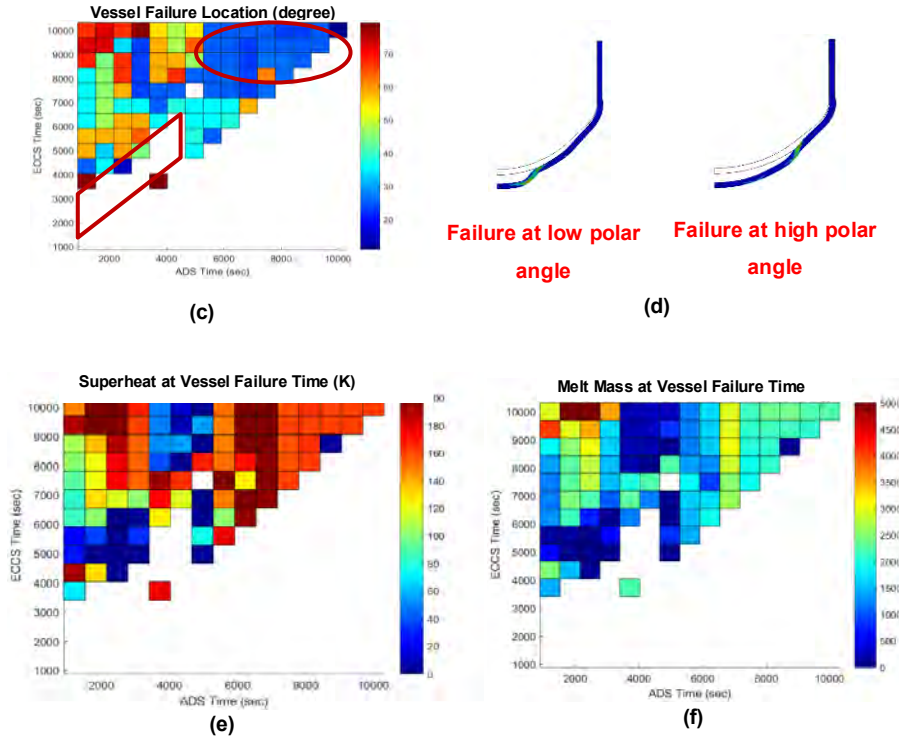


Figure 3-25: Simulation results of vessel wall failure.

Figure 3-25a shows the vessel failure time given by ANSYS simulations directly. Figure 3-25b is vessel wall failure time since SCRAM (the time needed from SCRAM to vessel failure) is the global failure time by adding  $t_{ref}+60\text{min}$  to the vessel failure time in ANSYS simulation. Figure 3-25c shows the vessel failure location indicated by polar angle in degree ( $0\sim 90^\circ$ ). Figure 3-25d illustrates two vessel snapshots of high polar angle failure and low polar angle failure. Figure 3-25e and Figure 3-25f show the superheat and melt mass at failure time respectively. Cases where failure does not occur are left empty in the corresponding block that represents the case in the figures. Some trends can be observed from the figures and are grouped into 4: 1) for the region satisfying  $t_{ADS}<4500\text{s}$  and  $t_{ECCS}-t_{ADS}<2000\text{s}$ , no vessel wall failure occurs; 2) for the remaining region satisfying  $t_{ADS} > 6000\text{s}$ : early failure/ low failure location/large super heat/large melt mass are expected; 3) for the remaining regions satisfying  $3500\text{s} < t_{ADS} < 6000\text{s}$ , late failure occurs; 4) for the remaining region satisfying  $t_{ADS}<3000\text{s}$ , most cases would have early failure.

CRGT welding points are 40 cm from the bottom while IGT points are 17 cm from the bottom. Failure criteria in the simulations are maximum temperature of any CRGTs/IGTs reaches (i) 1110K for accelerated creep, and (ii) 1670K for melting the CRGTs/IGTs. Figure 3-26 and Figure 3-27 give respectively CRGT and IGT failure times and corresponding maximum debris temperatures for both failure criteria. Figures show that: 1) for the domain  $t_{ADS}<4500\text{s}$ ,  $t_{ECCS}-t_{ADS}<2000\text{s}$ : no CRGT failure occurs, 2) for the domain  $t_{ADS}>7000\text{s}$ , early failure occurs, 3) for other cases, late CRGT failure occurs when ADS is activated during 4000-5000s (regardless of ECCS activation). No molten oxidic debris is expected in all cases at CRGT failure time, however metallic debris might be molten at observed temperatures. Same trends are observed in IGT failure mode as in CRGT failure mode.

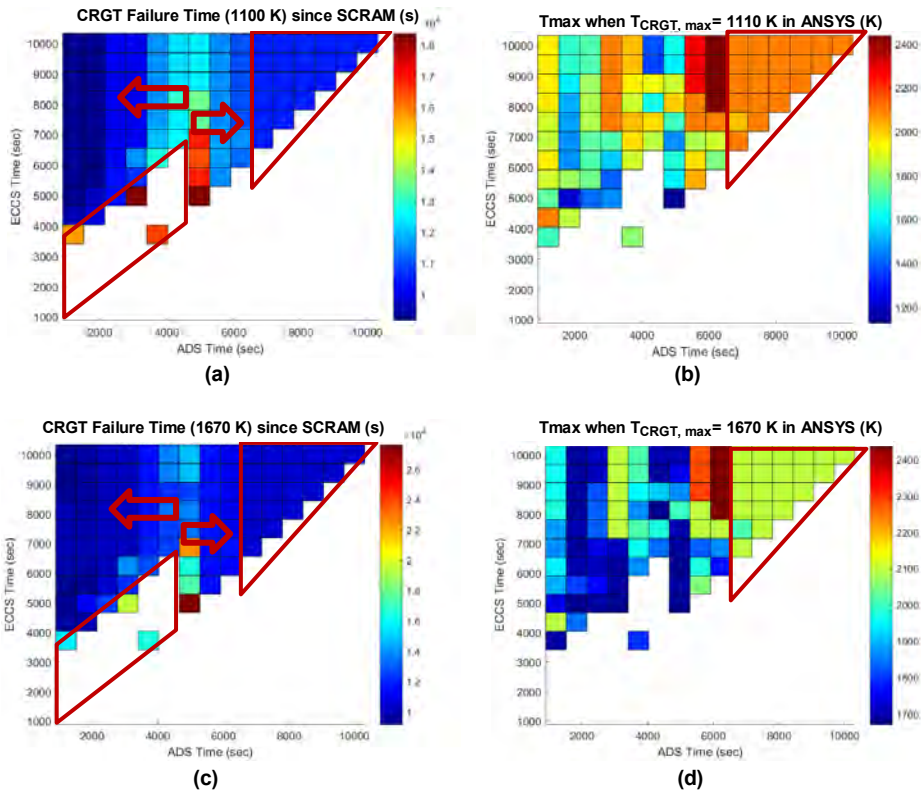


Figure 3-26: Simulation results of CRGT failures.

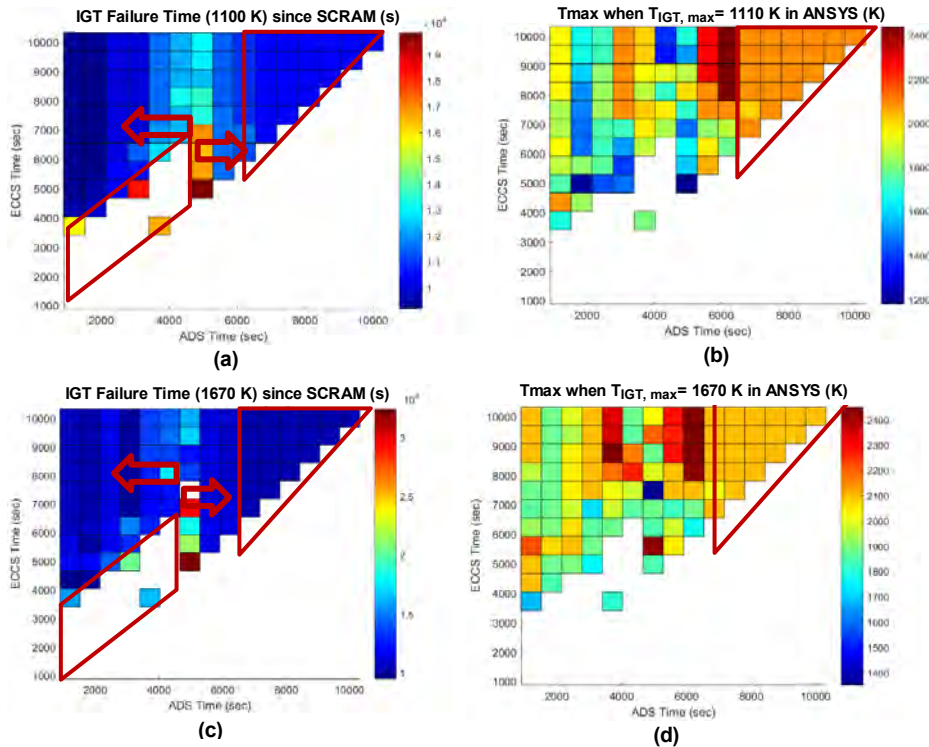


Figure 3-27: Simulation results of IGT failures.

### Vessel Failure Surrogate Model

After the database generation, the vessel failure surrogate model is developed using local linear regression. The target output  $y$  is assumed to be linear function of input

variables  $y = \beta_1 + \beta_2 x_1 + \beta_3 x_2$ .  $N$  known points can be used to determine the coefficients  $\beta_1, \beta_2$  and  $\beta_3$  which satisfy  $Y = X\beta$ ,  $\beta = (X^T X)^{-1} X^T Y$ . In our case, variables  $x_1$  and  $x_2$  can be ECCS and ADS activation time and  $y$  can be any output parameters of interest. So, given ECCS, ADS time  $x_1 = \tilde{x}_1$ ,  $x_2 = \tilde{x}_2$ , output  $y$  can be solved by the following expression  $\tilde{y} = [1 \ \tilde{x}_1 \ \tilde{x}_2] \beta$ .

The surrogate model was implemented as a MATLAB script implementing local interpolation using information from the neighbor points ( $n=4$ ). Minor change is needed to include more points ( $n=16$  or more). This model can accept the ECCS activation time and ADS activation time as input. The output would include vessel failure mode, failure time, location, corresponding melt mass and maximum temperature. The next step is to incorporate the surrogate model into ROAAM+ framework and test it.

### *Summary of Vessel Failure Modeling using MELCOR and PECM-ANSYS*

Debris bed configuration has significant influence on vessel failure mode and timing. There are several phenomena that can affect debris configuration: Multicomponent reheating and remelting; melt and water flow in a porous debris bed; debris configuration changes due to phase changes, oxidation, partial melt release; melting and collapse of IGT and CRGT pipes. MELCOR has models that address these phenomena, however, current approaches might be over-simplified and lacking necessary validation database due to the extreme complexity of the phenomena. Our approach is to focus on possible limiting factors in design, scenario, and phenomena that can simplify the analysis but still provide conservative coverage of possible scenarios.

Vessel failure Surrogate Model (SM) was developed using the database of vessel failure related parameters of interest and a local interpolation of the FM solution. Main findings from the analysis of MELCOR and PECM results are in a qualitative agreement, i.e. penetrations generally fail sooner than vessel wall, and, in some cases, amount of liquid melt can be relatively small at the time of failure. However, quantitatively, the results are quite different. The ranges of vessel wall failure timing obtained in MELCOR is much wider (~18000-37000 seconds after SCRAM) than in the ANSYS-PECM (~15000-20000 seconds). Melt superheat also varies in MELCOR in wider ranges ~0-1200 K than ~0-200 K in ANSYS-PECM. PECM predicts that penetrations will fail at the time when no liquid melt will be available, while MELCOR predicts that up to 60 tons of liquid metallic melt can be available at the time of penetration failure.

Main potential advantage of PECM model is the effective convection model that can take into account heat transfer in a large melt pool with 3D structures (such as cooled from inside CRGTs). However, amount of liquid melt predicted at the time of failure is relatively small, which makes potential advantage of PECM model less effective. On the other hand, MELCOR has models for considering non-homogeneous debris remelting and oxidation, which can affect local debris properties, thermal loads and allows to treat separately metallic and oxidic melt materials during melt ejection and the effect of partial melt release on the remelting of remaining debris. In summary, MELCOR, while lacking 3D features of PECM, provided wider ranges of possible scenarios of vessel failure and melt release, which should be taken as a reference for future analysis.

## DECOSIM Full Model for In-vessel Debris Coolability Analysis

The multifluid three-phase model implemented in DECOSIM includes the mass, momentum, and energy conservation equations for liquid water, vapor, and solid material taking into account the congesting structures [57]. Relevant closures and description of numerical implementation can be found in [110], [111], [112], [123]. The approach allows us to consider large-scale flowfields without resolving geometries of each individual CRGTs or IGTs.

### In-vessel Debris Coolability Analysis with DECOSIM: Initially Quenched Debris

Vessel geometry of a reference design of Nordic-type BWRs is used in simulations (Figure 3-28). The dashed lines (at the heights of 0.17 and 0.4 m above the vessel bottom) indicate positions of IGTs and CRGTs nozzle welding points. In the initially quenched debris bed case, the initial state of the debris bed was completely filled with water, and the temperature of solid particles was equal to the saturation temperature at the local pressure. Simulations have shown that debris bed coolability is strongly affected by the particle diameter. For 3 mm particles, the debris bed was coolable for all melt masses and relocation times; local dryout did not occur and cooling of the material was provided by water evaporation, the maximum solid particle temperature remained close to the local saturation temperature. For 2 mm particles, local dryout was observed for the largest mass of debris bed  $M = 200 \text{ t}$  at the relocation time  $t_r = 1.5 \text{ h}$ , however, in this case the maximum superheat of particles with respect to the saturation temperature was about 50 K, after about 1 hour the dry zone was reflooded again, the solid material temperature remained close to saturation afterwards. For 1 mm particles, debris bed coolability depends on the total mass  $M$  and relocation time  $t_r$ .

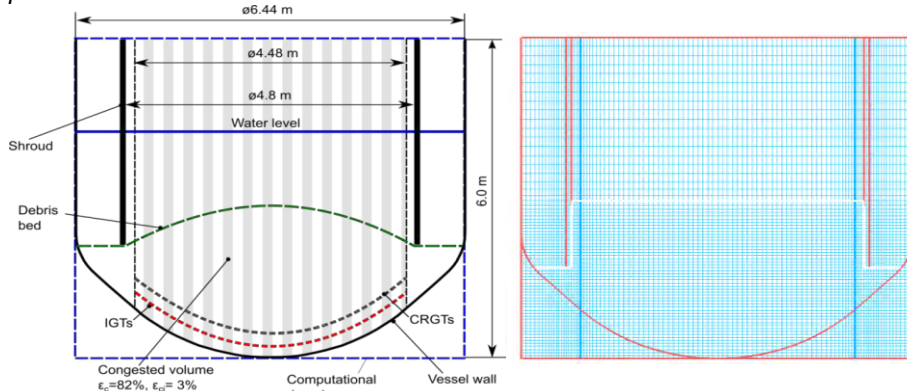


Figure 3-28: Reactor pressure vessel geometry and computational mesh.

	0.8	0.9	1	2	3
Debris bed mass M	0.8	0.9	1	2	3
200t	N	N	N	S	C
175t	N	N	N	C	C
150t	N	N	N	C	C
100t	N	S	S	C	C

Figure 3-29: Summary of coolability results for initially quenched debris bed. N - non-coolable with temperature escalation, S - dryout with temperature stabilization, C - coolable (no dryout, or dryout followed by reflooding).

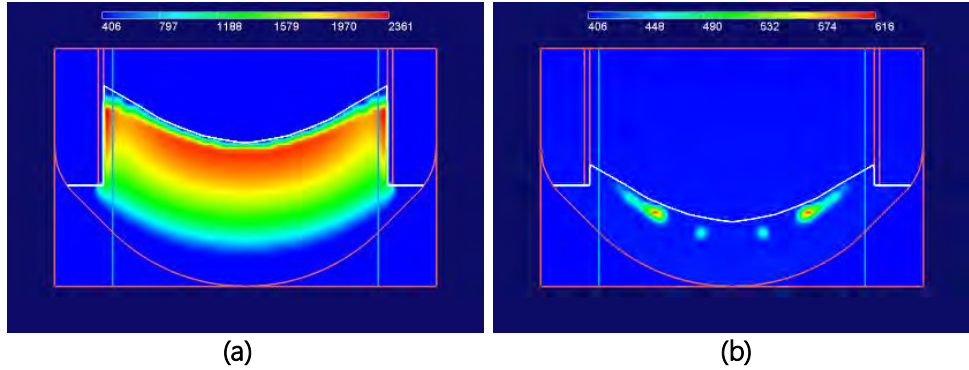


Figure 3-30: Particle temperature in initially quenched debris bed at time  $t=3$  h: (a)  $M = 200$  t,  $d = 1$  mm; (b)  $M = 100$  t,  $d = 1$  mm.

The coolability results obtained for initially quenched debris bed are summarized in Figure 3-29 where color coding is used to mark the cases where temperature escalation (red), temperature stabilization (green), or “no dryout” or “dryout followed by reflooding” (blue) was observed within 3 hours after core relocation. Spatial distributions of particle temperatures in debris beds are presented in Figure 3-30 for the debris bed masses of 200 and 100 t; the debris bed shape is shown by the white lines. Water ingress into the debris bed occurs in the bottom part of the debris bed, the vapor flow is directed upwards. The decay heat power is gradually decreasing with time, and even when the temperature looks stabilized, it will actually be decreasing slowly later on, and the size of dry zone will be shrinking accordingly.

#### *Initially Hot Debris bed with Unlimited Water Supply*

For an initially dry hot debris temperature of 1000K the debris bed was filled with vapor at the same temperature. The space above the debris bed is filled with saturated water. For larger particles, total reflooding of the debris bed occurs after 1–2 hours, and the maximum temperature of solid material falls down to the saturation temperature. For 1 mm particles, as well as for 2 mm particle and corium mass of 200 t, high drag prevents incoming water from reflooding the whole volume of the debris bed, and a steady temperature rise can be observed to the levels where remelting of the material can occur. In the case of 200 t – 2 mm debris bed, reflooding occurred for a relocation time of 3 h. The time to reach remelting is approximately 2.5 h after core relocation, or 4 h after SCRAM. In all the cases some part of debris remains dry; the temperature in these zones increases and reaches the melting point. To elucidate this, in Figure 3-31 the mass fractions of molten corium are shown at the final instant  $t = 3$  h (i. e., 4.5 h after SCRAM). Evidently, in the last two cases remelting and high temperatures are reached in the bottom part of the debris bed in the vicinity of the vessel wall.

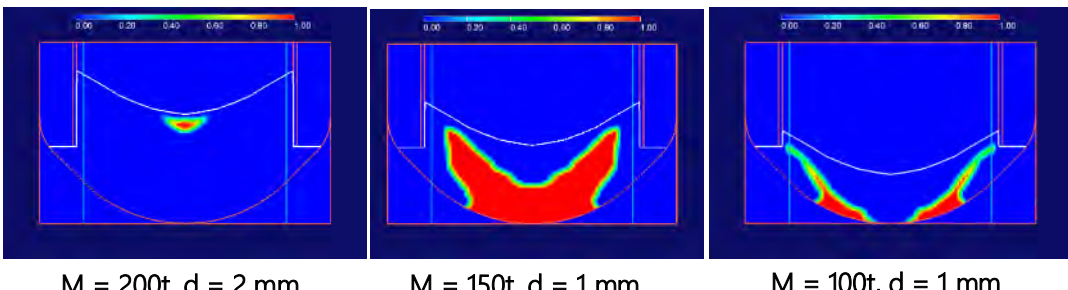


Figure 3-31: Melt fraction at time  $t=3$  hours in the initially dry debris bed.

In Figure 3-32, the temperatures at the levels of CRGT welding points are shown, demonstrating rapid quenching of debris bed for  $M=200$  t and  $d=2$  mm (the maximum temperature remains below the melting point for stainless steel). However, in the case of small particles ( $M=100$  t,  $d=1$  mm), only the central CGRTs are reflooded completely, while all other CRGTs feature some temporary temperature decrease, turning into secondary reheating because of shrinking of the reflooded zone with time.

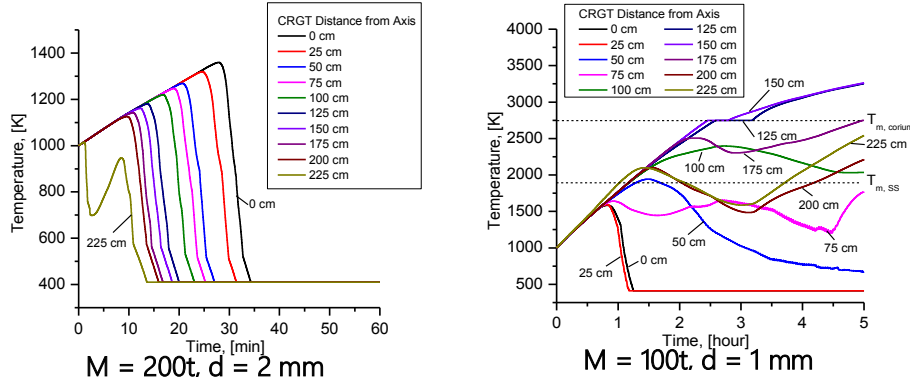


Figure 3-32: Time histories of temperatures at CRGT welding points.

Table 3-5 summarizes the coolability of the debris bed and possible model of melt release depending on the initial state of the debris bed. For an initially wet debris bed, it is found to be coolable if the debris mass is less than 100 tons with large particles ( $>2$  mm). On the other hand, if the debris mass is larger and the particle size smaller, a massive melt release is expected. The same scenario is expected for an initially dry debris bed with large mass and large particle sizes. A dripping melt release is expected for an initially dry debris bed with small mass and small particle sizes.

Table 3-5: Coolability of the debris bed and possible mode of melt release.

Initial state	Debris bed properties	Coolable bed	Dripping release	Massive release
Wet	Small mass (<100 t) Large particles (>2mm)	Yes	-	-
	Large mass (>100 t) Small particles (<1mm)	-	-	Yes
Dry	Small Mass (<150t) Small particles (~1mm)	-	Yes	-
	Large Mass (>150 t) Large particles (>2mm)	-	-	Yes

### Influence of Limited Water Inventory and Debris Bed Shape

Simulations with limited water inventory were run for 10,800 sec (3 hours), which, for the chosen relocation time  $t_r = 1.5$  h, corresponds to the period from 1.5 to 4.5 hours after SCRAM. During this period, the specific decay heat power drops from  $W = 179$  to 132 W/kg. In all cases, the initial temperature of debris bed was  $T_s^0 = 1000$  K, the porous medium was filled with single-phase water vapor at the same temperature. On the top boundary of the computational domain, constant pressure  $P_0 = 3$  bar was maintained, the pool is at saturation conditions with initial water level  $H_w = 4.0$  m. In Table 3-6, parameters of all simulations are summarized; also given are the maximum local melt fractions and total masses of melt at the final time. For large debris particles, water usually penetrates into the debris bed along the vessel

walls, quenching initially hot debris in the near-wall region. By about 1 h, the receding water level uncovers the top surface of debris bed, and by about 2 h, all debris bed becomes dry again. Simulations show no significant penetration of water through the top surface (unlike in infinite water supply case with smaller beds in [123]). Temperature rises steadily in the top part of debris bed where water cannot penetrate. Accordingly, remelting of the material occurs near the debris bed top surface, while temperature rise near the wall is delayed for the total water evaporation time. Water ingress in the debris bed depends on the drag determined by the mean particle diameter. To elucidate the differences caused by the drag, in Figure 3-33 void fraction distributions are shown at four consecutive instants for the same debris bed, but with smaller particles ( $d_p = 1.5$  mm), while in Figure 3-34 temperature fields are shown. Evidently, the reflooded near-wall zone is thinner in the case of smaller particles, water penetration proceeds slower, and the size of high-temperature zone is larger.

Behavior of initially dry debris beds of different shapes and masses are qualitatively similar to those considered previously. Since the amount of water is limited, debris reheating and remelting becomes inevitable after complete water evaporation. In all cases with remelting it occurs in the top part of debris bed, while temperature rise in the near-vessel wall region is delayed due to initial water penetration; therefore, the temperature distributions developing in the debris bed are non-uniform. Data in Table 3-6 suggests that the time to total water evaporation depends on the particle diameter. This is attributed to different rates at which water penetrates into initially dry debris beds. For larger particle diameters, water penetration is faster, and, therefore, with limited amount of water, total evaporation occurs faster.

Table 3-6: Parameters of simulations and melt masses at time  $t = 3$  h

Debris mass $M$ , ton	Initial water mass $M_w$ , ton	Particle diameter $d_p$ , mm	Total evaporation time $t_{ev}$ , h	Max. melt fraction $\chi$ , [-]	Mass of melt $M_m$ , ton
<b>Flat Top</b>					
100	55.0	1.5	2h55m	0.19	1.9
		2.0	2h15m	0.38	0.1
150	47.5	1.5	2h50m	0.45	15.8
		2.0	2h10m	0.64	17.3
200	39.1	1.5	2h30m	0.54	43.1
		2.0	2h15m	0.63	37.2
		3.0	1h55m	0.59	29.8
<b>Gaussian-shaped Heap</b>					
100	56.2	1.5	3h10m	0.55	7.2
		2.0	2h40m	0.64	2.3
		3.0	2h10m	0	0
150	47.2	1.5	2h45m	0.40	15.5
		2.0	2h10m	0.62	17.8
		3.0	1h50m	0.65	12.1

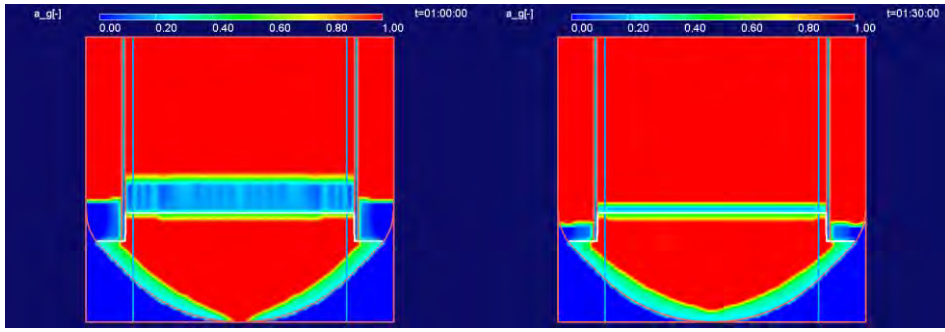


Figure 3-33: Void fraction distributions upon reflooding of initially dry debris bed ( $M = 150$  t,  $d_p = 1.5$  mm).

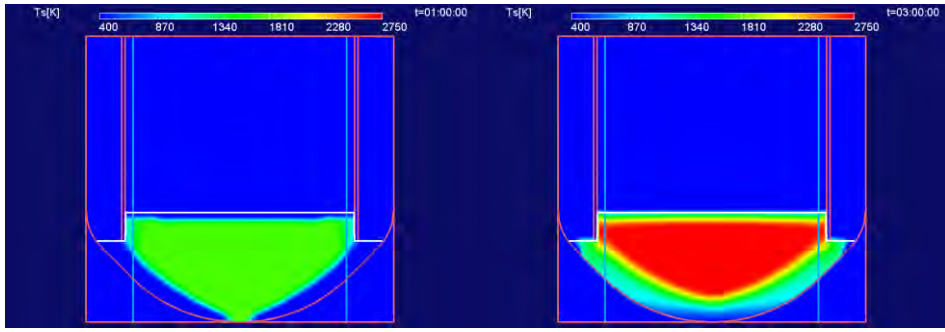


Figure 3-34: Temperature fields in the debris bed ( $M = 150$  t,  $d_p = 1.5$  mm).

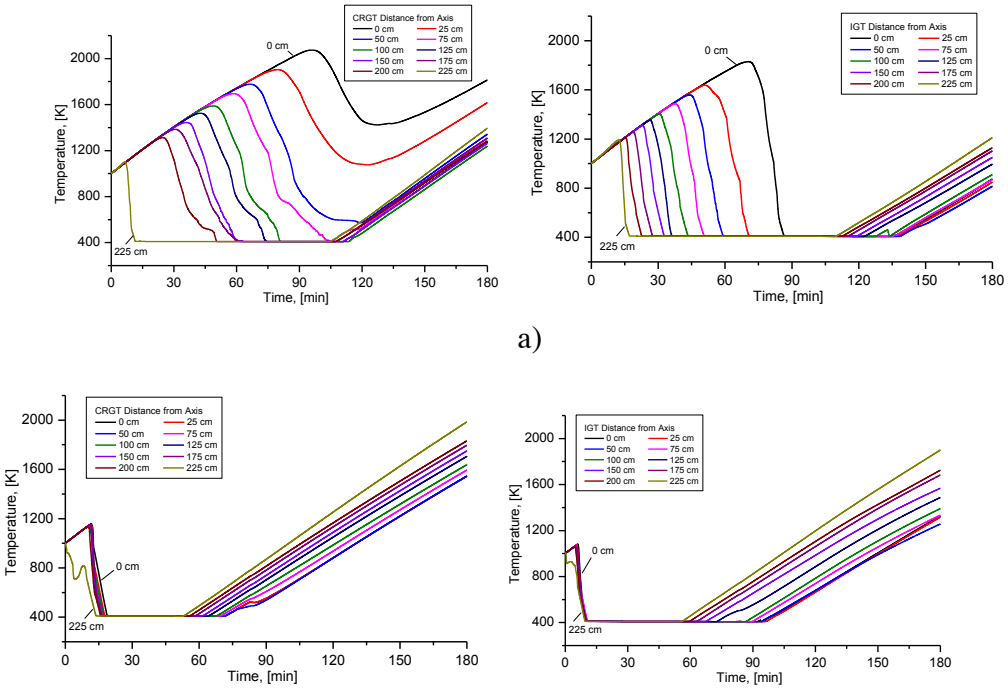


Figure 3-35: Temperature of CRGT (left) and IGT (right) welding points at heights 0.4 and 0.17 m above the bottom vessel wall, respectively, for heap-shaped debris bed with  $M = 150$  t; radial positions are indicated in the legends: a)  $d_p = 1.5$  mm, b),  $d_p = 3.0$  mm.

From the severe accident analysis point of view, it is important to know not only the integral characteristics of temperature rise and remelting in the dry zone, but also

location of hot zones with respect to the vessel wall and structures. One of the possible vessel failure modes is local failure of welding of CRGT and IGT to the penetration nozzles located at elevations of 0.4 and 0.17 m above the vessel wall (see Figure 3-28). In Figure 3-35, the time histories of CRGT and IGT temperatures at different radial locations are shown; these plots are also typical of those obtained for different debris bed configurations. One can see that the curves consist of two distinct parts: initial temperature rise followed by rapid drop after quenching of near-wall zone by water entering the debris bed along the vessel wall, and steady temperature rise starting with some delay over which water evaporates completely from the debris bed. These two stages are most clearly seen for the larger particles (Figure 3-35,b). Early melting of CRGTs and IGTs is not expected because temperature doesn't reach high enough values before reflooding. The secondary reheating starts with the delay of about 60-90 min, depending on the position; this time is determined by propagation of the receding water level as the amount of liquid in the debris bed is decreased. For smaller particles, however, water ingress is slower, reflected by longer duration of each stage in Figure 3-35,a. Moreover, for the near-axis CRGTs no complete quenching of the material occurs, so that quite early failure can be expected. The secondary reheating also begins later, reflecting slower water evaporation.

#### *Effect of Decay Heat and Debris Property Inhomogeneity*

As a result of core relocation the properties of debris can be inhomogeneous. Scoping simulations were carried out for water reflooding of an initially dry and hot (1000 K) debris bed; the decay heat power was reduced by 20% and 50% either in a lower half of the debris bed (by height), or in a 50 cm-thick spherical layer along the vessel wall. It was shown that a lower-power layer near RPV wall (metallic materials) promotes water penetration along the vessel wall in comparison with the homogeneous property case. In order to reduce the uncertainty in the initial conditions and debris property distributions, a link to MELCOR simulation results was implemented. A snapshot of MELCOR simulations were taken as initial data for DECOsim; Interface has been developed and implemented for data transfer (nodalization, materials, temperature, decay heat power per unit mass of UO<sub>2</sub>); Particulate debris (PD) volume fraction (COR\_VOLF\_PD) variable is used to determine the shape of debris bed; Parameters for each MELCOR cell are distributed evenly to all DECOsim cells falling within it; Porosity of debris is assumed to be 40%, mean particle diameter is an input parameter. DECOsim simulations were run for 3 hours. For comparison, simulations were also run starting with quenched conditions where debris was initially at the saturation temperature, and debris bed was initially filled with water. As an example, consider the case which was started with MELCOR simulation snapshot at time 13000 s. In Figure 3-36, DECOsim simulation of the reflooding of an initially dry debris bed with assumed particle diameter 1 mm is presented. It can be seen that, similar to the cases of homogeneous debris bed presented above, water penetration proceeds mainly along the bottom wall of reactor vessel lower plenum. By the time of 2 hours, water propagates about half of radial distance from the debris bed periphery to the axis. Also visible is water ingress in the top part of debris bed where the heat release rate is lower than in the bulk of debris. Similar results were obtained for 2 mm particles (Figure 3-37), with the same initial conditions as in Figure 3-36. However, water penetration proceeds much faster, leading to rapid cut-off of the hot zone from the vessel wall.

In Figure 3-38, the time histories of maximum particle temperatures are shown for input data from MELCOR at 7200 and 13000 s, particle diameters, and initial states

(quenched or hot and dry). It can be seen that initially quenched debris bed is coolable for 2 mm particles, but non-coolable for 1 mm particles. Also, initially dry debris are heated up to remelting despite partial quenching of debris near vessel wall.

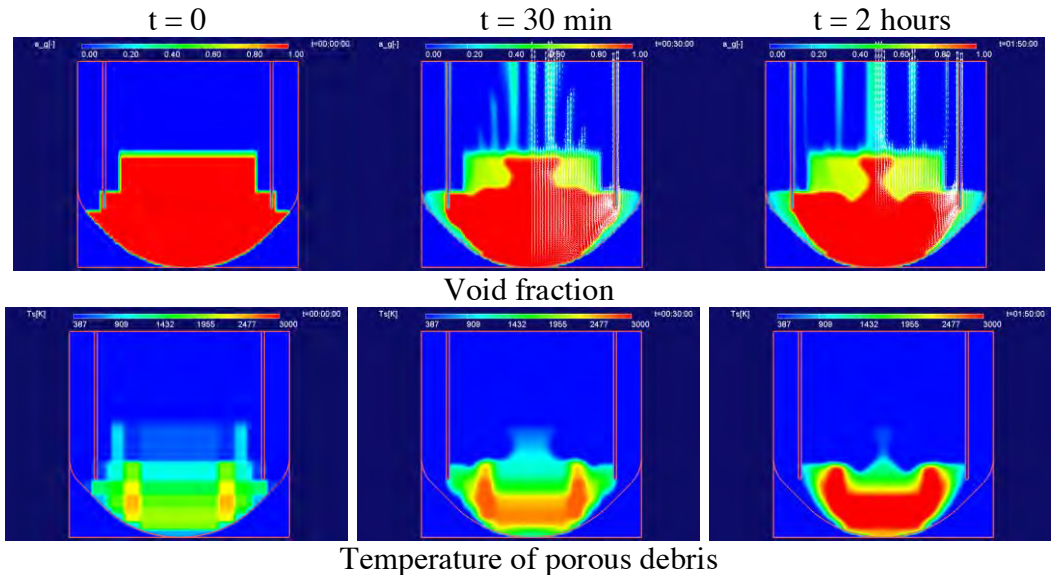


Figure 3-36: Reflooding of initially dry debris bed, 1 mm particles.

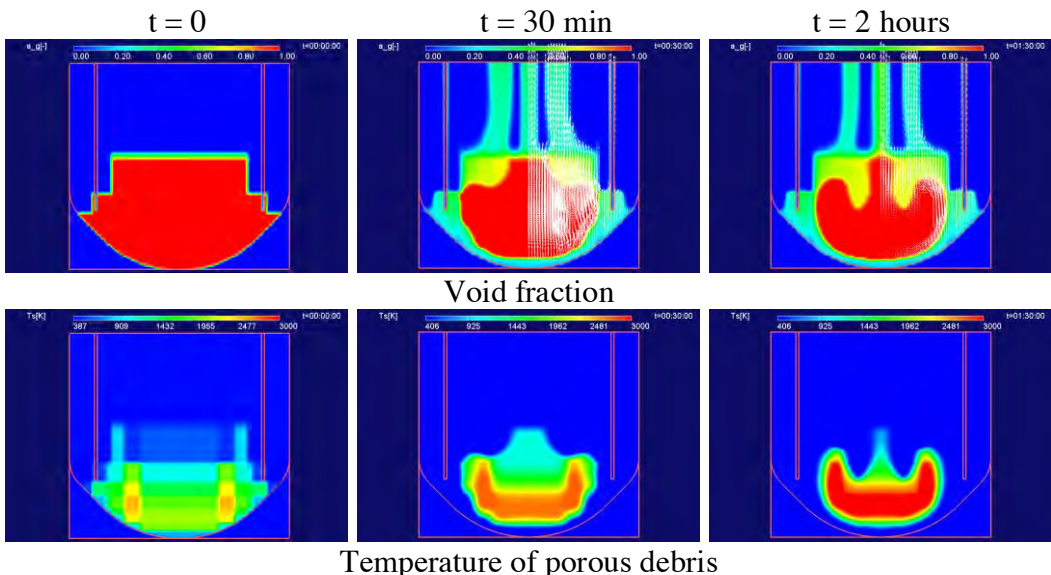


Figure 3-37: Reflooding of initially dry debris bed, 2 mm particles.

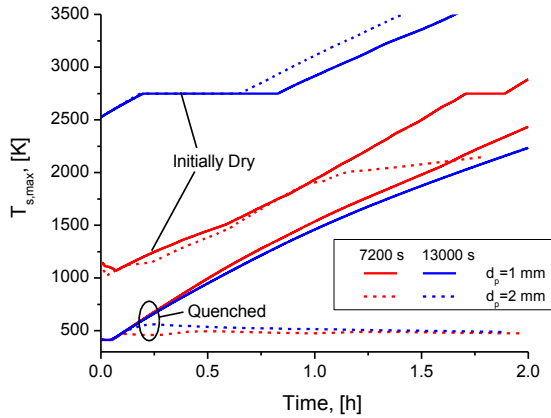


Figure 3-38: Maximum particle temperature in debris bed.

### Summary of Results on In-vessel Porous Debris Bed

The results obtained on coolability of a porous in-vessel debris bed reveal several common features: For large particles: the dry zone (if any) is located in the top part of the debris bed, where temperature escalation and remelting can occur; in this case, melt accumulation in a pool can be expected, with massive release to follow the RPV failure; thermal attack on CRGT and IGT welding is likely to occur only after complete water evaporation. For small particles: the debris bed remains mostly dry due to rapid evaporation of water in the bed and limited ingress of coolant due to high drag; CRGT and IGT welding are likely to fail early, resulting in water drainage and melt release in dripping mode. Inhomogeneity of debris bed affects its coolability: low decay power and high-conductivity (metallic) layers promote water ingress into the debris bed, improving its coolability; still, the effect of particle size on the outcome of porous debris bed formation in the RPV lower plenum is prevailing. Thus, the uncertainty associated with porous debris bed behavior in the in-vessel conditions remains contingent upon the debris formation processes.

#### 3.4.3. Melt ejection mode

Vessel failure mode provides initial conditions of lower head failure: (i) size of the opening (IGT, CRGT, pump, vessel wall) and (ii) amount, properties and superheat of the available melt. Note that these characteristics can change due to ablation or plugging of the opening in the vessel. The goal is to develop a tool for prediction of transient parameters of melt ejection, i.e. jet diameter and melt thermal properties. The development of MEM framework is depicted in the Figure 3-39. There are two key phenomena that should be addressed: flow of liquid melt through the solid porous debris can slow down the release while increasing the temperature of the melt; ablation / plugging of the initial breach during melt structure interaction alter the jet diameter. Currently, the melt filtration through porous debris bed requires adequate relevant experimental evidences.

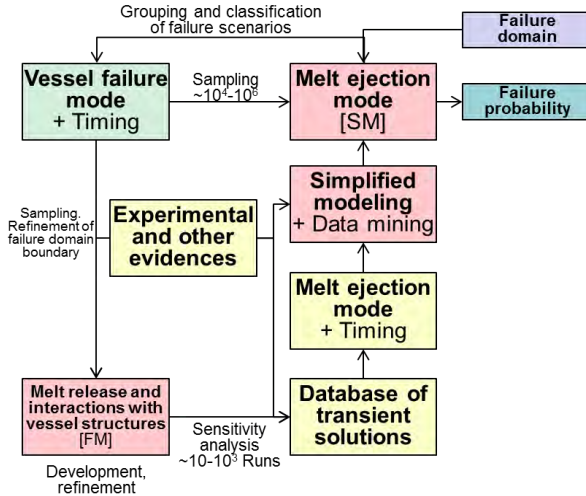


Figure 3-39: Melt ejection mode surrogate model.

### 1D Modeling Approach to Plugging and Ablation

Preliminary analysis suggested that 3D effect in the breach are not major contributors to the uncertainty in the melt ejection and ablation plugging phenomena [57]. Computational costs even for the 2D model are rather high for systematic parametric studies. Previously extensive analysis of breach ablation was done using conservative 0D approach. In this iteration of MEM model development, we add breach plugging as a potentially limiting mechanism that can reduce uncertainty in melt release.

We try to clarify the possibility to release the whole core in “dripping” mode i.e. avoiding “massive” release (in which debris agglomeration and steam explosion can lead to containment failure). This can be achieved if neither plugging of the breach, nor extensive ablation of the breach occurs. Definition of the dripping release can be based on estimated threshold value of jet enthalpy rate ( $\dot{H}$ ) for steam explosion  $\pi U_{\text{rel}}(t) \rho_m R(t)^2 (C_p \cdot (T - T_{\text{water}}) + H_f) < 30 \text{MW}$ ; and on the ratio of the jet penetration depth ( $L$ ) and the water pool depth ( $L_{\text{wat}}$ ), which determines conditions for agglomeration:  $\frac{L_{\text{wat}}}{L} = \frac{L_{\text{wat}}}{2.1D(t)\sqrt{Fr(t)}\sqrt{\frac{\rho_m}{\rho_w}}} < 1$ , where  $Fr = U^2/gD$  is jet Froude number estimated at the water level. Both criteria are dependent on the jet radius. The goals of the analysis are to assess (i) amount of melt that can be released before onset of plugging or ablation; (ii) respective melt enthalpy release rates; (iii) if decay heat can be a limiting factor for the enthalpy of melt release.

#### Steady state analysis for ablation/plugging map

The steady state axisymmetric model (Figure 3-40a) computes the thickness of the crust formed inside the breach given fixed melt release temperature  $T_m$  and vessel wall temperature  $T_{vw}$ . In steady state the heat flux from the melt is equal to the heat flux at the melt / crust interface  $q_m = q_c$ . The heat flux from the melt can be estimated as a function of Nusselt number  $Nu$ , melt thermal conductivity  $\lambda_m$ , melt superheat  $\Delta T_{\text{sup}}$  and jet radius  $r_m$ :

$$q_m = Nu \frac{\lambda_m}{2r_m} \Delta T_{\text{sup}} \quad (3-3)$$

where  $Nu = 0.5 \cdot Re^n \cdot Pr \cdot c_f$ ,  $c_f = 0.005$  and  $Re = 2 \frac{\rho_m V_m r_m}{\mu_m}$ ,  $Pr = \frac{\mu_m C_p \rho_m}{\lambda_m}$ . Taking  $n = 1$  makes  $q_m$  independent from the melt jet radius  $r_m$ . The heat flux at the

melt / crust interface is defined by crust thickness ( $R_{vw} - r_m$ ), crust thermal conductivity  $\lambda_c$  and temperatures at its boundaries:  $T_{vw}$  and  $T_m$ :

$$q_c = \frac{T_m - T_{vw}}{r_m \cdot \ln(\frac{r_m}{R_{vw}})} \lambda_c \quad (3-4)$$

where  $R_{vw}$  is initial breach radius (0.035 m in case of IGT failure and 0.075 m in case of CRGT failure). Due to the cylindrical divergence, the steady state heat fluxes at different radiiuses are not equal but related to each other through respective radiiuses. For example, the steady state heat flux  $q_c$  at the melt / crust interface is related to the heat flux at the crust / wall interface  $q_{vw}$  as:

$$q_c \cdot r_m = q_{vw} \cdot R_{vw}$$

With increase of the crust thickness (decrease of the melt radius  $r_m$ ) the heat flux at the vessel wall  $q_{vw}$  decreases (Figure 3-41). However, below the critical melt radius  $r_m < r_{crit}$  the heat flux at the melt / crust interface starts to increase. The critical radius depends only on the initial breach radius:  $r_{crit} = R_{vw} \cdot e^{-1}$ . Respective critical heat flux at the melt / crust interface  $q_{crit}$  is then given by

$$q_{crit} = -\frac{T_m - T_{vw}}{R_{vw} \cdot e^{-1}} \lambda_c \quad (3-5)$$

Depending on the value of the heat flux from the melt  $q_m$  three possible configurations can be established:

1.  $q_m > q_{crit}$ . There exist a stable equilibrium crust thickness and constant melt release radius. The case when  $q_m = 2 \cdot q_{crit}$  is demonstrated in the Figure 3-41, the respective jet radius  $r_m \approx 0.0275$  m. The solution is stable, meaning that small changes in the boundary conditions will result in small changes in the solution.
2.  $q_m = q_{crit}$ . There exist a steady state solution with  $r_m = R_{vw} \cdot e^{-1}$ . However, such solution is physically unstable: i.e. small changes in the boundary conditions (for example, reduction in melt release velocity or melt superheat) will lead to plugging of the breach.
3.  $q_m < q_{crit}$ . There is no steady state solution with melt flowing through the opening in the vessel, i.e. the breach will be plugged.

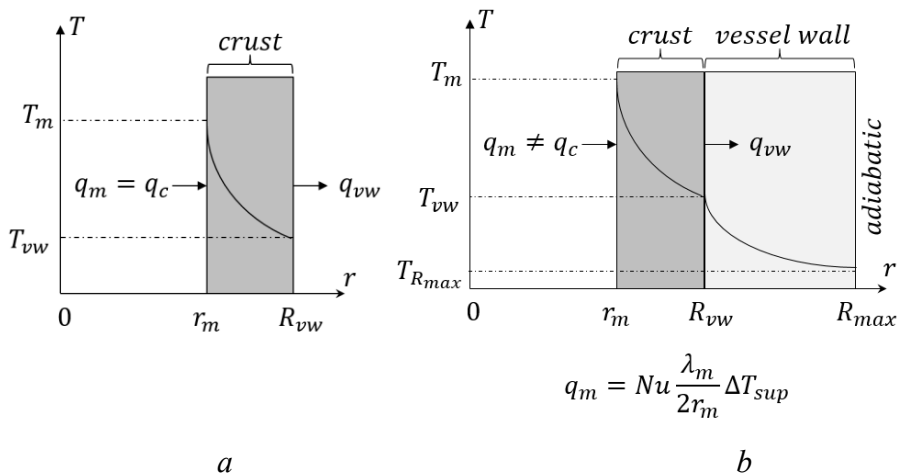


Figure 3-40: MEM: steady state (a) and transient (b) model.

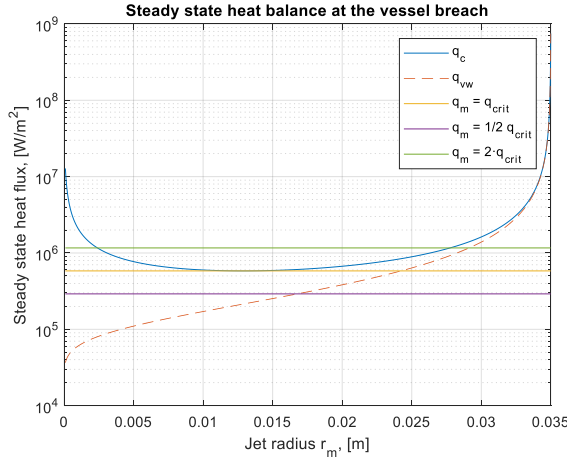


Figure 3-41: Steady state heat balance at the vessel breach.

An important finding from the steady state analysis is that *breach plugging* will occur if *heat flux from the melt*  $q_m \leq q_{crit}$ . Given fixed melt / crust thermophysical properties (specifically,  $T_m$  and  $\lambda_c$ ) a steady state map of breach plugging can be built in terms of  $\{T_{vw}, V_m, \Delta T_{sup}\}$ , see Figure 3-42. The diagonal lines in the map correspond to critical heat flux (a combination of  $\{T_{vw}^{crit}, V_m^{crit}, \Delta T_{sup}^{crit}\}$ ). If melt release conditions  $\{V_m, \Delta T_{sup}\}$  below/above a critical line, then plugging/ablation of the breach could occur respectively. In case of oxidic melt release (oxidic crust) vessel wall temperature has significantly smaller effect on the plugging conditions than in case of metallic melt release. The effect is due to significantly higher melting point of oxidic melt vs metallic melt. The plots in the Figure 3-42 further suggest that for given vessel wall temperature the dependence of critical melt release velocity and melt superheat is linear in logarithmic scale and therefore the product  $V_{exit}^{crit} \cdot \Delta T_{sup}^{crit}$  is constant. Steady state map of plugging and ablation can then be expressed in terms of  $\{V_{exit} \cdot \Delta T_{sup}, T_{vw}\}$ , see Figure 3-43. Domain of parameters where plugging is possible is limited but not physically impossible; the plugging domain is larger for the metallic release than for oxidic release; the size of the plugging domain for CRGT is smaller than for IGT; ablation of CRGT is consequently more likely to occur. The results of the steady state analysis, should be considered as qualitative because they don't take into account transient heating of the vessel wall. Assessment of the mass of melt released before plugging or onset of ablation cannot require transient analysis.

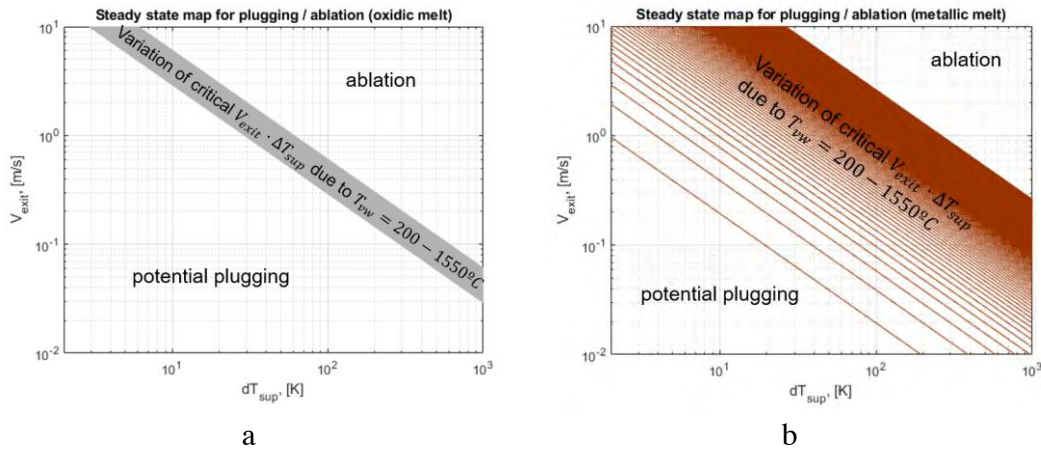


Figure 3-42: Steady state map of plugging and ablation in terms of  $\{T_{vw}, V_m, \Delta T_{sup}\}$  for  $(R_{vw} = 0.035 \text{ m})$  (a – oxidic melt, b – metallic melt)

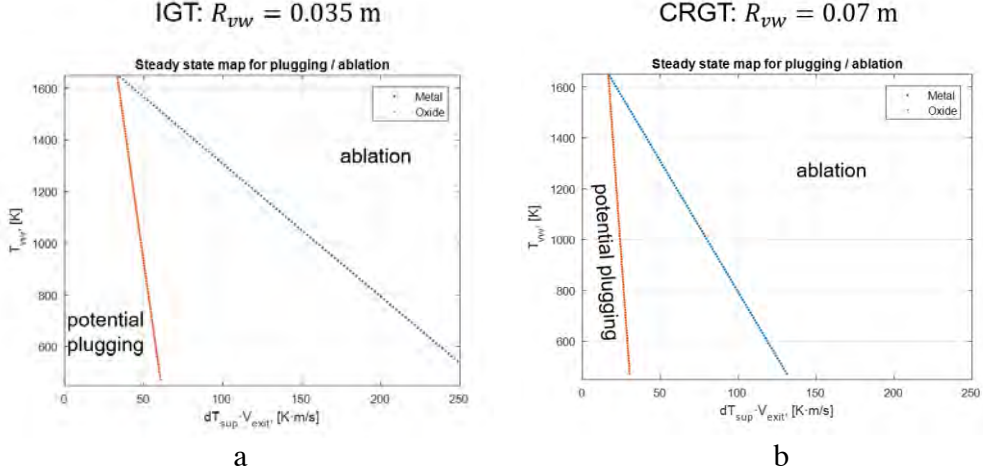


Figure 3-43: Steady state map of plugging and ablation in terms of  $\{T_{vw}, V_m \cdot \Delta T_{sup}\}$ . (a – IGT failure, b – CRGT failure)

### Transient analysis

The transient model is schematically shown in Figure 3-40b. The model resolves temperature profiles in the vessel wall and in the crust. Heat transfer equations are formulated in terms of enthalpy  $H$ :

$$-\frac{1}{r} \frac{dH}{dr} + \frac{d^2H}{dr^2} = \frac{1}{\alpha_v} \frac{dH}{dt}, \quad \frac{1}{r} \frac{dH}{dr} + \frac{d^2H}{dr^2} = \frac{1}{\alpha_c} \frac{dH}{dt}$$

where  $\alpha_{v,c}$  is thermal diffusivity of the vessel steel and melt crust respectively. The heat flux from the melt at the melt/crust interface is  $q_m = Nu \frac{\lambda_m}{2r_m} \Delta T_{sup}$ . The difference between the heat flux from the melt  $q_m$  and the heat flux into the crust at the melt / crust interface defines the rate of crust front displacement:

$$L \frac{dr_m}{dt} = \alpha_c \frac{dH}{dr} - \frac{Nu \lambda_m}{\rho_c C p_m 2r_m} (H_m - H_{inf})$$

where  $H_m$  is melt enthalpy at melting temperature;  $H_{inf}$  is melt enthalpy at the temperature of the melt;  $\rho_c$  is melt density;  $C p_m$  is melt heat capacity;  $L$  is the latent heat of solidification. The second boundary condition is adiabatic wall temperature at  $r_m = R_{max} \left. \frac{dH}{dr} \right|_{R_{max}} = 0$ ,  $R_{max} = 0.161 \text{ m}$  is set at the midpoint between two adjacent CRGTs. The third boundary condition is equality of the heat fluxes in the crust and in the vessel wall at the crust / vessel interface:  $\lambda_{vw} \left. \frac{dT}{dr_{vw}} \right|_{R_{vw}} = \lambda_c \left. \frac{dT}{dr_c} \right|_{R_{vw}}$ . The model has been verified for convergence. The model can estimate time evolution of the breach radius for a combination of  $\{T_{vw}, V_m \cdot \Delta T_{sup}\}$ , melt and vessel properties.

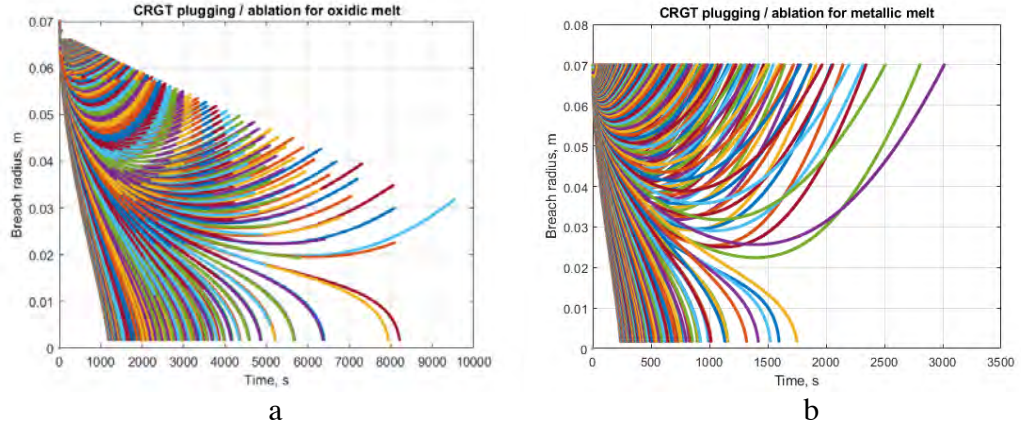


Figure 3-44: Transient solutions for CRGT (a – oxidic melt, b – metallic melt)

An example of calculations is provided in the Figure 3-44. Every curve represents an individual transient solution. Those solutions that end at zero radius correspond to the cases of breach plugging; non-zero value of the breach radius indicates conditions when vessel wall ablation starts. In the case of CRGT failure the time scale for plugging is in the order of ~100 to 1000 seconds. For the conditions with zero melt superheat (i.e. fastest possible plugging) the model predicts melt release time until plugging for oxidic melt: above 1000 sec; for metallic melt: above 200 sec. Time scales for the onset of the ablation are sensitive to the melt release conditions and vary from 0 to few thousands of seconds. In cases of melt release with breach ablation the jet radius first reduces (crust growth), then increases (crust melting) and only after that ablation of the vessel wall starts. Similar to the steady state analysis, in the Figure 3-45 the transient maps of breach plugging and ablation are provided for IGT and CRGT failure. The size of the plugging domain is smaller compared to the steady state analysis. The lines separating plugging from ablation are not linear (Figure 3-45b). Plugging domain is larger for metallic release than for oxidic release. Plugging of CRGT is less probable than IGT. Ablation is more likely in case of CRGT failure.

Using transient solutions (Figure 3-44) it is possible to calculate the mass of melt that can be released through a single breach before plugging or ablation will occur (Figure 3-46, Figure 3-47). All plots are in the range from 0 to 250t. The results suggest that while significant masses of melt can be released through a single breach, releases of large amount of material are possible in a limited domain of  $\{V_{exit} \cdot \Delta T_{sup}, V_{exit}\}$ . Further we consider the number of IGTs or CRGTs that should fail simultaneously to allow release of 250t of melt before plugging or ablation. The results are given in Figure 3-48. All plots are provided in the range from 0 to 60 for IGT and from 0 to 140 for CRGT. The domain of  $\{V_{exit} \cdot \Delta T_{sup}, V_{exit}\}$  where such release can be achieved is larger (especially for CRGTs) than for single failure. Note that multiple failures might have a positive effect on more uniform debris spreading in the pool, but also increase the mass of melt in premixture and thus steam explosion energetics.

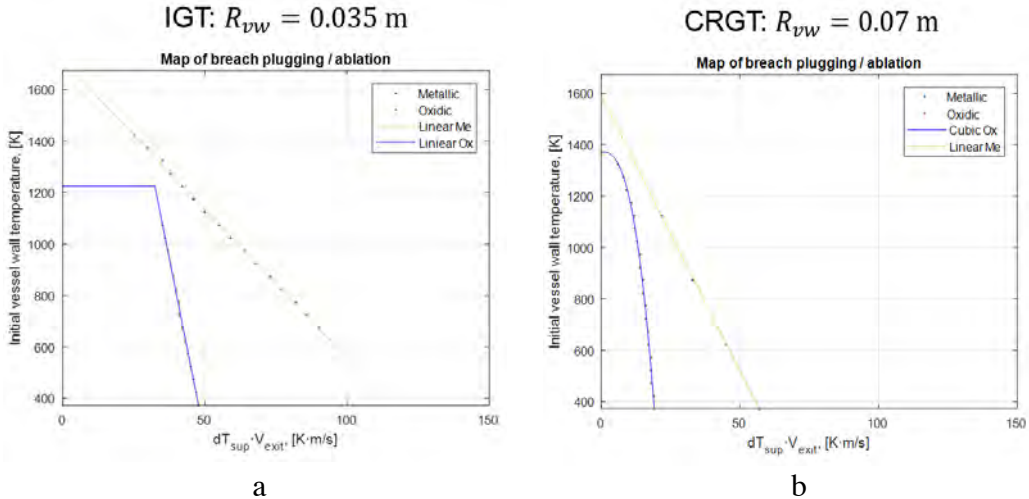


Figure 3-45: Transient map of plugging and ablation in terms of  $\{T_{vw}, V_m \cdot \Delta T_{sup}\}$ . (a – IGT failure, b – CRGT failure)

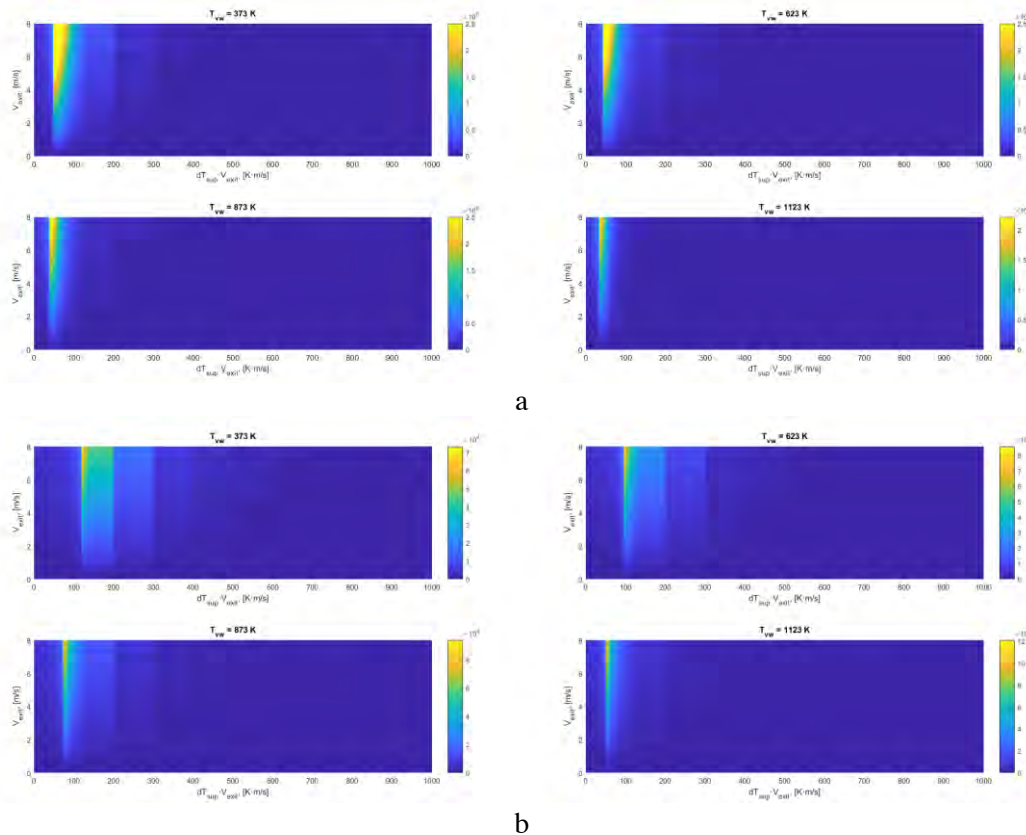


Figure 3-46: MEM: Mass of oxidic (a) and metallic (b) melt that can be released through a single IGT before plugging or ablation.

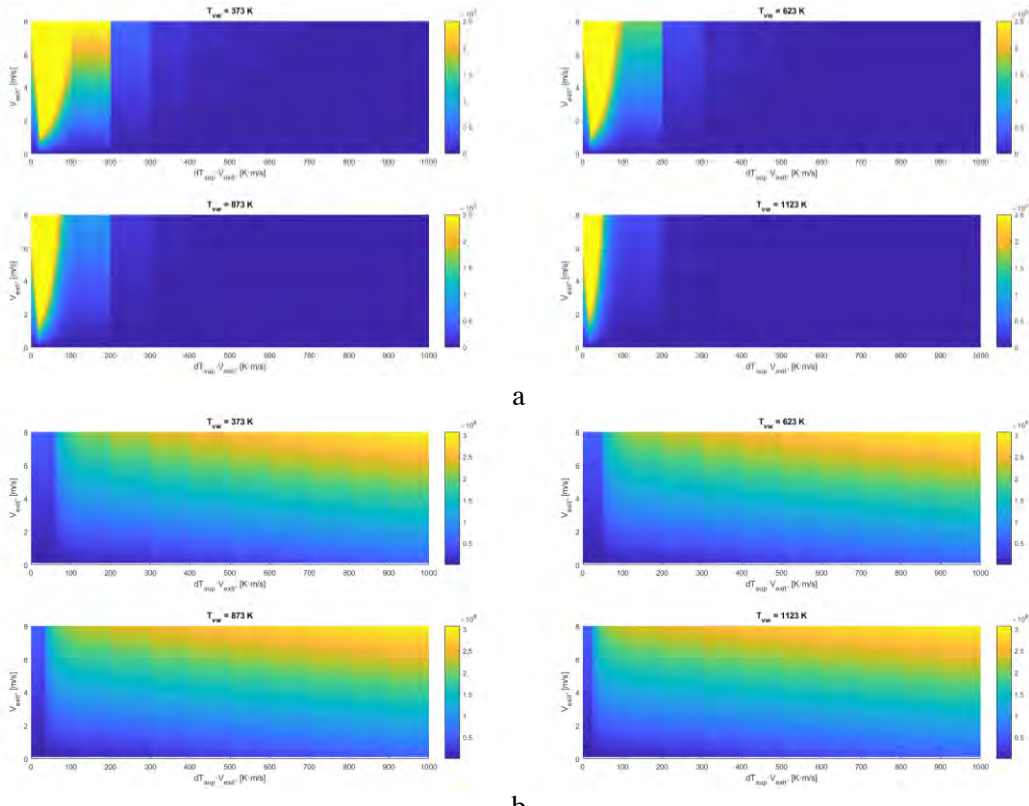


Figure 3-47: Mass of oxidic (a) and metallic (b) melt that can be released through a single CRGT before plugging or ablation

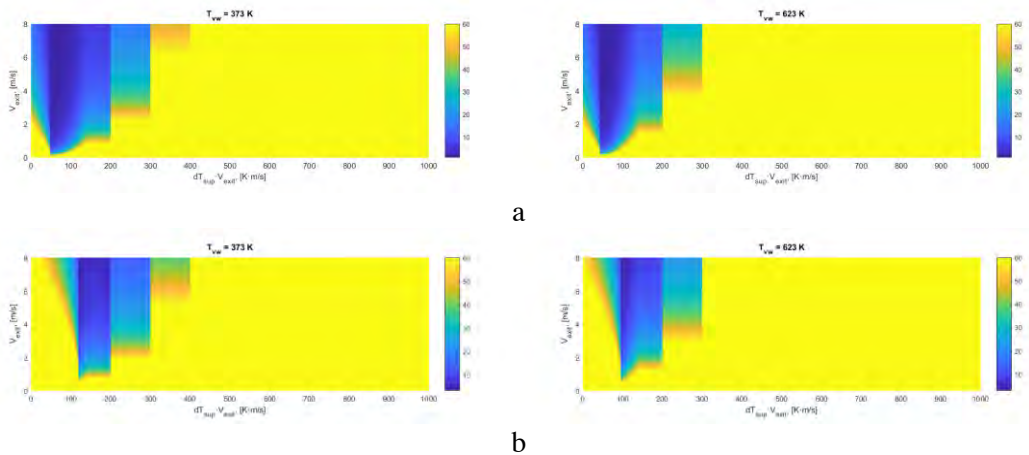


Figure 3-48: Number of failed IGTs required to release 250t of oxidic (a) and metallic (b) melt before plugging or ablation.

### Summary and outlook

Transient model of breach plugging has been developed. It was used to analyze melt release before breach plugging or ablation occurs. A map for transition from plugging to ablation has been proposed. It was found that plugging with metallic melt occurs in a wider range of melt release parameters (melt release velocity and melt superheat) compared to oxidic melt. Time scales of plugging and onset of ablation for metallic melts were found to be  $\sim 50\%$  smaller than for the oxidic melts. The time scales are in the range from 0 to 1000 sec. The range of melt release parameters where the whole core can be released before plugging or ablation is narrow. Currently possible ranges of melt release condition (velocity, superheat, vessel wall temperature) are much

wider. CRGT is much less prone to plugging and more prone to ablation than IGT. Multiple IGT failures potentially can increase melt fraction that can be released before start of plugging/ablation. However, effect of multiple jets on the risk of containment failure has not been studied yet.

Obtained results further suggest that release in dripping mode is possible, but only in a limited range of melt release parameters. It is important to point out that the presented analysis stopped at the onset of breach ablation. In reality, there is still a margin that can allow melt release through an ablating breach in dripping mode. Assessment of this margin, i.e. assessment of the rate of breach ablation using the numerical approach developed here, may increase the ranges of melt release parameters where melt release occurs in dripping mode. Further development of the MEM FM should include modelling of vessel breach ablation, which can be considered as a natural extension of the currently implemented model. Further reduction of uncertainty would require further development and coupling with the MECLOR to limit possible range of input parameter.

Currently MEM/VF SM is the largest source of uncertainty in the framework. Experimental evidences are required to develop models of debris remelting [54]. An experimental program for investigation of debris remelting is currently under development.

### 3.5 Debris Coolability Map (DECO)

Non-coolable debris bed presents a credible threat to containment integrity. Phenomenology of ex-vessel debris bed formation and coolability includes coupled (i) jet breakup, (ii) melt droplet cooling and solidification; (iii) debris agglomeration; (iv) particle spreading in the pool; (v) debris bed self-levelling; (vi) debris bed coolability; (vii) post-dryout behavior with possible remelting, etc. Debris bed cools by evaporating water that is pushed into the bed by the hydrostatic pressure. Steam generated inside the debris bed is escaping predominantly upwards, generating convection flows in the pool and changing conditions for melt-coolant interactions. This changes particle properties (size distribution and morphology), packing, agglomeration, and bed formation phenomena. The large-scale circulation in the pool can spread effectively the falling corium particles over the basemat floor, distributing the sedimentation flux beyond the projection area of particle source (e.g., size of reactor vessel). Debris is gradually spread under the influence of steam production in the bed, resulting in self-leveling of the settled portion of the debris and changing the shape of debris bed with time. Relevant phenomena have been extensively studied in the past. Experiments (Figure 3-49) on debris bed and particle properties (DEFOR-S) [61], debris agglomeration (DEFOR-A) [63], porous media coolability (POMEKO) [69], particulate debris spreading (PDS) [2] have been developed. A set of full and surrogate model has been developed and validated against produced experimental data for the debris formation [67], agglomeration ([41], [37]), coolability ([120], [107]) and spreading [3] of the debris.

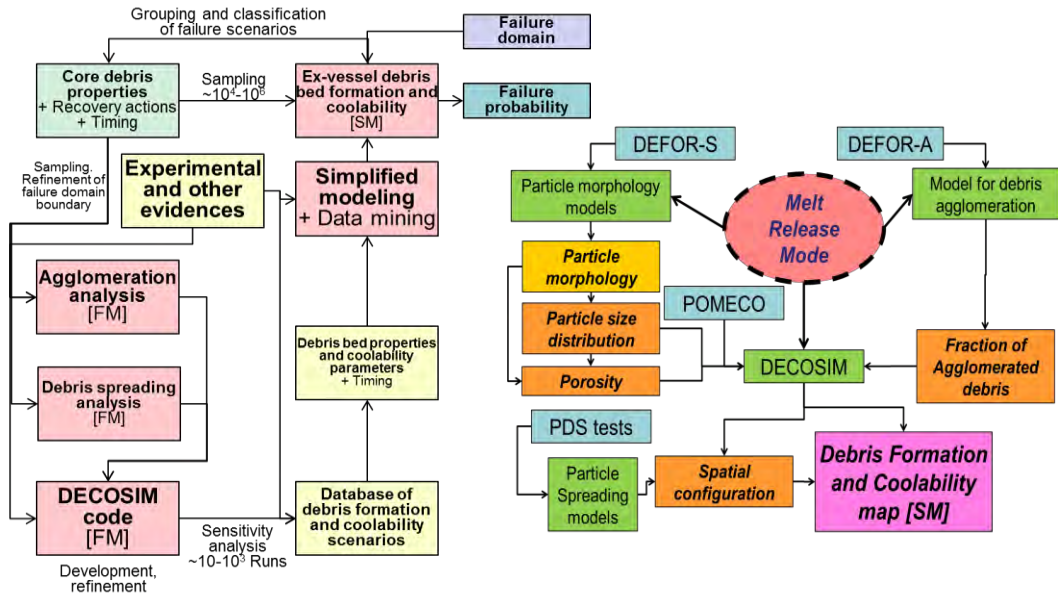


Figure 3-49. Ex-vessel debris bed formation and coolability framework.

The aim of the DECO framework is the integration of knowledge about different phenomena in the models that can resolve important feedbacks and, possibly, identify limiting mechanisms that can reduce uncertainty in assessment of debris coolability.

### 3.5.1. DECOSIM Models for Debris Bed Coolability Analysis

The mathematical models implemented in DECOSIM code are based on multifluid formulation, they include a number of submodels describing two-phase pool flows, disperse particle sedimentation, as well as flows in heat-releasing porous media related to debris bed coolability in in-vessel and ex-vessel configurations. In this work, we concentrate on validation of the models relevant to modeling natural convection flows in the pool, spreading of particles and their fallout onto the bottom surface of the pool [105]. Air-water flow in the pool is described by the mass and momentum, and energy conservation equations for liquid water and gas; turbulence is taken into account only in continuous liquid and described by the  $k - \epsilon$  model with additional terms for turbulence generation due to relative motion of liquid and gas phases [57]. Validity of  $k - \epsilon$  turbulence model in the context of two-fluid model has been addressed previously [36]. Flow-particle interaction due to drag depends on the diameter of the particle, relative velocity and phase composition of the ambient two-phase mixture. To account for turbulent dispersion of particles, the random walk model is applied. The effects of turbulence on particle dispersion are modeled by adding a fluctuating component to the liquid phase velocity. Note that PDS-P experiments [33], [34] were specifically designed to ensure that particle interaction and effect on the flow was negligible; therefore, their results are adequate for validation of the current DECOSIM model. Studies of high-concentration particle releases would require both different experimental conditions and model implementation with “two-way” particle-flow coupling; which is beyond the scope of the present work.

### 3.5.2. Experiment on Debris Formation and Agglomeration

First systematic study of the debris bed formation phenomena was carried out in the framework of DEFOR research program which includes experimental works [30],

[31], [59], [60], [61], [62], [63], [64], [65], [72], [55], [35] and development of analytical models and approaches [38], [39], [40], [41], [43], [44], [45], [66], [67], [104]. The goal of DEFOR (debris bed formation) experiments is to provide data necessary for the development of analytical models and approaches for prediction of debris bed formation and agglomeration phenomena. The DEFOR facility was developed for studies of melt fragmentation, particle and debris bed formation and agglomeration in deep water pool. The installation consists of (i) an induction furnace for melt generation, (ii) a funnel for melt deliver, (iii) a test section with optional metallic sample, and (iv) external water heating system. The scheme of the installation is given in Figure 3-50.

Inside the test section 4 debris catchers are positioned at different elevations, see Figure 3-50. Each catcher is covering one of four quadrants of the test vessel cross section and collects melt fragments ejected from the jet. This allows assessment of the water pool depth on debris bed formation: agglomeration and local particle size distribution. Typical agglomerated debris and cake obtained in DEFOR-A (agglomeration) tests are presented in Figure 3-51.

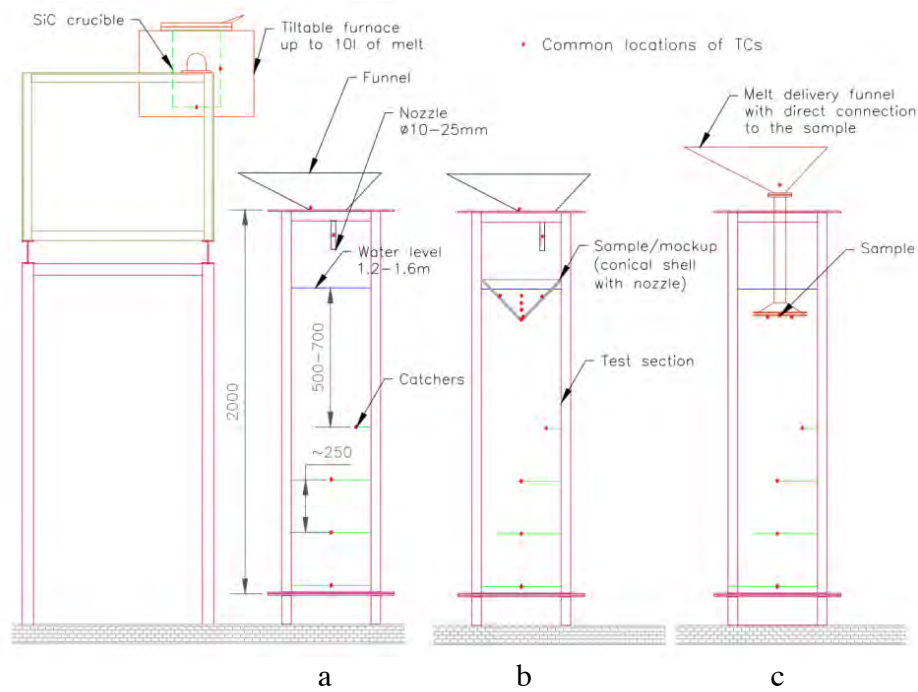


Figure 3-50. DEFOR facility: for a) A01-11;15, b) A12-14;16 and c) A17-21.

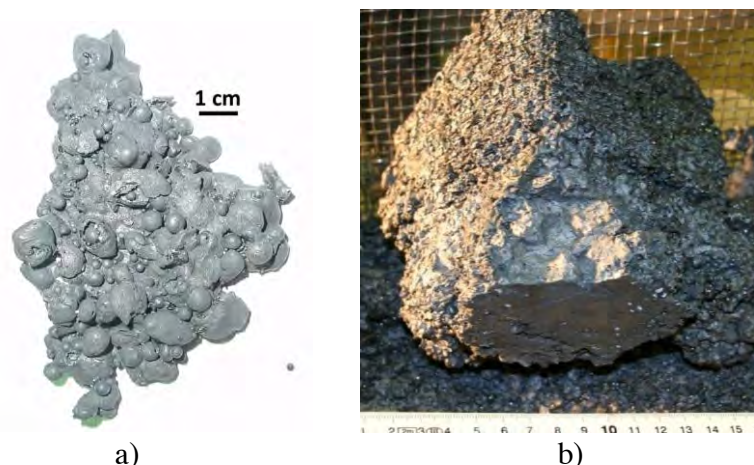


Figure 3-51. Agglomerated debris (DEFOR-A2) (a); a cake (DEFOR-A6) (b)

More than 20 DEFOR-A tests have been carried (Table 3-7). In the first test series (A1-A9 [64], [63], [82])  $\text{Bi}_2\text{O}_3\text{-WO}_3$  (eutectic) melt with melting temperature 870°C was used. Second test series (A10-A21) was carried out using  $\text{ZrO}_2\text{-WO}_3$  (eutectic) melt with melting temperature 1231°C. The Debris bed topology, total porosity, agglomerated mass, and particle size distribution were measured in each test. Melt was released above or below the water surface in order to assess the effect of the jet velocity on the particle size distribution. Experiments with different melting temperature simulant materials and melt release conditions provided a database which can be used for assessment of different test parameters on the properties of the debris bed. While obtained DEFOR experimental database is quite extensive, the maximum size of the jet investigated in the tests was limited to 25 mm. Further investigation of the debris bed formation phenomena can help to clarify possible effects of larger size jets and higher water subcooling on the debris size distribution, agglomeration, porosity and shape. The main goal and focus of the new experimental studies is extension of the experimental database obtained in previous DEFOR tests ([59], [60], [61], [62], [63], [64], [65]) towards more prototypic conditions and covering ranges of important parameters. Conditions of the DEFOR tests carried out in the new test series are summarized in Table 3-8.

Analysis of experimental data suggests that fraction of agglomerated debris decreases rapidly with the depth of the coolant as noticeable in Figure 3-52 for the whole set of experiments (A1-A26). Data on fraction of agglomerated debris from the new DEFOR-A tests agrees well with previously obtained results in the DEFOR-A and DEFOR-S experiments where smaller amount of melt (about 1.0 liter) was used [61]. We found that water subcooling is of minor importance until thermal stresses start to induce solid particle fracture.

Table 3-7: Ranges of the experimental parameters in DEFOR-A tests.

Parameters			A1	A2	A3	A4	A5	A6	A7	A8	A9	A10	A11	A12	A13	A14	A15	A16	A17	A18	A19	A20	A21
Melt temperature, K			110	1253																			
Melt superheat, K			103	1246	A2																		
Melt jet initial diameter, mm			-*	1483	A3																		
Elevation of nozzle outlet, m			20	78	1221	A4																	
Jet free fall height, m			10	102	1245	A5																	
Duration of melt release, s			12	136	1279	A6																	
Melt volume, l			25	206	1349	A7																	
Average flow rate, l/s			20	200	1343	A9																	
Initial average melt jet velocity, m/s			20	150	1644	A10																	
Water pool depth, m			112	1255	A8																		
Water initial temperature, K			15	196	1740	A14																	
Water subcooling, K			20	102	1606	A11																	

Table 3-8: DEFOR tests experimental conditions.

Parameters	A23	A24	A25	A26
Mixture	Bi <sub>2</sub> O <sub>3</sub> -WO <sub>3</sub>			
Composition	Eutectic	Eutectic	Eutectic	Eutectic
Melt density, kg/l	7.811	7.811	7.811	7.811
Melting temperature, K	1143	1143	1143	1143
Melt temperature in the funnel, K	1280	1248	1216	1299
Melt superheat in the funnel, K	137	105	73	156
Melt jet initial diameter, mm	25	34	34	34
Elevation of nozzle outlet, m	1.72	1.77	1.77	1.77
Jet free fall height, m	0.205	0.17	0.17	0.17
Duration of melt release, s	5.8	5.3	5.7	5.5
Melt volume, l	3.5	3.5	3.5	3.5
Average flow rate, l/s	0.54	0.62	0.59	0.59
Initial average melt jet velocity, m/s	-	-	-	-
Water pool depth, m	1.515	1.6	1.6	1.6
Water initial temperature, K	332	346	363	346
Water subcooling, K	41	27	10	27

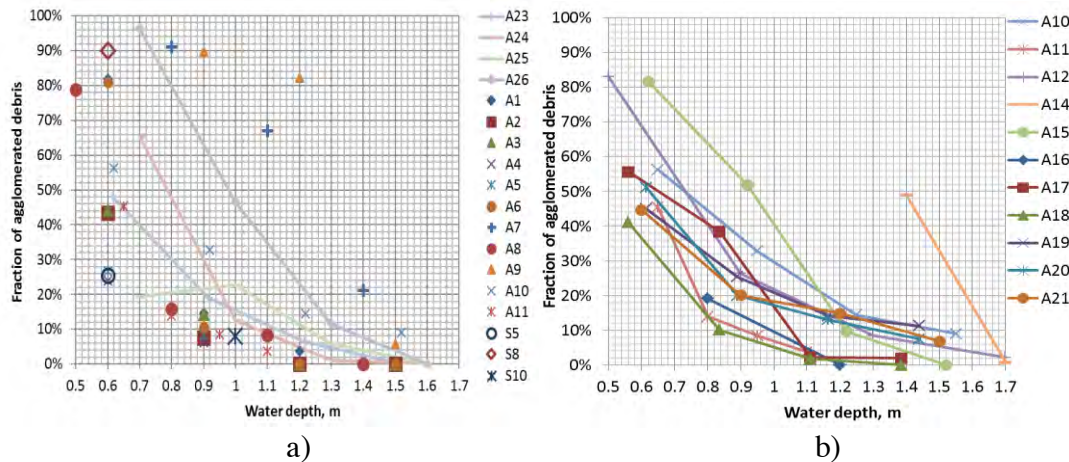


Figure 3-52. Debris bed agglomeration fraction as function of water pool depth for A1-A9, S8, S10, A23-26 (a) and A10-A21 (b) tests.

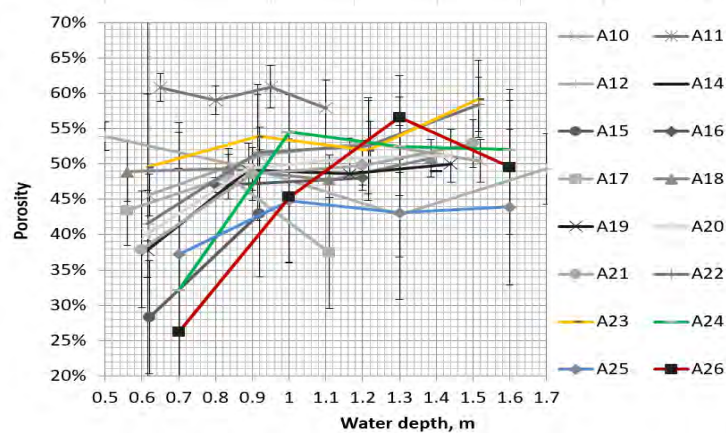


Figure 3-53: Comparison of the debris beds porosity.

On average, larger particles were obtained with ZrO<sub>2</sub>-WO<sub>3</sub> melt than with Bi<sub>2</sub>O<sub>3</sub>-WO<sub>3</sub>. Particle size distributions obtained in DEFOR-A overlap with the size distributions observed in FARO tests. The effect of jet free fall height was not noticeable. However, there is a tendency to generate larger particles in the tests with melt release

under water. Initial jet velocity seems to have no noticeable effect on the fraction of agglomerated debris. Estimated porosity of the bed is on average about 45-50%, which is also similar to the previous tests. On average higher fraction of agglomerated debris and lower porosity are obtained at lower pool depth. As seen in Figure 3-53, high superheat (as in DEFOR-A26 test) leads to higher agglomeration fraction and lower porosity of the debris bed.

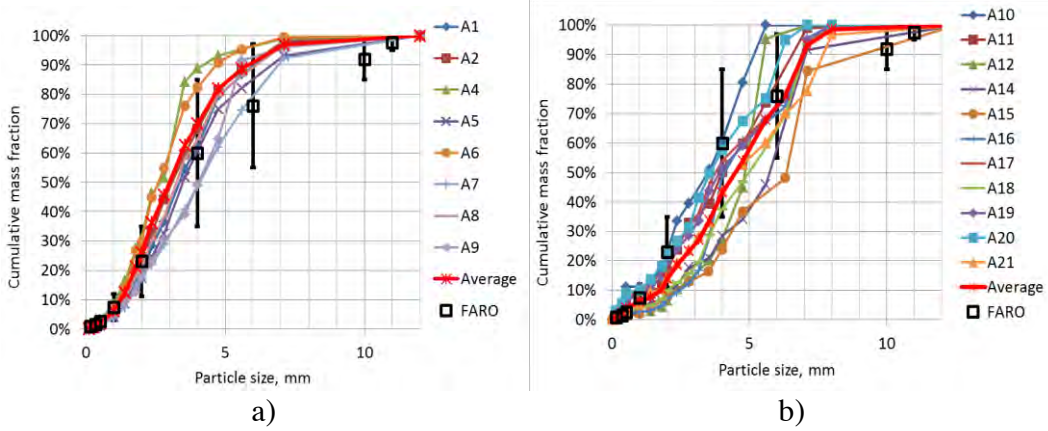


Figure 3-54. Cumulative mass fraction for the debris in DEFOR-A1-A9 (a) and DEOFR-A10-A21 (b) tests. For comparison, the data from FARO tests and averaged DEFOR curves for corresponding series of tests are provided.

The particle size distributions (Figure 3-54) were obtained by sieving the debris. For comparison, the previously obtained result from DEFOR-A1-A9 test series [64], [63], [82] is provided in Figure 3-54a. Distributions from the tests with higher melt superheat are located slightly below the average, corresponding to larger particles. Some variations in the data due to the inherent uncertainties in high temperature melt-coolant interaction experiments can be expected. The data from A10-A21 tests (Figure 3-54b) show on average larger particles obtained with  $\text{ZrO}_2\text{-WO}_3$  in comparison with the previous tests with  $\text{Bi}_2\text{O}_3\text{-WO}_3$ . Both series are within the ranges of FARO [71] data.

The small scale DEFOR tests have been carried out in order to clarify the influence of water subcooling on particle morphology [61]. The changes of particle morphology from mostly round shape to a fractured products at relatively small changes of water subcooling ( $\sim 10\text{-}20$  K) were explained in [66], [67] by the effect of particle cooling rate change at transition from film to nucleate boiling on the thermal stress of crystallized material. Experimental observations [61] and predictions [66], [67] also suggested that smaller particles (below 1 mm) would have higher chances to avoid fracturing. Experiments were conducted at the MISTEE (micro interactions in steam explosion energetic) small scale facility without steam explosion triggering. For a detailed description of the facility see [72], [73]. The first series of experiments were performed with  $\text{WO}_3\text{-Bi}_2\text{O}_3$  in eutectic composition (74:27 mol%,  $T_{\text{liq}}=870^\circ\text{C}$ ) with an initial melt superheat ( $\Delta T_{\text{sup}}$ ) of  $\sim 130^\circ\text{C}$ . The second series of experiments were performed with  $\text{WO}_3\text{-ZrO}_2$  in eutectic composition (73:26 mol%,  $T_{\text{liq}}=1231^\circ\text{C}$ ) with an initial melt superheat ( $\Delta T_{\text{sup}}$ ) of  $\sim 130$  to  $160^\circ\text{C}$ . A set of 3 experiments were performed for each water subcooling (at equal intervals of  $\sim 10\text{k}$ ) for confirmation of data repeatability. Experimental observations confirmed that at high subcooling, the solidification is faster compared to low subcooling of water. Film boiling conditions (highly dependent on water temperature) dictates the fragmentation process. A morphological transition i.e. from round shapes (smooth) to rock like shape with sharp

edges is observed, especially for the  $\text{WO}_3\text{-Bi}_2\text{O}_3$ . The mass fraction of fractured particles increases with increased water subcooling. A sharp transition in debris particle size distribution is observed at  $\sim 50$  K water subcooling for  $\text{WO}_3\text{-Bi}_2\text{O}_3$  and  $\sim 60$  to  $70$  K water subcooling for  $\text{WO}_3\text{-ZrO}_2$ . It is instructive to note that the average particle size of  $\text{WO}_3\text{-ZrO}_2$  is predominantly larger, where at high subcooling conditions  $\sim 60$  to  $70\%$  of the debris particles were above  $3$  mm and at low subcooling conditions  $\sim 90\%$  of the debris particles were above  $3$  mm.  $\text{WO}_3\text{-ZrO}_2$  consistently produced mostly round shaped particles at even high subcooling conditions.

### 3.5.3. Debris Agglomeration Surrogate Model

Hydraulic resistance is a limiting factor that determines maximum decay heat that can be removed from the bed. If decay heat exceeds this maximum value, it will lead to the bed dryout, reheating and remelting of the debris. If melt is not completely solidified prior to settlement on top of the debris bed, agglomeration of the debris and even “cake” formation is possible [70], [61], [31], [62], [63], [64], [55]. Formation of agglomerated debris can significantly increase hydraulic resistance and reduce maximum decay heat which can be removed without reaching dryout of the debris bed. Thus agglomeration is important factor which can inhibit effectiveness of ex-vessel debris coolability [114]. Although agglomeration of the debris and “cake” formation have been observed in previous fuel-coolant interaction (FCI) experiments with prototypic corium mixtures (e.g. in FARO [70], CWTI and CCM [81] tests) and with corium simulant materials (e.g. in DEFOR-E [31] and DEFOR-S [61] tests), the first systematic experimental data was provided in DEFOR-A [62], [63], [64], [55] tests.

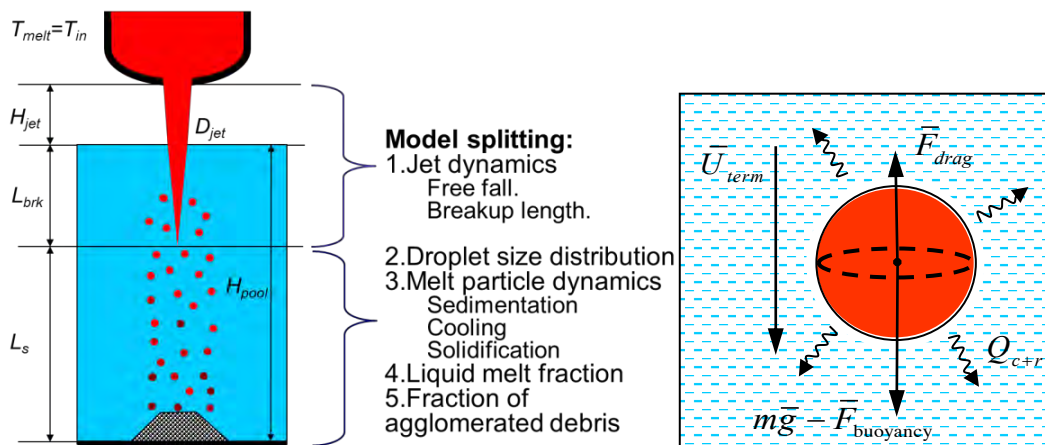


Figure 3-55. Splitting of physical processes for development of the SM.

The data obtained in DEFOR-A tests was used for development and validation of modeling approaches for prediction of agglomerated debris in various scenarios of melt ejection [39], [38], [40], [42], [43], [41], [48]. Proposed model for agglomeration is implemented in deterministic code VAPEX-P [10], that simulates Fuel-Coolant-Interaction (FCI) phenomena including melt jet breakup, formation of liquid droplets, heat transfer between melt and coolant, sedimentation and solidification of the particles.

The goal of this work is to develop and validate a surrogate models for prediction of mass fraction of agglomerated debris. Physics based surrogate modeling approach is employed where computational efficiency and numerical stability are achieved by (i) considering only most important physical phenomena, and by (ii) decomposing

tightly coupled problem into a set of loosely coupled ones with information exchange through initial and boundary conditions. The merits of physics based SM are (i) reduced number of the full model runs which are necessary for the calibration process; (ii) application of the SM beyond the domain covered with the original model. Physical phenomena and parameters important for assessment of agglomeration fraction are presented in Figure 3-55. The most important physical phenomena are modeled in the SM explicitly. Mutual feedbacks between such parameters as jet breakup length, coolant void fraction and velocity are taken into account as closures. Details of model implementation, calibration and verification are provided in [39], [38], [40], [42], [43], [41], [48]. Quite good agreement between FM and SM solutions is illustrated in Figure 3-56. It is instructive to note that in order to obtain one point on the agglomeration map (single combination of jet size and pool depth) with FM takes ~24 - 168 hours of computational time. Obtaining complete agglomeration map using SM takes about half an hour including post processing of the results.

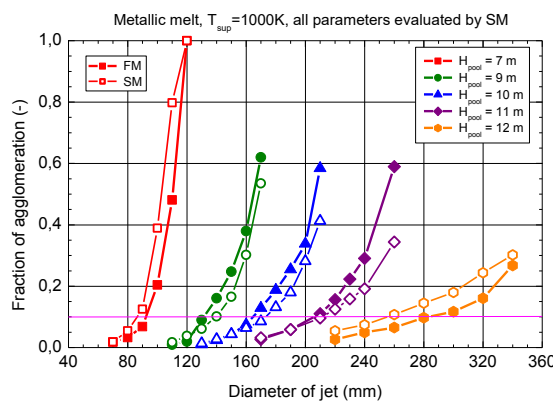


Figure 3-56. Comparison of predictions of mass fraction of agglomerated debris with full model and SM. Solid symbols – FM, half-filled symbols – SM.

Table 3-9: VAPEX SD model input parameters

Variable Name	Description	Units	Range
RHOP	Fuel density	kg/m <sup>3</sup>	[7500 ; 8500]
PHEAT	Fuel latent heat	J/kg	[2.6e5 ; 4.0e5]
CP	Fuel heat capacity	J/kg*K	[350 ; 650]
KFUEL	Fuel thermal conductivity	W/m*K	[2 ; 42]
Em	Emissivity	-	[0.1 ; 1.0]
TLIQSOL	Liquidus/Solidus Temperature	K	[1600 ; 2800]
Po	Containment pressure	Pa	[1e5 ; 4e5]
Tlo	Water pool temperature	K	[288 ; 368]

Global sensitivity analysis was carried out [48] using Morris method [75], [80] and the physics based SM in order to identify the most influential parameters for debris agglomeration. In the analysis we considered both parameters of the melt release scenario and calibrated coefficients used in the SM closure parameters. The execution of the model is performed in two steps: (i) calculation of the data base of cooling histories of a single spherical particle falling through a fluid (VAPEX-SD), given properties of the melt, particles sizes and other parameters that can affect particle interaction with a fluid (see Table 3-9); (ii) calculation of the fraction of agglomerated debris, given single particle cooling histories, particle size distribution, jet properties (jet size, jet release velocity), pool conditions and closure parameters ranges, which are based on the results of models calibration (see Table 3-10).

Table 3-10: Agglomeration SM Model input parameters

Variable Name	Description	Units	Range
DPARN	Jet diameter	m	[0.07 ; 0.6]
UPIN	Melt release velocity(initial)	m/s	[1 ; 8]
TSH	Melt superheat	K	[10 ; 1000]
xpw	Pool depth	m	[5 ; 9]
CBR = $C_{brk}$	Jet break up correlation coefficients		[0.0002 ; 0.001]
BBR = $B_L$			[0.0 ; 0.01]
AFCI = $A_{FCI}$	Pool void model;		[5 ; 15]
BFCI = $B_{FCI}$			[0.5 ; 3]
AVW = $A_{vw}$	Pool vertical velocity model;		[19.78 ; 19.78]
BVW = $B_{vw}$			[13.19 ; 19.78]
CVW = $C_{vw}$			[-0.35 ; -0.25]
AUW = $A_{uw}$	Pool lateral velocity model;		[10 ; 14]
BUW = $B_{uw}$			[-1.5 ; -0.5]
CUW = $C_{uw}$			[-0.1 ; -0.05]
UMIN = $U_{min}$			[0.0 ; 0.05]

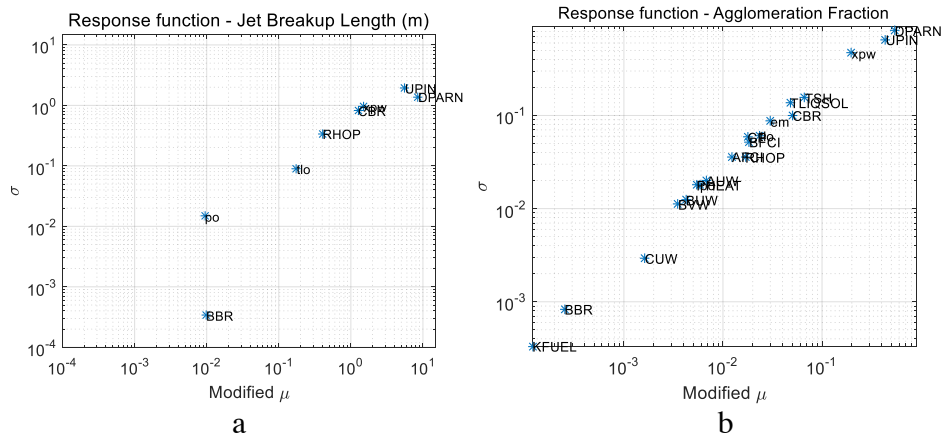


Figure 3-57: Morris Sensitivity results a) Jet Breakup Length; b) Debris agglomeration fraction.

Figure 3-57 presents the results of Morris sensitivity analysis. The results show that the fraction of agglomerated debris is mostly influenced by the parameters of the melt release scenarios DPARN (jet diameter), UPIN (initial melt release velocity) and XPW (pool depth). This is because the jet breakup length, which is one of the most important factors for debris bed agglomeration, is mostly influenced by DPARN, UPIN, XPW and closure coefficient CBR, however, the relative importance of CBR and XPW is significantly smaller compared to DPARN and UPIN for the selected ranges of the parameters. Further analysis is necessary, to determine the relative importance of jet break up model parameters on the results. This concerns mainly relatively small jet diameters (e.g. IGT failure), where uncertainty in the results due modelling parameters might be more important.

### 3.5.4. Particulate Debris Spreading

Debris bed height is one of the important factors for coolability. A tall, mound shape debris bed can be barely coolable, while the same mass of the debris can be easily cooled if spread uniformly [121], [119]. Two-phase flow inside the bed can help to

flatten the debris bed by so called “self-leveling” phenomenon. The goal is to assess characteristic time scale of the self-leveling process and compare with the time scale for debris remelting. Following tasks are addressed: (i) separate effect studies to quantify particulate debris flux at different conditions; (ii) generalization of the observed dependencies in non-dimensional variables; (iii) development of the model and code, extensive sensitivity and uncertainties analyses.

### Experimental approach

The phenomenon of particle self-leveling is determined by the interactions between particles (solid phase), steam bubbles (gas phase) and water (liquid phase). Several PDS (particulate debris spreading) facilities were designed and built in order to study spreading phenomena. It has been demonstrated that local particle flow rate depends on the local slope angle of the debris bed and local gas velocity, while the bulk volume of the debris bed is immobile (Figure 3-58). The particles are moving only in the topmost layer of the bed having a thickness of few particle diameters. The local nature of the gas-coolant-particle interactions suggests that experiments in reduced size laboratory facilities can capture key physical phenomena.

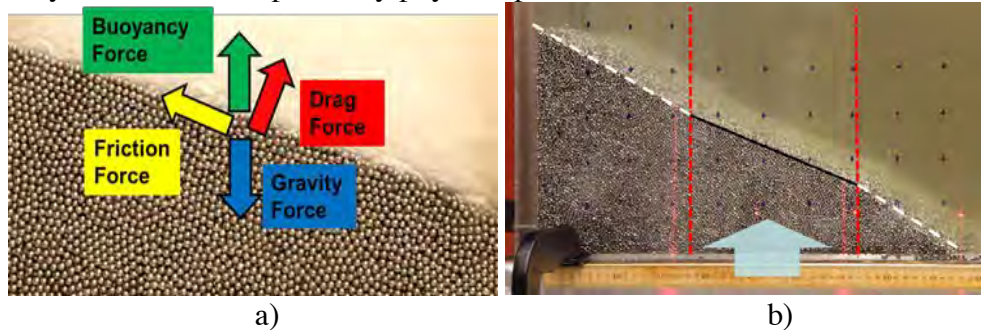


Figure 3-58. (a) Forces acting on particles near the top bed surface; (b) shape of the bed when gas is injected only under one section of the bed.

Debris bed slope  $\theta(t)$  angle and particle flow rate  $Q_p(t)$  as function of time  $t$  are assessed using image processing in order to obtain  $Q_p = Q_p(Q_g, \theta)$ . Hundreds of the tests in PDS-C facility have been carried out with different particles at different gas injection flow rates  $Q_g$ . The database of the dependencies  $Q_p = Q_p(Q_g, \theta)$  has been analyzed and used for development of the generalized scaling approach allowing application of the self-leveling model to reactor scale. A model based on the closures was developed. The first results on experimental approach and successful model validation are reported in [2], [3], [4], [5], [6], [7]. Scaling approach is based on the fact that particle flow rate can be expressed as a function of the main forces (Figure 3-58) (i) buoyancy ( $F_B$ ), (ii) aerodynamic drag ( $F_D$ ), (iii) gravity ( $F_G$ ), and (iv) inter-particle friction ( $F_{Fr}$ ), and parameters which determine the forces:

$$Q_p = f(d_p, U_g, \rho_p, \rho_l, \rho_g, \mu_g, \mu_l, \sigma, g, \alpha, k_{Fr}), \quad (3-6)$$

where  $\alpha$  is a local slope angle;  $k_{Fr} = \tan \theta_{rep}(Q_g)$  is friction coefficient which is a function of gas flow rate and for the coarse, cohesion-less materials is equal to the tangent of the repose angle. Non-dimensional particle flow rate  $Q_p^*$

$$Q_p^* = \frac{Q_p}{(\rho_p - \rho_l)\sigma/\mu_l \cdot d_p} = F(u_g, Ar_{lg}, \gamma, \beta) = K \cdot u_g^a \cdot Ar_{lg}^b \cdot \gamma^c \cdot \beta^d \quad (3-7)$$

$$u_g = \frac{U_g}{U_{mf}}, \quad Ar_{lg} = \frac{\rho_g \cdot (\rho_p - \rho_l) \cdot g \cdot d_p^3}{\mu_g^2}, \quad \gamma = \frac{\tan \theta_{rep}(u_g)}{\tan \theta_{rep}^0}, \quad \beta = \frac{\tan \theta_p}{\tan \theta_{rep}(u_g)}. \quad (3-8)$$

Table 3-11: Empirical constants

$Q_p^*$	$K$	$a$	$b$	$c$	$d$
<0.0024	3.356	1.089	-0.325	2.628	4.306
>0.0024	0.159	0.432	-0.162	1.366	0.876

where: i) normalized gas velocity  $u_g$  defined as the ratio of the superficial gas velocity  $U_g$  at the debris bed top surface and the minimum fluidization velocity  $U_{mf}$ , ii) gas phase Archimedes number  $Ar_{lg}$ , iii) normalized tangent of repose angle  $\gamma$  (characterizing the friction force), with  $\theta_{rep}(u_g)$  being the repose angle at  $u_g$  and  $\theta_{rep}^0$  the repose angle at zero gas velocity, and iv) normalized tangent of slope angle  $\beta$ , where  $\theta_p$  is the local slope angle. In equations (3-8)  $\rho_i$  and  $\mu_i$  are the densities and viscosities of the respective phases (subscripts  $p$ ,  $l$ , and  $g$  refer to particles, liquid and gas phases),  $\sigma$  is the surface tension,  $d_p$  is the equivolume sphere diameter. In eq. (3-7) the  $Ar_{lg}$  represents the effect of gravitational and buoyancy forces,  $Q_g$  the effect of aerodynamic drag and finally  $\gamma$  and  $\beta$  describe friction forces. Larger particles made of denser material will resist to the spreading according to the effect of the Archimedes number in Eq. (3-7). The minimum fluidization velocity  $U_{mf}$  is obtained from the correlation between the corresponding Reynolds number  $Re_{gmf} = \rho_g d_p U_{mf} / \mu_g$  and the gas phase Archimedes number  $Ar_{lg}$ . Based on the PDS-C experimental data, the constants  $K$ ,  $a$ ,  $b$ ,  $c$  and  $d$  are evaluated by performing regression analysis (RA). Two separate RAs were necessary in order to represent different regimes of particle spreading: rapid avalanche and slow particle spreading (see Table 3-11). Parameter  $R(t)$  is introduced and defined as ratio between heap slope angle at time  $t$  and the repose angle at zero gas velocity  $R(t) = \frac{\alpha(t)}{\theta_{rep}^0}$ . The predicted  $R(t)$  is calculated by finding the corresponding  $\alpha(t)$  after implementing the proposed closure in the mass balance equation. It is possible to write the mass balance equation in a differential form with respect to the local height of the bed  $h$

$$\frac{\partial h(x,t)}{\partial t} + \frac{1}{\rho_b x^{n-1}} \frac{\partial}{\partial r} \left( x^{n-1} \cdot Q_p \left( u_g(h), \frac{\partial h}{\partial x}, p \right) \right) = 0 \quad (3-9)$$

where, local slope angle  $\theta_p = \tan^{-1}(\frac{\partial h}{\partial x})$  and  $Q_p \left( u_g(h), \tan(\theta_p) \right) = Q_p \left( u_g(h), \frac{\partial h}{\partial x} \right)$  is the particle flow rate per unit width obtained by a scalable empirical closure developed as the generalization of PDS-C experiments (Basso et al., 2016a) [5],  $\rho_b$  is the bulk density of the heap,  $x$  is the spatial coordinate,  $n = 1$  for planar geometry and  $n = 2$  for axisymmetric geometry,  $p$  is the set of properties of particles and fluids (assumed to be spatially homogeneous). The equations are then solved numerically with the Crank–Nicolson implicit integration scheme of 2<sup>nd</sup> order of accuracy. A detailed formulation of this approach can be found in [3].

Parity plot of predicted and experimental  $R(t)$  is presented in Figure 3-59, here  $R(t)$  is shown illustratively at 5% 10% 20% 50% 80% of the total spreading time in the experiment. The data points from all experiments with different particles and particle mixtures are clustered along the diagonal of the plot, suggesting that proposed scaling approach captures most important physical phenomena and can predict the debris bed self-leveling behavior. Obtained correlation has been used to predict evolution of the debris bed shape in time for reactor accident conditions. A comprehensive sensitivity and uncertainty analyses of the spreading efficiency are presented in [3].

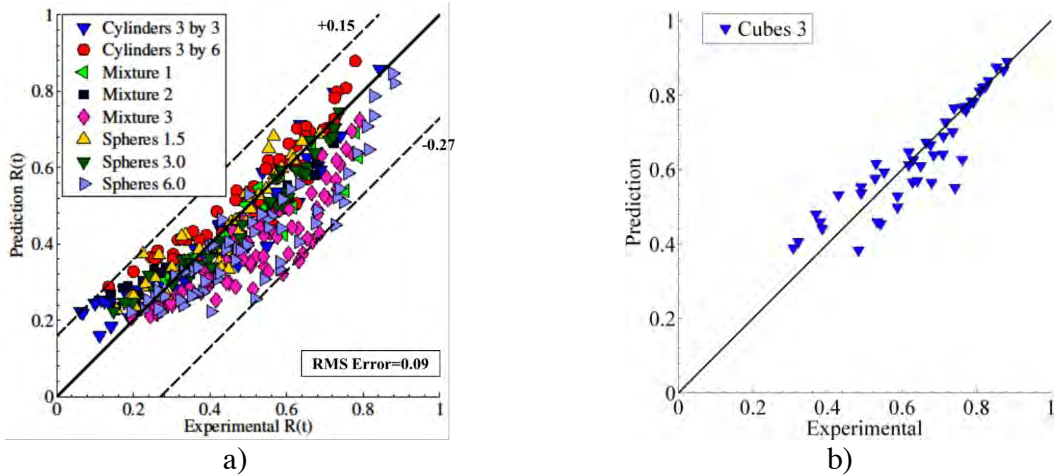


Figure 3-59: Comparison between predicted and experimental  $R(t)$  in the PDS-C experiments.  $R(t)$  is calculated at 5%, 10%, 20%, 50% and 80% of the total experimental time. Root mean square (RMS) error is equal to 0.09.

#### Debris Bed Spreading and Coolability Full (DECOSIM) Model Analysis

DECOSIM simulations were carried out in order to investigate post-dryout debris bed. The studies extended the results obtained earlier in [107] to wider ranges of debris bed parameters (particle diameters and porosities), as well as to more debris bed shapes (Gaussian shape was studied in addition to conical and mound shapes). DECOSIM simulations were carried out in order to study the coupled debris bed spreading by self-leveelling and coolability. The results of DECOSIM predictions for debris bed height are compared with those obtained from a simple model in which the superficial gas velocity is evaluated from the heat released in the debris layer of local debris bed height [3]. Also, post-dryout stage is considered at which the maximum temperatures reached in the debris bed are compared with those calculated without particle spreading taken into account (fixed-shaped debris bed). Generally, three main outcomes were observed: (i) a coolable debris bed without dryout occurrence; (ii) dryout in the top part of debris bed persisting for some time, followed by reflooding and quenching of the dry zone, and (iii) dryout with steady temperature escalation. All these cases are discussed in detail from the debris bed shape and coolability points of view in the following two sections. An important finding of the analysis was that in the case of dryout the self-leveelling mechanism remains effective, i.e., reduction in the debris bed height with time is not deteriorated. This also allows one to apply the simple model [3] for evaluation of debris bed self-leveelling and coolability in order to obtain conservative estimates of the time after which the debris bed becomes coolable. Figure 3-60 summarizes the predicted time histories of solid particle maximum temperatures in the simulations where dryout occurred (simulations with particle diameter of 2 mm resulted in no dryout, therefore, temperatures were near the saturation point and are not shown due to triviality). One can see that debris beds with 1 mm particles are non-coolable, regardless of whether particle spreading is taken into account or not; these are featured by steady temperature escalation. On the other hand, debris beds with particle diameter of 1.5 mm are featured by dryout, however, temperature is stabilized due to vapor cooling, and even in the case of fixed-shape debris bed it gradually decreases due to decrease in the decay heat power with time. If particle spreading is active, slumping of the debris bed results in its faster reflooding (compare the solid lines with corresponding dashed lines in Figure 3-60).

Table 3-12: Simulations of debris bed self-leveling and coolability

Particle diameter $d_p$ , [m]	Relocation time $t_r$ , [hours]	Bed height after 1 h (DECOSIM)	Bed height after 1 h (SM Model)	Coolability
1.0	1.5	1.55	1.63	Dryout
	3.0	1.55	1.66	Dryout
1.5	1.5	1.61	1.67	Dryout/Reflooding
	3.0	1.67	1.70	Dryout/Reflooding
2.0	1.5	1.65	1.68	No Dryout

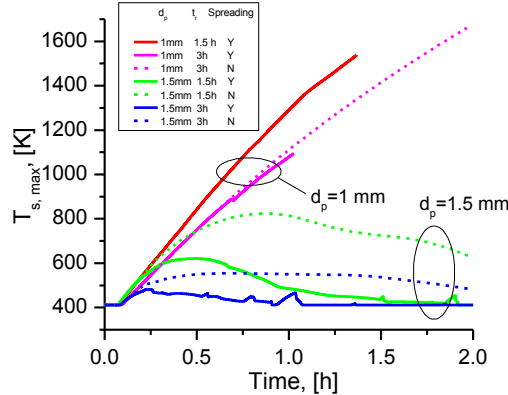


Figure 3-60: Maximum temperatures of solid particles in simulations with (Y) and without (N) particle spreading.

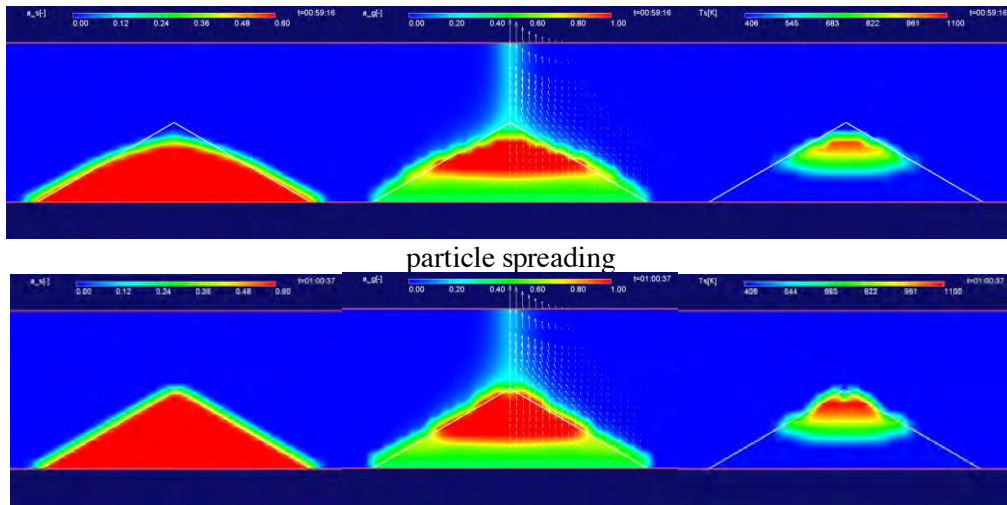


Figure 3-61: Volume fraction of debris (left), void fraction (middle) and debris temperature (right) in the bed with 1 mm particles 1h after relocation.

In Figure 3-61, the case of debris bed with 1 mm particles is demonstrated. The relocation time for this case was 3 h, the distributions are shown at time 1 h after relocation, i.e., 4 h after SCRAM. One can see that significant part of debris bed (roughly, upper half of its height) is dry; slumping of the debris bed due to particle spreading reduces somewhat the size of high-temperature zone, but effect of the slumping is insufficient to prevent material reheating.

#### Surrogate Model for Cone-Shaped Debris Bed

Coolability analysis of arbitrary-shaped debris bed requires determination of dryout heat flux  $DHF$  as a function of porous medium properties (mean particle diameter  $d$ ,

porosity  $\varepsilon$ ), system pressure  $P_{sys}$ , as well as the debris bed shape. For a flat debris bed, well-known analytical formulas can be used. For multidimensional (even axisymmetric) debris beds dryout conditions have to be obtained from computationally expensive numerical simulations. The way forward is in the development of surrogate models approximating the DHF by computationally inexpensive and sufficiently accurate analytical formulas. The generic approach to the construction of surrogate models for debris bed coolability problems has been developed in [120], where ready-to-use formulas are presented for the case of cone-shaped debris bed, possibly residing on a cylindrical base if the lateral spread of debris is limited by the water pool size. The SM for debris bed dryout is formulated in non-dimensional form as:

$$\frac{DHF}{\rho_g \sqrt{\eta g} \Delta H_{ev}} = f(\chi, P_{sys}) \quad (3-10)$$

where DHF stands for the dryout heat flux, while

$$\chi = \frac{K \rho_g g}{\mu_g \sqrt{\eta g}}; K = \frac{\varepsilon^3 d_p^2}{150(1-\varepsilon)^2}; \eta = \frac{\varepsilon^3 d_p}{1.75(1-\varepsilon)} \quad (3-11)$$

Here,  $P_{sys}$  is the system pressure,  $K$  is the permeability,  $\eta$  is the passability,  $g$  is the gravity acceleration,  $\Delta H_{ev}$  is the latent heat of evaporation,  $\rho_g$  and  $\mu_g$  are the density and viscosity of water vapor, respectively,  $\varepsilon$  is the porosity, and  $d_p$  is the particle diameter. For a flat (one-dimensional) debris bed, the function  $f(\chi, P_{sys})$  was determined from the asymptotic analysis of analytical solution for the dryout heat flux. Further analysis in (Yakush et al., 2013) [120] has revealed that these functions are also applicable to 2D debris beds shown in Figure 3-62 in the range of slope angles  $0 \leq \theta \leq 45^\circ$ , if DHF is multiplied by the shape factor  $\Omega(\theta)$  approximated by

$$\Omega(\theta) = 1 + \frac{h_{cone}}{h_{max}} (0.53 + 0.005 \cdot \theta) \quad (3-12)$$

Equation (3-12) describes the effect of lateral ingress of water which improves debris bed coolability. Here,  $h_{cone}$  is the debris cone height,  $h_{max}$  is the debris total height,  $\theta$  indicates the slope angle of the cone (Figure 3-62). Using the proposed SM, it is possible to estimate directly the DHF of a non-flat debris configuration by knowing i)  $P_{sys}$ , ii)  $d_p$ , iii)  $\varepsilon$  and iv) geometrical characteristics (total debris mass and volume, pool diameter, slope angle).

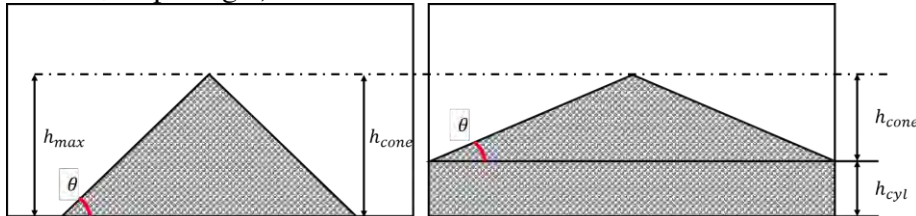


Figure 3-62: Bed shapes: a) conical and b) cone on a cylindrical-base.

#### Sensitivity analysis of the coupled Spreading Full Model and Coolability SM

Two models, the debris bed self-leveling FM and coolability SM (described in [120]), have been coupled in order to estimate the time to reach a coolable configuration  $t_c$ . The debris bed heat flux  $Q_{HF} = \rho_b Wh$  calculated at the maximum local height  $h = h_{max}$  is compared at each time step to the dryout heat flux (DHF). The debris bed is considered coolable if the decay heat released in the material is lower than DHF. The extended Morris method [8], [75], [79] has been applied to the coupled code in order to rank the relative importance of the parameters affecting the debris bed coolability. The time  $t_c$  when  $Q_{HF}(h_{max}) \leq DHF$  is satisfied, has been chosen

as a target function of the analysis. The ranges of the uncertain model input parameters are selected in order to conservatively cover uncertainties **Table 3-13**. The Morris indexes are plotted in **Figure 3-63** with the modified mean shown on the x-axis and the standard deviation shown on the y-axis. All parameters have apparently higher-order interactions with other parameters as the standard deviation is much larger than the modified mean.

Table 3-13: Input parameters with corresponding uncertainty ranges.

Input parameter	Uncertainty range	
	Lower boundary	Upper boundary
<i>Scenario-related conditions</i>		
Drywell radius [m]	Fixed to 6	
Total Debris mass [tons]	10	250
Containment Pressure [Bar]	1	4
Effective operation Time [days]	365	1095
Time from scram [hours]	2.5	5.25
Reactor Thermal Power [GW]	1.4	3.9
Initial angle factor [-]	0.1	1
<i>Physical properties</i>		
Material density [kg/m <sup>3</sup> ]	7500	9000
Debris Bed Porosity [-]	0.3	0.6
Effective Particle diameter [mm]	1.0	6.0
Critical angle of repose at zero gas flow [degree]	22°	35°
<i>Modeling parameters</i>		
Closures uncertainty	-0.25	0.27
Number of cells [-]	50	
Time step	Adaptive: between 10 msec and 10 sec	
<i>Output parameter</i>		
Analyzed function for sensitivity:	Time to reach a coolable configuration ( $t_c$ )	

Table 3-14: Model input parameters ranked using the Morris.

Ranking	Parameter	Normalized modified mean [%]	Cumulated Statistic [%]
1	<b>Porosity</b>	<b>0.22</b>	<b>0.22</b>
2	<b>Effective Particle Diameter</b>	<b>0.19</b>	<b>0.41</b>
3	<b>Reactor Thermal Power</b>	<b>0.18</b>	<b>0.59</b>
4	<b>Total Debris Mass</b>	<b>0.16</b>	<b>0.75</b>
5	<b>Pressure</b>	<b>0.08</b>	<b>0.83</b>
6	<b>Critical Angle of Repose</b>	<b>0.06</b>	<b>0.89</b>
7	<b>Density</b>	<b>0.04</b>	<b>0.93</b>
8	<b>Initial Angle Factor</b>	<b>0.03</b>	<b>0.96</b>
9	<b>Effective Operation Time</b>	<b>0.01</b>	<b>0.98</b>
10	<b>Closure Uncertainty</b>	<b>0.01</b>	<b>0.99</b>
11	<b>Time since Scram</b>	<b>0.01</b>	<b>1.0</b>

It is instructive to compare these results with the sensitivity study conducted exclusively on the self-leveling phenomenon and reported in [6]. In **Figure 3-64** the Morris indexes for the maximum debris height after 2 hours are plotted. A clear difference is that all the input parameters exhibit mostly a linear influence on the output. In contrast, once it is coupled to the SM for predicting the debris bed dryout the resulting code demonstrates to have a strong interplay between parameters as seen in **Figure 3-63**. This behavior is ascribable to the fact that the dryout condition, applied at each time step is strongly affected by parameters interactions.

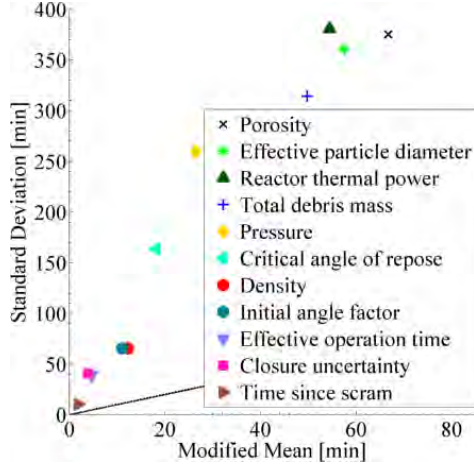


**Figure 3-63:** Modified mean and standard deviation of the time to reach a coolable configuration analyzed with Morris sensitivity method. The dashed line represents the first quadrant diagonal.

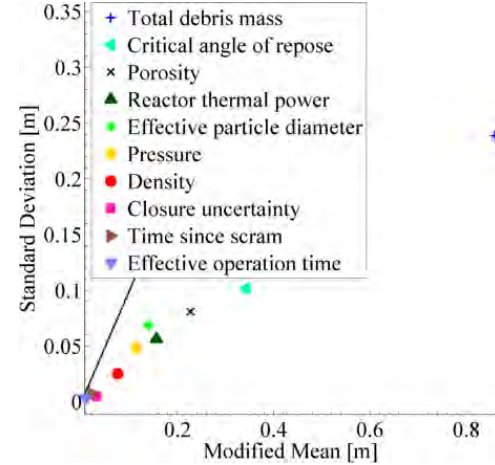


**Figure 3-64:** Modified mean and standard deviation of the maximal bed height analyzed with Morris sensitivity method at time 2 hours. The dashed line represents the first quadrant diagonal.

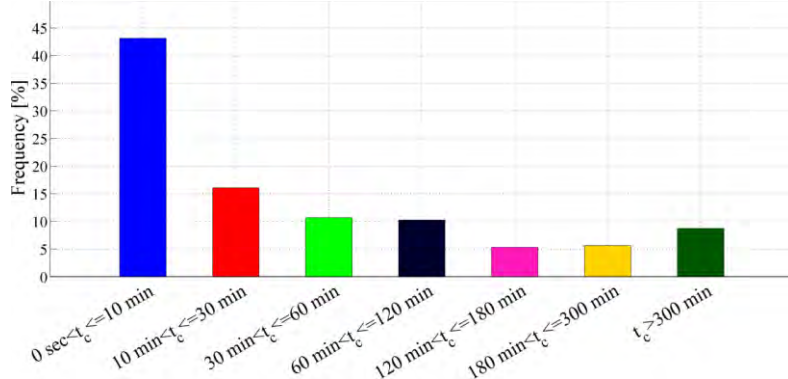


**Figure 3-65:** Relative frequencies plot of the model results for the time to reach a coolable configuration. Results are filtered to consider exclusively time greater than zero and successively split between time intervals.

In order to provide data on the relative probability for the time to reach a coolable configuration a Monte-Carlo experiment has been conducted by using a Halton sampling method [27] with  $\sim 10.5$  millions of input sets in the space given by the significant parameters reported in **Table 3-14**. The generated input sequences are evaluated computing the coolability time  $t_c$ . Only a small fraction,  $\sim 3\%$ , of the total runs appear to be initially non-coolable. In **Figure 3-65** only the realizations of the model with initially non-coolable debris configuration are considered and the relative frequencies of discrete intervals are reported. By interpreting the results in **Figure 3-65** we can estimate that less than the 1.5% of the all possible cases will result in a non-coolable configuration at time 30 minutes from the relocation.

#### Development of a Surrogate Model for Coupled Coolability and Spreading Analysis

In order to estimate the probability of failure, a fundamental step is the definition of the failure criterion. In the most conservative approach, the initially formed debris bed should be coolable. It will remain coolable afterwards because the decay heat power decreases with time. Unfortunately, with the state of the art knowledge, it is not possible to demonstrate that the formation of an initially non-coolable debris bed

is physically impossible, see Yakush et al., (2013, 2012) [120], [119]. A less conservative success criterion admits that the initial debris bed may be non-coolable, so that a dry zone will be formed where debris will be heated up due to deterioration of heat removal. However, if the debris bed is reflooded before re-melting becomes imminent, the cooling strategy can also be considered successful. Following this less conservative criterion in the present study the failure of the containment is assumed to occur once the dry zone of the debris bed reaches 2750 K, the onset temperature of corium re-melting. Thus, a debris bed can be classified as coolable if its  $t_c$  is shorter than the time  $t_{rm}$  necessary for the debris to reach the onset temperature of re-melting.

Table 3-15: Time (in minutes) for onset of re-melting for different conditions of initial bed temperature ( $T_{ini}$ ) and heat-up rate ( $\dot{T}_{rate}$ ).

	$\dot{T}_{rate}=0.2 \text{ K/s}$	$\dot{T}_{rate}=1 \text{ K/s}$	$\dot{T}_{rate}=10 \text{ K/s}$
$T_{ini}=400 \text{ K}$	12000	2400	240
$T_{ini}=600 \text{ K}$	11000	2200	220
$T_{ini}=900 \text{ K}$	9500	1900	190
$T_{ini}=1200 \text{ K}$	8000	1600	160
$T_{ini}=1700 \text{ K}$	5000	1000	100

The initial temperature  $T_{ini}$  of the settled particles was also varied: 400 K, 600 K, 900 K, 1200 and 1700 K. In **Table 3-15**  $t_{rm}$  values are provided for all combinations of  $\dot{T}_{rate}$  and  $T_{ini}$ . As a result  $t_{rm}$  can change by about two orders of magnitude. The quantification of  $t_{rm}$  is made on the assumption that if the model input does not give an immediate coolable debris bed (i.e.  $t_c = 0$ ), the temperature of the established dry-zone will start to raise with a certain heat-up rate  $\dot{T}_{rate}$ . Since the heat transfer is not resolved in the current model, the parameter  $\dot{T}_{rate}$  has to be assumed. Three hypothetical cases were considered:  $\dot{T}_{rate} = 0.2 \text{ K/s}$ ;  $\dot{T}_{rate} = 1.0 \text{ K/s}$  in case of no steam cooling, i.e. the debris inside the dry zone is only heated by the decay heat produced in the dry zone;  $\dot{T}_{rate} = 10 \text{ K/s}$ , an assumption implying additional heat source(e.g. zirconium oxidation).

A surrogate model was developed in the form of an artificial neural network (ANN) to proxy the coupled code for coupled spreading and coolability analysis. The chosen ANN structure consists of two hidden layers formed by 10 sigmoid neurons and 4 sigmoid neurons respectively, followed by a single linear output layer [57]. The developed ANN-based SM gives very satisfactory results in terms of the coefficients of determination  $R^2 = 0.9995$  values. In our particular case the performance win factor with ANN is about  $10^7$  with respect to original model.

#### *Probabilistic framework for uncertainty quantification*

Two nested loops were implemented: the outer-loop where the distribution parameters were pseudo-randomly generated and the inner-loop where distributions were fixed and the values of the input parameters were pseudo-randomly sampled along the relative PDFs. Sampling for each set of randomly selected PDFs provides an estimate of respective failure probability. Sampling of the PDFs result in a distribution of possible failure probabilities. The resulting sets of failure probabilities,  $P(t_c > t_{rm}|e_i)$  are reported as complementary cumulative distribution functions (CCDFs) in Figure 3-66, Figure 3-67, for all values of  $t_{rm}$  listed in Table 3-15 and uncertain input parameters in (**Table 3-16**). The vertical (y-axis) indicates the degrees

of belief associated with respective failure probability (horizontal x-axis). All the CCDFs obtained for different  $T_{ini}$  converge gradually into a single curve as the rate of temperature increase  $\dot{T}_{rate}$  becomes larger. In other words, the influence of the initial temperature on the failure probability gradually diminishes as  $\dot{T}_{rate}$  increases.

**Table 3-16:** Input parameters with corresponding uncertainty ranges.

Input parameters	Parameter range
Total debris mass [tons]	10-250
Containment pressure [Bar]	1-4
Initial angle factor [-]	0.1-1.0
Particle density [ $\text{kg}/\text{m}^3$ ]	7500-9000
Debris bed porosity [-]	0.3-0.6
Effective particle diameter [mm]	1.0-6.0
Critical angle of repose at zero gas flow [degree]	22-35

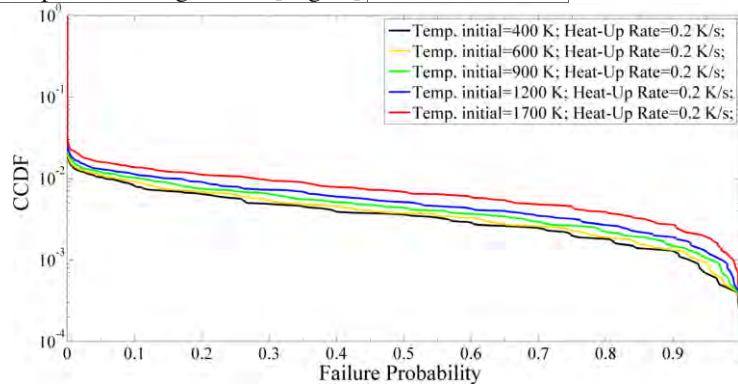


**Figure 3-66:** Failure Probability CCDFs for heat-up rate value of 0.2 K/s.

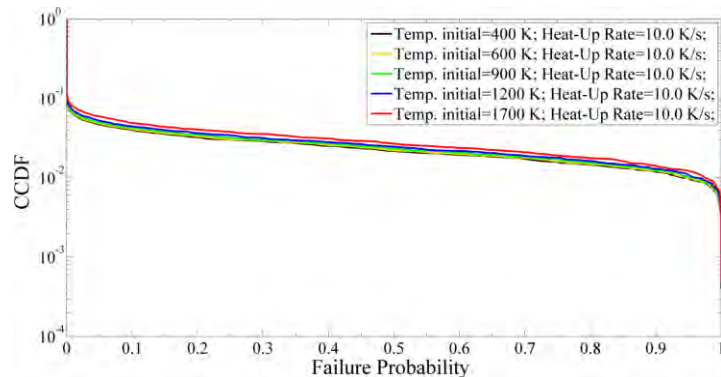


**Figure 3-67:** Failure Probability CCDFs for heat-up rate value of 10 K/s

### Summary of Particulate Debris Spreading and Coolability Analysis

A coupled model for particulate debris spreading and a surrogate model for the determination of the coolability has been developed. The spreading model is based on the PDS-C experimental data and generalized scalable closures. It allows to predict the time to reach a coolable configuration for a conical (or conical + cylindrical base) porous debris bed after relocation in the hypothetical case of SA in Nordic

Risk analysis was performed to quantify conditional containment failure probability due to formation of non-coolable debris bed for severe accident conditions. Nested pseudo-random sampling was employed in order to quantify the effect of lack of knowledge about the distributions of the uncertain input parameters. Assumptions about the ranges for the input parameters were made using available information from

previous studies. Families of different distributions with unknown shape factors were used to characterize the uncertainty in the distributions. All input parameters were assumed to be mutually independent due to the lack of data on possible correlations. Further analysis will be necessary in order to determine dependencies (if any) between the input parameters.

#### *PDS-P Experiments for Validation of Particulate Debris Spreading Models*

The large-scale turbulent two-phase flows may affect the particle lateral spreading over the basemat [114], preventing formation of a tall debris bed. In some accident scenarios the pool can be initially subcooled. In this case, boiling in the pool can start when the hot water plume stemming from the debris bed approaches the surface and its temperature exceeds the local saturation temperature corresponding to the local hydrostatic pressure head [106]. The influence of two-phase flow on sedimentation of the different in size particles has been investigated experimentally [32]. Numerical approaches employing discrete element analysis for particle spreading are also under development [44]. The main goal of PDS-P work is to provide separate effect data for code validation [33].

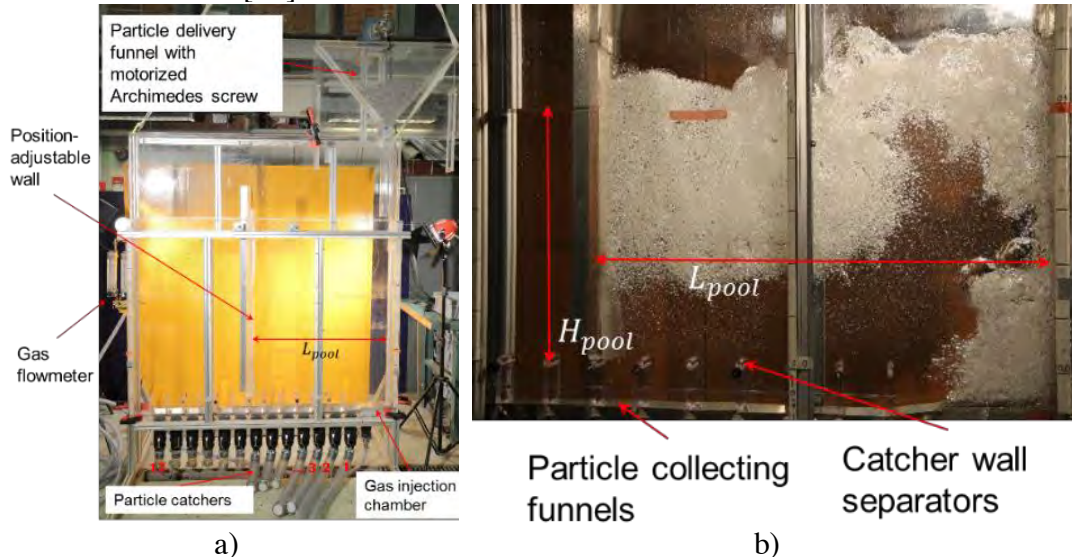


Figure 3-68: PDS-P facility: general view (a) and test section in operation (b).

The general view of the facility is illustrated in Figure 3-68. Particles reaching the pool bottom were collected by several catchers. The particle supply rates were maintained low in order to produce separate effect data for code validation. Conditions of all tests are provided in Table I, Table II and Table III respectively of APPENDIX A in [34]. In the new series of tests chamber for air injection it is replaced by a point injection source and as a result the spatial resolution of the catchers under the particle source increased. The maximum deposition of the particles are not exactly below the particle source (Figure 3-69). At higher flow rates, particles spread away from the particle source. Notably, in case of 0.9 m pool depth with air flow rate 7.01 g/s, the particle distribution is almost evenly spread for a couple of catchers and little mass is deposited at the center.

A new technique is employed where particles are painted with a fluorescent paint. The diameter of the painted particles is between 3.16-3.37 mm. with effective density of 6350-6450 kg/m<sup>3</sup>. Particles can be released simultaneously, see Figure 3-69b, or one-by-one to identify individual trajectories, see Figure 3-69c. Videos are processed using a software called Tracker. A calibration shows that the error in calculating the

coordinates is less than 1%. The particle tracking experiments are carried out using conditions similar to the earlier experiments. The pool length is fixed at 1.2 m and the pool height of 0.5 m and 0.9 m. The air flow rate is varied as 40, 100 and 300 LPM (Liter per minute). Figure 3-70 shows the trajectories from the experiments at different flow rates.

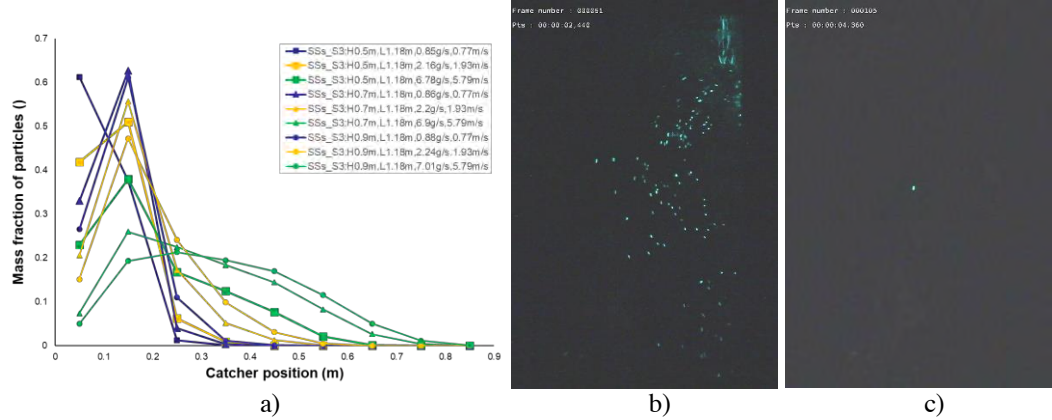


Figure 3-69: Mass fraction of particles collected in catchers (a) and glowing particles' (b) simultaneous release; (c) single particle release.

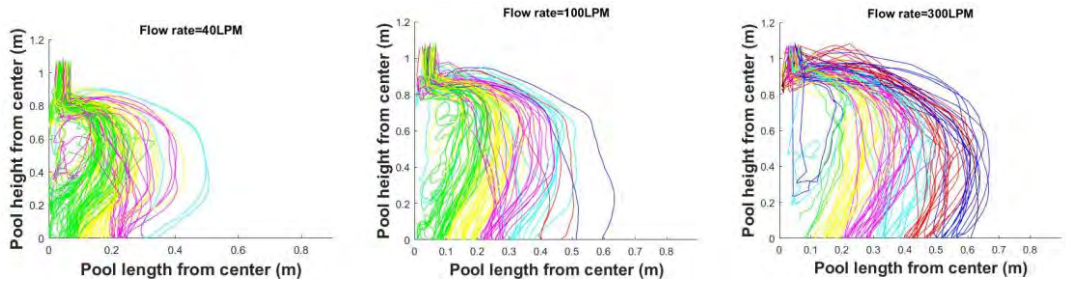


Figure 3-70: Particles trajectories

The colors of the trajectories are according to the catchers where particles settle. The particles can levitate near the central region with strong upward flow. At 40 LPM, more closed loop trajectories are seen near the center. At higher flow rates, the center region is having lesser loop trajectories and more particles spread away from it. Distribution of settled particles was compared with the earlier data with non-painted (SS) particles. Also additional experiments are carried out with large amount of painted particles (around 1.9 kg). Comparison of the particles distribution between largescale painted and non-painted particles showed [57] that for higher pool depths with smaller flow rates the effect of density is small but noticeable. For the same pool depth but higher flow rates, the density effect becomes less significant.

#### DECOSIM validation

DECOSIM simulations are carried out using the similar conditions and the results are compared with PDS-P data. Figure 3-71 shows the comparison for two different pool depths and flow rates. In most of the cases, DECOSIM slightly underestimates the particles spreading as compared to the experimental results. The trajectories are smoother in DECOSIM. The particles are pushed towards the center by the opposite side of flow circulation in simulations, once they cross half of the length of the pool. There are catchers at the bottom in experimental setup whereas there is a smooth bottom floor modeled in DECOSIM, which might affect the flow and particle spreading. Hence, it becomes important to compare the flow structure for the code validation.

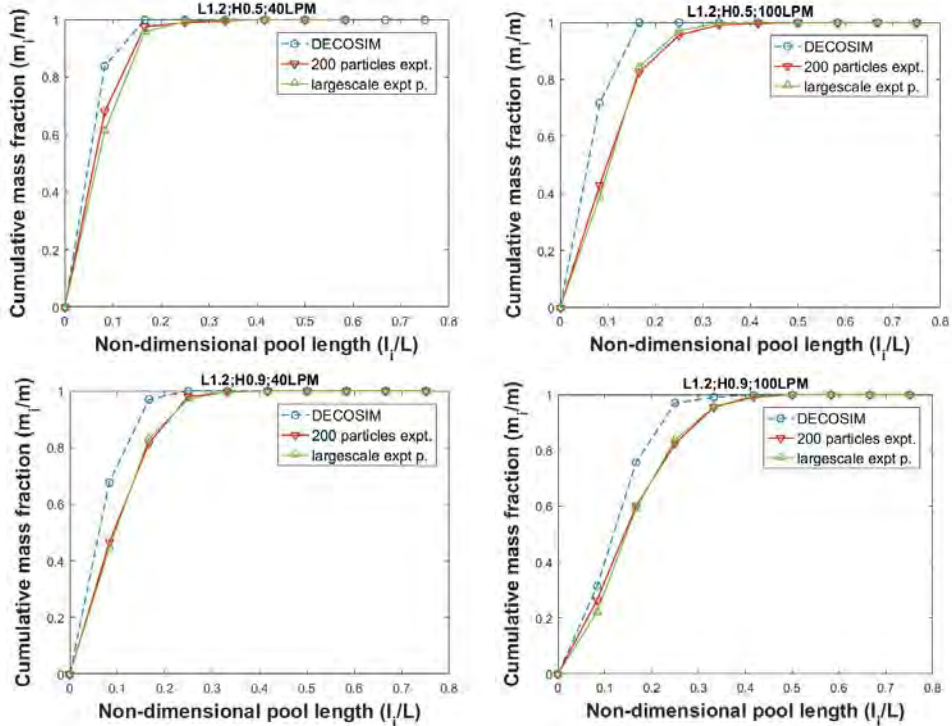


Figure 3-71: Comparison of DECOsim results with PDS-P experimental data.

### Summary

Initially on the particle debris spreading in pool (PDS-P) experimental facility, two-phase flow experiments are carried out, where the void fraction calculation is done and the correlation is derived as a function of pool dimensions and air flow rate. It was followed by three-phase flow studies, where solid standard shape particles are poured into the largescale two-phase flow and the particle spreading is investigated. As a next step, modification was done in the facility where the box air injection system is replaced by a point injection system. It is done for the spatial resolution of the initial catcher. Further in the studies, the unique particle tracking technique was implemented to plot the particles trajectories and generate the validation data for DECOsim code. Using this technique, further resolution of the particles distribution is carried out.

### Debris Bed Formation and Coolability Surrogate Models

Full model (DECOsim) simulation results were used as the basis for development of computationally efficient surrogate models for debris bed formation and coolability [104]. In the case of gradual melt release into a deep pool of saturated water the interaction of falling particles with the flow results in spreading of melt over the pool basemat, the smaller the particles and higher the decay heat power, the more effective is the spreading. In order to estimate the efficiency of particle spreading, a simple empirical model can be developed which generalizes the results of simulations [115]. Consider a droplet of diameter  $d_p$  falling in the water pool of depth  $H_p$ . A non-dimensional parameter  $\chi$  was introduced

$$\tan \phi = f(\chi), \quad \chi = \frac{\Delta H_{ev} \rho_g}{\rho_p (1 - \varepsilon) W H_p} \left( \frac{4 g d_p}{3 C_d} \frac{\rho_p - \rho_l}{\rho_l} \right)^{1/2} \quad \text{where droplet of diameter}$$

$d_p$  falling in the water pool of depth  $H_p$  drag coefficient  $C_d$  is a function of particle

Reynolds number, the vapor density must be evaluated at the pressure near the pool bottom, i.e., with the hydrostatic head taken into account:  $\rho_g = \rho_g(P_{sys} + \rho_l g H_p)$ , with  $P_{sys}$  being the system pressure in the gas space above the pool level. For each simulation [115], the final shape of debris bed was processed, and the characteristic tangent of slope angle determined. The solid line shows the best fit to the data. By the horizontal dashed line, the tangent of typical avalanche angle  $\theta_{rep}^0 = 35^\circ$  is plotted. Approximation (Figure 3-72), shows that for prototypic conditions particle spreading in the saturated pool is an effective mechanism for reducing the height of debris bed. The decay heat power can be expected to be in the range 100–150 W/kg. The largest mean particle diameter, can be expected in the range of 1–5 mm. The largest slope angle expected can be about 8 degrees, reached for the largest particle diameter and lowest decay heat power. Smaller particles are distributed almost evenly over the pool basemat.

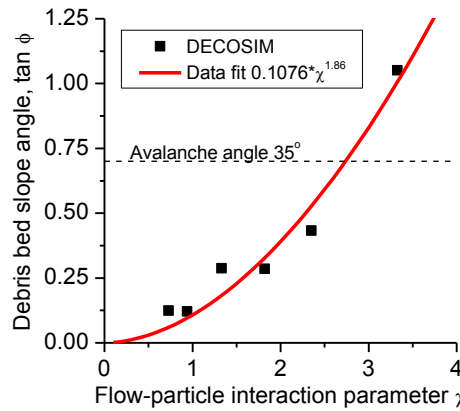


Figure 3-72: Slope angle for gradually formation bed in saturated water pool.

If the pool is subcooled it remains single-phase above the debris bed for a substantial period. Simulations of debris bed formation in a subcooled pool performed in [106] showed that temperature differences arising in the pool cause some natural circulation, but it is much weaker than that in a saturated pool and, therefore, the shape of debris bed at the initial stage is governed by particle avalanching only. However, gradual increase in the pool temperature due to latent and fusion heat transferred from hot melt particles, as well as decay heat released in corium results in boil-up of the pool after some delay time. The boil-up starts at the top layer of the pool where hot water plume from the debris bed reaches saturation conditions, while the rest of the pool remains subcooled. After the onset of boiling, intensive convection starts in the pool, so that the remaining part of melt interacts with the circulatory flow in the pool and is dispersed efficiently over the pool basemat. Thus the debris bed grows upwards mainly at the pre-boiling stage, while afterwards it mostly grows laterally, with the particle sedimentation flux distributed evenly over the pool bottom. This simple scheme can be used to set up the intermediate or final shape of the debris bed.

The time to boil-up of a pool having initial subcooling  $\Delta T_w^0 = T_{sat}^0 - T_w^0$  ( $T_{sat}^0$  is the saturation temperature at the pool pressure,  $T_w^0$  is the initial water temperature) can be evaluated from a simple energy balance model offered in [106] and confirmed by numerical simulations at different subcoolings.

### Surrogate model for post-dryout debris bed behavior

The numerical results obtained by DECOsim indicate that in the cases where dryout occurs in the debris bed: dryout zone is located in the top part of the debris bed; vapor flows through the dry zone vertically upwards; temperatures of solid particles and vapor increase in the vertical direction almost linearly, the difference between them being few degrees; maximum temperatures of solid particles and vapor are attained in the top part of the dry zone; vapor cooling is capable of stabilizing the solid material temperature, provided that its flowrate through the dry zone is sufficient.

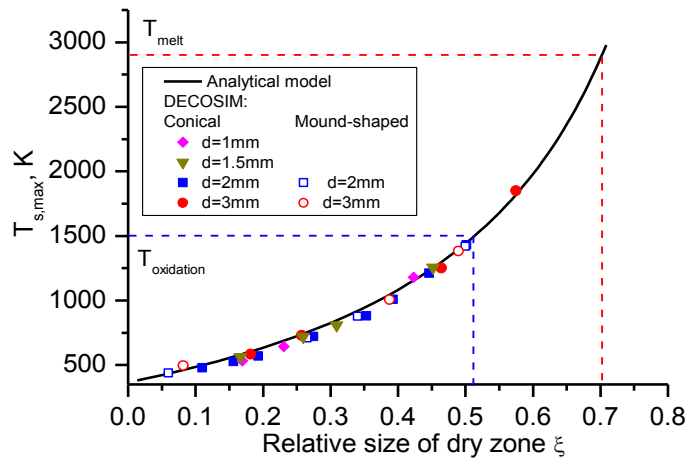


Figure 3-73: Maximum particle temperature vs relative size of dry zone.

These observations allowed an analytical model for the maximum temperature in the dry zone to be developed, laying the basis for post-dryout debris bed surrogate model [107]. The model was confirmed by further numerical simulations carried out by DECOsim. In Figure 3-73, the maximum temperature of solid particles in the dry zone,  $T_{s,\max}$ , is presented as a function of relative size of the dry zone with respect to debris bed height,  $\xi$ . The solid line corresponds to the analytical formula [107]

$$T_{s,\max} = T_{\text{sat}} + \frac{\Lambda}{C_p} \frac{\xi}{1-\xi} \quad \Lambda \text{ is the heat of evaporation, } C_p \text{ is the heat capacity of vapor.}$$

In order to apply the above formula in a surrogate model, it is necessary to define the relative size of dry zone  $\xi$  as a function of other problem parameters. DECOsim simulations on post-dryout debris beds were processed in order to obtain a unified relationship for the dry zone size. It was shown that linear dependence exists between the dry zone size and the overheating parameter  $\psi = (W - W_0)/W_0$ , where  $W_0$  as the dryout decay heat power. This is illustrated in Figure 3-74 where results of DECOsim simulations are given in the “raw” form (a), as well as in the non-dimensional form (b).

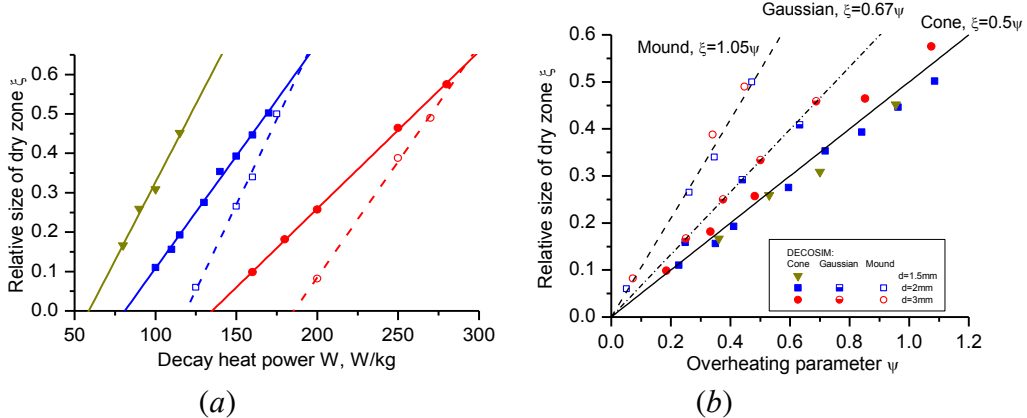


Figure 3-74: Dependence of the relative size of dry zone on decay heat power  $W$  (a) and overheating parameter  $\Psi$  (b). The legend applies to both Figures.

Thus a surrogate model for the relative size of the dry zone in a post-dryout debris bed can be developed taking into account the debris bed properties (particle size and porosity), system conditions (system pressure, pool depth), and debris bed shape (geometry, aspect ratio, etc.). The model will require a shape-dependent factor  $b(\Pi_{\text{shape}})$  for which further research is needed. Current results suggest that  $b(\Pi_{\text{shape}})$  lies in the range between 0.5 and 1.05, see Figure 3-74 (b).

#### Effect of Melt Agglomeration on Debris Bed Coolability

Numerical and experimental studies demonstrate that presence of low-permeability zones (e.g. due to agglomeration) decreases the dryout heat flux [83]. In order to evaluate the effect of melt agglomeration on the coolability of debris bed, two main cases were considered: i) an impermeable “cake”, and ii) a low-permeability zone (distributed agglomerates). Coolability of a debris bed with impermeable “cake” occupied the top  $H_c = 10$  cm of a mound-shaped debris bed with height  $H_{DB} = 2$  m was studied numerically in [108]. Cases with diameter of bed top  $D_{\text{top}}$  = 0.5, 1, 2, and 3 m are referred to as “Narrowest” (NN), “Narrow” (N), “Wide” (W), and “Widest” (WW) respectively. Vapor accumulates in a dry zone beneath the “cake”. However, vapor flow through the dry zone provides some cooling. **Figure 3-75** shows the time histories of maximum particle temperatures. Beds with smaller “cakes” and larger particles are better coolable. The temperatures can either stabilize or escalate and lead to remelting.

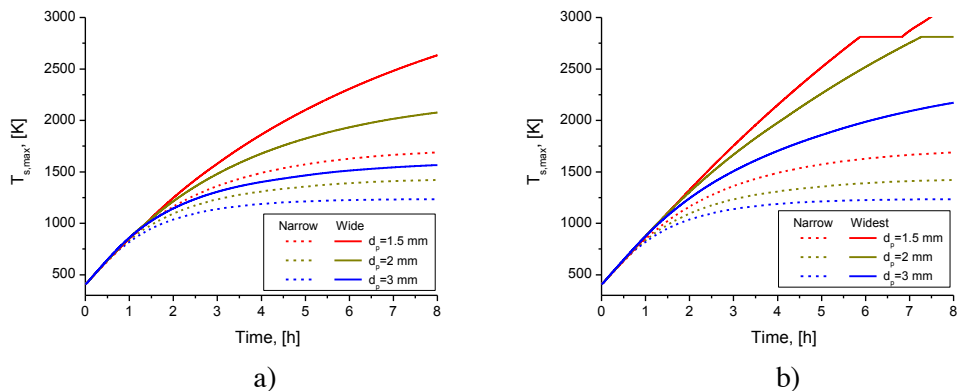
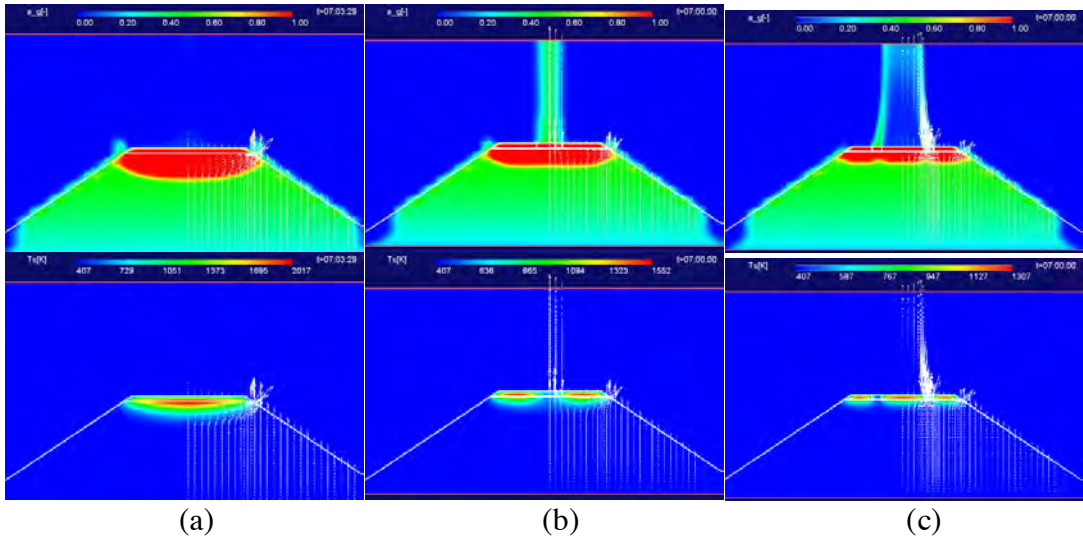
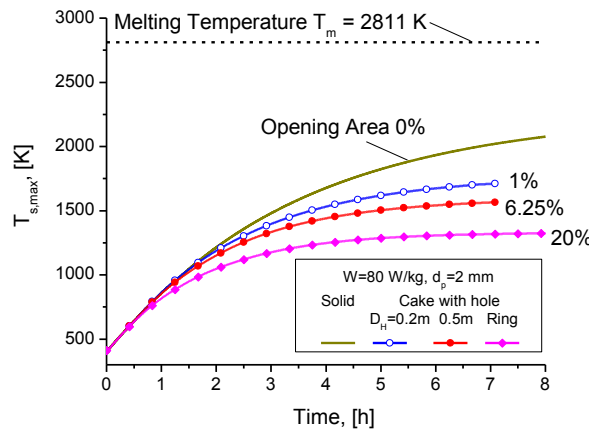


Figure 3-75: Maximum temperatures of solid material for different debris bed geometries for decay heat power  $W = 80$  W/kg.

Possible effect of vapor release through localized openings (e.g. a central hole) in the cake was studied using the same geometry as in [108]. Three cases were considered [109]: (i) a central hole, 0.2 m in diameter, which is equivalent to 1% opening area; (ii) a central hole, 0.5 m in diameter, which is equivalent to 6.25% opening area; (iii) a ring hole with the inner and outer diameters of 0.4 and 0.6 m respectively, equivalent to 20% opening by area. In **Figure 3-76**, the states of debris beds are presented at time 7 h. Time histories of the maximum temperature of solid material are shown in **Figure 3-77**. Even a small (by fraction of area) opening in the cake provides additional escape path for vapor from the dry zone. Larger opening provides better coolability, smaller vertical size of the dry zone (see Figure 3-76) and lower stabilization temperature (see Figure 3-77).



**Figure 3-76:** Void fraction (top row) and solid material temperature (bottom row) distributions at time 7 hours: (a) solid cake, (b) 0.5 m central hole, (c) ring hole. Vapor velocity is shown by arrows. Decay heat power  $W = 80$  W/kg



**Figure 3-77:** Time histories of maximum temperature of solid material for various openings in the cake.

Growth of the debris bed reduces the water pool depth above the debris bed top, so that at some point the depth of water becomes insufficient and molten particles reaching the debris bed form agglomerates. The taller the debris bed, the smaller is the effective pool depth, and the higher is the fraction of agglomerates. The vertical distribution of mass fraction of agglomerates,  $\chi_{agg}(z)$ , was determined from the surrogate model generalizing the results of numerical simulations. A relationship between

the volume-averaged properties of debris (effective porosity, permeability, decay heat etc.) and mass fraction of agglomerates was obtained in [109]. To simplify the coupling of the agglomeration model with DECOSSIM, a unified dependency was suggested. In **Figure 3-78a** the pool depth  $H_{agg}(D_J)$  at which the mass fraction of agglomerates reaches 100% is plotted (this value corresponds to the distinct kink points dividing the plateau  $\chi_{agg} = 1$  for  $H < H_{agg}$  and rapidly decreasing curve for  $H > H_{agg}$ ). In **Figure 3-78b**, the points from the decreasing parts of all curves in **Figure 3-78a** are replotted as a unified function of the reduced depth  $\zeta$  found by fitting all curves by exponential functions. The following approximations were obtained (both  $D_J$  and  $H_{agg}$  are measured in meters):

$$H_{agg}(D_J) = 131.32D_J^{0.02843} - 116.43, \quad \zeta = \frac{H - H_{agg}}{0.06H_{agg}} \quad (3-13)$$

One can see in **Figure 3-78b** that with this scaling, all points collapse to a single curve which, within 5% accuracy, can be approximated by exponential function:  $\chi_{agg} = \exp(-\zeta)$  for  $\zeta \geq 0$ , and  $\chi_{agg} = 1$  for  $\zeta < 0$ . Note that both formulas can be combined in a single one:

$$\chi_{agg} = \min(\exp(-\zeta), 1.0) \quad (3-14)$$

Equations (3-13) and (3-14) provide an easy way to evaluate the mass fraction of agglomerates for a particular pool depth and melt jet diameter. It is assumed that the mass fraction  $\chi_{agg}(\zeta(z))$  is the same at all radial positions for a given height, i.e., debris bed is stratified in horizontal layers with respect to fraction of agglomerates.

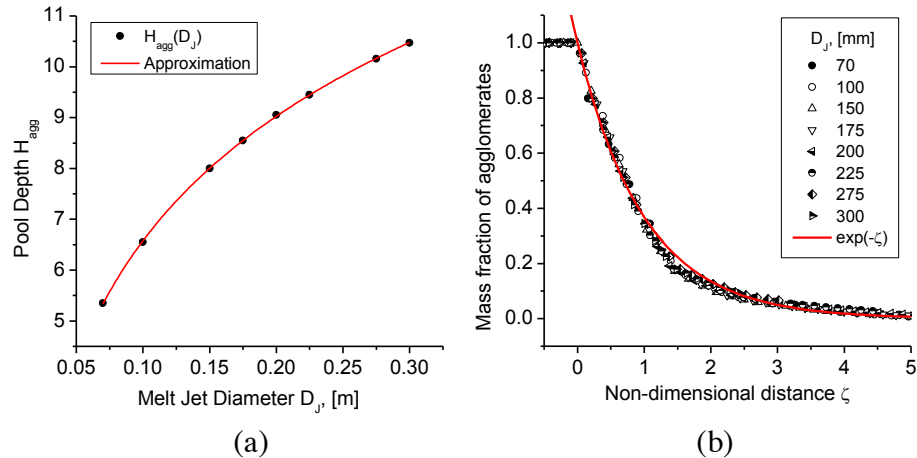


**Figure 3-78:** Generalization of melt agglomeration results: (a) pool depth corresponding to onset of 100% agglomeration; (b) dependence of mass fraction of agglomerates on the reduced vertical distance  $\zeta$ .

Using the above relationships, it is straightforward to evaluate the mass fraction of agglomerates on the debris bed top:

$$\chi_{top} = \min(\exp(-\zeta_{top}), 1.0), \quad \zeta_{top} = 16.67(\hat{H} - 1), \quad \hat{H} = \frac{H_P - H_{DB}}{H_{agg}(D_J)} \quad (3-15)$$

after which the volume fraction of agglomerates and the effective porosity can be found. Note that the transition from with very little to complete agglomeration occurs in quite a narrow range of effective pool depths [57]. Simulations for distributed fraction of agglomerates were performed for the same debris bed geometry as for partially permeable cake, see **Figure 3-76**. Note that in the absence of agglomerates selected debris beds are coolable. The cases for simulations were chosen such that the maximum agglomerate mass fraction  $\chi_{top}$  was 10%, 20%, 50%, and 90%. The effective

pool depth was assumed  $H_p - H_{DB} = 7$  m. Results are summarized in Table 3-17. Cases with dryout are marked with “Y” symbol, and the maximum temperature obtained is given. In cases where temperature stabilization did not occur only the maximum temperature at time 4 hours is shown in bold italic and eventually material remelting is expected. The time histories of the maximum temperature of solid material in all the cases where dryout occurred are plotted in Figure 3-79. The distributions of void fractions and temperatures of solid material obtained for  $W = 150$  W/kg, particle diameter  $d_p = 1.5$  mm are presented in Figure 3-80. One can see that temperature stabilization occurs when the dry zone is of small vertical size, whereas large dry zone results in temperature escalation. Significant deterioration of debris bed coolability occurs when the fraction of agglomerates on the debris bed top is above 50%, with very noticeable effect observed for 90% fraction of agglomerates. Nevertheless, the effect of these agglomerates is still weaker than the effect of completely impermeable cake, or a cake with partial openings (holes).

Table 3-17: Results of simulations for vertically distributed agglomerates.

Decay heat power $W$ , W/kg	Particle Diameter $d_p$ , mm	Melt Jet Diameter $D_J$ , cm	Mass fraction of agglomerates on top of the bed, %	Dryout	Maximum Debris Temperature $T_{s,max}$ , K
80	2	8.9–10.5	10-50	N	410
		11.2	90	Y	703
100	2	8.9–10.5	10-50	N	410
		11.2	90	Y	929
120	2	8.9–10.5	10-50	N	410
		11.2	90	Y	1172
	1.5	8.9-9.5	10-20	N	410
		10.5	50	Y	538
		11.2	90	Y	<b>1933</b>
		8.9-9.5	10-20	N	410
150	2	10.5	50	Y	453
		11.2	90	Y	<b>1907</b>
		8.9	10	N	410
	1.5	9.5	20	Y	583
		10.5	50	Y	955
		11.2	90	Y	<b>3300</b>
		8.9	10	N	410
		9.5	20	Y	583

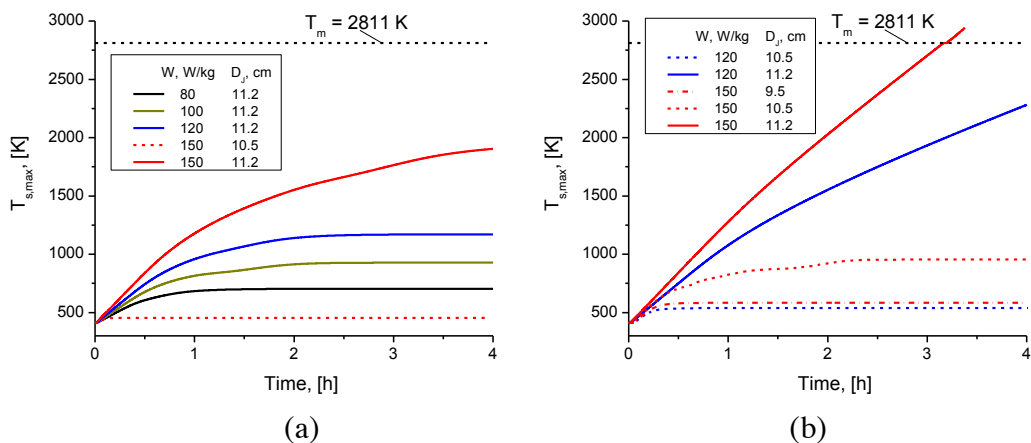
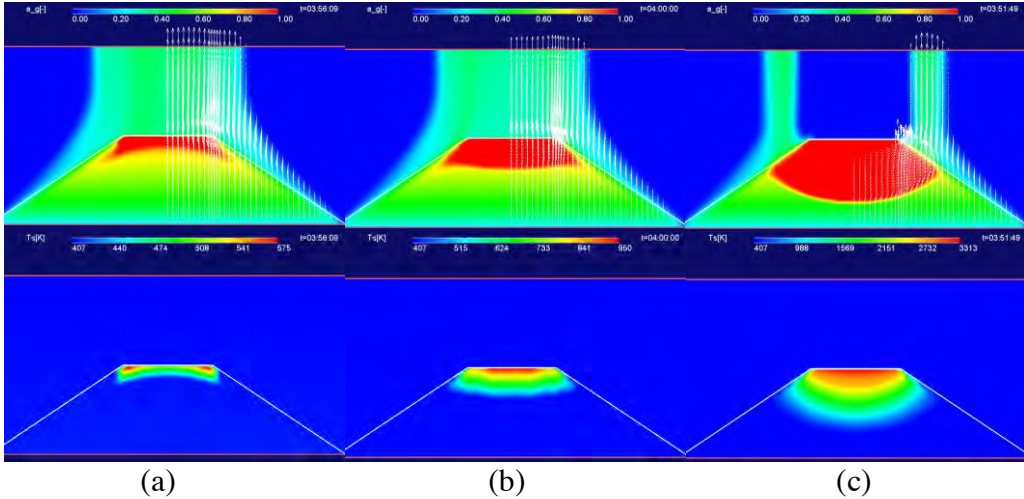


Figure 3-79: Time histories of maximum temperature in the cases where dryout occurred: particle diameter  $d_p = 2$  mm (a) and  $d_p = 1.5$  mm (b).



**Figure 3-80:** Void fraction (top row) and solid material temperature (bottom row) distributions at time 4 hours: (a)  $D_J = 9.5 \text{ cm}$ , (b)  $D_J = 10.5 \text{ cm}$ , (c)  $D_J = 11.2 \text{ cm}$ . Vapor velocity is shown by arrows.

Detailed analysis confirmed that coolability of debris bed can be deteriorated significantly in the presence of low-permeability zone (cake, distributed agglomerates). The effect of agglomerates on debris coolability becomes significant as soon as the mass fraction of agglomerates exceeds some 50% at the top of the bed. In this case, temperature escalation and remelting of material can be expected. Fraction of agglomerates in the top part of debris bed is very sensitive to melt jet diameter and pool depth.

#### Surrogate Model for Debris Bed Coolability in Presence of Agglomerates

Results of numerical simulations by DECOSSIM code can be used as a database for development of a surrogate model (SM) for debris bed coolability taking into account the presence of agglomerates and providing a link between melt ejection mode (MEM) and debris coolability (DECO).

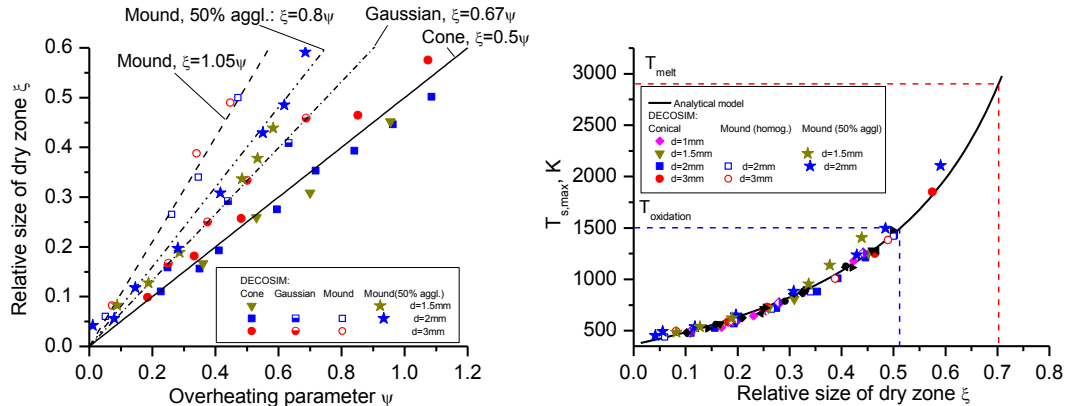


**Figure 3-81:** Relative size of dry zone vs overheating parameter (a), maximum temperature of particles as a function of dry zone size (b): stars correspond to debris bed with agglomerates, other points obtained for homogeneous bed.

The tentative surrogate model was developed by extending the approach which proved successful for homogeneous debris bed: Simulations performed for few values of decay heat power  $W$ ; Relative size of dry zone  $\xi(W)$  is determined; Extrapolation to  $\xi = 0$  gives the dryout power  $W_{DHF}$ ; Overheating parameter is determined

as  $\psi = (W - W_{DHF})/W_{DHF}$ , dependence  $\xi(\psi)$  is obtained; Maximum particle temperature is obtained as  $T_{s,max}(\xi)$ , compared with analytical model. So far, the surrogate model is based on simulations performed for 2 m-tall mound-shaped debris bed, with mass fraction of agglomerates on its top was 50%. Simulations were run until the particle temperature either stabilized, or reached the remelting temperature of corium. Results are presented in **Figure 3-81** (points obtained for homogeneous beds are also plotted). One can see that results for 50% mass fraction agglomerates can be described pretty well by the surrogate model developed for homogeneous debris bed. Further simulations are necessary to establish the applicability boundaries in terms of the fraction of agglomerates.

### 3.5.5. DECO: Summary and Outlook

Significant progress has been achieved towards the main goal of DECO, i.e. development of the debris bed formation and coolability map. DECOSIM (Debris Coolability SIMulator) code capabilities were significantly extended in order to simulate (i) debris bed coolability in subcooled pool, (ii) post-dryout coolability of the debris bed, (iii) self-levelling of the debris bed, (iv) effect of agglomeration on coolability. However, no melt pool formation model is implemented yet. Several computationally efficient surrogate models have been developed and validated against DECOSIM (full model) predictions. Namely a surrogate model (SM) for prediction of the dryout, and a model for prediction of the maximum temperature in a bed with a dry zone with and without agglomerates, a surrogate model for prediction of debris spreading in the pool.

Particulate debris spreading in the pool and self-levelling of the debris bed have been investigated both experimentally and analytically. PDS-C (closures) experimental database was generalized and a universal non-dimensional closure has been proposed for determining particle flux as a function of the local slope angle and gas velocity. Developed closure has been used in a standalone 1D code for modeling of debris bed self-levelling in plant accident conditions and also implemented in DECOSIM code. The 1D debris spreading model has been used for extensive sensitivity and uncertainty analysis. Further reduction of uncertainty in extrapolation to prototypic accident conditions requires extension of the PDS-C database to particles of different properties, morphologies and size distributions. PDS-P (pool) facility was used to provide data for model validation relevant to particle spreading in a pool. New experimental techniques have been proposed for visualization of particle trajectories. Further work is necessary for obtaining velocity fields of the coolant flow.

The surrogate model for prediction of dryout coupled with self-levelling model has been used in extensive sensitivity, uncertainty and risk analysis by evaluating the conditional dryout probabilities. Sensitivity analyses suggest that the PDFs of the effective particle diameter and porosity are the main contributors to the uncertainty in the conditional containment failure probability (CCFP) and should be prioritized for future research. Clarification of the combination of the possible initial temperatures and heat-up rates would be also beneficial. It was found that the self-leveling phenomenon reduces the effect of initial angle factor on the CCFP. Nevertheless, the development of a model to predict the initial shape of the debris bed (initial angle factor) after spreading in the pool would be useful in the scenarios where the efficacy of self-leveling is small (i.e. due to high initial temperature). Further studies on the morphology of prototypic debris particles and angle of repose are necessary as well

as new sets of PDS-C experiments with extend ranges of  $\theta_{rep}^0$  in order to extend the validity ranges of the full and surrogate models.

Analysis of post dryout debris coolability with DECOsim suggest that in all the cases with particle diameters of 3 mm, temperature stabilization occurred, while for the smallest particles (1 mm) steady temperature rise is observed at a rate proportional to specific power  $W$ . DECOsim simulations have been carried in order to investigate the effect of lateral debris bed spreading on coolability. It has been shown that (i) for 1 mm particles, debris bed remains non-coolable, temperature escalation is observed with or without particle spreading; (ii) for 1.5 mm particles temperature stabilization is observed, for spreading debris bed; (iii) for 2 mm particles, debris bed is coolable, regardless of particle spreading.

Agglomeration surrogate model has been developed and validated. The model is based on problem decomposition into a set of loosely coupled models (i.e. jet breakup, particle sedimentation, cooling and solidification, agglomeration) that can be linked together through initial and boundary conditions. Several parameters in the SM model are calibrated, using analytical assessments and data from the full model in order to take into account phenomena and dependencies, which are not modeled explicitly in the SM. Comparison of the results predicted with the full and calibrated SM suggest that SM provides acceptable accuracy obtained with about hundred times smaller computational effort. Sensitivity analysis of the model suggest that jet diameter water pool depth and initial velocity of the melt are the major contributor dot the uncertainty in prediction.

A new series of DEFOR-A experiments has been carried out with increased sizes of the jet and wider ranges of water subcooling. The data on particle size distribution, debris bed porosity and agglomeration is in good agreement with the previous DEFOR-S, DEFOR-A and FARO tests. On average, larger particles were obtained with  $ZrO_2-WO_3$  melt than with  $Bi_2O_3-WO_3$ , size distributions for both melt simulant materials are within the ranges of size distributions observed in FARO tests. The difference between particle sizes in the tests with free falling jets was found to be insignificant. There is a tendency to form slightly larger particles only in the tests with submerged nozzles where melt is released under water with initially small jet velocity. Initial jet velocity also seems to have no visible effect on the fraction of aggregated debris. Increased size jet had no significant effect on particle size distributions and fractions of agglomerates. Small-scale DEFOR experiments were carried out for clarification and confirmation of previous DEFOR-S data, analytical results hypotheses. In general, results of this experimental program are in good agreement with the previous data.

The results presented in this section demonstrate coupling of the agglomeration model developed with the model for debris bed coolability. Simple formulas are offered for the spatial distribution of mass fraction of agglomerates allowing setup of debris bed properties as functions of height for different melt jet diameters and effective pool height. Numerical simulations are carried out demonstrating the effect of low-permeability zoned in the top part of porous debris bed on its coolability, including solid cake with some openings, as well as distributed agglomerates. An approach to development of the surrogate model that can take into account the effect of debris agglomeration on the coolability has been proposed.

### 3.6 Steam Explosion Impact Map (SEIM)

Steam explosion in a deep pool is a credible threat to containment integrity potentially leading to large early release of radioactive products to the environment. Recent experiments carried out at KTH suggest that the risk of steam explosion in a relatively shallow pool might also need to be revisited [55], [56], [23]. The goal of this work is to develop ex-vessel Steam Explosion Impact Map (SEIM) framework to connect melt ejection mode with steam explosion loads on the containment structures for estimation of containment failure probability. General approach to the development of the SEIM SM is illustrated in Figure 3-82. Following tasks are addressed: (i) develop a well-posed full model (FM) taking into account melt ejection mode and pool conditions; (ii) develop a computationally efficient surrogate model (SM) for prediction of ex-vessel steam explosion impulse.

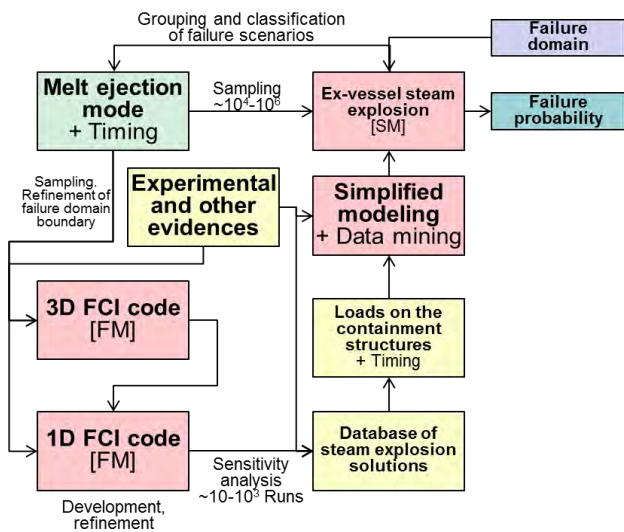
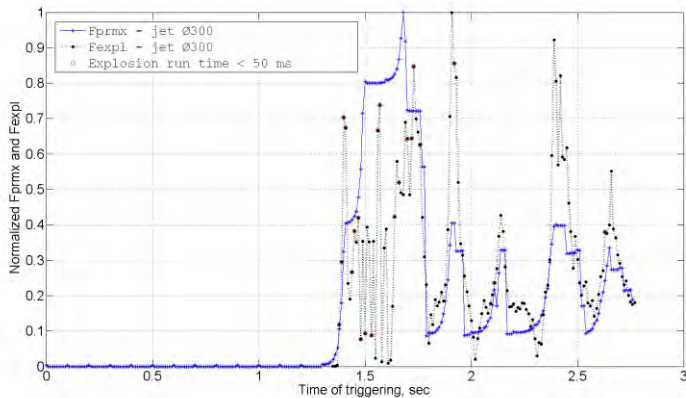


Figure 3-82: Ex-vessel steam explosion surrogate model.

#### 3.6.1. Probabilistic treatment of the triggering time

Development of the SM relies on a database of solutions generated by a 1D FCI code TEXAS-V. Texas-V is a 1D 3-field transient code with Eulerian fields for gas and liquid and a Lagrangian field for fuel particles. It is comprised of two modules for calculation of premixing and steam explosion. One of the issues for development of a well posed full model is the high sensitivity of the explosion impulse to the triggering time [20]. In [21] premixing was calculated starting from melt release till the jet front arrival to the bottom of the domain and instantaneous premixing configurations were saved with 1 ms time step; steam explosion calculations were carried out for every saved premixing configuration. The results in the Figure 3-83 indicate that *small variations in the triggering time may lead to large changes in the explosion energetics*. For example, between 1.90 and 2.01 s, i.e. within 110 ms time window, the explosion impulse changes almost 50 times from 377 kPa·s to 8 kPa·s. From the risk perspective, the choice of the triggering time can change prediction of containment failure from physically unreasonable (at ~8 kPa·s) to unavoidable (at ~377 of kPa·s).



*Figure 3-83: The dependence of normalized premixing function  $F_{\text{prmx}}$  and explosion impulse  $F_{\text{expl}}$  on the triggering time (release of oxidic corium melt with jet Ø300 mm into a 7 m deep water pool).*

Chaotic behavior of the steam explosion impulse with respect to the timing of the trigger makes the problem ill-posed. Ill-posedness is one of the main reasons for the large spread of (i) predictions with different FCI codes, and (ii) predictions with the same FCI code obtained by different users (see also discussion in [57]). In order to make model output well-posed and independent from the choice of the triggering time we introduced statistical treatment of explosion impulse. For every melt release scenario, we estimate the values of the impulses that correspond to 50, 75, 95, 99 and 100 percentiles of the impulse CDF obtained by simulating multiple explosion phases with different triggering times for a single melt release scenario.

### 3.6.2. Database of full model solutions

The database of full model simulations consists of 1500 premixing sets and 455,386 explosion calculations. The list of input parameters and respective ranges is provided in the Table 3-18. Out of about 160 TEXAS-V input parameters 23 were selected for further analysis. Ranges of parameters used in the sensitivity study were defined for typical scenario of melt release in Nordic BWR [22], [21]. Other parameters were set in accord with default values defined in the TEXAS-V manual [9]. The sensitivity study used extended Morris method [79], [8] and addressed 16 independent input parameters. Parameters were considered as independent, except for TPIN > TMELT. Halton method [27] was used for the generation of the input. Explosion calculations were performed with 4 ms time step starting from melt contact with water and till melt contact with the bottom of the water pool.

### 3.6.3. Steam explosion Surrogate Model

The surrogate model has been developed using a feedforward Artificial Neural Networks (ANNs) with Bayesian regularization and backpropagation. The ANN predicts impulses which correspond to certain percentiles of the impulse distribution for given melt release characteristics and arbitrary triggering time. The uncertainty of SM in approximation of the FM can be characterized as a difference between FM and SM predictions ( $Err_i = R_{\text{FM},i} - R_{\text{SM},i}$ ). The relative error  $2 \frac{R_{\text{FM},i} - R_{\text{SM},i}}{R_{\text{FM},i} + R_{\text{SM},i}} \cdot 100\%$  of steam explosion SM are plotted in the Figure 3-84. The SM predicts a single output value ( $R_{\text{SM},i}$ ), see Figure 3-85a. Then a distribution that quantifies the SM uncertainty in approximating the FM output for given value of SM is used, see Figure 3-85b.

Table 3-18: Ranges of input parameters used for generation of FM database

#	Parameter	Units	Range		Explanation
			min	max	
1	XPW	M	2	9	Water level
2	PO	Bar	1	4	System pressure
3	TLO	K	288	368	Water temperature
4	RPARN	m	0.035	0.25	Initial jet radius
5	CP	J/kg·K	350	650	Fuel heat capacity
6	RHOP	kg/m <sup>3</sup>	7500	8500	Fuel density
7	PHEAT	J/kg	260 000	400 000	Fuel latent heat
8	TMELT	K	1600	2800	Fuel melting point
9	TPIN	K	1620	3150	Melt superheat
10	UPIN	m/s	-8	-1	Melt release velocity
11	KFUEL	W/m·K	2	42	Fuel thermal conductivity
12	CFR	-	0.002	0.0027	Proportionality constant for the rate of fine fragmentation
13	TFRAGLIMT	ms	0.5	2.5	Fragmentation time

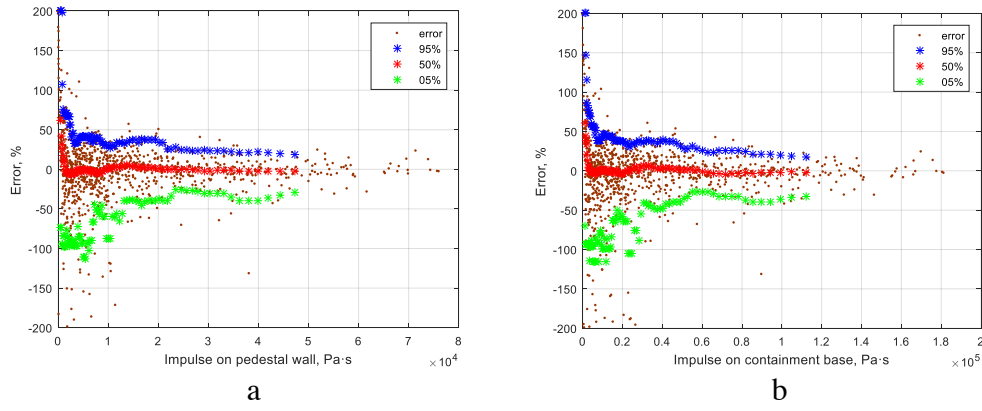


Figure 3-84: SM error distribution as a function of the SM output.

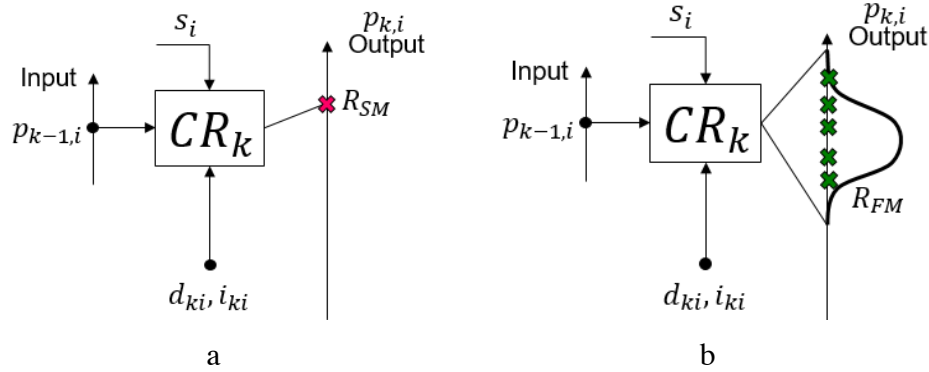


Figure 3-85: SM output without (a) and with error quantification (b).

Quantification of the error as a function of the SM output can be done by binning the SM output space (Figure 3-86a) and providing a distribution of the SM error for every bin (Figure 3-86b). Alternative approach would be to use the data on the SM error in the vicinity of predicted by SM output and construct respective CDF.

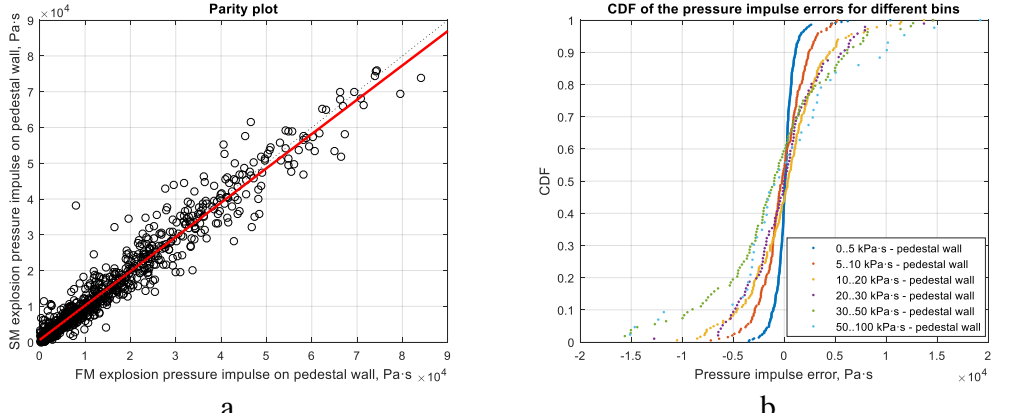


Figure 3-86: Example binning of the SM output space (a) and respective CDFs of the SM errors (b).

### 3.6.4. SM sensitivity study

The magnitude of the error in the SM approximation of the FM can be relatively high. Therefore we study the sensitivity of the SM model output to the error magnitude (introduced by parameter  $c_{err}$ ) in comparison with the other model input parameters. The results provided in the Figure 3-87 suggest that  $c_{err}$  is among the influential parameters, though it is much less important than other significant parameters such as jet diameter. The diagram also includes the model sensitivity to the enthalpy rate which is computed using the following expression  $\frac{dH}{dt} = -\pi R^2 \rho (C_p T_m + H_f) U$ , where  $R$  is initial jet radius;  $\rho$  is melt density;  $C_p$  is melt heat capacity  $T_m$  is melt temperature,  $H_f$  is melt latent heat and  $U$  is melt inlet velocity. High sensitivity of the model output to the enthalpy rate (which is a combination of SM input parameters) indicates that uncertainty in the SM output is dominated by the input parameters and SM error in approximation of the FM is not a major contributor to uncertainty.

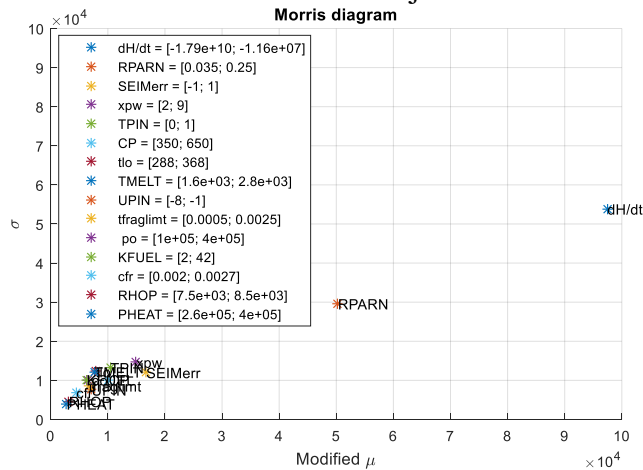


Figure 3-87: Morris diagram for 95% of the explosion pressure impulse CDF on the pedestal wall. Parameters are sorted in order of importance.

### 3.6.5. Approaches to reduction of SM uncertainty

For further reduction of the SM uncertainty approaches are currently being considered and implemented [57]: selection of optimum training methods and architecture (number of hidden layers and neurons) for single ANN and Bootstrap ANN (BANN); use ensemble average of the BANN; dimensionality reduction of SM input: BANN was shown to perform better than a single best ANN in different applications [57].

### 3.6.6. Summary and conclusions

A fast running surrogate model has been developed for the assessment of the risk of containment failure due to steam explosion. Three primary tasks have been accomplished: (i) development of the Full Model (TEXAS-V and a statistical approach to characterize the effect of triggering time on the explosion impulse), (ii) generation of the Full Model solution database (1500 premixing sets comprised of 455000 of premixing/explosion calculations), and (iii) development of the surrogate model using ANN. An approach for quantification of the SM uncertainty is proposed and implemented in the ROAAM+ framework. We found that uncertainty in the containment failure is dominated by the melt enthalpy rate and jet diameter. Failure domains (see Chapter 3.7) suggest that reinforcement of the hatch-door significantly reduces the risk of the containment failure. SM uncertainty does not affect the conclusion on the benefit of the hatch door reinforcement [57]. There are several issues that still should be addressed: Melt releases with multiple jets; Multiple consecutive steam explosions; Effect of crust formation around melt particles on the energetics of the steam explosions; Generation of non-condensable gases during premixing.

## 3.7 Results of Risk Analysis using ROAAM+ Framework

The goal of this section is to present uncertainty analysis results for clarification of (i) main contributors to the uncertainty; (ii) importance of the dependencies between different accident stages in different scenarios; (iii) the needs for further refinement of the knowledge and tools (models, experimental data, etc.). The surrogate models used in the analysis and their aims are detailed in the Table 3-19. Failure criteria are determined for SEIM and DECO frameworks. Current implementation of DECO is a combination of two surrogate models: (i) spreading of particles during sedimentation in the pool which estimates the height of the debris bed; (ii) debris bed coolability (returning actual and critical heat flux for given debris bed configuration).

Table 3-19: Surrogate models of the ROAAM+ framework.

<b>SM</b>	<b>Type</b>	<b>Aim</b>
CORE	Mapping	Given timings of ADS and ECCS recovery provides time, composition and mass of core relocation and conditions in the lower drywall: pressure, pool temperature and depth
Vessel failure	Polynomial	Given mass and composition of the debris in the lower head computes timings of the IGT, CRGT and vessel failures and corresponding mass and composition of liquid melt available for release
Melt release	Physics based	Given timings and mode of lower head failure computes conditions of melt release, i.e. ablation of the breach, rate and duration of the release, thermal properties of the melt
SEIM	ANN	Given conditions of melt release and LDW characteristics, returns three explosion impulses and three values of containment capacity
DECO	Physics based	Given conditions of melt release and LDW characteristics, returns dryout heat flux and max debris bed heat flux

For assessment of the risk of containment failure in Swedish type BWRs we employ failure domains approach. We use second order probability analysis where uncertain distributions are also varied. As a result, a set of possible failure probability values are obtained and characterized by cumulative distribution function (CDF) of the failure probability ( $P_F$ ). Failure domains are obtained by sampling output of the SMs (by

varying deterministic and intangible parameters) in each cell of the regular mesh defined in the input parameter space. The number of “fail” and “success” cases is counted in each cell using failure criteria and normalized to provide conditional failure probability which is compared to the screening probability. The cells where fraction of conditional failure probabilities exceeding screening probability is above 95% ( $\text{CCDF } \{P_F \geq P_S\} > 0.95$ ) are grouped into a “failure domain” indicating conditions at which the mitigation strategy fails. The red domain represents the area where with 95% confidence level failure probability exceeds physically unreasonable threshold. The green domain ( $\text{CCDF } \{P_F \geq P_S\} < 0.05$ ) represent the area where SAM is successful and containment failure (due to ex-vessel steam explosion or ex-vessel debris coolability) is physically unreasonable [84] with 95% confidence level. The domains colored purple and blue represent domains of scenario space where the confidence that failure probability will exceed the screening one is  $>50\%$  and  $<50\%$  respectively.

### 3.7.1. Analysis for Steam Explosion using SEIM Surrogate Model

Three scenarios of melt release are considered: oxidic and metallic Case 01 with up to 1150 K melt superheat and Case 02 with superheat of 300 K (the same as for oxidic melt). Parameters and their ranges are provided in the Table 3-20. Estimated failure domain maps are given in the Figure 3-88. The maps were estimated taking 95% of the explosion impulse, 0.001 as the screening probability. Based on the results of the sensitivity study [57] jet radius, XPW – water pool depth, UPIN – melt jet release velocity; RPARN – Jet radius were chosen as scenario parameters for plotting failure domain maps (Figure 3-88). In case of non-reinforced hatch (fragility limit 6 kPa·s), the failure probability exceeds screening one (red domain) for most of possible combinations of scenario parameters (RPARN, XPW and UPIN). If the hatch door is reinforced (50 kPa·s) there is no risk of containment failure. Note that the jet diameter is limited to Ø300 mm in this analysis. For larger size jets, the risk of containment failure will be larger. It is instructive to note that SM error ( $c_{err} \neq 0$ ) enlarges the failure domains.

Table 3-20: Ranges of model input parameters for failure domain maps.

#	Parameter	Units	Oxicid		Metallic (Case 01/Case 02)	
Name	Meaning		min	Max	min	max
<b>Scenario parameters</b>						
RPARN	Initial jet radius	m	0.035	0.150	0.035	0.150
UPIN	Melt release velocity	m/s	-8	-1	-8	-1
XPW	Water level	m	5	9	5	9
<b>Deterministic and intangible parameters</b>						
PO	System pressure	Bar	100000	400000	100000	400000
CP	Fuel heat capacity	J/kg·K	490	650	350	490
RHOP	Fuel density	kg/m <sup>3</sup>	7900	8500	7500	7900
PHEAT	Fuel heat capacity	J/kg	300000	400000	250000	300000
TMELT	Fuel melting point	K	2800	2800	1650	1650
TPIN	Melt temperature	K	2810	3150	1660	2800 / 1966
TLO	Water temperature	K	288	368	288	368
KFUEL	Fuel thermal conductivity	W/m·K	2	6	6	32
CFR	Proportionality constant for the rate of fuel fine fragmentation	-	0.00200	0.00270	0.00200	0.00270
TFRAGLIMT	Fragmentation time	ms	0.00050	0.00250	0.00050	0.00250

Comparison of Case 01 vs Case 02 suggests that with increase of melt superheat failure domain increases. Current version of the TEXAS-V SM predicts larger failure

domain for the oxidic melt than for the metallic one (Figure 3-88). This is attributed to the higher enthalpy of oxidic melt. It is instructive to note that there is no modelling of crust formation effect on the explosion energetics in TEXAS-V, and melt emissivity was not considered in development of the current SM (it was identified as less important parameter in the preliminary sensitivity analysis [22]).

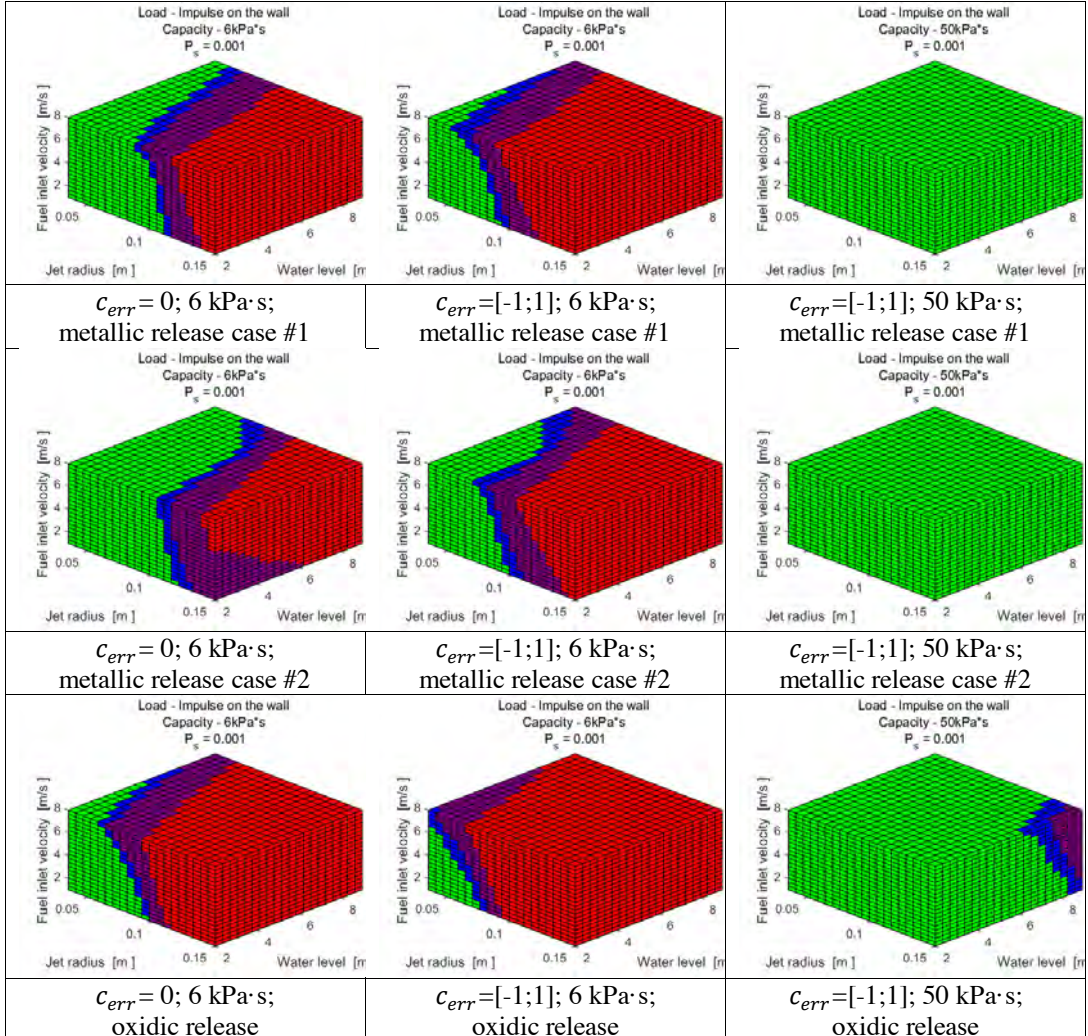


Figure 3-88: Failure domain maps for containments with reinforced and non-reinforced hatch door.

### 3.7.2. Analysis for Debris Bed Coolability

Sensitivity analysis using Morris method for Debris Bed Coolability SM has been carried out in order to identify the most important DECO SM input parameters. In Figure 3-89 results of the sensitivity analysis for DECO SM output HF-DHF (MW/m<sup>2</sup>) (the difference between heat flux and dryout heat flux) for the “Base Case” scenario and ranges (see Table 3-21) are shown. The results indicate the dominant effect of DPAR (particle diameter) and porosity together with tsub (water subcooling) on the results. Initial water subcooling affects time delay for onset of the debris bed spreading and thus height of the debris bed. Figure 3-90 presents the results of failure domain analysis for DECO SM. The figure illustrates the effect of the screening probability in the space of water subcooling and debris porosity. Note that only spreading in the pool is considered currently in this model. The results in Figure 3-90a can be

interpreted as follows: the probability of failure ( $P_f = P(\text{HF} > \text{DHF})$ ) does not exceed screening probability  $P_f \leq P_s = 10^{-3}$  only for scenarios with high debris porosity (>40%) and low water pool subcooling (<5-10 K) in more than 95% of possible combinations of distributions of uncertain input parameters. In other words, green domain in Figure 3-90a shows that “possibility” of failure is very small. The necessity of failure is assessed in Figure 3-90c. With small debris porosity (<38%) and high water subcooling (>30K) probability of failure  $P_f$  exceed  $P_s = 0.99$  in approximately 5-50% of possible combinations of the distributions of the uncertain parameters.

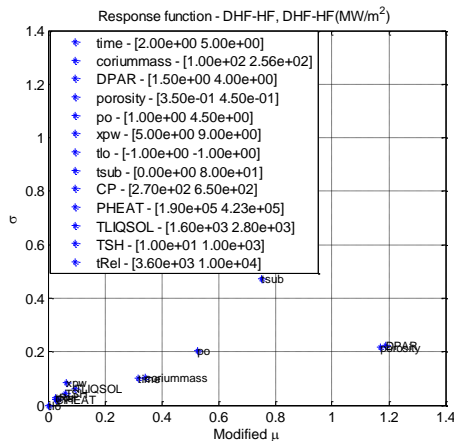


Figure 3-89: Morris diagram for Debris bed coolability input parameters.

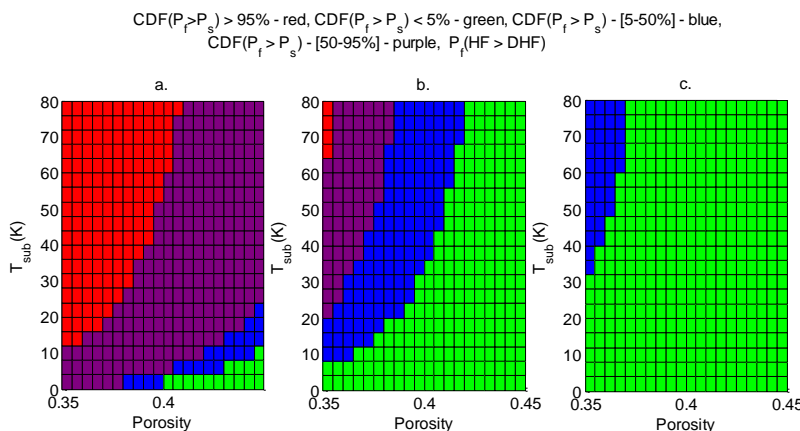


Figure 3-90: Failure domain analysis for DECO SM with different values of screening probability a)  $P_s = 10^{-3}$ ; b)  $P_s = 0.5$ ; c)  $P_s = 0.99$

Figure 3-91 presents similar results but in the space of particle size and porosity. The possibility of formation of a non-coolable debris bed is low for porosity >0.4 and effective particle size >2.5 mm (Figure 3-91a). There is high (~5-50%) necessity of failure for smaller particles and porosity Figure 3-91b,c. Better knowledge about particle size and porosity would be the most effective means for reduction of the uncertainty in coolability.

Uncertainty in water subcooling depends on the accident scenario and its ranges can be quantified through modeling of different possible sequences. The effect of water subcooling on debris bed height is an epistemic uncertainty that can be reduced through (i) further development and extensive validation of DCOSIM models against PDS-P type experiments; (ii) analysis of the accident sequences and possible ranges of water subcooling. Combining the modeling of particle spreading in the pool and particulate debris bed spreading after debris settling due to self-leveling phenomenon

might be the most effective approach to reduction of the uncertainty in the assessment of the risks associated with porous debris bed coolability. Among the other parameters only system pressure, mass of debris and time after SCRAM can noticeably affect selected failure criteria. The uncertainty in mass of debris and time after SCRAM can be reduced through improved modeling of the melt release mode in MEM. Employment of less conservative failure criteria (e.g. post dryout temperature stabilization) can further help to clarify the safety margins.

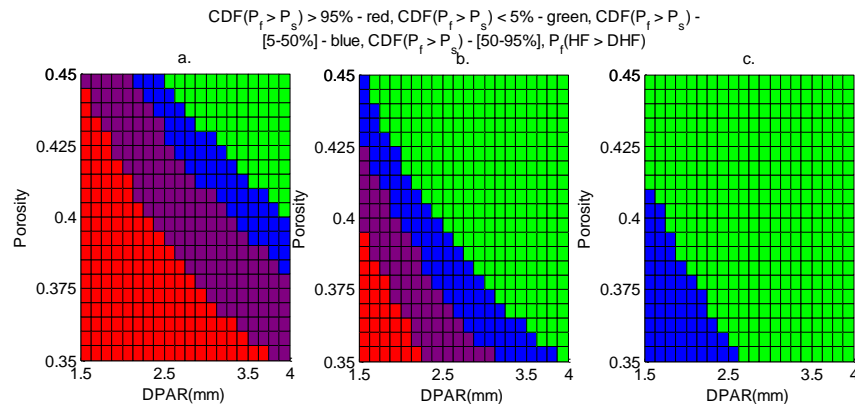


Figure 3-91: Failure domain analysis for DECO SM with different values of screening probability a)  $P_s = 10^{-3}$ ; b)  $P_s = 0.5$ ; c)  $P_s = 0.99$

Table 3-21: DECO SM ranges for the “Base Case”

Name	Description	Range	Units
Time	Time after SCRAM	[2-5]	Hours
coriummass	Debris mass in LP	[100-256]	Tons
DPAR	Particle diameter	[1.5-4]	Mm
Porosity	Debris porosity	[0.35-0.45]	-
PO	System pressure	[1-4.5]	Bar
XPW	LDW water pool depth	[5-9]	M
Tsub	Water pool subcooling	[0-80]	K
CP	Fuel heat capacity	[270-650]	J/kg·K
PHEAT	Fuel latent heat	[1.9e5-4.23e5]	J/kg
TLIQSOL	Temperature of Liquidus\Solidus	[1600-2800]	K
TSH		[10-1000]	K
tRel	Duration of melt release	[3600-10000]	sec

### 3.7.3. Reverse and Failure Domain Analysis using Combined SM on Debris Bed Coolability and Particulate Debris Spreading

The ANN-based SM of the coolability of debris bed with taking into account the effect of bed self-leveling (particulate debris spreading PDS) has been used in reverse analysis to identify the failure domains. The input parameters and their varied ranges used in both, sensitivity study and FD identification, are provided in Table 3-22. Three most influential input parameters identified from Morris diagram Figure 3-89 are: (i) Particle diameter (DPAR); (ii) Bed porosity (porosity); (iii) Initial bed heat-up rate (trat). The failure domains are shown for any two combinations of the above listed parameters: porosity-DPAR (Figure 3-93); TRAT-DPAR (Figure 3-94) and TRAT-porosity. Highly porous debris bed composed of large particles has higher probability to be coolable Figure 3-93. Comparison of Figure 3-91 and Figure 3-93 suggest that self-leveling and consideration of possible temporary dryout lead

to large “safe” domains than consideration of debris spreading in the pool and no dryout condition.

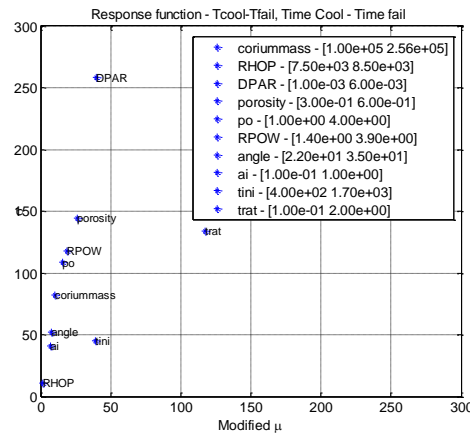


Figure 3-92: Morris diagram for coolability and self-leveling.

Table 3-22: SM ranges for the input parameters

	Name	Range	Description	Units
1	coriummass	1e5	2.5e5	Kg
2	RHOP	7500	8500	JKg/m <sup>3</sup>
3	DPAR	1e-3	6e-3	m
4	porosity	0.3	0.6	-
5	PO	1	4	bar
6	RPOW	1.4	3.9	GW
7	angle	22	35	degrees
8	ai	0.1	1.0	-
9	tini	400	1700	K
10	trat	0.1	2.0	K

CDF( $P_f > P_s$ ) > 95% - red, CDF( $P_f > P_s$ ) < 5% - green, CDF( $P_f > P_s$ ) - [5-50%] - blue, CDF( $P_f > P_s$ ) - [50-95%] - purple,  $P_f(T_{cool} > T_{fail})$

a.

b.

c.

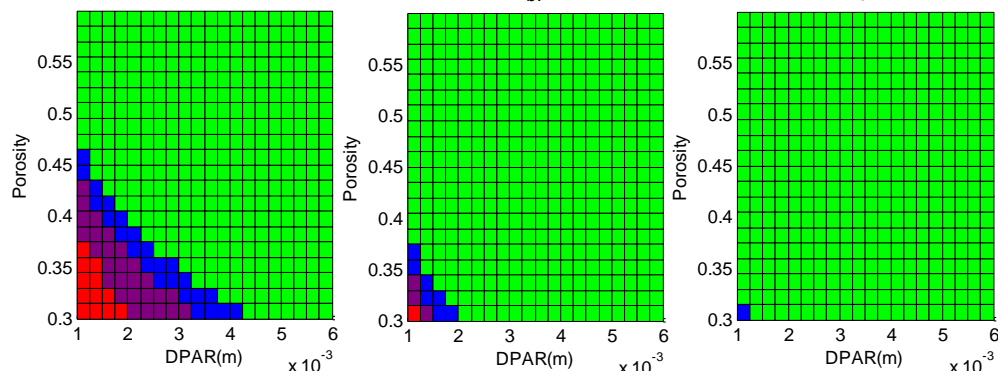


Figure 3-93: Failure domain analysis for PDS SM with different values of screening probability a)  $P_s = 10^{-3}$ ; b)  $P_s = 0.5$ ; c)  $P_s = 0.99$

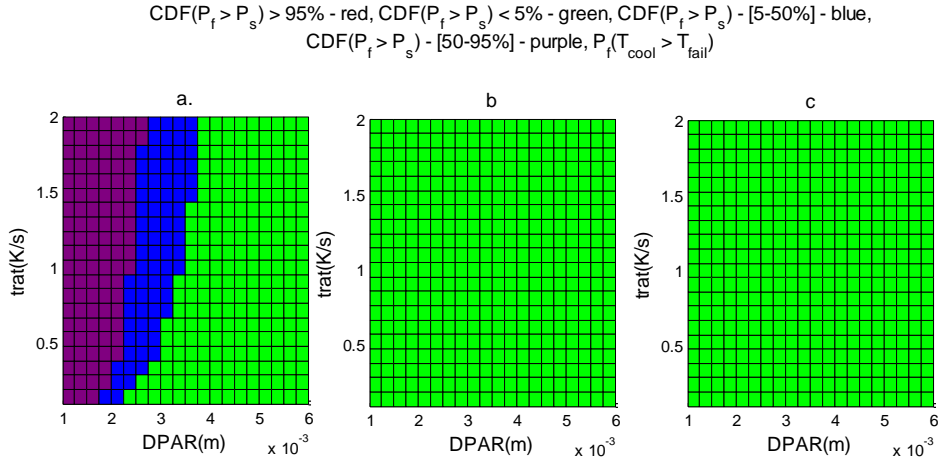


Figure 3-94: Failure domain analysis for PDS SM with different values of screening probability a)  $P_s = 10^{-3}$ ; b)  $P_s = 0.5$ ; c)  $P_s = 0.99$

### 3.7.4. Debris Agglomeration Failure Domain Analysis

Figure 3-95 show that fraction of agglomeration larger than 5-10% is practically imminent ( $P_s = 0.99$ ) in case of relatively shallow pools, large jets and large melt release velocities.

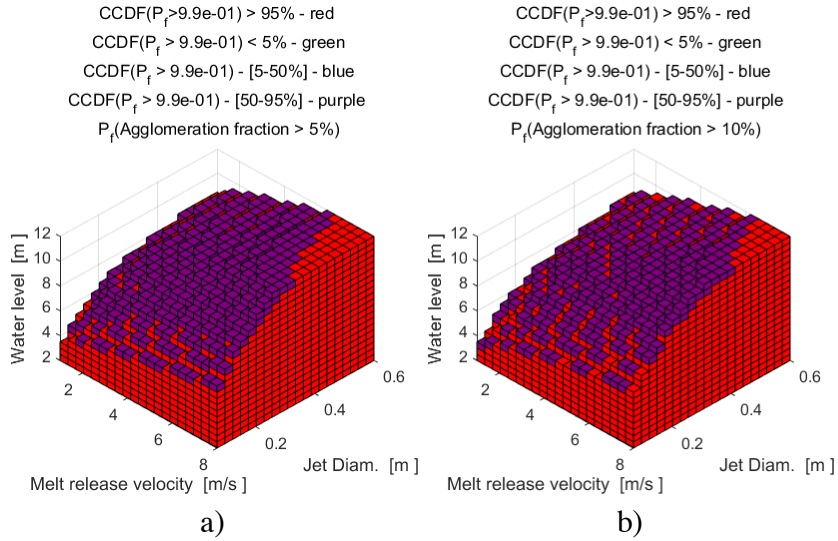


Figure 3-95: Failure domain analysis for Debris Agglomeration SM ( $P_s=0.99$ ) in terms of Jet Diameter (m), Melt release velocity(m/s) and LDW water level (m), with different values of debris agglomeration fraction threshold a) 5%; b) 10%. Only domain with  $CDF(P_f > P_s) > 50\%$  are shown.

Figure 3-96 shows failure domain for Debris Agglomeration as a function of Jet Diameter, LDW Pool Temperature and Pool depth. Current model suggest that agglomeration can be avoided only in dripping mode of melt release (very small jet, deep pool). Note that fraction of agglomeration larger than 50% leads to significant reduction of coolability. Currently debris agglomeration is the major factor that negatively affect coolability. There is some degree of conservatism in current modeling of agglomeration, especially in jet breakup length and modeling of the effect of agglomeration on coolability (see results obtained with DECODSIM). Thus possible ways to reduce the uncertainty in prediction of coolability are: (i) significant reduction of the uncertainty in the melt release; (ii) reduction of uncertainty in effect of jet breakup

on agglomeration modeling, (iii) coolability analysis for partially agglomerated debris.

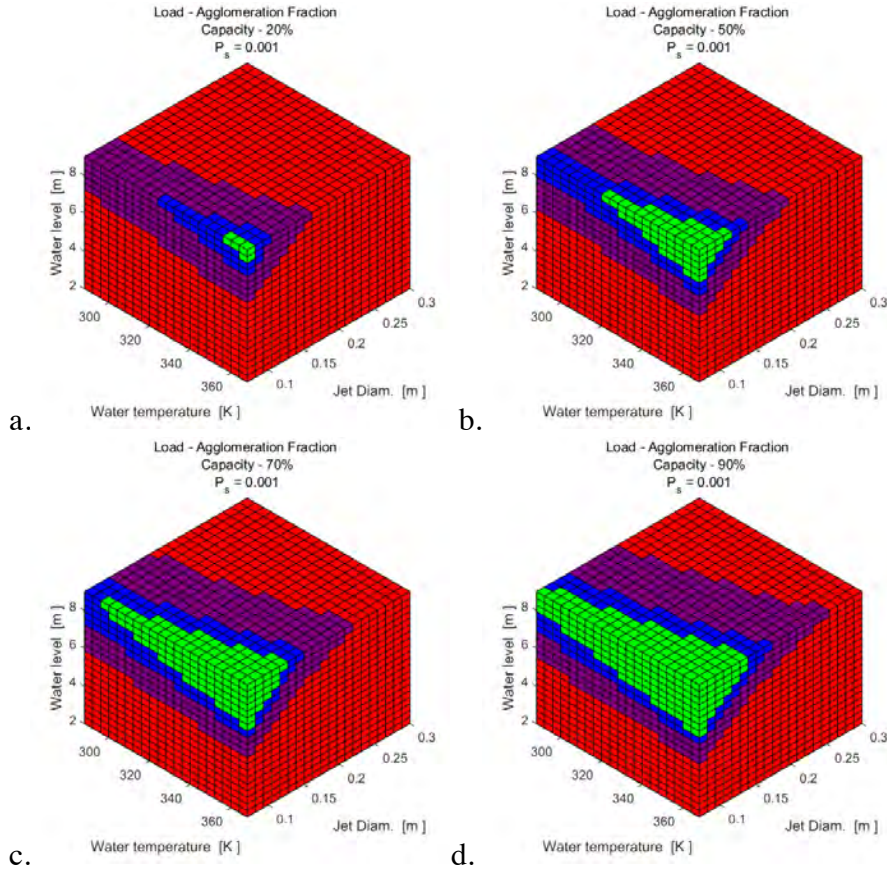


Figure 3-96: Failure domain analysis for Debris Agglomeration SM ( $P_s=0.001$ ) in terms of Jet Diameter (m), Melt release velocity(m/s) and LDW water level (m), with different values of debris agglomeration fraction threshold a) 20%; b) 50% c) 70%. d) 90%.

### 3.8 Improvements in PSA Modelling using Integration with ROAAM+.

In this section we discuss possible enhancements of PSA using ROAAM+ generated data and a feasibility study performed for a large scale PSA model in [50]. The first phase of an accident is studied in PSA L1 and the result is a number of sequences ending with either success or core damage. For those sequences ending with core damage the following accident progression is studied in PSA level 2 (L2). The link between PSA L1 and L2 is (normally around 20-40) plant damage states (PDS). For each of the PDS there is a containment event tree (CET). The events represented in a PSA Level 2 can result in containment rupture; different type of bypass; activation of filter. Current PSA models are static and grouping of sequences (failure combinations that have similar effect) as well as simplified treatment of timing of failure combinations are needed.

The enhanced information from a ROAAM+ can be used in the PSA in several ways: (i) Improved sequence definitions when phenomena can be relevant; (ii) Estimation of probabilities for phenomena; (iii) Improved knowledge of timing in sequences, which can be another base for improved realism in PSA quantification. One example is how recovery of emergency cooling system (ECCS) and ADS might help to avoid more severe consequences. A successful recovery early in the sequence would allow

the core to be arrested in the reactor pressure vessel (RPV) and hence provide the best possibility to limit the releases. The human reliability analysis regarding recovery actions is based on the available time for the operator action.

In addition to a better representation of the sequences, it is important to improve our ability to estimate the probability that a certain phenomenon with risk significant consequences can occur. When likelihoods used in ROAAM+ are translated into PSA probabilities, the arbitrary scale of probability should be applied in reverse in order to achieve the same meaning between “physically unreasonable” level in ROAAM and screening frequency in PSA. The analysis with ROAAM+ provides insights regarding under what conditions each phenomenon is relevant.

A generic PSA for Nordic BWR is used here as a reference case [50] with a function event where all the phenomena are treated in a common fault tree. The probability for steam explosion resulting in containment failure is 0.001 for low pressure melt through and 0.003 for high pressure melt through. These values are always applied even if the lower drywell (LDW) flooding system fails. The reason for this modeling is that no positive credit should be taken for system failures. Furthermore, there may be water enough for steam explosion but not enough to avoid melt through of the penetrations in the LDW floor. The probability for melt through of the penetrations in the LDW floor is: 0.001 after successful LDW flooding; 1.0 after failure of the LDW flooding system.

In this feasibility study the reference large scale PSA model is modified to consider the depth of the water pool and the mass flow of corium at vessel melt through (parameters identified in ROAAM+ among most influential). The containment event trees for the plant damage states HS2-TH1 (high pressure) and HS2-TL4 (low pressure) are modified to consider the depth of the water pool in lower drywell (LDW) and the mass flow of corium at vessel melt through. The water depth alternatives are: (i) Deep water pool in LDW; (ii) Shallow water pool in LDW; (iii) No water in LDW. The melt flow alternatives are correspond to the diameter of the melt jet:  $d_{jet} < 0.075$  m - Dripping flow;  $0.075 < d_{jet} < 0.150$  m - Medium Flow;  $d_{jet} > 0.150$  m - Large Flow. For each combination of water depth and melt flow there is a unique probability for steam explosion and not coolable debris bed in LDW. This is explicitly modeled in the CET Figure 3-97. ROAAM+ provides probability distributions for containment damage by steam explosion and coolability given a certain combination of temperature, water depth and diameter of the melt jet. For steam explosion the non-reinforced door (6 kPa\*s) fragilities are used. This gives the highest probabilities for the steam explosion damage of the containment structures. For coolability the 90 % agglomeration is used as a fragility limit, which might be an optimistic assumption. If LDW flooding fails completely the following probabilities are assumed: Steam explosion 0.0; Debris bed not coolable 1.0. At present there is no probability distribution for the different melt flow sizes so uniform distribution is used.

The probabilities for steam explosion and non-coolability is calculated as the average value of different melt flows in each size respectively, given the depth and the temperature described above. This results in the following probabilities for steam explosion and non coolable debris bed in LDW:

Containment failure by:	Steam explosion	No-coolable debris
Deep pool, dripping flow	0	3.61E-02
Deep pool, medium flow	1.55E-02	2.83E-01
Deep pool, large flow	6.36E-01	8.52E-01
Shallow pool, dripping flow	0	1.0
Shallow pool, medium flow	3.60E-04	1.0
Shallow pool, large flow	3.78E-01	1.0

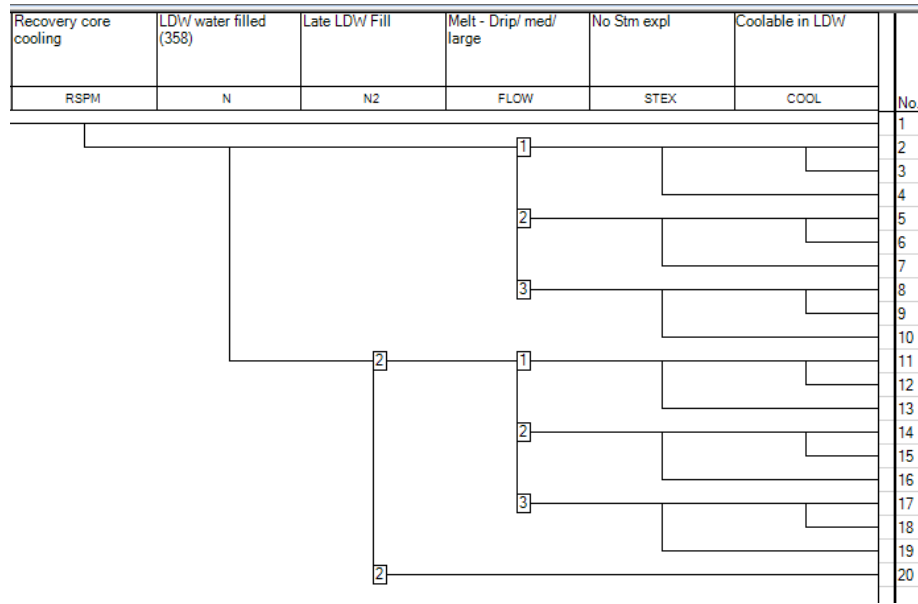


Figure 3-97: Containment Event Tree with explicit modeling of steam explosion and coolability [50].

In the PSA model it is not the average values that are given, instead the distributions of the containment damage probabilities obtained by the uncertainty analysis in ROAAM+ for each of the phenomenon are used. A non-standard interface, allowing use of externally developed simulation data, is used in RiskSpectrum to enable the uncertainty distribution for the phenomena to be consistently treated.

All transients and CCIs leading to the plant damage states HS2-TH1 and HS2-TL4 are analyzed for all analyzed Level 2 release categories. Release categories leading to release frequencies over 0.1% of the core inventory of an 1800 MW BWR are grouped as non-acceptable. The normalized result for non-acceptable release per type of initiating event is shown in Figure 3-98 and Table 3-23. The result for Loss of offsite power and non-acceptable release is set to 1.0 for the reference case and all the other results are divided by the same scaling factor.

The analysis shows that the non-acceptable release frequency is doubled in the enhanced model. The release frequency related to the release category “*Penetration of the LDW floor (basemat melt through)*” is shown in Table 3-24. The frequency approximately increases with a factor of 42 due to the increased probability for non-coolable debris bed. Note that basemat melt through is not grouped as a non-acceptable release. If this release category would be included the frequency for non-acceptable release would increase much more.

The release frequency related to the release category “*Containment failure due to phenomena (always early and no DW spray is credited)*” is shown in Table 3-25. The frequency approximately increases with a factor of 4 due to the increased probability for steam explosion. The release frequency related to the release category “*Filtered*

*release, Early opening, No DW spray*" decreases to 50 % of the reference case. The release frequency related to the remaining release categories changes only slightly between the reference model and the enhanced model.

The results of the uncertainty analysis for non-acceptable release is shown in Table 3-26. The results show that the uncertainty ranges from roughly half the point estimate frequency up to about 1.5 of the point estimate frequency. This is a reasonably narrow interval, which is positive – as the uncertainty is an important factor in PSA-L2. It could be relevant to further study the cases where the uncertainty range is greater – to understand if the uncertainty can be reduced.

Table

3-24

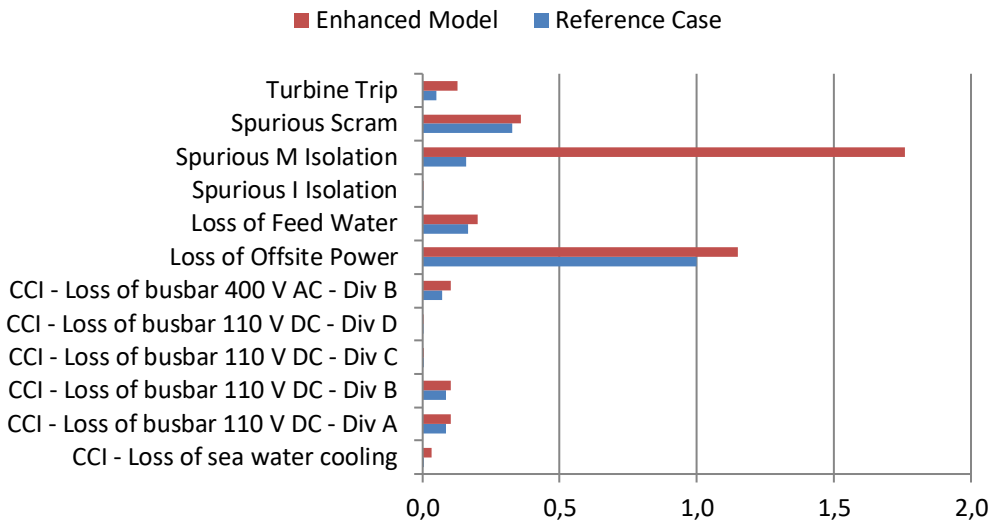


Figure 3-98: Comparison between the reference case and the modified model for non-acceptable release (normalized) [50].

Table 3-23: Comparison between the reference case and the modified model for non-acceptable release (normalized) [50]

Initiating event	Reference Case	Enhanced Model	Difference
CCI - Loss of sea water cooling	5,0E-03	3,2E-02	541%
CCI - Loss of busbar 110 V DC - Div A	8,7E-02	1,0E-01	19%
CCI - Loss of busbar 110 V DC - Div B	8,5E-02	1,0E-01	18%
CCI - Loss of busbar 110 V DC - Div C	4,7E-03	4,7E-03	0%
CCI - Loss of busbar 110 V DC - Div D	1,4E-03	1,2E-03	-16%
CCI - Loss of busbar 400 V AC - Div B	7,0E-02	1,0E-01	47%
Loss of Offsite Power	1,0E+00	1,2E+00	15%
Loss of Feed Water	1,7E-01	2,0E-01	21%
Spurious I Isolation	7,9E-04	1,7E-03	118%
Spurious M Isolation	1,6E-01	1,8E+00	1014%
Spurious Scram	3,3E-01	3,6E-01	9%
Turbine Trip	4,9E-02	1,3E-01	158%
<b>Total result</b>	<b>2,0E+00</b>	<b>3,9E+00</b>	<b>102%</b>

The results of the uncertainty analysis for non-acceptable release is shown in Table 3-26. The results show that the uncertainty ranges from roughly half the point estimate frequency up to about 1.5 of the point estimate frequency. This is a reasonably narrow interval, which is positive – as the uncertainty is an important factor in PSA-L2.

L2. It could be relevant to further study the cases where the uncertainty range is greater – to understand if the uncertainty can be reduced.

Table 3-24: Comparison between the reference case and the modified model for basemat melt through (normalized) [50]

<b>Initiating event</b>	<b>Reference Case</b>	<b>Enhanced Model</b>	<b>Difference</b>
CCI - Loss of sea water cooling		2,6E-02	
CCI - Loss of busbar 110 V DC - Div A	2,6E-03	1,7E-02	540%
CCI - Loss of busbar 110 V DC - Div B		1,5E-02	
CCI - Loss of busbar 110 V DC - Div C	2,7E-03	2,2E-03	-18%
CCI - Loss of busbar 110 V DC - Div D			
CCI - Loss of busbar 400 V AC - Div B		3,0E-02	
Loss of Offsite Power		1,4E-01	
Loss of Feed Water	7,0E-05	2,4E-02	33661%
Spurious I Isolation	7,0E-05	6,8E-04	874%
Spurious M Isolation	3,0E-02	1,6E+00	5256%
Spurious Scram	5,5E-03	4,2E-02	656%
Turbine Trip	5,3E-03	8,4E-02	1489%
<b>Total result</b>	<b>4,6E-02</b>	<b>2,0E+00</b>	<b>4179%</b>

Table 3-25: Comparison between the reference case and the modified model for containment failure due to phenomena (normalized) [50]

<b>Initiating event</b>	<b>Reference Case</b>	<b>Enhanced Model</b>	<b>Difference</b>
CCI - Loss of sea water cooling	4,8E-03	3,2E-02	561%
CCI - Loss of busbar 110 V DC - Div A	4,1E-03	2,1E-02	406%
CCI - Loss of busbar 110 V DC - Div B	1,8E-03	1,8E-02	873%
CCI - Loss of busbar 110 V DC - Div C	3,2E-03	3,2E-03	0%
CCI - Loss of busbar 110 V DC - Div D	2,4E-04		-100%
CCI - Loss of busbar 400 V AC - Div B	1,5E-03	3,4E-02	2240%
Loss of Offsite Power	2,7E-01	4,2E-01	56%
Loss of Feed Water	6,6E-04	3,5E-02	5180%
Spurious I Isolation	6,6E-04	1,7E-03	150%
Spurious M Isolation	1,6E-01	1,8E+00	1035%
Spurious Scram	5,6E-02	8,8E-02	56%
Turbine Trip	4,4E-02	1,2E-01	178%
<b>Total result</b>	<b>5,4E-01</b>	<b>2,5E+00</b>	<b>370%</b>

Table 3-26: Uncertainty analysis for non-acceptable release (All the median values are normalized.) [50]

<b>Initiating event</b>	<b>5%</b>	<b>median</b>	<b>95%</b>
CCI - Loss of sea water cooling	56%	100%	158%
CCI - Loss of busbar 110 V DC - Div A	91%	100%	112%
CCI - Loss of busbar 110 V DC - Div B	91%	100%	112%
CCI - Loss of busbar 110 V DC - Div C	95%	100%	107%
CCI - Loss of busbar 110 V DC - Div D	100%	100%	100%
CCI - Loss of busbar 400 V AC - Div B	84%	100%	123%
Loss of Offsite Power	93%	100%	109%
Loss of Feed Water	91%	100%	112%
Spurious I Isolation	58%	100%	163%
Spurious M Isolation	54%	100%	161%
Spurious Scram	95%	100%	107%
Turbine Trip	66%	100%	147%

There is a number of assumptions and limitations in the implementation in the enhanced PSA model that influence the result and are discussed in [50], [57]. There is

a need to make the feasibility study more realistic regarding some of the related parameters discussed in [50], [57]. The quantitative results should therefore be seen as indicative.

### **3.9 Summary of the ROAAM+ Development and Risk Analysis Results**

This report presents research results of APRI-9 project, namely development of risk oriented accident analysis frameworks for quantifying conditional threats to containment integrity for a reference plant design of Nordic type BWRs. Further extension of the Risk Oriented Accident Analysis Methodology (ROAAM+) has been proposed and implemented in order to address the challenges presented by the Nordic BWR severe accident management strategy, namely, the importance of uncertainty in both scenarios and phenomena and the complex multistage accident progression.

The key element of ROAAM+ is a two-level coarse-fine adaptive iterative refinement process of the development of risk assessment framework and necessary knowledge. The top level of the risk assessment framework is based on computationally efficient surrogate models (SMs) that can be used for extensive sensitivity and uncertainty analysis in order to guide identification of the main sources of uncertainty, failure domains in the space of uncertain scenarios and modeling parameters, and ultimate risk assessment. The bottom layer of the framework consists of detailed computationally expensive full models (FMs) and databases of their solutions as well as experimental data and evidences, which are used in the development of the SMs.

In this project detailed mechanistic full models (FM) have been further developed for deterministic analysis of steam explosion and coolability phenomena. When necessary and feasible, new experimental data was produced in order to create new models or reduce uncertainty in existing models. Databases of the full model solutions were obtained. A set of computationally efficient surrogate models (SM) has been developed using the databases of FM solutions. The SMs were used in extensive sensitivity and uncertainty analysis implemented in the ROAAM+ framework. The reverse analysis in the ROAAM+ helped to identify failure domains in the space of the accident scenario parameters. Uncertainty in the containment failure probability has been quantified according to the state-of-the-art knowledge using the forward analysis. An approach has been developed and demonstrated for using obtained in ROAAM+ data on the failure probability for different combinations of scenario parameters in a large scale PSA model. Results of the pilot study show clear benefits for PSA improvement in more realistic understanding and modeling of the risks.

Main highlights and findings from the development of ROAAM+ methodology, full and surrogate models for different stages of the accident progression and phenomena are summarized below.

**ROAAM+ methodology:** Methodological guidelines and approaches to development of the full surrogate models, supporting experiments and risk assessment frameworks have been developed, implemented and demonstrated. Advanced methods for quantification of uncertainty in the assessment of the overall failure probability and identification of failure domains in the space of scenario parameters have been proven crucial for adequate representation of uncertainty. A framework has been implemented as a set of customizable tools and interfaces using MATLAB. Approaches to consideration of the FM and SM uncertainty in the risk assessment have been implemented. Connection of the ROAAM+ data to different decision making approaches

and tools including PSA have been suggested. ROAAM+ provides a variety of techniques, including expensive sensitivity analysis, that enable identification of the major contributors to uncertainty both for risk assessment and for guiding research programs that aim to reduce the uncertainty in assessment of effectiveness of a severe accident management strategy. Extensive analysis for quantification of risks of steam explosion and formation of non-coolable debris has been carried out. It has been shown that the major source of uncertainty is the melt release conditions. Results suggest that the failure of containment due to steam explosion or formation of non-coolable debris can be considered as physically unreasonable only if the melt is released in a dripping mode by a small size (<100 mm) jet. It has been also demonstrated that system resilience with respect to steam explosion threat can be significantly improved by reinforcing the weak elements of the containment (e.g. hatch doors) by increasing their fragility levels up to ~50 kPa\*s. The major negative factor for formation of non-coolable debris bed is agglomeration, which can be mitigated by decreasing melt jet size below 100 mm.

Core degradation and relocation to the lower head: Extensive study of the scenarios of core degradation and relocation to the reactor vessel lower head has been undertaken. The goals were to quantify the properties of debris in the lower head and characteristics of the vessel failure and melt release as an input to analysis of the ex-vessel accident progression. Different version of the MELCOR code (1.86, 2.1, 2.2) were employed. Sensitivity analysis suggests importance of the modeling uncertainty (between different codes that use different models and in the same code using different values for the model closure parameters). An effort to quantify the uncertainty due to modeling and scenario factors has been made and a large database of MELCOR simulations (~thousands scenarios) has been generated. Two major modes of core degradation were observed depending on the timing of recovery of the core cooling system: (i) retention of debris in the damaged core region with only small (up to ~20 tons) relocation of mostly metallic debris to the lower head; (ii) relocation of large fraction of the core (>150 tons). Significant effect due to the delay of vessel depressurization on the properties of the debris in the lower plenum was identified. Vessel failure and melt release analysis was carried out using different assumptions (e.g. about the possibility of ejection of solid/liquid debris upon vessel failure). The results suggest that neither dripping nor massive release conditions cannot be positively excluded. A possibility of release of highly superheated metallic melt (up to ~1200 K) was observed in significant fraction of scenarios. Failure of penetrations was observed on average earlier than vessel wall.

In Vessel Debris Coolability and Vessel Failure: PECM-ANSYS model provides means for coupled-thermo-mechanical analysis of debris melting and heat transfer in a melt pool, and thermal creep in the vessel wall. The model addresses specific case when debris represents a non-porous cake. A new database of simulations was obtained using a 3D slice model in PECM-ANSYS, using data on the debris properties obtained from MELCOR. An interpolation of the database lookup table was proposed as a surrogate modeling approach. The database of the FM solutions is in a qualitative agreement with the previous results that indicated importance of thermal conductivity and decay heat distribution on the location and timing of the vessel and penetration failure. In most cases, failure is observed before formation of a large superheated melt pool, for modeling of which PECM was initially developed. It is instructive to note that the ranges of possible vessel failure timing, melt mass and superheat obtained in PECM-ANSYS are considerably narrower than those obtained in

MELCOR. This can be explained by the fact that PECM currently doesn't model heterogeneous multicomponent debris remelting process (i.e. there is only one melting temperature for the debris material).

DECOSIM code was further developed in order to address in-vessel coolability phenomena in case when debris bed is porous. Extensive parametric studies suggested that it is not possible to exclude neither formation of a large melt pool (when water present in the vessel can temporary protect vessel wall and penetration, in scenarios with relatively large ( $> 2\text{mm}$ ) debris size) neither early failure of the penetrations and melt release in the dripping mode (in case when a dry hot zone is located near the vessel wall, in scenarios with relatively small size of debris  $< 1.5 \text{ mm}$ ).

**Melt release:** A set of models has been developed to study potential limiting mechanisms in the melt release, breach ablation and plugging phenomena. Importance of the multicomponent debris remelting phenomena and respective possibility of melt accumulation have been demonstrated. Domains of melt release parameter were plugging and ablation are expected have been quantified. It is demonstrated that neither plugging (leading to formation of a melt pool) nor ablation (leading to increase of the jet diameter and melt mass flow rate) cannot be positively excluded. Release of the melt in the dripping mode (without plugging or significant ablation) cannot be excluded either according to the analysis results, however the range of melt release parameters where whole core can be released in a dripping mode is relatively narrow.

**Ex-vessel debris bed formation and coolability:** A comprehensive research program has been carried out to address major phenomena that can affect formation of a non-coolable debris bed. Full (DECOSIM) and surrogate model have been developed for prediction of dryout and post-dryout debris bed behavior. Particulate debris spreading and bed self-leveling phenomena have been studied experimental and a set of analytical models have been developed and validated. It has been shown that the debris bed spreading mechanisms are quite effective in prevention of formation of a tall non-coolable debris bed. Further validation of the codes and models would be necessary in order to reduce uncertainty on predictions and extend the domain of model applicability.

Debris agglomeration is currently the major factor that can lead to formation of non-coolable debris bed. Full and surrogate models have been developed in order to quantify the phenomena of agglomeration and the impact of these phenomena on the coolability. DECOSIM model was further developed in order to adequately represent domains in the bed with variable mass fraction of agglomerated debris. The DECOSIM simulations were carried out using data on spatial distribution of agglomerates using the surrogate model for agglomeration. Results suggest that coolability can be significantly impaired when fraction of agglomerated reaches  $>20\text{--}50\%$  (depending on the particle size). This corresponds to jet diameters of  $>100 \text{ mm}$ . Further model development and validation would be necessary in order to reduce and quantify associated phenomenological uncertainty.

**Steam explosion:** A surrogate model has been developed using the database of TEXAS-V code (FM) simulations (in total 455000 cases of premixing/explosion calculations) for Nordic type BWRs. A statistical treatment for the chaotic response of the explosion impulse to small variations in the triggering time has been proposed. Most important parameters where identified using sensitivity analysis. The surrogate model was implemented using different artificial neural network (ANN) approaches. An approach for quantification of the SM uncertainty was implemented. We found

that uncertainty in the containment failure is still dominated by the enthalpy rate of the jet and jet diameter even if the SM uncertainty can be relatively large for single comparisons of SM vs FM predictions. Consideration of SM uncertainty lead to increased size of the failure domain. New approaches are currently under development for improved SM for reduced error and faster performance. For more comprehensive risk assessment there are several issues that can be addressed in the future such as melt releases with multiple jets; multiple consecutive steam explosions; effect of crust formation around melt particles on the energetics of the steam explosions; generation of non-condensable gases during premixing etc.

Pilot application of the ROAAM+ generated data for improvement of a large scale PSA model provided following insights. The feasibility study has shown an example of coupling PSA with ROAAM+. The results from the deterministic analysis are used in the PSA to improve sequence definition as well as improve the estimation of frequency of unacceptable release due to phenomena depending on the sequence. The changes in the enhanced PSA-model are limited and easy to implement.

ROAAM+ results can be used to refine and improve the PSA in several ways. The integrated approach requires improvement in scenario definition, which practically leads to larger number of plant damage states (PDS). The PDS should consider all necessary scenario parameters, that may affect the calculation of phenomena and hence consider also the system availability normally represented within containment event trees (CETs). One example is the analysis of recovery of core cooling, where ROAAM+ has provided usable information regarding the timing and possibility of core coolability (re-flooding). This information can be used as a basis material for the HRA, to re-define the binning of plant damage states as well as provide probabilities for failure of coolability.

The implementation in a large scale PSA model shows that the integration of the ROAAM+ results and the PSA model is not only feasible, but could potentially lead to a considerable change of the frequency for non-acceptable release. The results show that the parameters indicated by the ROAAM+ approach as being of high importance to the quantitative results. It also emphasizes the need to distinguish between different probabilities of phenomena depending on different scenario, physical and intangible parameters.

The approach has demonstrated that the vision, to develop the sequence from core melting, and to understand what are the important factors, is possible to meet. The integrated approach will have the ability to give a more comprehensive estimation of the uncertainty compared to the standard approach. The uncertainty related to phenomena will consider the interdependency between phenomena (all the way back to relevant intangible and physical parameters, and of course scenario parameters).

### **3.10 Infrastructure development for high-temperature melt experiments**

In order to understand the micro interactions of fuel coolant interactions (FCI) and mechanisms of steam explosion which may occur during a severe accident in light water reactors (LWR), the MISTEE test facility was developed at KTH, and a series of experiments have been successfully carried out to investigate fine fragmentation mechanism during steam explosion and also to study the jet breakup and debris formation mechanisms during FCI with low-temperature (<1500°C) simulant materials [73], [128], [129], [130], [131], [133], [134], [135]. While the use of low-temperature

simulant materials has been useful in pursuit of the physical mechanisms at well-controlled experimental conditions, it is not difficult to address the mechanisms related to high temperatures. Therefore, the objectives of this work are: (i) Improvement of the MISTEE infrastructure to work with high temperature materials ( $>2000^{\circ}\text{C}$ ); (ii) Separate effect analysis for clarification of mechanisms related to material effects and oxidation during FCI.

Various upgraded designs of the MISTEE facility (called MISTEE-HT) have been conducted for high-temperature melt preparation and molten droplet delivery. The old furnace utilized in the previous MISTEE experiments was replaced with a completely new design. A new methodology for generation of single droplets of molten materials at high temperature involves constant purge of inert gas through a hole of the crucible's bottom to aerodynamically plug the melt droplet in the crucible. The methodology resolves the complexities associated with high temperatures, corrosion, low melt mass (1~2g), controllable discharge of melt from the furnace. Various materials including high temperature melt mixtures (e.g.  $\text{CeO}_2 - \text{ZrO}_2$ :  $T_{\text{liq}}$ :  $2400^{\circ}\text{C}$ , 40:60 mol%) have been used. The MISTEE-HT facility is as shown in Figure 3-99. For a detailed description of the facility and instrumentation see [138].

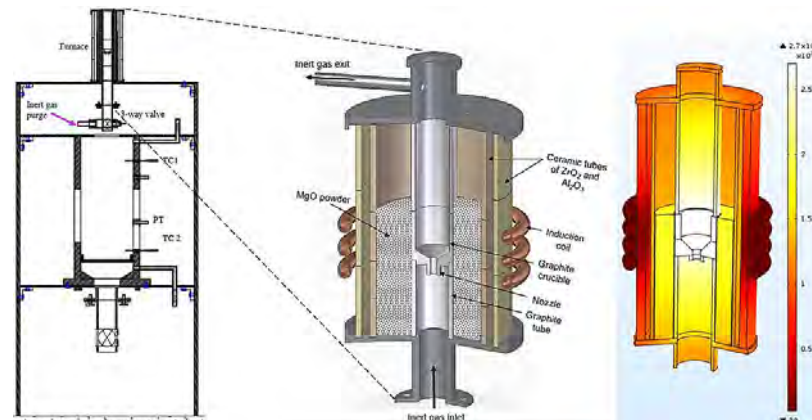


Figure 3-99: Illustration of the MISTEE-HT facility.

### 3.10.1. MISTEE-HT tests with alumina

As the first campaign of tests of single droplet steam explosion on the MISTEE-HT facility, alumina (melting point:  $2072^{\circ}\text{C}$ ) was employed as the melt material (see Table 3-27 for experimental conditions). The reason for such investigation is that in the KROTOS experiment [132] where spontaneous steam explosions were observed with alumina, giving rise to the issue of so-called “material effect” on steam explosion. The focus of the tests is on the micro triggering mechanism. The effect of water subcooling and melt superheat were studied. An example of the droplet and surrounding vapour evolution during the experiment is shown in Figure 3-100. The droplet behaviour is similar to what was observed for other materials previously studied in MISTEE (see [131]) and consistent with the observations of Nelson & Duda [136]. After meeting the pressure wave, the droplet and surrounding vapour exhibit three successive cycles of isotropic expansion and collapse. In what follows, time  $t=0$  ms corresponds to the beginning of the second cycle which is the most important and expected to be the beginning of the fine fragmentation process. The main pieces of information that include the droplet falling velocity, aspect ratio of the droplet surrounded by vapour and the equivalent bubble diameter  $D$  (Figure 3-101) are acquired by image processing. For a detailed description of the image processing technique, see [129].

Water subcooling is a crucial parameter. Steam explosions are observed after triggering for cases with high ( $\sim 80\text{K}$ ) and moderate subcooling ( $\sim 50\text{K}$ ). For the low subcooling, no steam explosion was observed, despite triggering. More vapour production is expected when the subcooling is low. The pressure wave might be not strong enough to destabilize the film and create liquid-liquid contact to start the fragmentation process. For all the exploding cases, a conversion ratio of up to 0.7% is evaluated.

Table 3-27: Experimental conditions ( $\text{Al}_2\text{O}_3$ ).

	Case type	Water temperature range	Melt temperature range	Number of tests
W1	High subcooling	16-21°C	2132-2217°C	10
W2	Moderate subcooling	45°C	2211°C	1
W3	Low subcooling	77-87°C	2071-2265°C	8
W5	High superheat	19°C	2259°C	1

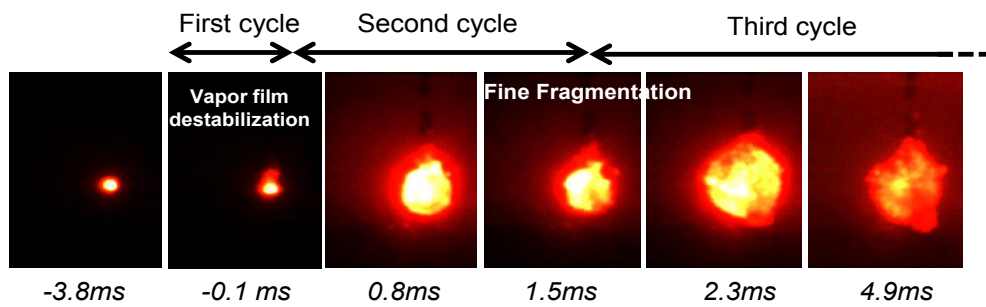


Figure 3-100: Snapshots of alumina droplet dynamics in a steam explosion ( $\Delta T_{\text{subcooling}}=82\text{K}$ ,  $T_{\text{melt}}=2217^\circ\text{C}$ ,  $\Delta T_{\text{superheat}}\approx 160\text{K}$ ).

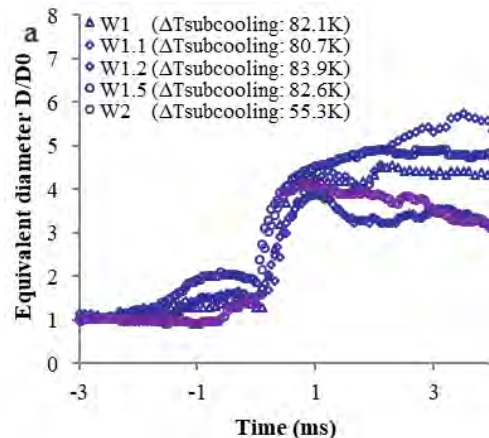


Figure 3-101: Alumina tests with high and medium water subcooling.

The mass median fragment size acquired from the alumina tests that exploded and at high subcooling conditions is between 100 and 200 $\mu\text{m}$ . Compared with the other materials previously studied in MISTEE, alumina gives the smallest fragment size. Hansson et al. [129] showed for example that for eutectic  $\text{WO}_3\text{-CaO}$ , D50 is around 0.25 mm while it is around 0.4 mm for the non-eutectic binary oxide. The reason why alumina produces smaller fragments are not clear. A spontaneous steam explosion was observed for a melt superheat of 215°C and a water temperature of 19°C. Figure 3-102 shows the visualization of the explosion given by the camera. This case confirms that alumina can exhibit spontaneous steam explosion under certain conditions. More results of MISTEE-HT tests with alumina can be found in [138].

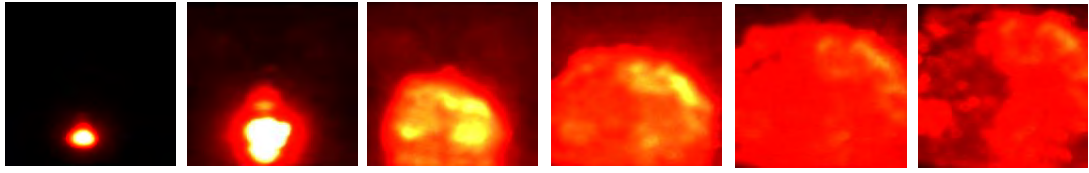


Figure 3-102: Observation of a spontaneous steam explosion with alumina melt ( $\Delta T_{subcooling} \approx 81K$ ,  $T_{melt}=2259^{\circ}C$ ,  $\Delta T_{superheat} \approx 215K$ ).

### 3.10.2. MISTEE oxidation tests

Oxidation is among the most uncertain phenomena in modelling of fuel-coolant interaction [74]. Experimental data on oxidation during FCI is rather scarce. Therefore, MISTEE-HT facility was employed to study the zirconium melt water interactions. The Zr metal can react with water, producing zirconium oxide and hydrogen gas. Experimental conditions for the series of tests conducted at the MISTEE-HT droplet facility is summarized in Table 3-28. The quenched melt droplet is captured in a debris catcher suspended inside the water pool. In the tests, interaction between the melt and water are recorded visually at high speed. Scanning Electron Microscopy (SEM) combined with Energy-Dispersive X-Ray Spectroscopy (EDS) were used to study distribution of phases and oxygen content in the solid debris.

Table 3-28: Experimental conditions (Zr).

Case type	Water subcooling range	Melt superheat range	Number of tests
High subcooling (HSUB)	85K	150K	3
Moderate subcooling (MSUB)	45K	150K	2

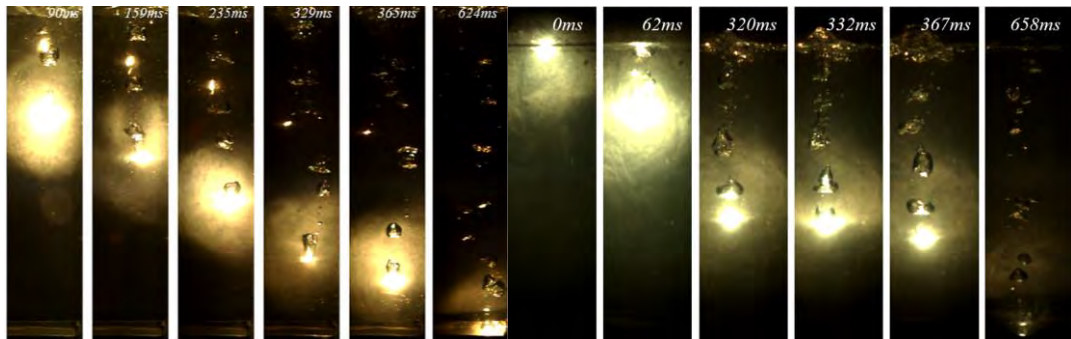
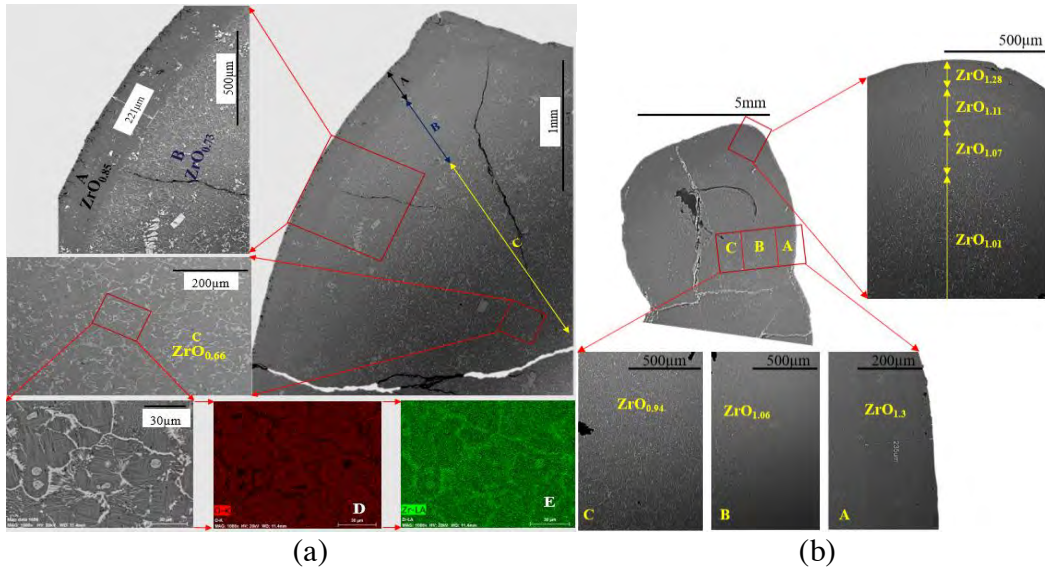


Figure 3-103: Time sequence raw snapshots depicting interaction between single droplet of zirconium melt and water at high water subcooling  $\Delta T_{sub} \approx 85K$  (above) and medium water subcooling  $\Delta T_{sub} \approx 45K$  (below).

Single droplets of molten zirconium metal quenched in water depict a pattern of repetitive bubble growth and detachment along the zirconium melt droplet rear periphery as shown in Figure 3-103. The trail of bubbles left behind the droplet trajectory do not seem to condense even under the high subcooling conditions indicating that the bubbles are mostly filled with non-condensable gas (hydrogen).



*Figure 3-104: SEM micrographs of the metal oxide interfaces developed on a pure zirconium melt droplet after quenching in water at (a) 15°C (b) 55°C showing stratified degrees of oxygen (Labels A, B and C correspond to the stratified regions with varying oxidation levels; Labels D and E show SEM and EDS mapping of the elemental species in the region near to the center of the quenched droplet where D is O map and E is Zr map).*

The SEM images that depict the interphases of the individual regions of metal and oxide of a zirconium metal melt quenched in water are shown in Figure 3-104. Interestingly, the analysis reveals layers where the oxygen content varies significantly. The outermost surface (indicated as region A) shows the highest degree of oxygen content. Further, concentric layers of varied levels of oxidation seem to have uniform thickness. Under high subcooling conditions ( $\Delta T_{sub}$ : 85K) and a nominal melt superheat ( $\Delta T_{superheat}$ : 150K), the thickness of the outermost layer with the highest degree of oxidation is approximately 220μm. The thickness of the other inner layers is however comparatively larger than the outermost layer.

Figure 3-105 shows the radial stratification of oxygen content in the sample. The oxygen content in the center of the droplet reduces by approximately 4 times the oxidation level on the outer surface following a linear trend. Figure 3-106 depicts the morphology of a quenched particle with a hollow core. Formation of pores in rapidly quenched particles can generally be related to hydrogen gas precipitation from the solidifying melt. SEM analysis of the sample shows stratification in the degree of oxidation from the external surface. Most interestingly the access to steam in the hollow pore seems to have resulted in formation of an oxygen rich layer near the pore surface. The pattern of oxidation in the pore region is almost similar to that of the oxidation of melt external layer.

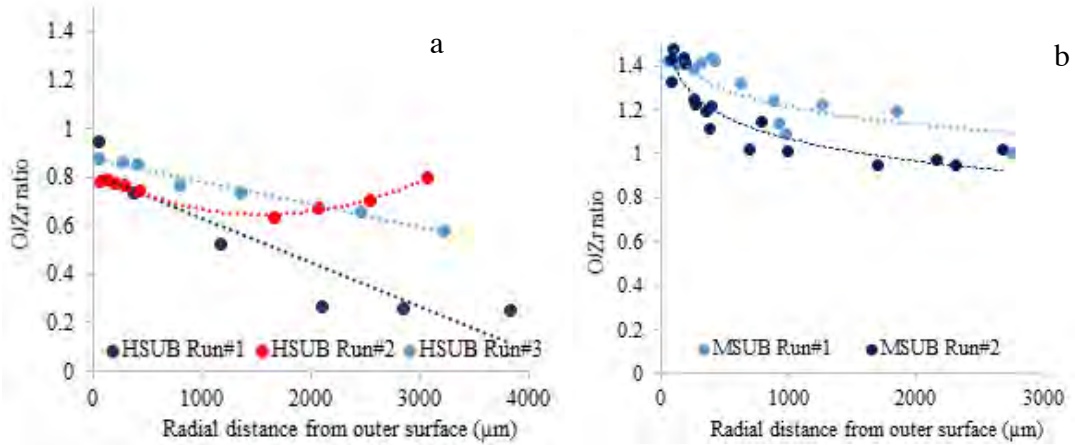


Figure 3-105: Measured O/Zr ratio in the quenched samples under a) high subcooling ( $\Delta T_{\text{sub}}=85\text{K}$ ; HSUB series), and b) medium subcooling ( $\Delta T_{\text{sub}}=45\text{K}$ ; MSUB series).

The observations show that only a limited extent of oxidation is possible under high subcooling conditions while the oxidation capacity increases drastically with decreased degree of water subcooling. A simplified rationale to the observation is the limit in vapor flow to the melt considering the combined effects of rapid solidification of the melt and rapid condensation of water vapor. Furthermore, to study the influence of oxidation on the hydrodynamic aspects of FCI and debris properties, experiments with small jets of zirconium (see Figure 3-107) have been performed. The experiments performed at a low melt superheat ( $\Delta T_{\text{superheat}}$ : 85K) has shown that the melt solidifies in the form of the jet which can be attributed to the phase change characteristic as a result of melt oxidation. However, microstructure analysis of the solidified jet is yet to be performed. In addition to the aforementioned works, several experiments at the scale of droplets and jets are still underway to attain necessary estimates and an in-depth understanding of chemical augmentation during FCI.

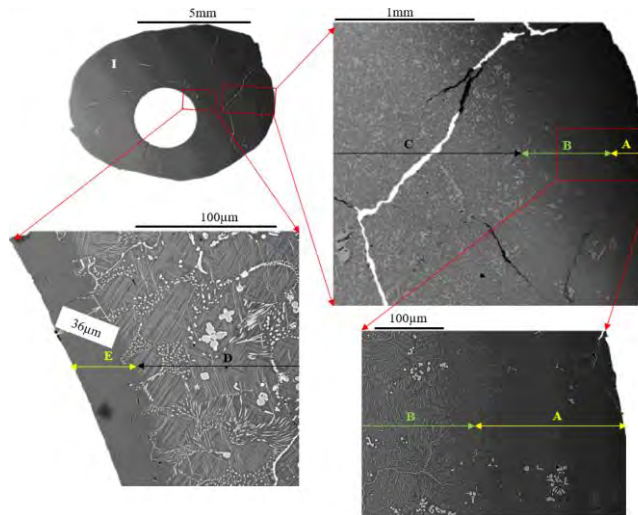


Figure 3-106: SEM micrographs of the porous solid solution showing stratified degrees of oxidation (Label I shows the morphology of the solid solution; Labels A, B, C, D and E correspond to the different regions where A is the outer surface, B, C, D are the intermediate regions and E is the pore surface).

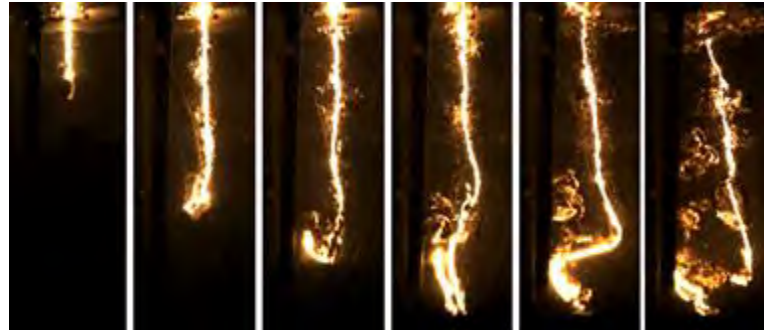


Figure 3-107: Time sequence raw snapshots depicting interaction between zirconium melt jet ( $D_{jet} \approx 5\text{mm}$ ,  $\Delta T_{superheat} \approx 85\text{K}$ ) and water ( $\Delta T_{sub} \approx 83\text{K}$ ).

### 3.10.3. MISTEE tests with CeO<sub>2</sub>-ZrO<sub>2</sub> melt

To further increase the operational temperature, the binary oxides of CeO<sub>2</sub>-ZrO<sub>2</sub> (melting temperature  $\approx 2400^\circ\text{C}$ ) was chosen to simulate corium (UO<sub>2</sub>-ZrO<sub>2</sub>), since the equilibrium phase diagram of the binary composition of CeO<sub>2</sub>-ZrO<sub>2</sub> shows similarities in structure comparative to that of UO<sub>2</sub>-ZrO<sub>2</sub>. Exploratory tests have been carried out (see Table 3-29 for experimental conditions). The tests have not resulted in spontaneous triggering of steam explosion. The observations indicate non-condensable gas release during the quench as shown in Figure 3-108. One possible explanation is that oxygen over-stoichiometry may exist with CeO<sub>2</sub>-ZrO<sub>2</sub>-vapor system, resulting in production of hydrogen during the melt-water interaction, as mentioned for corium [137]. Another hypothesis is the thermal decomposition of water at such high temperatures. Further analysis is required to verify these hypotheses.

Table 3-29: Experimental conditions (CeO<sub>2</sub>-ZrO<sub>2</sub>).

Material	Melting point $T_{liq}$ (°C)	Melt mass (g)	$\Delta T_{superheat}$ (K)	$\Delta T_{subcool}$ (K)	No: of tests
CeO <sub>2</sub> -ZrO <sub>2</sub>	$\approx 2400^\circ\text{C}$	$\approx 2$	$\pm 100$	$\approx 80$	7



Figure 3-108: Raw snapshots depicting interaction between CeO<sub>2</sub>-ZrO<sub>2</sub> ( $\Delta T_{superheat}: 100\text{K}$ ) and water ( $\Delta T_{sub} \approx 80\text{K}$ ).

### 3.10.4. MISTEE tests for steam explosion suppression

The intensity of a steam explosion is associated with the fine fragmentation of the melt that increases the melt-coolant contact surface area thereby rapid heat transfer rates and phase change of the cold liquid. The study is concerned with suppression of steam explosion, through coolant conditioning, i.e., by adding chemical additives in coolant (water) to form a solution which may mitigate steam explosion energetics. For this purpose, an experimental study is performed on the MISTEE facility for spontaneous steam explosion of a single molten droplet in a cold water pool with

different chemical additives. The chemical substances chosen in the study are salt, calcium stearate and sodium dodecyl sulphate (SDS), which are dissolved into the water pool, respectively. The solution of salt is employed to simulate seawater. The concentrations of the chemicals in the solutions are also varied to investigate their impacts on steam explosion. Preliminary results suggest that simulated sea water enhances the occurrence probability of a spontaneous steam explosion. A further in-depth analysis of the surfactant effect is under-way.

### 3.10.5. Summary of Infrastructure Development

The experimental infrastructure project is focused on the development of the MISTEE-HT facility which can be used to perform fundamental investigation on steam explosion energetics of corium simulant with high melting temperature or prototypical corium. By testing various designs through proof of concept prototypes, a new furnace has been developed with a capability to melt metallic/oxidic material whose melting point is 2200 °C and above, as well as good instrumentation and well-controlled mechanisms for melt preparation, and droplet levitation and delivery.

The unique experimental infrastructure and the team of reactor safety experts developed with APRI project support contributes to the retention and development of national expertise in analysis of severe accident phenomena and complex reactor safety issues specific to the Nordic plants. KTH participation in the international activities (EU, OECD, NKS, etc.) related to severe accident analysis brings the international efforts and knowledge to Nordic context.

## 3.11 References

- [1] Apostolakis G., Cunningham M., Lui C., Pangburn G., Reckley W., “A Proposed Risk Management Regulatory Framework,” U.S. Nuclear Regulatory Commission, NUREG-2150, Washington, DC, April 2012.
- [2] Basso S., Konovalenko A. and Kudinov P., “Development of scalable empirical closures for self-leveling of particulate debris bed”, In Proceedings of ICAPP-2014, Charlotte NC, USA, April 6-9, Paper 14330, 2014.
- [3] Basso S., Konovalenko A. and Kudinov P., “Sensitivity and Uncertainty Analysis for Prediction of Particulate Debris Bed Self-Leveling in Prototypic SA conditions”, In Proceedings of ICAPP-2014, Charlotte NC, USA, April 6-9, paper 14329, 2014.
- [4] Basso S., Konovalenko A. and Kudinov P., “Scaling Approaches to Experimental studies of Debris Bed Self-Leveling,” Nuclear Engineering and Design, Submitted, 2015.
- [5] Basso, S., Konovalenko, A., Kudinov, P. ‘Empirical Closures for Particulate Debris Bed Spreading Induced by Gas-Liquid Flow’, Nuclear Engineering and Design, 297, 19-25, (2016).
- [6] Basso S., Konovalenko A., Yakush S. E. and Kudinov P., “Effectiveness of the debris bed self-leveling under severe accident conditions,” Annals of Nuclear Energy, Volume 95, September 2016, Pages 75-85, 2016.
- [7] Basso S., Konovalenko A., Yakush S. E. and Kudinov P., “The Effect of Self-Leveling on Debris Bed Coolability Under Severe Accident Conditions,” Nuclear Engineering and Design, Volume 305, 246-259, 2016.
- [8] Campolongo, F., J. Cariboni, and A. Saltelli, An effective screening design for sensitivity analysis of large models. Environmental Modelling & Software, 22, pp. 1509-1518, 2007.

- [9] Corradini, M.L., et al., Users' manual for Texas-V: One dimensional transient fluid model for fuel-coolant interaction analysis. 2002, University of Wisconsin-Madison: Madison WI 53706.
- [10] Davydov, M.V., "Mathematical modeling of the process of interaction between high temperature melt and coolant in severe accident at NPP with water cooled reactor installation," PhD thesis: 05.14.03. 2010. 197p. (in Russian)
- [11] Dombrovsky, L.A., Davydov, M.V., Kudinov, P., "Thermal radiation modeling in numerical simulation of melt-coolant interaction," Comp. Therm. Sci. 1 (1) 2009, pp. 1-35.
- [12] Dombrovsky, L.A., Davydov, M.V., and Kudinov, P., Thermal radiation modeling in numerical simulation of melt-coolant interaction, Proc. Int. Symp. Adv. Comput. Heat Transfer (CHT-08), May 11–16, 2008, paper 155.
- [13] Galushin S., and Kudinov P., "An Approach to Grouping and Classification of Scenarios in Integrated Deterministic-Probabilistic Safety Analysis," Probabilistic Safety Assessment and Management PSAM 12, June 22-27, 2014, Honolulu, Hawaii, Paper 330, 2014.
- [14] Galushin S. and Kudinov P., "Analysis of Core Degradation and Relocation Phenomena and Scenarios in a Nordic-type BWR," Nuclear Engineering and Design, Volume 310, 15 December 2016, Pages 125–141, 2016.
- [15] Galushin S. and Kudinov P., "An Approach to Grouping and Classification of Scenarios in Integrated Deterministic-Probabilistic Safety Analysis," Science and Technology of Nuclear Installations, Article ID 278638, 13 pages, 2015.
- [16] Galushin S., Villanueva W., Grishchenko D., Kudinov P., "Development of core relocation surrogate model for prediction of debris properties in lower plenum of a Nordic BWR", NUTHOS-11: The 11th International Topical Meeting on Nuclear Reactor Thermal Hydraulics, Operation and Safety, Gyeongju, Korea, October 9-13, (2016).
- [17] Galushin S., Kudinov P., "Comparison of MELCOR code versions predictions of the properties of relocated debris in lower plenum of Nordic BWR" 17th International Topical Meeting on Nuclear Reactor Thermal Hydraulics, Xi'an, Shaanxi, China, Sept. 3-8, (2017)
- [18] Galushin S., Kudinov P., "Effect of Severe Accident Scenario and Modeling Options in MELCOR on the Properties of Relocated Debris in Nordic BWR Lower Plenum" 17th International Topical Meeting on Nuclear Reactor Thermal Hydraulics, Xi'an, Shaanxi, China, Sept. 3-8, (2017).
- [19] Randall Gauntt, Donald Kalinich, Jeff Cardoni, Jesse Phillips, Andrew Goldmann, Susan Pickering, Matthew Francis, Kevin Robb, Larry Ott, Dean Wang, Curtis Smith, Shawn St.Germain, David Schwieder, Cherie Phelan, "Fukushima Daiichi Accident Study", SAND2012-6173, Sandia Report, SNL, 2012.
- [20] Grishchenko, D., et al., KROTOS KS-4 test data report 2011, CEA: France, Cadarache.
- [21] Grishchenko, D., Basso, S., Galushin, S., Kudinov P., "Development of TEXAS-V Code Surrogate Model for Assessment of Steam Explosion Impact in Nordic BWR," The 16th International Topical Meeting on Nuclear Reactor Thermal Hydraulics (NURETH-16), Chicago, IL, USA, August 30-September 4, paper 13937, 2015.
- [22] Grishchenko D., Basso S., Kudinov P., and Bechta S. "Sensitivity Study of Steam Explosion Characteristics to Uncertain Input Parameters Using TEXAS-

- V Code," The 10th International Topical Meeting on Nuclear Thermal-Hydraulics, Operation and Safety (NUTHOS-10), Okinawa, Japan, December 14-18, 2014, Paper 1293, 2014.
- [23] Grishchenko, D., Konovalenko, A., Karbojian, A., Kudinova, V., Bechta, S., and Kudinov, P., "Insight into steam explosion in stratified melt-coolant configuration," 15th International Topical Meeting on Nuclear Reactor Thermal Hydraulics, NURETH 15, May 12 to 17, 2013, Pisa, Italy, Paper 599. (Best paper award).
  - [24] Grishchenko D., Basso S., Kudinov P., "Development of a surrogate model for analysis of ex-vessel steam explosion in Nordic type BWRs," Nuclear Engineering and Design, Volume 310, 15 December 2016, Pages 311-327, 2016.
  - [25] Goronovski A., Villanueva W., Kudinov P., Tran C.-T. "Effect of Corium Non-Homogeneity on Nordic BWR Vessel Failure Mode and Timing," Proceedings of ICAPP 2015, May 03-06, Nice, France, Paper 15160, 2015.
  - [26] Goronovski, A., Villanueva, W., Tran, C.-T., and Kudinov, P., "The Effect of Internal Pressure and Debris Bed Thermal Properties on BWR Vessel Lower Head Failure and Timing," 15th International Topical Meeting on Nuclear Reactor Thermal Hydraulics, NURETH 15, May 12 to 17, 2013, Pisa, Italy, Paper 500.
  - [27] Halton, J., Smith, G. "Algorithm 247: Radical-Inverse Quasi-Random Point Sequence." Commun. ACM 7, 701–702. (1964).
  - [28] Helton, J.C., Johnson, J.D., Oberkampf, W.L., Sallaberry, C.J., "Representation of analysis results involving aleatory and epistemic uncertainty," International Journal of General Systems, Vol.39(6),pp.605-646, (2010).
  - [29] Kaplan S. and Garrick, B. J., "*On The Quantitative Definition of Risk*," Risk Analysis, 1: pp.11–27, (1981).
  - [30] Karbojian, A., Ma, W.M., Kudinov, P., Davydov, M., Dinh, N., "A scoping study of debris formation in DEFOR experimental facility", 15th International Conference on Nuclear Engineering, Nagoya, Japan, April 22-26, 2007, Paper number ICON15-10620.
  - [31] Karbojian, A., Ma, W., Kudinov, P., and Dinh, T.-N., "A Scoping Study of Debris Bed Formation in the DEFOR Test Facility", Nuclear Engineering and Design, 239, 2009, 1653-1659.
  - [32] Kim E., J. H. Park, M. H. Kim and H. S. Park, "The influence of two-phase flow on pore clogging by fine particle settlement during ex-vessel debris bed formation in severe accident," in Proceedings of the 2014 22nd International Conference on Nuclear Engineering (ICONE22), Prague, Czech Republic, July 7-11, (2014).
  - [33] Konovalenko A., Basso S., and Kudinov P. "Experiments and Characterization of the Two-Phase Flow Driven Particulate Debris Spreading in the Pool," The 10th International Topical Meeting on Nuclear Thermal-Hydraulics, Operation and Safety (NUTHOS-10), Okinawa, Japan, December 14-18, 2014, Paper 1257, 2014.
  - [34] Konovalenko A., Basso S., Kudinov P., Yakush S. E., "Experimental Investigation of Particulate Debris Spreading in a Pool", Nuclear Engineering and Design, Volume 297, pp208-219, 2016.
  - [35] Konovalenko A., Basso S., Kudinov P., Yakush S. E., "Experiments and Modeling of Particulate Debris Spreading in a Pool," The 16th International Topical Meeting on Nuclear Reactor Thermal Hydraulics (NURETH-16), Chicago, IL, USA, August 30-September 4, paper 14221, 2015.

- [36] Kolev N., Multiphase Flow Dynamics, Vol. 2, Ch. 2, Springer, Berlin, Heidelberg, NY (2005).
- [37] Kudinov, P. and Davydov M., “Development of Surrogate Model for Prediction of Corium Debris Agglomeration,” In Proceedings of ICAPP-2014, Charlotte, USA, April 6-9, Paper 14366, 2014.
- [38] Kudinov, P. and Davydov, M., “Approach to Prediction of Melt Debris Agglomeration Modes in a LWR Severe Accident,” Proceedings of ISAMM-2009, Böttstein, Switzerland, October 26 - 28, 2009.
- [39] Kudinov, P. and Davydov, M., “Development of Ex-Vessel Debris Agglomeration Mode Map for a LWR Severe Accident Conditions,” Proceedings of the 17th International Conference on Nuclear Engineering, July 12-16, 2009, Brussels, Belgium, Paper ICONE17-75080.
- [40] Kudinov, P. and Davydov, M., “Development and Validation of the Approach to Prediction of Mass Fraction of Agglomerated Debris,” The 8th International Topical Meeting on Nuclear Thermal-Hydraulics, Operation and Safety (NUTHOS-8), Shanghai, China, October 10-14, N8P0298, 2010.
- [41] Kudinov P., Davydov M.V., “Development and validation of conservative-mechanistic and best estimate approaches to quantifying mass fractions of agglomerated debris,” Nuclear Engineering and Design, 262, September 2013, pp. 452-461.
- [42] Kudinov and Davydov M., “Prediction of Mass Fraction of Agglomerated Debris in a LWR Severe Accident,” The 14th International Topical Meeting on Nuclear Reactor Thermal Hydraulics (NURETH-14), Toronto, Ontario, Canada, September 25-29, 2011.
- [43] Kudinov, P., Davydov, M., Pohlner G., Bürger M., Buck M., and Meignen R., “Validation of the FCI codes against DEFOR-A data on the mass fraction of agglomerated debris,” 5th European Review Meeting on Severe Accident Research (ERMSAR-2012) Cologne (Germany), March 21-23, 2012.
- [44] Kudinov, P. and Dinh, T.-N., “An analytical study of mechanisms that govern debris packing in a LWR severe accident”, The 12th International Topical Meeting on Nuclear Reactor Thermal Hydraulics (NURETH-12), Sheraton Station Square, Pittsburgh, Pennsylvania, U.S.A. September 30-October 4, 2007. Paper 247.
- [45] Kudinov, P. and Dinh, T.-N., “A Computational Study of Debris Bed Formation,” ANS Transactions, 2008, paper 193463.
- [46] Kudinov P., Galushin S., Goronovski A., and Villanueva W., “RES1: Definition of a Reference Nordic BWR Plant Design and Plant Damage States for Application of ROAAM to Resolution of Severe Accident Issues,” Research Report, The Eighth Framework of Accident Phenomena of Risk Importance (APRI-8), Division of Nuclear Power Safety, Royal Institute of Technology (KTH), Stockholm, Sweden, April 04, 2014.
- [47] Kudinov P, Galushin S., Grishchenko D., Yakush S., Adolfsson Y., Ranlöf L., Bäckström O., Enerholm A., Krcal P., Tuvelid A., “Deterministic-Probabilistic Safety Analysis Methodology for Analysis of Core Degradation, Ex-vessel Steam Explosion and Debris Coolability”, NKS-345, ISBN 978-87-7893-427-7. Jul 2015.
- [48] Kudinov P., Galushin S., Davydov M., “Analysis of the Risk of Formation of Agglomerated Debris in Nordic BWRs,” NUTHOS-11: The 11th International Topical Meeting on Nuclear Reactor Thermal Hydraulics, Operation and Safety, Gyeongju, Korea, October 9-13, N11P0592, 2016.

- [49] Kudinov P., Galushin S., Raub S., Phung V.-A., Kööp K., Karanta I., Silvonen T., Adolfsson Y., Bäckström O., Enerholm A., Krcal P., Sunnevik K., “Feasibility Study for Connection Between IDPSA and conventional PSA Approach to Analysis of Nordic type BWR’s,” NKS-DPSA Project, NKS-R, Report: NKS-315, 2014.
- [50] Kudinov P., Galushin S., Grishchenko D., Yakush S., Adolfsson Y., Ranlöf L., Bäckström O., Enerholm A., “Scenarios and Phenomena Affecting Risk of Containment Failure and Release Characteristics,” SPARC Project, NKS-395 22 Aug 2017, 2017.
- [51] Pavel Kudinov, Sergey Galushin, Dmitry Grishchenko, Sergey Yakush, Simone Basso, Alexander Konovalenko, Mikhail Davydov, “Application of Integrated Deterministic-Probabilistic Safety Analysis to Assessment of Severe Accident Management Effectiveness in Nordic BWRs,” The 17th International Topical Meeting on Nuclear Reactor Thermal Hydraulics (NURETH-17) Paper: 21590, Qujiang Int’l Conference Center, Xi’an, China, September 3-8, 2017.
- [52] Kudinov P., Galushin S., Yakush S., Villanueva W., Phung V.-A., Grishchenko D., Dinh N., “A Framework for Assessment of Severe Accident Management Effectiveness in Nordic BWR Plants,” Probabilistic Safety Assessment and Management PSAM 12, June 22-27, 2014, Honolulu, Hawaii, Paper 154, 2014.
- [53] Kudinov P., Grishchenko D., Konovalenko A., Karbojian A. “Premixing and Steam Explosion Phenomena in the Tests with Stratified Melt-Coolant Configuration and Binary Oxidic Melt Simulant Materials,” Nuclear Engineering and Design, Volume 314, Pages 1-338 (1 April 2017).
- [54] Kudinov P., Grishchenko D., Karbojian A., Villanueva W., “Design and development of experiments for validation of debris remelting and interactions with structures,” Accident Phenomena of Risk Importance (APRI-8), Report MEM1, Rev.2, January 10, 2015.
- [55] Kudinov P., Grishchenko D., Konovalenko A., Karbojian A., “Experimental Investigation of Debris Bed Agglomeration and Particle Size Distribution Using WO<sub>3</sub>-ZrO<sub>2</sub> Melt,” The 16th International Topical Meeting on Nuclear Reactor Thermal Hydraulics (NURETH-16), Chicago, IL, USA, August 30-September 4, paper 14220, 2015.
- [56] Kudinov P., Grishchenko D., Konovalenko A., Karbojian A., Bechta S. “Investigation of Steam Explosion in Stratified Melt-Coolant Configuration,” The 10th International Topical Meeting on Nuclear Thermal-Hydraulics, Operation and Safety (NUTHOS-10), Okinawa, Japan, December 14-18, 2014, Paper 1316, 2014.
- [57] Kudinov P., Grishchenko D., Galushin S., Yakush S., Konovalenko A., Basso S., Davydov M., Thakre S., Villanueva W., Ma W., Yu P., Manickam L., “Integrated ROAAM+ Development and Analysis Results for Nordic BWRs”. Accident Phenomena of Risk Importance (APRI-9) Report, January 2017.
- [58] Kudinov P., Grishchenko D., Galushin S., Yakush S., Konovalenko A., Basso S., Davydov M., Villanueva W., Goronovski A., “RES3: Preliminary Analysis of Conditional Containment Failure Probabilities Using ROAAM+ Frameworks.” Risk Oriented Framework for Safety Analysis of Severe Accident Issues in Nordic BWRs. Accident Phenomena of Risk Importance (APRI-8), January 2016.

- [59] Kudinov, P., Karbojian, A., Ma, W.M., Davydov, M., and Dinh, T.-N., "A Study of Ex-Vessel Debris Formation in a LWR Severe Accident", Proceedings of ICAPP 2007, Nice, France, May 13-18, 2007, Paper 7512.
- [60] Kudinov, P., Karbojian, A., Ma, W.M., and Dinh, T.-N., "An experimental study on debris formation with corium simulant materials," Proc. ICAPP'08, Anaheim, CA USA, June 8–12, 2008, paper 8390.
- [61] Kudinov, P., Karbojian, A., Ma, W., and Dinh, T.-N. "The DEFOR-S Experimental Study of Debris Formation with Corium Simulant Materials," Nuclear Technology, 170(1), April 2010, pp. 219-230, 2010.
- [62] Kudinov, P., Karbojian, A., and Tran, C.-T., "Experimental Investigation of Melt Debris Agglomeration with High Melting Temperature Simulant Materials," Proceedings of ISAMM-2009, Böttstein, Switzerland, October 26 - 28, 2009.
- [63] Kudinov, P., Karbojian, A., Tran, C.-T., and Villanueva, W., "The DEFOR-A Experiment on Fraction of Agglomerated Debris as a Function of Water Pool Depth," The 8th International Topical Meeting on Nuclear Thermal-Hydraulics, Operation and Safety (NUTHOS-8), Shanghai, China, October 10-14, N8P0296, 2010.
- [64] Kudinov, P., Karbojian, A., Tran, C.-T., Villanueva, W., "Experimental Data on Fraction of Agglomerated Debris Obtained in the DEFOR-A Melt-Coolant Interaction Tests with High Melting Temperature Simulant Materials," Nuclear Engineering and Design, 263, October 2013, Pages 284-295, 2013.
- [65] Kudinov, P., Ma, W.M., Tran, C.-T., Hansson, R., Karbojian, A., and Dinh, T.-N. "Multiscale Phenomena of Severe Accident," NKS-R and NKS-B Joint Summary Seminar, Armémuseum, Stockholm, 26th - 27th March 2009.
- [66] Kudinov, P. and Kudinova, V., "Influence of Water Subcooling on Fracture of Melt Debris Particle," ANS Transactions, 2009, paper 210646.
- [67] Kudinov, P., Kudinova, V., and Dinh, T.-N., "Molten Oxidic Particle Fracture during Quenching in Water," 7th International Conference on Multiphase Flow ICMF 2010, Tampa, FL USA, May 30-June 4, 2010.
- [68] Kudinov P., Vorobyev Y., Sánchez-Perea M., Queral C., Jiménez Varas G., Rebollo M. J., Mena L., Gómez-Magán J., "Integrated Deterministic-Probabilistic Safety Assessment Methodologies", Nuclear España, 347, Enero, pp.32-38, 2014.
- [69] Li L., Karbojian A., Kudinov P., Ma W., "An Experimental Study on Dryout Heat Flux of Particulate Beds Packed with Irregular Particles," Proceedings of ICAPP 2011, Nice, France, May 2-5, 2011, Paper 11185. 2011.
- [70] Magallon, D., Huhtiniemi, I., Hohmann, H., "Lessons Learnt from FARO/TERMOS Corium Melt Quenching Experiments," In: Proceedings of the OECD/CSNI Specialists Meeting on Fuel-Coolant Interactions, Tokai-Mura, Japan, NEA/CSNI/R(97)26, Part II, 1997, pp.431-446.
- [71] Magallon, D., "Characteristics of corium debris bed generated in large-scale fuel-coolant interaction experiments," Nuclear Engineering and Design, 236, 2006, pp.1998–2009.
- [72] Manickam L., Kudinov P, Bechta S., "On the Influence of Water Subcooling and Melt Jet Parameters on Debris Formation," 15th International Topical Meeting on Nuclear Reactor Thermal Hydraulics, NURETH 15, May 12 to 17, 2013, Pisa, Italy, Paper 512.

- [73] Manickam, L., Kudinov, P., Ma, W., Bechta, S., Grishchenko, D., 2016. “On the influence of water subcooling and melt jet parameters on debris formation,” Nucl. Eng. Des. 309, 265–276, 2016.
- [74] Meignen R., Raverdy B., Buck M., Pohlner G., Kudinov P., Ma W., Brayer C., Piluso P., Hong S.-W., Leskovar M., Ursič M., Albrecht G., Lindholm I., Ivanov I., “Status of steam explosion understanding and modelling,” Annals of Nuclear Energy, Article in Press, Available online 23 August 2014.
- [75] Morris M. D., “Factorial sampling plans for preliminary computational experiments”, Technometrics, 33, (2), pp. 161–174, 1991.
- [76] Phung, V. -A., Grishchenko, D., Galushin, S., Kudinov, P., “Prediction of In-Vessel Debris Bed Properties in BWR Severe Accident Scenarios using MELCOR and Neural Networks,” Journal of Annals of Nuclear Energy, submitted January 2017.
- [77] Phung, V.-A. Galushin, S. Raub, S. Goronovski, A., Villanueva, W., Kööp, K., Grishchenko, D., Kudinov, P., “Characteristics of debris in the lower head of a BWR in different severe accident scenarios,” NED, Volume 305, 15, August 2016, pages 359-370, 2016.
- [78] Rempe, J.L., Chavez, S.A., Thennes, G.L., Allison, C.M., Korth, G.E., Witt, R.J., Sienicki, J.J., Wang, S.K., Stickler, L.A., Heath, C.H., and Snow, S.D., “Light Water Reactor Lower Head Failure,” Report NUREG/CR-5642, Idaho Falls (1993).
- [79] Saltelli A., Tarantola S., Campolongo F., Ratto M., Sensitivity Analysis in Practice, John Wiley & Sons Ltd, p. 94, 2004.
- [80] Saltelli, A., Ratto, M., Andres, T., Campolongo, F., Cariboni, J., Gatelli, D., Saisan, M., Tarantola, S., 2008. Global Sensitivity Analysis: The Primer. John Wiley & Sons Ltd., (2008).
- [81] Spencer, B.W., Wang K., Blomquist, C.A., McMumber, L.M., and Schneider, J.P., “Fragmentation and Quench Behaviour of Corium Melt Streams in Water,” NUREG/CR-6133 ANL-93/32, Argonne National Laboratory. 1994.
- [82] Strålsäkerhetsmyndigheten, “APRI-7 Accident Phenomena of Risk Importance”, En lägesrapport om forskningen inom svåra havarer under åren 2009-2011, rapportnummer 2012:12, ISSN:2000-0456, 2012.
- [83] Takasuo E., Kinnunen T., Lehtikuusi T. and Holmström S., “COOLOCE Debris Bed Coolability Experiments with an Agglomerate Simulant: Test Series 11,” VTT Report VTT-R-03316-13 (2013).
- [84] Theofanous, T. G., “On Proper Formulation of Safety Goals and Assessment of Safety Margins for Rare and High-Consequence Hazards,” Reliability Engineering and System Safety, 54, pp.243-257, (1996).
- [85] Theofanous, T. G. and Dinh, T.-N., “Integration of multiphase Science and Technology with Risk Management in Nuclear Power reactors: Application of the Risk-Oriented Accident Analysis Methodology to the Economic, Simplified Boiling Water Reactor Design,” Multiphase Science and Technology, V20(2), 2008, Pages 81-211.
- [86] Torregrosa, C., Villanueva, W., Tran, C.-T., and Kudinov, P., “Coupled 3D Thermo-Mechanical Analysis of a Nordic BWR Vessel Failure and Timing,” 15th International Topical Meeting on Nuclear Reactor Thermal Hydraulics, NURETH 15, May 12 to 17, 2013, Pisa, Italy, Paper 495.
- [87] Torregrosa, M.C., “Coupled 3D Thermo-Mechanical Analysis of Nordic BWR Lower Head Failure in case of Core Melt Severe Accident” MSc Thesis, Royal Institute of Technology (KTH), 2013.

- [88] Tran, C.T., and Dinh, T. N., "The Effective Convectivity Model for Simulation of Melt Pool Heat Transfer in a Light Water Reactor Pressure Vessel Lower Head. Part I: Physical Processes, Modeling and Model Implementation", pp.849-859, 2009. "Part II: Model Assessment and Application", Progress in Nuclear Energy, Vol.51, N.8, pp.860-871, 2009.
- [89] Tran, C.-T. and Kudinov P., "Local Heat Transfer From The Corium Melt Pool to the BWR Vessel Wall," The 14th International Topical Meeting on Nuclear Reactor Thermal Hydraulics (NURETH-14), Toronto, Ontario, Canada, September 25-29, 2011.
- [90] Tran, C.-T. and Kudinov P., "A Synergistic use of CFD, Experiments and Effective Convectivity Model to Reduce Uncertainty in BWR Severe Accident Analysis," CFD4NRS-3 Workshop, Bethesda, MD, USA, September 14-16, 2010.
- [91] Tran, C.-T. and Kudinov, P., "The effective convectivity model for simulation of molten metal layer heat transfer in a boiling water reactor lower head," Proceedings of ICAPP '09, Tokyo, Japan, May 10-14, 2009 Paper 9114.
- [92] Tran, C. T., Kudinov P., and Dinh, T. N. "An approach to numerical simulation and analysis of molten corium coolability in a BWR lower head," XCFD4NRS Workshop, Grenoble, France, September 10-12, 2008.
- [93] Tran, C. T., Kudinov, P., and Dinh, T. N., "An approach to numerical simulation and analysis of molten corium coolability in a BWR lower head," Nuclear Engineering and Design, 240, 2010, 2148–2159.
- [94] Tran, C.-T., Villanueva, W., and Kudinov, P., "A Study on the Integral Effect of Corium Material Properties on Melt Pool Heat Transfer in a Boiling Water Reactor," Proceedings of The 9th International Topical Meeting on Nuclear Thermal-Hydraulics, Operation and Safety (NUTHOS-9), Kaohsiung, Taiwan, September 9-13, , N9P0289, 2012.
- [95] Villanueva, W., Tran, C.-T., Kudinov, P., "Coupled thermo-mechanical creep analysis for boiling water reactor pressure vessel lower head," Nuclear Engineering and Design, 249, 2012, 146-153.
- [96] Villanueva, W., Tran C.-T., and Kudinov P., "Analysis of Instrumentation Guide Tube Failure in a BWR Lower Head," Proceedings of The 9th International Topical Meeting on Nuclear Thermal-Hydraulics, Operation and Safety (NUTHOS-9), Kaohsiung, Taiwan, September 9-13, , N9P0268, 2012.
- [97] Villanueva, W., Tran, C.-T., and Kudinov, P., "Effect of CRGT Cooling on Modes of Global Vessel Failure of a BWR Lower Head," Proceedings of the 20th International Conference on Nuclear Engineering (ICON-E-20), Anaheim, CA, USA, July 30 - August 3, Paper 54955, 2012.
- [98] Villanueva W., Tran C.-T., and Kudinov P., "A Computational Study On Instrumentation Guide Tube Failure During a Severe Accident in Boiling Water Reactors," The 14th International Topical Meeting on Nuclear Reactor Thermal Hydraulics (NURETH-14), Toronto, Ontario, Canada, September 25-29, 2011.
- [99] Villanueva W., Tran C.-T., and Kudinov P., "Assessment with Coupled Thermo-Mechanical Creep Analysis of Combined CRGT and External Vessel Cooling Efficiency for a BWR," The 14th International Topical Meeting on Nuclear Reactor Thermal Hydraulics (NURETH-14), Toronto, Ontario, Canada, September 25-29, 2011.
- [100] Villanueva W., Tran C.-T. and Kudinov P., "Coupled Thermo-Mechanical Creep Analysis for Boiling Water Reactor Pressure Vessel Lower Head" The

- 8th International Topical Meeting on Nuclear Thermal-Hydraulics, Operation and Safety (NUTHOS-8), Shanghai, China, October 10-14, N8P0248, 2010.
- [101] Vorobyov, Y. and Dinh, T.N., A Genetic Algorithm-Based Approach to Dynamic PRA Simulation. in ANS PSA 2008 Topical Meeting - Challenges to PSA during the nuclear renaissance. 2008. Knoxville, Tennessee: American Nuclear Society, LaGrange Park, IL.
  - [102] Vorobyev Y., Kudinov P., Development and Application of a Genetic Algorithm Based Dynamic PRA Methodology to Plant Vulnerability Search, ANS PSA 2011 International Topical Meeting on Probabilistic Safety Assessment and Analysis, Wilmington, NC, March 13-17, 2011, on CD-ROM, American Nuclear Society, LaGrange Park, IL (2011).
  - [103] Vorobyev Yu.B., Kudinov P., Jeltsov M., Kööp K., Nhat T.V.K., "Application of information technologies (genetic algorithms, neural networks, parallel calculations) in safety analysis of Nuclear Power Plants," Proceedings of the Institute for System Programming of RAS, 26(2), pp.137-158, 2014.
  - [104] Yakush S. E., Konovalenko A., Basso S. and Kudinov P., "Effect of Particle Spreading on Coolability of Ex-Vessel Debris Bed" The 16th International Topical Meeting on Nuclear Reactor Thermal Hydraulics (NURETH-16), Chicago, IL, USA, August 30-September 4, paper 14112, 13p, 2015.
  - [105] S. E. Yakush, A. Konovalenko, S. Basso, P. Kudinov, " Validation of DECODIM Code Against Experiments on Particle Spreading by Two-Phase Flows in Water Pool", NUTHOS-11: The 11th International Topical Meeting on Nuclear Reactor Thermal Hydraulics, Operation and Safety, Gyeongju, Korea, October 9-13, 2016.
  - [106] Yakush, S., Kudinov, P. "Effects of Water Pool Subcooling on the Debris Bed Spreading by Coolant Flow," Proceedings of the 11th International Conference on Advanced Nuclear Power Plants (ICAPP 2011), Nice, France, May 2011, paper 11416, 14 p. 2011.
  - [107] Yakush S. and Kudinov P., "A Model for Prediction of Maximum Post-Dryout Temperature in Decay-Heated Debris Bed," Proceedings of the 2014 22nd International Conference on Nuclear Engineering, ICONE22, July 7-11, Prague, Czech Republic, ICONE22-31214. 2014.
  - [108] Yakush S. E., and Kudinov P., "Effect of Melt Agglomeration on Coolability of a Debris Bed". NUTHOS-11: The 11th International Topical Meeting on Nuclear Reactor Thermal Hydraulics, Operation and Safety, Gyeongju, Korea, October 9-13, 2016. N11A0590.
  - [109] Yakush S. E., and Kudinov P., "Melt Agglomeration Influence on Ex-vessel Debris Bed Coolability" The 17th International Topical Meeting on Nuclear Reactor Thermal Hydraulics (NURETH-17), Paper: 21455, Qujiang Int'l Conference Center, Xi'an, China, September 3-8, 2017.
  - [110] Yakush S., Kudinov P., "In-vessel debris bed coolability and implications for vessel failure mode" NUTHOS-11: The 11th International Topical Meeting on Nuclear Reactor Thermal Hydraulics, Operation and Safety, Gyeongju, Korea, October 9-13, N11P0532, 2016.
  - [111] Yakush, S. E., Kudinov, P., Villanueva, W., and Basso, S., "In-Vessel Debris Bed Coolability and its Influence on the Vessel Failure," 15th International Topical Meeting on Nuclear Reactor Thermal Hydraulics, NURETH 15, May 12 to 17, 2013, Pisa, Italy, Paper 464.
  - [112] Yakush, S. E., Kudinov, P., Villanueva, W., and Basso, S., "In-Vessel Debris Bed Coolability and its Influence on the Vessel Failure," 15th International

- Topical Meeting on Nuclear Reactor Thermal Hydraulics, NURETH 15, May 12 to 17, 2013, Pisa, Italy, Paper 464.
- [113] Yakush, S. and Kudinov, P., "Transient Phenomena of Ex-vessel Debris Bed Formation in a LWR Severe Accident," ANS Transactions, 2009, paper 210830.
  - [114] Yakush, S. and Kudinov, P., "Simulation of Ex-Vessel Debris Bed Formation and Coolability in a LWR Severe Accident," Proceedings of ISAMM-2009, Böttstein, Switzerland, October 26 - 28, 2009.
  - [115] Yakush, S., Kudinov, P., and Dinh, T.-N., "Multiscale Simulations of Self-organization Phenomena in the Formation and Coolability of Corium Debris Bed," Proc. The 13th International Topical Meeting on Nuclear Reactor Thermal Hydraulics (NURETH-13), September 27-October 2, 2009. Kanazawa City, Ishikawa Prefecture, Japan, Paper N13P1143.
  - [116] Yakush, S., Kudinov, P., and Dinh, T.-N., "Modeling of Two-Phase Natural Convection Flows in a Water Pool with a Decay-Heated Debris Bed," Proc. ICAPP'08, Anaheim, CA USA, June 8–12, 2008, paper 8409.
  - [117] Yakush, S., Kudinov, P., and Lubchenko, N., "Coolability of heat-releasing debris bed. Part 1: Sensitivity analysis and model calibration," Annals of Nuclear Energy, 52, February 2013, pp. 59-71, 2013
  - [118] Yakush, S., Kudinov, P., and Lubchenko, N., "Coolability of heat-releasing debris bed. Part 2: Uncertainty of dryout heat flux," Annals of Nuclear Energy, 52, February 2013, pp. 72-79.
  - [119] Yakush, S., Lubchenko, N., and Kudinov, P., "Risk-Informed Approach to Debris Bed Coolability Issue," Proceedings of the 20th International Conference on Nuclear Engineering (ICONE-20), Anaheim, CA, USA, July 30 - August 3, Paper 55186, 2012.
  - [120] Yakush S. E., Lubchenko, N.T., and Kudinov P., "Surrogate Models for Debris Bed Dryout," 15th International Topical Meeting on Nuclear Reactor Thermal Hydraulics, NURETH 15, May 12 to 17, 2013, Pisa, Italy, Paper 278.
  - [121] Yakush, S. E., Lubchenko, N. T., and Kudinov, P., "Risk and Uncertainty Quantification in Debris Bed Coolability," 15th International Topical Meeting on Nuclear Reactor Thermal Hydraulics, NURETH 15, May 12 to 17, 2013, Pisa, Italy, Paper 283.
  - [122] Yakush S., Kudinov P., "In-vessel debris bed coolability and implications for vessel failure mode" NUTHOS-11:The 11th International Topical Meeting on Nuclear Reactor Thermal Hydraulics, Operation and Safety, Gyeongju, Korea, October 9-13, N11P0532, 2016.
  - [123] Yakush S. E., Villanueva W., Basso S. and Kudinov P., "Simulation of In-vessel Debris Bed Coolability and Remelting," The 10th International Topical Meeting on Nuclear Thermal-Hydraulics, Operation and Safety (NUTHOS-10), Okinawa, Japan, December 14-18, 2014, Paper 1281, 2014.
  - [124] L.L. Humphries, B.A. Beeny, F. Gelbard, D.L. Louie, J. Phillips, "MELCOR Computer Code Manuals", Vol. 1: Primer and Users' Guide Version 2.2.9541, SAND2017-0455 O, (2017).
  - [125] L.L. Humphries, B.A. Beeny, F. Gelbard, D.L. Louie, J. Phillips, "MELCOR Computer Code Manuals", Vol. 2: Reference Manual Version 2.2.9541, SAND2017-0876 O, (2017).
  - [126] R.O Gauntt, J. C. (2005). MELCOR Computer Code Manual Vol.2 Reference Manual Version 1.8.6. Albuquerque: Sandia National Laboratories.

- [127] R.O Gauntt, J. C. (2005). MELCOR Computer Code Manuals Vol. 1 Primer and User's Guide Version 1.8.6 . Albuquerque: Sandia National Laboratories.
- [128] Hansson, R. C., Park, H.S., Dinh, T.N., "Dynamics and preconditioning in a single droplet vapor explosion", Nuclear Technology, Vol.167, pp.223-234, 2008.
- [129] Hansson, R. C., Park, H.S., Dinh, T.N., "Simultaneous high speed digital cinematographic and X-ray radiographic imaging of a multi-fluid interaction with rapid phase changes", Experimental Thermal and Fluid Science, Vol.33, pp.754-763, 2009.
- [130] Hansson, R.C., "Triggering and energetics of a single drop vapor explosion: The role of entrapped nob-condensable gases", Nuclear Engineering and Technology, Vol.41, pp.1215-1222, 2009.
- [131] Hansson, R. C., Dinh, T. N., Manickam, L., "A study of the effect of binary oxide materials in a single droplet vapor explosion triggering", Nuclear Engineering and Design, Vol 264, pp. 168-175, 2013.
- [132] Huhtiniemi, I., Magallon, D., Hohmann, H., "Results of recent KROTOS FCI tests: alumina versus corium melts", Nuclear Engineering and Design, 189, 379-389, 1999.
- [133] Manickam, L., Thakre, S., Ma, W., Bechta, S., "Simultaneous visual acquisition of melt jet breakup in water by high speed videography and radiography", Proc. of NUTHOS-10, Okinawa, Japan, December 14-18, 2014.
- [134] Manickam, L., Thakre, S., Ma, W., "An experimental study on void generation around a hot metal particle quenched into water pool", Proc. of NURETH-16, Chicago, U.S.A, Aug 30 –Sep4, 2015.
- [135] Manickam, L., Bechta, S., Ma, W., "On the fragmentation characteristics of melt jets quenched in water", International Journal of Multiphase Flow, Vol 91: pp. 262-275, 2017.
- [136] Nelson, L.S., Duda, P.M., "Steam explosion experiments with single drops of iron oxide: PART II: parametric studies", NUREG CR-2718, April, 1985.
- [137] Trypekl, V., Piluso, P., S. Bakardijeva, S., Niznansky, D., Rehspringer, J., Bezdicka, P., Dugne, O., "Prototypic corium oxidation and hydrogen release during the Fuel–Coolant Interaction", Annals of Nuclear Energy, 75: 210-218, 2015.
- [138] Zambaux, J.A., Manickam, L., Meignen, R., Ma, W., Bechta, S., Picchi, S., "Study on thermal fragmentation characteristics of a superheated alumina droplet", Proc. of ERMSAR-17, Warsaw, Poland, May 16-18, 2017.

## 4. CHALMERS FORSKNING INOM SVÅRA HAVERIER

### 4.1 Inledning på svenska

En fortsatt utmaning inom haverikemi är att förbättra förståelsen för vad som sker med de radioaktiva ämnen som frigörs från härden i samband med ett svårt haveri. Gasformiga ämnen frigörs redan då bränslekapslingen brister i haveriets inledning. Andra ämnen frigörs vartefter härden smälter till följd av otillräcklig kylning. Det är viktigt att förstå den fortsatta processen som gör det möjligt för olika ämnen att sprida sig i primärsystemet och sedan transportereras vidare ut i inneslutningen. Omgivningskonsekvenser uppstår i det fall de radioaktiva ämnena som har frigjorts i inneslutningen även passerar inneslutningsbarriären, som är det sista skyddet för att förhindra spridning till omgivningen.

Filtrerad tryckavlastning via haverifilter är en planerad åtgärd som utförs för att reducera det övertryck som uppstår under haveriet. Detta leder till att radioaktiva utsläpp passerar inneslutningsbarriären, men åtgärden är nödvändig för att minska de påfrestningar som medför risk för större utsläpp om inneslutningen brister. Radioaktivt utsläpp förväntas även från det diffusa läckage som sker kontinuerligt, så länge det råder övertryck i den isolerade inneslutningen. För att kunna göra en realistisk bedömning av konsekvenserna av dessa utsläpp, så är det viktigt att skaffa sig kunskap om de radioaktiva ämnen som frigörs i inneslutningen. Lika viktigt är det att förstå de processer som möjliggör transport av dessa ämnen i inneslutningen och som leder fram till att de blir tillgängliga att följa med utsläppen, i den s.k. källtermen för utsläppet.

Flyktigheten för ett ämne är den egenskap som avgör hur väl ämnet sprids. Den bestäms bl.a. av ämnets kemiska sammansättning och beror även av den aktuella temperaturen. Flyktigheten kan också förändras genom interaktion med andra ämnen under transporten. Kemiska reaktioner mellan ämnen, eller radiolytiska reaktioner som uppstår vid gammabestrålning, kan leda till bildande av produkter med förändrade egenskaper bl.a. vad gäller flyktighet. Reaktioner kan ske både i gasfas och i det vattnen som samlas i botten av inneslutningen. Liksom i gasfas påverkas kemin i vattenlösning av både temperatur och strålningsnivåer, samt i vissa fall även av vattnets surhetsgrad, det s.k. pH-värdet. Interaktion mellan olika ämnen i vatten påverkar löslighetsförhållandena, vilket kan leda till att fällningar bildas. Detta medför att den fortsatta spridningen i inneslutningen begränsas. I gasfas finns processer som leder till bildande av luftburna partiklar, s.k. aerosoler, som har ett annat transportbeteende än fria gaser. Interaktion kan även ske med metallytor eller målade ytor då luftburet material deponeras, vilket begränsar vidare spridning. Deponerat material kan emellertid frigöras på nytt under vissa förhållanden. I vissa fall kan det deponerade materialet även reagera med den underliggande ytan. Radioaktivt sönderfall komplicerar bilden ytterligare, när det gäller att bestämma källtermen i det utsläpp som till sist lämnar inneslutningen. Kemiska processer och radioaktivt sönderfall fortsätter dessutom även sedan ämnena har lämnat inneslutningen och fortsätter spridas i omgivningen.

Ädelgaser, som t.ex. xenon och krypton, domineras i tidiga utsläpp vid ett svårt haveri. Detta är en grupp ämnen som inte kan filtreras eller kondenseras. Detta gör att de inte reagerar med andra ämnen eller interagerar med ytor. Ädelgasinventariet påverkas i stort sett endast genom det radioaktiva sönderfall som de olika ädelgasnukliderna genomgår, vilket leder till andra ämnen.

Jod är ett ämne som har betydligt mer komplexa egenskaper än ädelgaserna. Jod har en synnerligen rik kemi och förekommer i ett stort antal kemiska föreningar med vitt skilda egenskaper. Jod förekommer både i gasform, som deponerad på ytor och löst i vattenfasen. Vissa former är stabila medan andra är reaktiva. Kemiska reaktioner gör att jod lätt bildar produkter med andra ämnen som får nya egenskaper, bl.a. vad gäller flyktighet. Fortsatta kemiska reaktioner kan göra att flyktigheten förändras genom att gasformig jod deponeras på olika ytor, eller att deponerat material frigörs på nytt. Jod bidrar liksom ädelgaser också till en betydande del av källtermen i utsläppet i början av ett haveri, vilket vore problematiskt om inget görs för att reducera det radioaktiva innehållet. Mängden jod i utsläppet kan dock reduceras betydligt genom att man låter det filtreras genom en skrubberlösning vid tryckavlastning. Genom denna metod överförs flyktig elementär jod till en vattenlöslig form som stannar i skrubbern, men det finns även s.k. organiska jodformer som inte reduceras i nämnvärd utsträckning av filtreringen utan de behåller sin ädelgasliknande flyktighet.

Jodkemin har varit föremål för forskning i flera årtionden där syftet har varit att förstå alla de processer där jod ingår, samt att samla data för att bygga beräkningsmodeller som kan förutsäga hur jod beter sig under ett haveri. Jod ingår också i de studier som alltid pågår inom OECD/NEA-projekten BIP, STEM och THAI (se avsnitt 2.2-2.4).

Den forskning som Chalmers har bedrivit inom APRI-9 syftar till att kartlägga kemin hos andra viktiga fissionsprodukter, såsom rutenium och tellur, för att på så sätt öka kunskapen bl.a. om hur dessa ämnen transporteras och interagerar med ytor av olika material som förekommer i inneslutningen. Liksom forskningen om jod rör det sig om att förstå vilka processer som påverkar flyktigheten för dessa ämnen och hur de påverkas av de betingelser som kan råda vid havertilförlitligheten, t.ex. höga temperaturer, varierande ånghalt eller oxidativ miljö. De experimentella resultaten utgör viktig kunskap för möjligheten att bygga beräkningsmodeller också för dessa ämnen.

Efter olyckan i Fukushima Dai-ichi upptäckte man vid mätningar i de närliggande samhällena, att markstrålningen den första tiden till stor del kom från radioaktiv tellur som hade deponerat. Radionukliden tellur-132 bidrog med nära 70 % av den totala markdosen i det inledande skedet. Tellur-132 har en halveringstid på ca 3 dagar och omvandlas successivt till jod-132, som har en halveringstid på ett par timmar. Det dröjde dock bortåt tre veckor innan bidraget från dessa båda nuklider hade klingat av. Lägg in ett diagram här (från Anders)??

Chalmers har utfört experiment för att studera tellurs uppförande under förhållanden som kan råda i samband med ett haveri. Experimenten har utförts i en försöksuppsättning med en rörugn, se Figur 4.1. I ena änden av rörugnen placerar man ett litet ”skepp” med metallpulver av tellur. Provet upphettas sedan till temperaturer på flera hundra grader, vilket motsvarar de temperaturer som man kan förvänta sig under ett haveri. Upphetningen gör att tellur förflyktigas, dvs. övergår i gasfas. Genom rörugnen har man sedan ett lagt på ett gasflöde som gör att den gasformiga telluren kan transporteras i röret. Temperaturen avtar med avståndet till ”skeppet”. Efter en transportsträcka på en dryg meter, så deponerar telluren i den bortre änden av rörugnen. En stor del av telluren deponeras på rörugnens väggar men deposition sker också på den ”metallkupong” som är utplacerad i rörets ände. Metallkupongen analyseras sedan med olika tekniker för att ge indikation på vilka olika tellurföreningar som har bildats och transporterats i försöket. Man vill även undersöka om det förekommer någon kemisk interaktion mellan den deponerade telluren och metallytan. Metallytor

av koppar, zink och aluminium har använts i försöken, vilka representerar de olika ytor som är vanliga i en reaktorinneslutning.

Försöken visar så här långt att tellur transporteras både i form av tellurmetall och som tellurdioxid ( $\text{TeO}_2$ , paratellurit). I motsats till de fall då man låter jod deponera på metallytor, så har man inte sett någon reaktion mellan tellur och de olika metallytorna. Tellur förfaller därför inte ha samma förmåga som jod att binda till ytan. Upphettning av ytan under et haveri skulle således få den deponerade telluren att förflyktigas på nytt. Ett gasflöde som uppstår t.ex. vid en tryckavlastning skulle också kunna sätta den deponerade telluren i rörelse. Kartläggning pågår också med olika tekniker för att bestämma strukturen på de partiklar som deponeras.

I en annan försöksserie söker man kunskap om hur metallernas flyktighet kan påverkas genom kemisk omvandling till andra ämnen såsom metallhalider eller s.k. metalloxyhalider. Studien har sin bakgrund i att man använde sig av havsvatten i Fukushima Dai-ichi för att upprätthålla kylning av härdens vid haveriet. Det medförde att man fick in havssalt i anläggningen, vilket gör att det finns en misstanke om att kemisk interaktion mellan tellur och havssalt kan ha påverkat tellurs flyktighet.

Försöken genomförs på så vis att man upphettar en fast blandning av tellurmetall och koksalt för att se om man kan påvisa någon kemisk reaktion som påverkar flyktigheten, som t.ex. bildande av tellurklorid som är ett flyktigt ämne. Försök har också utförts under oxidativa betingelser (under luftatmosfär) med syfte att påvisa bildande av telluroxyklorid, som också har förhöjd flyktighet jämfört med den rena tellurmallen. Preliminära resultat visar att det är möjligt att det kan uppstå betingelser i närväro av havssalt som gynna kemiska processer som ökar tellurs flyktighet.

Rutenium är en annan fissionsprodukt som har studerats i samarbete med VTT i Finland. Med hjälp av en liknande rörugn som den om används för tellurförsöken, har man undersökt olika betingelser som kan påverka ruteniumpolymerens flyktighet, se Figur 4.15. Man har studerat hur utgångsmaterialet ruteniumdioxid ( $\text{RuO}_2$ ) påverkas under de oxidativa betingelser som förväntas uppstå under ett haveri som ett resultat av att det då det kan bildas bl.a. nitrösa gaser ( $\text{NO}_x$ ) och ozon ( $\text{O}_3$ ) genom radiolys av atmosfären. Dessa ämnen visade sig i försöken ge en signifikant ökning av ruteniumpolymerens flyktighet vid förhöjd temperatur. Ökad flyktighet observerades också i närväro av aerosoler av cesiumjodid ( $\text{CsI}$ ). I studien har den kemiska sammansättningens bestämts av de ämnen som bildas och mätningar har gjorts för att bestämma vilka mängder som transportereras. Bildandet av s.k. oxyhalider av metaller bedöms vara en generell process som underlättar metaller flyktighet. Exempelvis bildas lättflyktig ruteniumoxyjodid då rutenium utsätts för oxidativa betingelser i närväro av jod. Ökande flyktighet har observerats också för metallerna tellur och niob under liknande betingelser.

Resultaten från Chalmers forskning under APRI-9 har bidragit med ny kunskap om fissionsprodukters beteende i primärsystem och reaktorinneslutning under ett haveri. Detta kan ge utökade möjligheter att förutsäga bidraget till källtermen från nuklidor som inte tidigare har ägnats mycket uppmärksamhet. Det kan också ge nya uppslag till hur man skulle kunna begränsa källtermsbidraget från dessa ämnen i utsläppen vid ett haveri.

## 4.2 Tellurium Chemistry

Iodine is one of the fission products of greatest concern in the event of a nuclear accident. Several different reasons for this concern exist, such as high fission yield, accumulation in the thyroid gland [MEI01] and volatility [HOU12]. Tellurium is another fission product that could be a potential issue in the event of a nuclear accident. It is directly problematic as it appears in highly volatile and very reactive forms. There are also indirect issues with tellurium, as iodine is part of the decay chain and, as such, tellurium contributes to the source term of radioactive iodine [ALO91]. Furthermore, tellurium is likely to affect kidneys, skin, nervous system and foetal tissue if taken up in the human body, and its chemical toxicity is on the level of selenium and arsenic [TAY96].

From a radiological perspective,  $^{131}\text{Te}$  ( $t_{1/2} = 25.0$  min),  $^{132}\text{Te}$  ( $t_{1/2} = 76.3$  h),  $^{133\text{m}}\text{Te}$  ( $t_{1/2} = 55.4$  min) and  $^{134}\text{Te}$  ( $t_{1/2} = 41.8$  min) can be considered to be the most relevant tellurium isotopes as these account for 60% of the total radioactivity of tellurium in the fuel [ALO91]. The half-lives of these isotopes suggest that the most relevant stage in the event of a nuclear accident for tellurium would be the early stage. The actual releases of tellurium to the environment were considerable (in air at Takasaki) during the Fukushima accident, as reported by Le Petit et. al. [LEP14].

The behaviour of tellurium in the core is well established. The form in the fuel, releases to the fuel gap, interaction with zircaloy cladding and with stainless steel are well known. However, less is known about tellurium transport, and knowledge of when tellurium enters the containment is based mostly on modelling and on data from other research fields (e.g. water chemistry based on geological information).

Regarding tellurium releases in general, one important specific limiting factor exists that can delay significant releases of tellurium. The zircaloy cladding material can act as a trap for tellurium by forming zirconium telluride. The cladding needs to be oxidized for tellurium to be released from the cladding. Tellurium is then released either as tellurium or as SnTe [BOE97, COL87, JOH88, LEW08]. Thus, releases of tellurium could be significant, not only in the early stage of an accident, but also later in the accident sequence.

## 4.3 Tellurium, behavior and interaction in the containment of an NPP

### 4.3.1. Background

The chemical speciation of the tellurium that enters the containment depends on e.g. the prior conditions, other fission products and humidity. In essence,  $\text{Te}/\text{Te}_2$ ,  $\text{H}_2\text{Te}$ ,  $\text{TeO}$ ,  $\text{Te}_2\text{O}_2$ ,  $\text{Cs}_2\text{Te}$  and  $\text{SnTe}$  all have the potential to reach the containment [MCF96]. As mentioned previously, tellurium is a reactive element. Metallic tellurium is likely to react with surfaces found throughout the reactor containment, e.g. metal surfaces (aluminium, zinc, copper) [GLA04] and epoxy painted surfaces. However, as the speciation of tellurium depends on the atmosphere (e.g. oxidizing or inert), humidity [MAL70] and other species, it is relevant to study more than one tellurium species.

Considering the reactive nature of tellurium, it is possible that it could react with these surfaces and consequently enhance or diminish the source term of tellurium by forming more volatile compounds or by being trapped at the surface. If no interaction takes

place, the deposited tellurium would instead be prone to re-volatilization (due to e.g. higher temperature or increasing flow). There is then a need to know the potential morphology of the absorbed and the re-volatilized species.

A tubular furnace, where tellurium can be heated to the temperature needed to induce volatilization, was used for the speciation investigations. The volatilized species were transported in the furnace to different surfaces of interest for potential reaction or deposition. The surfaces and the depositions were characterized using scanning electron microscopy (morphology), x-rad diffraction (speciation) and x-ray photoelectron spectroscopy (speciation).

#### 4.3.2. Method

Special furnaces have to be used in the investigations due to the high melting point (725 K) and boiling point (1263 K) [JOH18] of tellurium. The experimental setup had to be designed with the furnace as a base. The tellurium was heated (10 K/min) to 1273 K using a tubular furnace (ETF 30-50/18-S, Entech). A high purity alumina tube ( $\text{Al}_2\text{O}_3$ , 99.7%, Aliaxis) was used to contain the tellurium, which extended 96 cm outside the heating zone. The temperature at the end of the tube remained close to room temperature during the whole experiment (verified by n-thermocouples). A coupon consisting of the material investigated was positioned at the end. A gas flow (1.5 l/min) was maintained inside the tube during the heating phase, to transport the volatilized material to the surface. To be able to increase the humidity of the gas flow, a bottle filled with MQ water (Millipore, 18 M $\Omega$ ) was connected to the system prior to the furnace, through which the gas was bubbled. The experimental set-up is shown schematically in Figure 4.1.

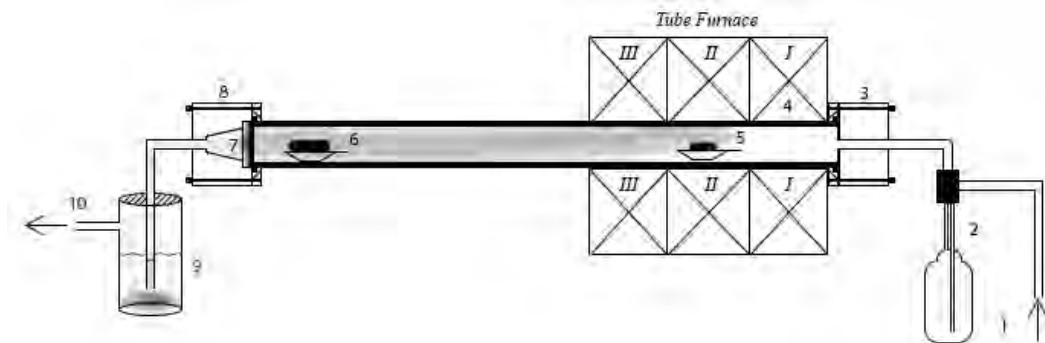


**Figure 4.1:** The experimental setup used for the experiments: (1) gas flow inlet, (2) the water source, either an atomizer or a water bottle, (3) cylindrical formed inlet connector made from stainless steel, (4) a tube made from  $\text{Al}_2\text{O}_3$  with a length of 130 cm, (5) the source material to be volatilized, (6) the metallic coupon, (7) a filter positioned at the end of the tube, (8) cone formed outlet connector made from stainless steel, (9) one or several cold traps used to prevent particles escaping, and (10) gas flow outlet. The furnace is divided into three heat zones: in Heat Zone I the gas flow is heated to the programmed temperature, in Heat Zone II the gas flow maintains at least the programmed temperature and in Heat Zone III the gas flow starts to cool down.

The focus of the experiment was on the metal surfaces. Aluminium rods (99.5%, Alfa Aesar), zinc rods (99.5%, Alfa Aesar) and a copper sheet (99.5%, Sigma Aldric) were made into coupons. The aluminium and zinc rods were made into discs (3-4 mm thickness) with diameters of 19 mm and 13 mm, respectively. The copper sheet was cut into 10x10 mm square coupons (3 mm thickness). Prior to use, the surfaces were

cleaned with ethanol, acetone and MQ-water (Millipore, 18 MΩ), in that order, to remove any organic impurities. The tellurium powder (99.8%, Sigma Aldrich) was used as supplied. Both the tellurium and the coupon were located in or on an alumina crucible (non-glazed porcelain boat, 85x13x8 mm, VWR). Three different carrier gases were investigated, with and without increased humidity. Each carrier gas represents different conditions; oxidizing (dry air, compressed air), inert (Ar, 99.999%, Air liquid) or reducing (Ar with 5% H<sub>2</sub>, AGA) conditions. Scanning electron microscopy (SEM), glancing angle x-ray diffraction spectroscopy (XRD) and x-ray photo-electron spectroscopy (XPS) were utilized to determine the speciation, morphology and possible interactions with the surface.

#### 4.3.3. Results

In the long term plan a total of 18 different experiments were planned. Out of these the results for the oxidizing and inert conditions are presented, as they are the most complete from an analysis standpoint. An overview of the experimental results can be found in Figures 4.2, 4.3 and 4.4.

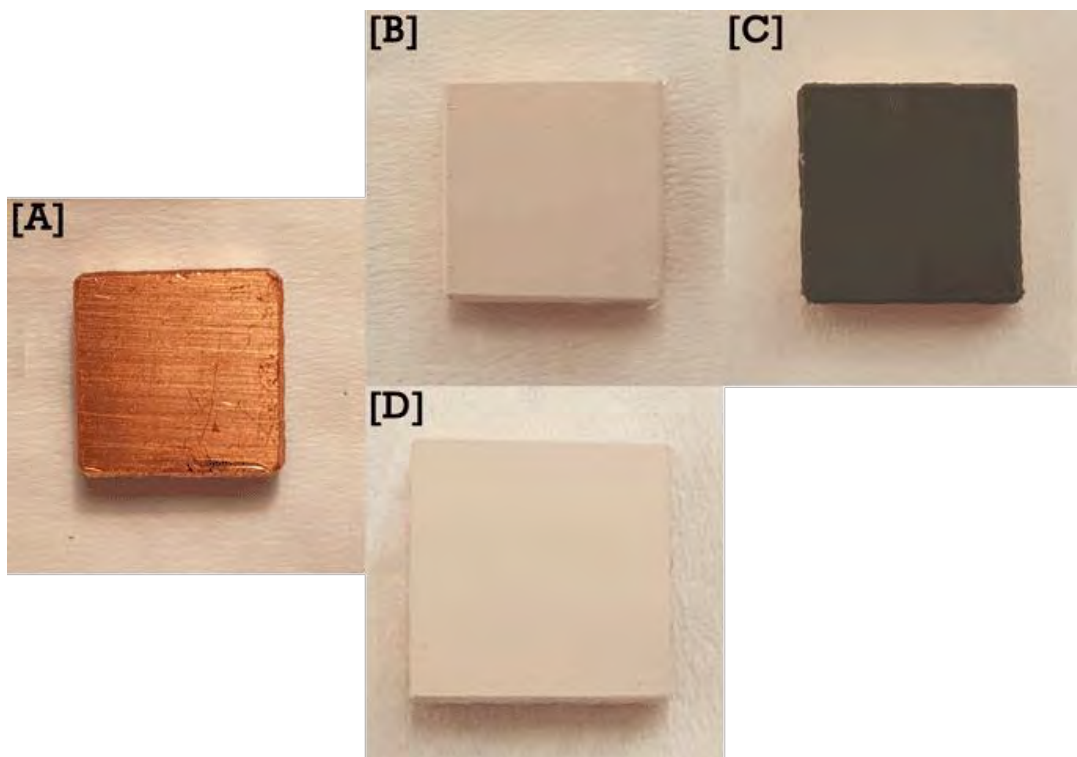


**Figure 4.2:** The results from exposing a copper coupon to tellurium in different atmospheres at room temperature. (A) A generic image of the copper coupons used, prior to the experiment. Image (B) shows the copper coupon after using air as the atmosphere during heating of the tellurium to 1273 K and (C) shows the coupon heated as in B, but using an argon atmosphere instead of air. The coupon in (D) is similar to (B), the difference is that the humidity of the gas has been increased significantly in (D). During the experiment, the atmosphere was maintained by a flow corresponding to 1.5 l/min that also transported the volatilized material to the coupon.

Observing the surfaces of the copper coupons in Figure 4.2, after deposition (B, C and D) in the different atmospheres, a significant deposition can be seen to have oc-

curred. For oxidizing conditions with increased humidity (D) or without (B), the colour is white in both cases. For inert conditions (C) the colour remains black (similar to the original tellurium powder colour).

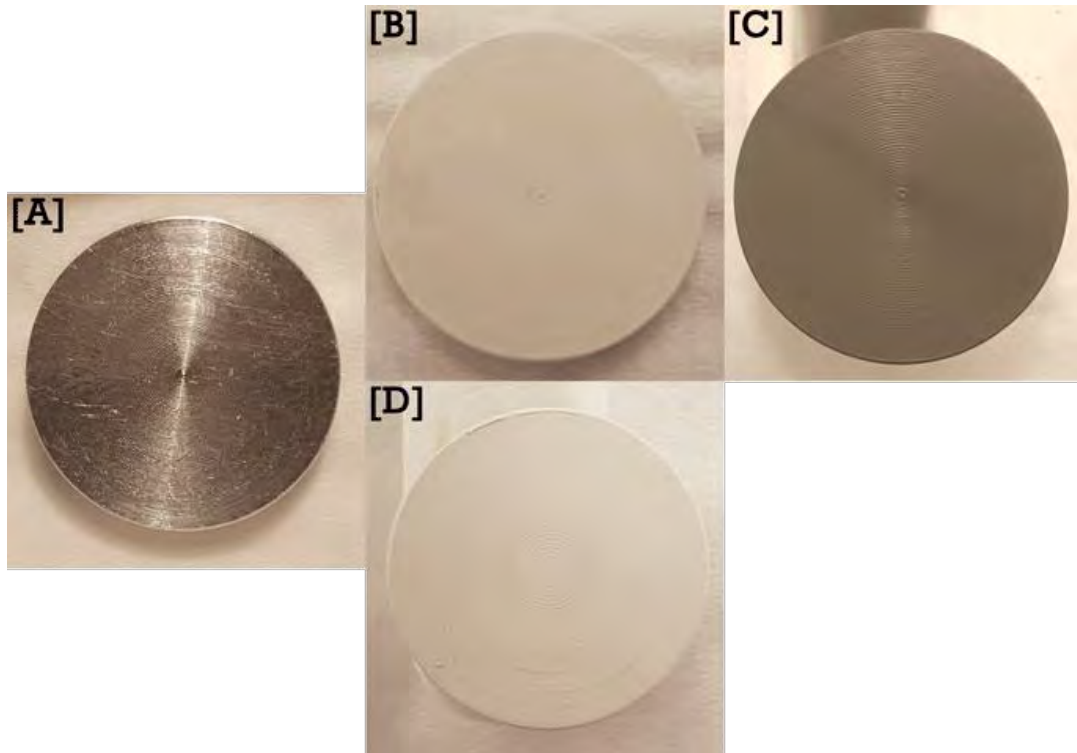


**Figure 4.3:** The results from exposing an aluminium coupon to tellurium in different atmospheres at room temperature. (A) A generic image of the aluminium coupons used, prior to the experiment. Image (B) shows the aluminium coupon after using air as the atmosphere during heating of the tellurium to 1273 K and (C) shows the coupon heated as in (B), but using an argon atmosphere instead of air. The coupon in (D) is similar to (B), the difference is that the humidity of the gas has been increased significantly. During the experiment, the atmosphere was maintained by a flow corresponding to 1.5 l/min that also transported the volatilized material to the coupon.

The deposition on the aluminium surfaces in Figure 4.3 is white for oxidizing conditions, both with humidity (D) and without (B), which is similar to what is observed from deposition on the copper coupons. For the inert experiment (C) the deposition remains black (the slightly greyer tone due to the underlying aluminium surface).

#### Scanning electron microscopy studies

The first step in the identification of the deposition was made using a SEM (Quanta 200 FEG ESEM) analysis. An indication of the morphology of the deposition can be observed in the micrographs produced.

The result from the SEM performed on the deposition made on the copper coupon can be seen in Figure 4.5.

A micrograph of the depositions in oxidizing conditions is shown in the left part of Figure 4.5 (A). Smooth spherical particles can be observed, with a wide range of varying diameters. The micrograph of the deposition under inert conditions is shown on the left side of Figure 4.5 (B). Here the smooth spherical particles are not present anymore. Instead “knobby” particles can be seen, with the occasional rectangular shaped particle. Furthermore, the micrographs indicate that there is no reaction with

the copper surface. This is further indicated, as the deposition is easily scraped off without any change to the copper surface.

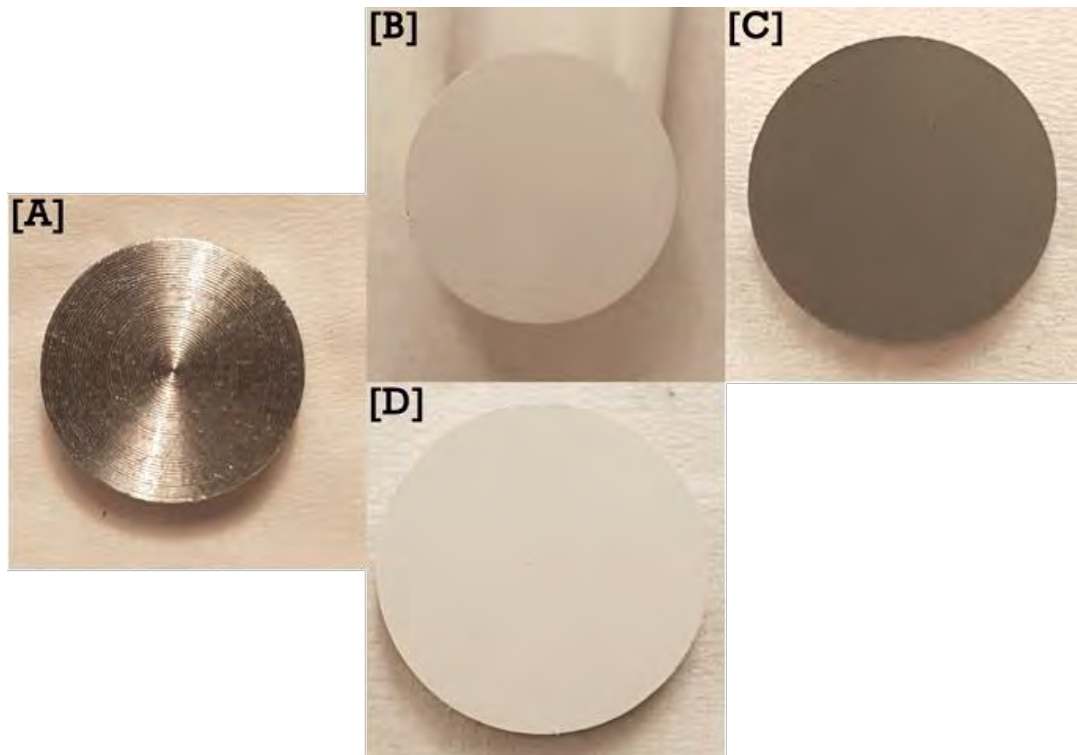


**Figure 4.4:** The results from exposing a zinc coupon to tellurium in different atmospheres at room temperature. (A) A generic image of the zinc coupons used, prior to the experiment. Image (B) shows the zinc coupon after using air as the atmosphere during heating of the tellurium to 1273 K and (C) shows the coupon heated as in (B), but using an argon atmosphere instead of air. The coupon in (D) is similar to (B), the difference is that the humidity of the gas has been increased significantly. During the experiment, the atmosphere was maintained by a flow corresponding to 1.5 l/min that also transported the volatilized material to the coupon.

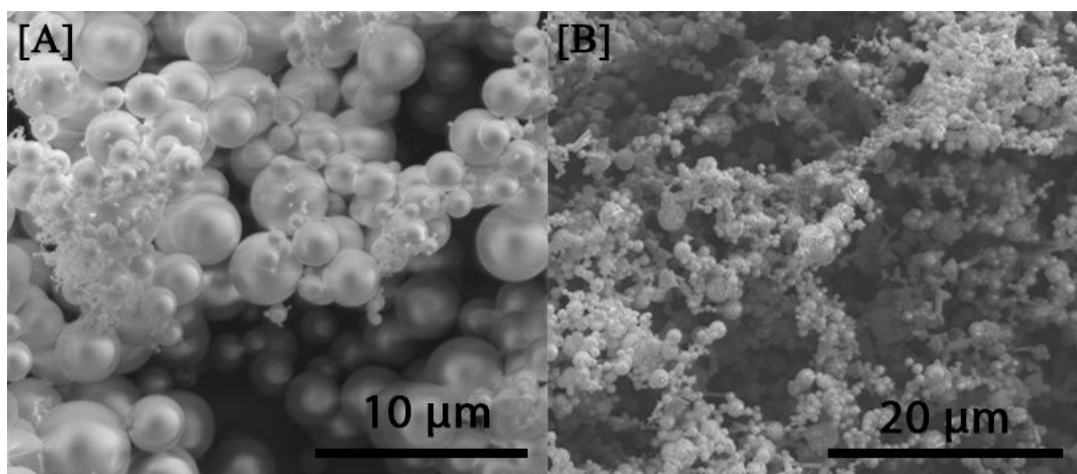


**Figure 4.5:** Micrographs of the depositions made on the copper coupon in (A) oxidizing non-humid and (B) inert non-humid conditions.

The micrographs of the depositions made on the aluminium coupon for oxidizing and inert conditions can be seen in Figure 4.6.

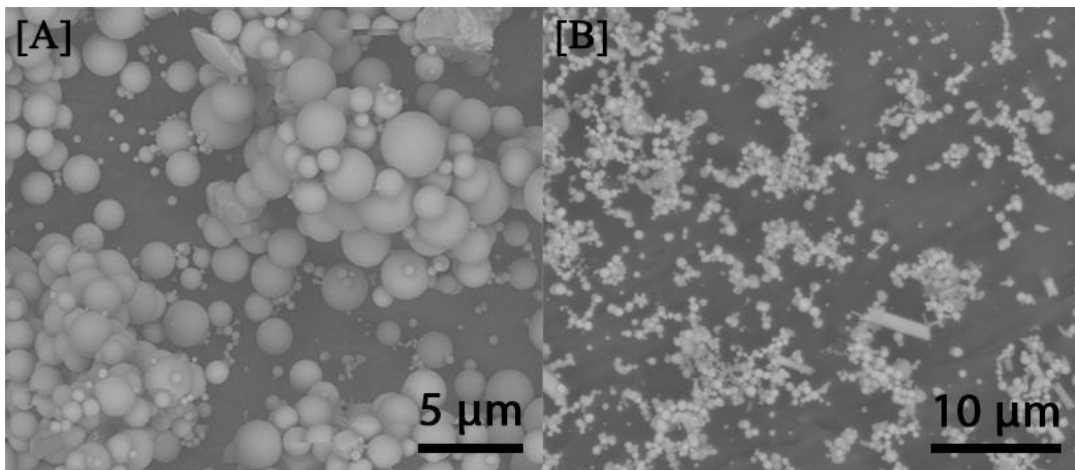


**Figure 4.6:** Micrographs of the depositions made on the aluminium coupon in (A) oxidizing non-humid, and (B) inert non-humid conditions. In the micrograph for inert conditions (B), the depositions were slightly damaged prior to the analysis.

From these micrographs it is observable for oxidizing conditions (A) that the main shape of the particles are smooth spheres. Occasionally, square or rectangular particles can also be seen. For inert conditions (B), the main particle type is smooth spheres. However, in this atmosphere considerably more rectangular objects can be seen. As for the copper coupon, no reaction of tellurium with the surface can be observed. This is supported by the fact that scraping away the deposition leaves the aluminium surface unaffected.

Micrographs of the depositions made on the zinc coupon under oxidizing and inert conditions can be seen in Figure 4.7.

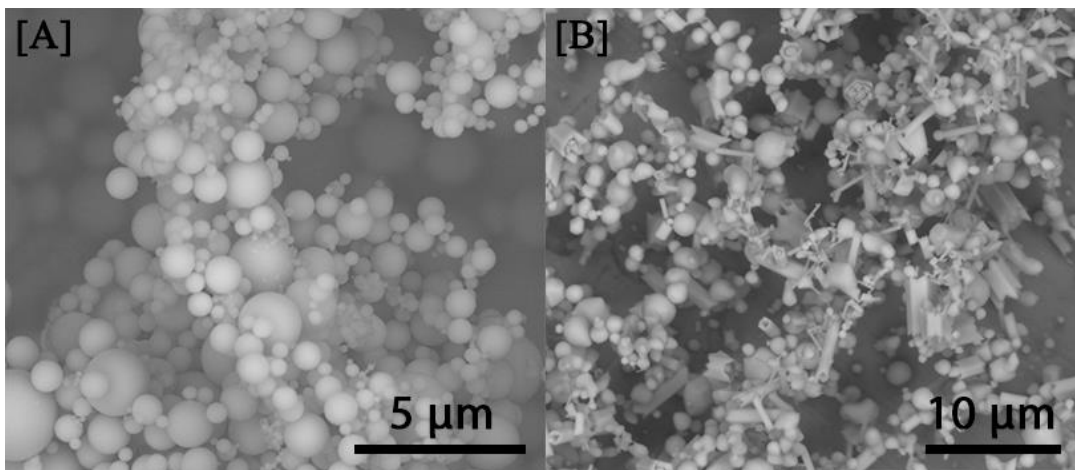


**Figure 4.7:** Micrographs of the depositions made on the zinc coupon in (A) oxidizing non-humid, and (B) inert non-humid conditions.

The first micrograph (A) shows the deposition made under oxidizing conditions. The main shape of the particles is smooth spheres. For inert conditions (B) there is a mixture of shapes, where the main format is a mix of non-spherical particle (e.g. rectangular spikes). However, there is also a considerable amount of smooth spheres present as well. As observed for the other two surfaces, no observable reaction has occurred. This is also supported by the observation of an unaffected surface when removing the deposition.

The SEM investigation seems to concur with the ocular inspection that the surfaces are similar, even though some smaller differences are observed.

#### X-ray diffraction spectroscopy studies

The depositions were also analysed using glancing angle XRD (Siemens Diffractometer D5000) and the spectra can be seen in Figures 4.8, 4.9 and 4.10. These spectra are obtained with a glancing angle of 5°. This was chosen based on the most prominent surface signal. The black spectrum represents the coupon analysis without deposition at a 5° angle (e.g. reference for the underlying surface). This means that when peaks appear in the black spectrum these peaks belong to the bulk material. Thus, the difference between the total spectra and this background represents the deposition signal. All identifications of compounds were made using the software's database (DIFFRAC.SUITE EVA, Bruker AXS version 4.1.1.), used in conjunction with the XRD equipment.

The results for the deposition on the copper coupons can be seen in Figure 4.8. The deposition produced on the copper coupon under oxidizing conditions (blue, line dots) can be seen in Figure 4.8. The appearance of a bulge can be seen between 20° and 35° (2θ). As this bulge does not appear in the dotted spectrum, it can be concluded that it belongs to the deposition. Furthermore, in this bulge two small peaks are visible. According to the software used, these peaks correspond to TeO<sub>2</sub> (paratellurite). The other spectrum (pink dots) represents the experiment carried out under inert conditions. By comparing this to the reference case, it can be seen that several new peaks have appeared. These peaks were positively identified as Te (metallic). This again supports the observation that no reaction has occurred, as no copper-tellurides can be observed.

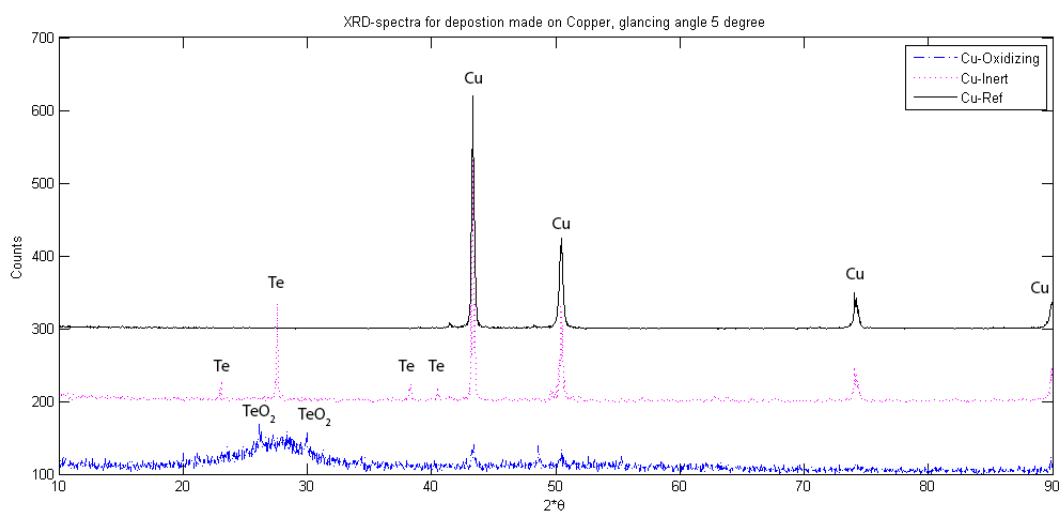


**Figure 4.8:** The results from X-ray diffraction analysis of the depositions made on the copper coupon under oxidizing (blue, line dots) and inert (pink, dots) conditions. The black spectrum represents an analysis made on a clean copper coupon surface. Each peak has been annotated with the identification made by the software used in conjunction with the XRD. Spectra have been scaled to fit in the figure.

The XRD results for the deposition made on the aluminium coupons can be seen in Figure 4.9.

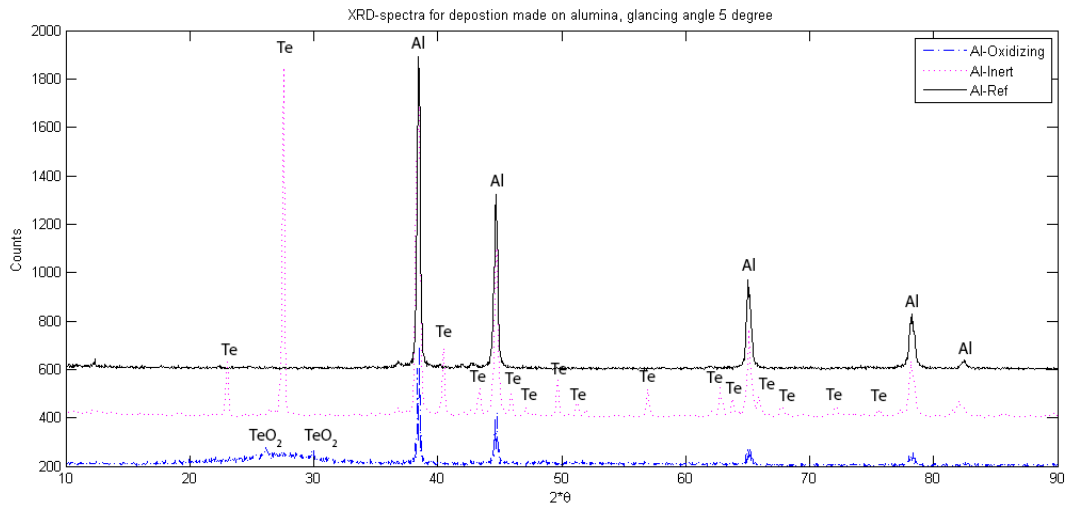


**Figure 4.9109:** The result from X-ray diffraction analysis of the depositions made on the aluminium coupon under oxidizing (blue, line dots) and inert (pink, dots) conditions. The black spectrum represents an analysis made on a clean aluminium coupon surface. Each peak has been annotated with the identification made by the software used in conjunction with the XRD. Spectra have been scaled to fit in the figure.

The XRD analysis (Figure 4.9) of the depositions on aluminium made in oxidizing conditions produced a spectrum (blue, line dots) with a bulge between  $20^\circ$  and  $35^\circ$  ( $2\theta$ ). As this bulge is lacking in the black spectrum (e.g. reference), this most likely belongs to the deposition. What can be observed in this bulge are two small peaks. These peaks correspond to  $\text{TeO}_2$  (paratellurite). The spectrum (pink, dots) representing inert conditions shows that the main composition of the deposition is Te (metallic). By comparing the number of tellurium peaks seen in the pink spectra in Figures 8 and 9, several more peaks can be found in Figure 9. This observation can be explained by a better levelled surface, as this is manually levelled before analysis.

Two spectra exist for the third metal surface, zinc, and these are shown in Figure 4.10. These correspond to oxidizing and inert conditions.

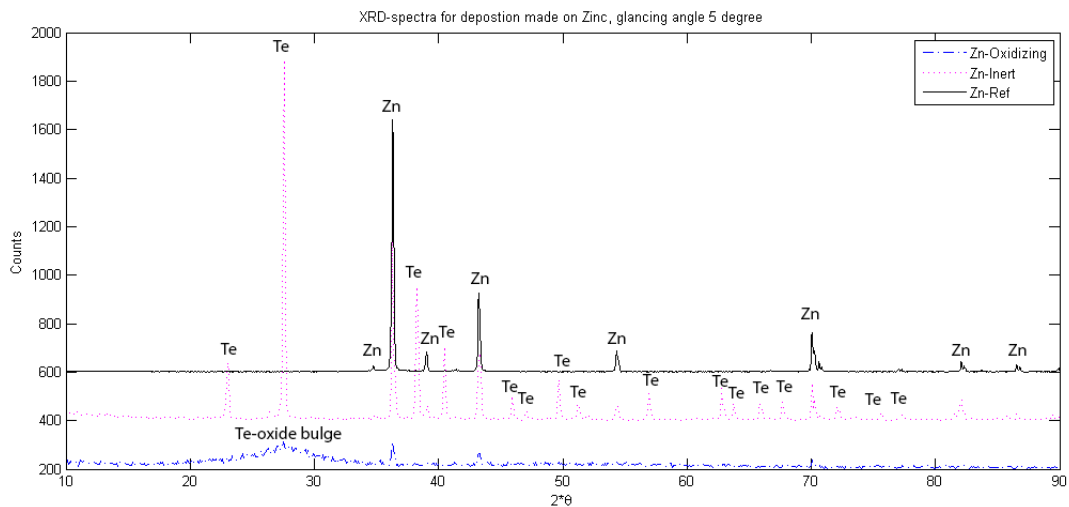


**Figure 4.10:** The results from X-ray diffraction analysis of the depositions made on the zinc coupon under oxidizing (blue, line dots) and inert (pink, dots) conditions. The black spectrum represents an analysis made on a clean zinc coupon surface. Each peak has been annotated

with the identification made by the software used in conjunction with the XRD. Spectra have been scaled to fit in the figure.

The XRD spectrum in Figure 4.10 (blue, line dots) of the deposition on the zinc coupon made during oxidizing conditions includes a bulge between  $20^\circ$  and  $35^\circ$  ( $2\theta$ ). Unlike the results presented above, this bulge does not contain the two peaks that were seen previously. As such, no positive indication of what this bulge could be is gained. However, as this bulge has appeared before with positive identification, it could be indicative of some sort of tellurium-oxide. The other spectrum (pink, dots) shows the deposition made under inert conditions. In this spectrum several peaks are present that do not appear in the reference spectrum. These peaks belong to Te (metallic), as in the previous cases.

#### X-ray photoelectron spectroscopy studies

XPS analysis was performed on the depositions made under inert conditions. As XPS uses high vacuum, the deposition had to be removed from the surface with a carbon tape (carbon adhesive discs). As such, the bulk material does not appear in these spectra. For each sample an overview scan and an in-focus scan is produced. The first scan is to determine which ranges are relevant for the sample. Following this, a more detailed scan over each range of interest is done. Herein, only the focused scans are presented. The XPS spectra for the deposition made under inert conditions on the copper coupon can be seen in Figure 4.11.

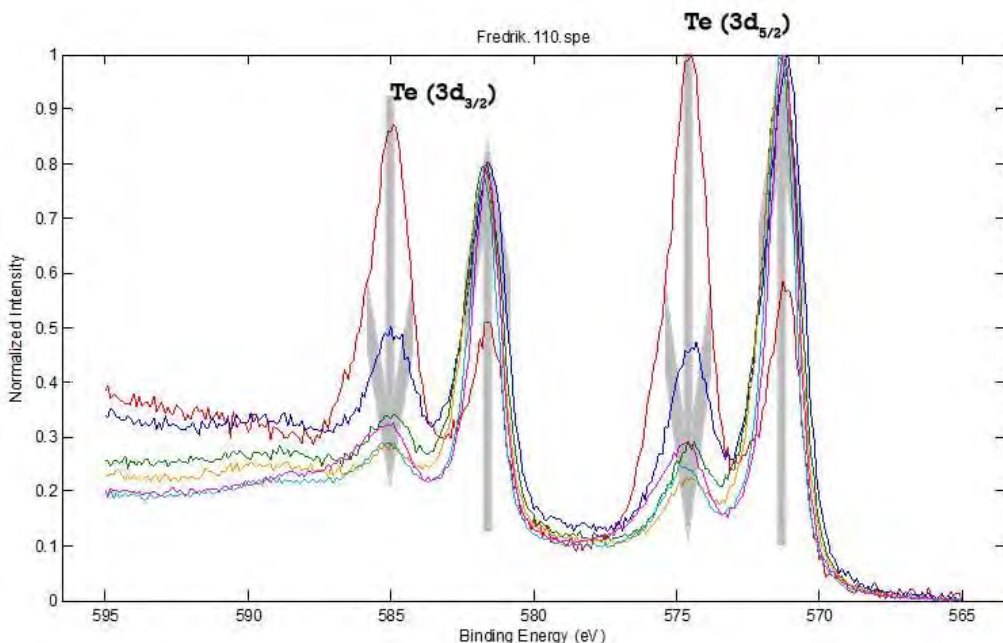


**Figure 4.11:** The spectra produced for the deposition made on the copper coupon under inert conditions. Two pairs of peaks can be seen; pair one is at 586.6 eV and 576.3 eV ( $3d_{3/2}$  and  $3d_{5/2}$ ) and the second pair at 583.3 eV and 572.9 eV ( $3d_{5/2}$  and  $3d_{5/2}$ ). Each spectrum represents different levels of sputtering, e.g. removal of a layer of atoms. Thus, as more sputtering is done, one pair decreases and the other pair increases. This change is indicated by arrows.

To gain a depth analysis of the deposition, a sputtering technique was used. This essentially means that layers of atoms are removed, and another analysis is performed

on the surface that emerges. The effect of the sputtering is indicated by arrows, showing that two peaks are decreasing as the other two are increasing.

The main peaks related to tellurium observed for the deposition on the copper surface obtained under inert conditions are at binding energies of 572.9, 576.3, 583.3, and 586.6 eV, respectively. According to what can be found in the literature [BAG77], the peaks at 586.6 ( $3d_{3/2}$ ) and 576.3 ( $3d_{5/2}$ ) are closest to  $\text{TeO}_2$  as this is reported to have binding energies at 586.5 eV ( $\pm 0.2$  eV,  $3d_{3/2}$ ) and 576.1 eV ( $\pm 0.2$  eV,  $3d_{5/2}$ ). Using the same literature, the other two peaks, at 583.3 ( $3d_{3/2}$ ) and 572.9 ( $3d_{5/2}$ ) can be positively matched as Te (metallic), as the reference peaks for this are 583.5 eV ( $\pm 0.2$  eV,  $3d_{3/2}$ ) and 573.1 eV ( $\pm 0.2$  eV,  $3d_{5/2}$ ).

The binding energy peaks seen in the XPS spectrum correlate to the energy of the photoelectron emitted during the XPS spectroscopy. Thus, one of these energies would represent an electron having been emitted that originated in a specific atomic orbital (e.g. s, p, d, f) of the atom. An example of the nomenclature used is  $3d_{3/2}$ . This represents an electron emitted from atomic orbital 3d, and the 3/2 indicates what spin it has (another spin would be 5/2). These energies are specific for each element and therefore become a signature of an element. If the atom is in a molecule, this will alter the energy (to which extent depends on the atom/molecule). Thus, it is possible to use reference data to identify what the analysed material chemically consists of. As the analysis is on an atomic scale, there is a restriction in the penetration of the sample.

The XPS spectrum produced in Figure 4.12 is of the deposition made on the zinc coupon.

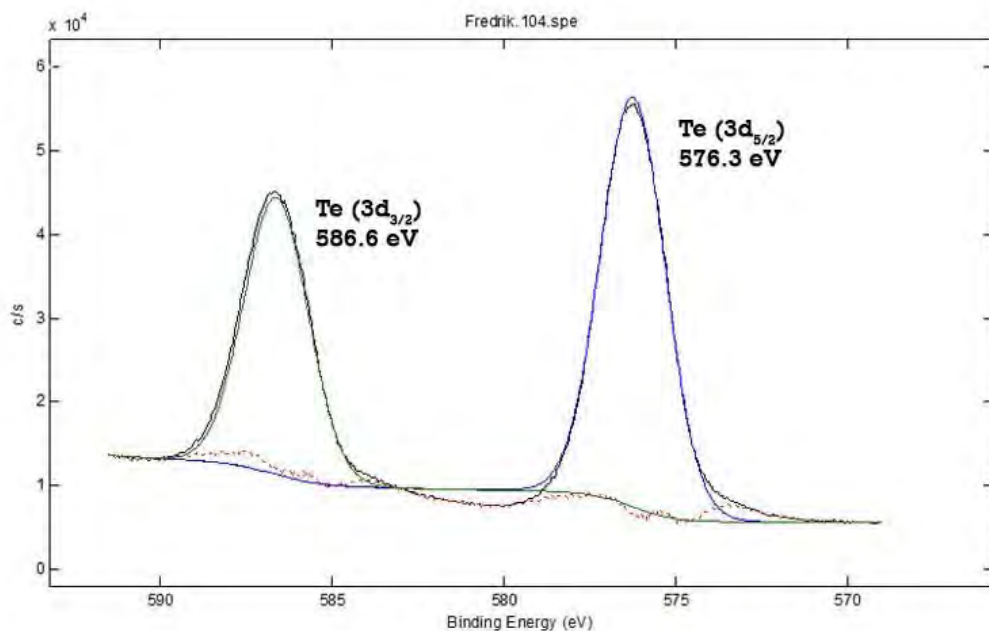


**Figure 4.12:** The spectrum (black) produced for the deposition made on the zinc coupon under oxidizing conditions. Two peaks can be seen, one located at the binding energy of 586.6 eV ( $3d_{3/2}$ ) and the second at 576.3 eV ( $3d_{5/2}$ ). The other colour indications (blue, green) represent the individual peaks.

No sputtering was performed for this sample. Two peaks are observed in Figure 4.12. These peaks are located at binding energies 586.6 eV and 576.3 eV, which according to the literature [BAG77] is close to the values of  $\text{TeO}_2$  at 586.5 eV ( $\pm 0.2$  eV,  $3\text{d}_{3/2}$ ) and 576.1 eV ( $\pm 0.2$  eV,  $3\text{d}_{5/2}$ ).

#### 4.3.4. Discussion and Conclusions

In the experiments so far no interaction between tellurium and the surfaces has been observed for oxidizing or inert conditions at near room temperature.

For the depositions made under oxidizing conditions, the results were almost completely indifferent of the underlying surface. The particles found after oxidizing conditions were smooth spheres of varying diameters. These seemingly deposited as “strings” extending out from the surfaces. The particles on all surfaces were indicated to be tellurium dioxide. However, only the deposition on the zinc coupon has been sufficiently analysed, as it has been investigated using XPS. The others have only been characterized by XRD, with minor peaks in the spectra indicating tellurium dioxide.

Under inert conditions the results are generally independent of the surface exposed. Only the deposition made on the copper surface showed a slight deviation from the other surfaces, as “knobby” particles could be observed. However, additional replicates are needed to confirm this difference. These “knobby” particles did not appear in the other depositions made on the other surface; instead smooth spherical particles were observed. A common particle on all surfaces was a non-spherical particle shaped as rectangular objects or spikes. For all surfaces the XRD spectra showed very distinct peaks indicating metallic tellurium. Only the XPS spectrum for the deposition made on the copper coupon showed a possible indication of tellurium oxides. However, as the XPS works on depths of atom layers and the XRD on a few micrometres, there is the possibility of tellurium self-oxidizing in air at the outermost layer of atoms. The latter requires verification with unused tellurium.

Another conclusion that can be made is that very small amounts of tellurium will be retained by these surfaces if conditions are changed after the depositions occurs. As there is no interaction with the surface, nothing would prevent tellurium from re-volatilizing if a fast-moving gas volume sweeps over the surface. Alternatively, heat could re-volatilize the deposit. This would then be limited to the melting point of the chemical species of the tellurium. However, if the temperature is high enough, reactions could take place between the surface and tellurium.

### 4.4 Investigation of the effects of seawater on the tellurium source term

#### 4.4.1. Background

Seawater was used to maintain cooling of the reactor units 1-3 during the Fukushima accident, and the possibility of longer times of an uncovered reactor core in unit 3 was even reported [IAE15]. The uncovering was reported to have occurred after the use of seawater for cooling, thus possibly depositing sea-salt on the surfaces inside the reactor. This could enable salt to react with the fission products on the surface of the fuel, cladding or in the gas phase.

Furthermore, other more long-lived radionuclides were reported to have unexpected behaviour [KAN15], i.e. monitoring the physical decay of released fission products. This monitoring showed that some of these long-lived radionuclides did not follow the expected physical decay; instead of decreasing they were increasing. This was suggested to be due to halide formation of these nuclides (as the relevant halide has a lower boiling point), which would then continue to leak from the reactor. The latter is feasible if the seawater used to maintain cooling of the reactors during the Fukushima accident is considered, as the halide chloride is thus introduced to the reactor core.

Tellurium was also included in this report [KAN15] and it was reported to be behaving as expected. However, due to the short half-life of the tellurium isotopes measured, the effect due to possible halide formation could have been undetectable at the time of the first measurement (20 days).

Considering the actions taken during Fukushima and what has been reported in the literature [KAN15], experiments were designed to determine to which extent sodium chloride could affect the volatilization of tellurium and if tellurium chloride species are formed.

#### 4.4.2. Method

To determine if any reaction can be determined between tellurium and sodium chloride, thermogravimetric analysis (TGA) studies were performed. These studies were carried out with TGA (TGAQ500, TA instrument) using alumina pans (TA instrument). The pans were cleaned prior to use with 1 M HNO<sub>3</sub> (70%, ACS reagent, Sigma Aldrich), MQ-water (Millipore, 18 MΩ) and were dried in a heating cabinet. The samples were prepared by mixing tellurium (99.8%, 200 mesh, Sigma Aldrich), as supplied, with sodium chloride (99.5%, ACROS ORGANICS). To create a more homogenous mixture, the sodium chloride was ground down using a mortar and pestle prior to mixing. Three ratios (by weight) of tellurium and sodium chloride were investigated (5:1, 2:2, 1:5), as well as two reference cases containing only either tellurium or sodium chloride. The samples (9 mg) were added to the pans and gentle tapping was done on the side of the pan to spread out the sample.

Two atmospheres were investigated, inert conditions, using nitrogen (99.98%, in house gas), and oxidizing conditions, using synthetic air (79%/21% nitrogen/oxygen, AGA). During the experiment, two gas flows were maintained; one to establish the atmosphere investigated and to transport away volatilized material (90 ml/min), and the second, to support the pan (10 ml/min). The flow rates were monitored by the equipment.

The method used for the TGA was as follows:

1. Heating (5 K/min) from ambient temperature to the isothermal temperature (1137 K).
2. Maintaining the isothermal temperature (20 min).
3. Cooling of the system (10 K/min).

Cleaning was performed between all experiments by removing residues from all piping extending from the furnace. A “zero” experiment, under inert conditions, with the same configuration as described for the TGA method was also made.

#### 4.4.3. Results

The results produced by the TGA can be found in Figures 4.13 and 4.14. These show the three different ratios (black, pink and red lines), as well as the two reference cases (blue and green), for each atmosphere. No replicates have been made, but will be produced at a later stage. What each line represents is the temperature-dependence of the normalized mass loss.

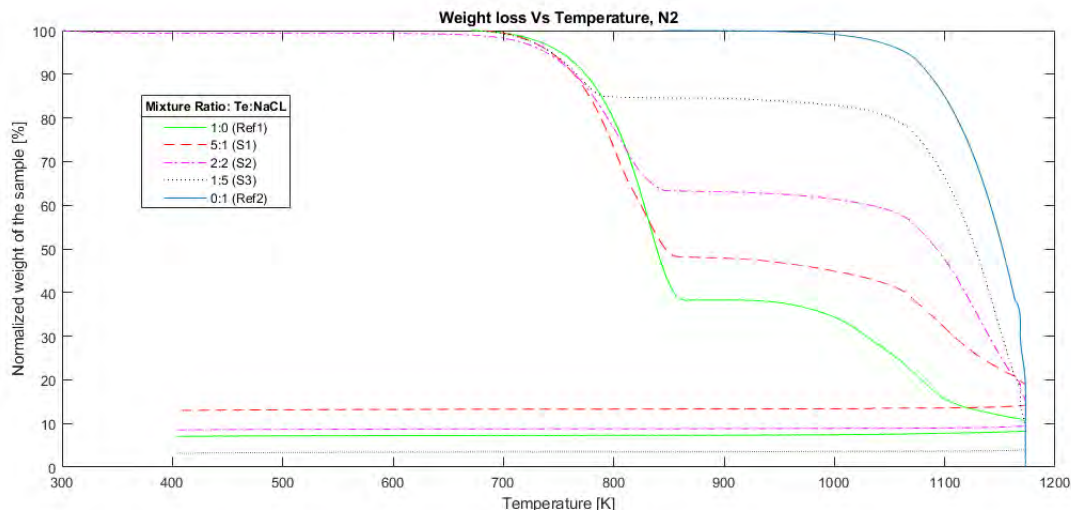


**Figure 4.13:** The thermogravimetric analysis results for the different Te:NaCl-ratios (weight basis) heated under inert conditions. The different lines represent: 1:0 (Ref 1, green), 5:1 (S1, red dashes), 2:2 (S2, pink line dots), 1:5 (S3, black dots) and 0:1 (Ref2, blue) of tellurium and sodium chloride, respectively. The weight shown has been normalized towards the first measured point by the thermogravimetric analysis.

The results for inert conditions can be seen in Figure 4.13. For the mixtures and tellurium reference case, the mass starts to decrease at 700 K. This decrease continues until 790-860 K (the temperature is slightly different for each case). At this temperature the mass change flattens out. After this the mass change starts to occur again. However, depending on the tellurium content, mass change starts at a different temperature. For pure tellurium and when the ratio between tellurium and sodium chloride is 5:1, mass decrease starts at 930 K. For the other two mixtures and the sodium chloride reference case, the mass decrease starts above 980 K. For tellurium alone there is a third gradient for the mass loss, starting at 1080 K.

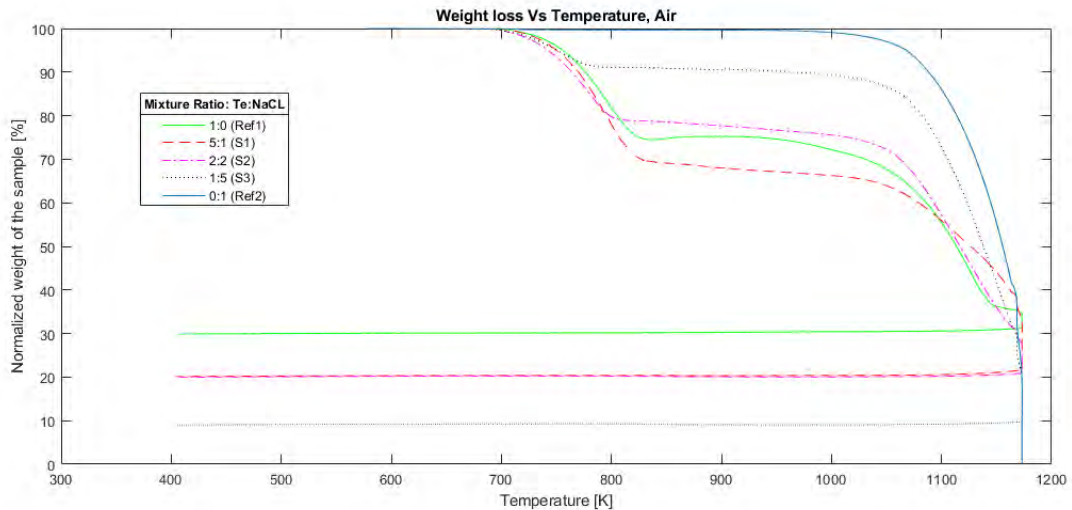


**Figure 4.14:** The thermogravimetric analysis results for the different Te:NaCl-ratios (weight basis) heated in oxidizing conditions. The different lines represent: 1:0 (Ref 1, green), 5:1 (S1, red dashes), 2:2 (S2, pink line dots), 1:5 (S3, black dots) and 0:1 (Ref2, blue) of tellurium and sodium chloride, respectively. The weight shown has been normalized towards the first measured point by the thermogravimetric analysis.

The results for oxidizing conditions can be seen in Figure 4.14. When sodium chloride is present in the sample the mass change is similar to the inert conditions (Figure 4.13). However, this is true only for the general behaviour, as the mass losses occur to different degrees. Moreover, the flattening never becomes completely flat. It is slightly decreasing for all mixtures. Similarly, to the inert conditions, there is a second distinct mass decrease phase starting at 1040 K for the mixtures in oxidizing conditions. The reference case with only sodium chloride shows no difference at all from the inert conditions and follows the same trend. However, the reference case with only tellurium is considerably different. Instead of flattening out, there is an increase in mass. This increase continues until roughly 970 K, and then the mass starts to decrease again. This mass decreasing phase consists of two slightly different gradients.

#### 4.4.4. Conclusions

The results from the inert conditions (Figure 4.13), showed no indication of interaction between tellurium and sodium chloride. Considering the difference in melting point of the two, 722.66 K and 1075.168 K, respectively [JOH18] it is likely that most of the tellurium would have volatilized at this point, potentially preventing a reaction from occurring. Furthermore, comparing the reference cases seen in Figure 4.13 , it can be observed that at the time when the sodium chloride starts to melt, roughly 20% of the tellurium remains. Thus, the amount of tellurium left could become a limiting factor for a possible reaction between tellurium and sodium chloride.

Observing the result for oxidizing conditions, a significant change can be seen when sodium chloride is mixed with tellurium, as the mass increase observed in the tellurium reference case is completely gone when sodium chloride is present, even in small amounts. Instead a slight decrease occurs, which at 1040 K starts to be significant. This could be explained by sodium chloride interacting with oxygen and forming more volatile species. However, as can be seen in the sodium chloride reference case, oxygen alone does not seemingly affect the sodium chloride. Thus, something

is occurring between either tellurium and sodium chloride or tellurium, sodium chloride and oxygen that induces a mass decrease that overtakes the mass increase caused by possible oxidation. Alternatively, it prevents the oxidation completely.

Thus, there is evidence that seawater used for reactor for cooling could have an impact on the tellurium source term. However, it is still unclear which the formed species are. It is also unclear if the formed species could further react with their surroundings. Furthermore, other fission products could also be affected by halide formation and thus increase their source terms. In this report the scenario envisaged is if a dry-out of the reactor occurs, which supposedly occurred during the Fukushima accident. If a dry-out occurs after the use of seawater for cooling, the salt present would deposit on all possible surfaces.

## 4.5 Ruthenium chemistry in severe accident conditions

### 4.5.1. Introduction

Along with iodine and cesium, ruthenium is considered to be one of the important elements released during a nuclear accident. This is due to the high radiological risk ruthenium presents, as well as its semi-volatile properties. From the chemical point of view a semi-volatile element can be characterized by high vapor pressure in metal or oxide form but not in both [HUN94]. Several ruthenium oxides have a high vapor pressure, thus ruthenium needs to be first oxidized from its metallic state to become volatile. In the case of a nuclear accident several factors will affect the behavior of ruthenium. The burn up, physical state of the fuel, reducing or oxidizing atmosphere and temperature will influence the amount and the kinetics of the released ruthenium. Once ruthenium is released from the fuel and the consistency of the reactor cooling system (RCS) is lost, it can be transported through the RCS into the containment. Previously under the Ruthenium Separate Effect Test (RUSET) experimental program both release and transport of ruthenium under oxidizing conditions were examined. It was shown that ruthenium evaporation occurs mainly in the forms of RuO<sub>3</sub> and RuO<sub>4</sub> [NAG05, VER10]. Partial pressure of RuO<sub>4</sub> at the outlet of the experimental facility was in the range of 10<sup>-6</sup> bar, which is about 4 orders higher than thermodynamic equilibrium calculations predict [SCH63]. Experiments performed under the APRI8 project also revealed significant effect of silver seed particles as well as nitrogen oxides on the partial pressure of gaseous ruthenium species in the reactor cooling system-simulated conditions. In order to gain a deeper insight into ruthenium chemistry with respect to interaction with air radiolysis products (NO<sub>2</sub>, N<sub>2</sub>O, HNO<sub>3</sub>), as well as other fission products (Cs, I) released from the fuel matrix during severe nuclear accident, several sets of experiments were designed and performed.

### 4.5.2. Experimental setup

Experiments on the ruthenium transport were performed in cooperation with VTT Technical centre of Finland. This cooperation between Chalmers and VTT in the case of severe nuclear accidents has been ongoing for almost a decade, partially under NKS and SARNET financing. The basic set-up of the VTT ruthenium transport facility is schematically described in Figure 4.15. The main component of the facility was the horizontal, tubular flow furnace (Entech, ETF20/18-II-L), which was used to heat the anhydrous RuO<sub>2</sub> powder (99.95%, Alfa Aesar). The furnace was 110 cm long with two heating sections, each 40 cm long. These zones were separated by a 38 mm

layer of insulation. At both ends of the furnace there was 131 mm of thermal insulation.

The furnace tube was made of high purity alumina ( $\text{Al}_2\text{O}_3$ , 99.7%) and its inner diameter was 22 mm. The alumina crucible with the  $\text{RuO}_2$  powder (mass 1 or 2 g) was placed over the second heated zone of the furnace, 25 cm from the outlet. The  $\text{RuO}_2$  powder was heated to the temperature desired for the experiment (1300 K-1700K) in an oxidizing flow and the formation of gaseous ruthenium oxides took place. In experiments with  $\text{NO}_2$ ,  $\text{N}_2\text{O}$  and  $\text{HNO}_3$  precursors, a second alumina tube ( $\text{Al}_2\text{O}_3$ , 99.7%, outer diameter 6 mm with a wall thickness of 1 mm) was inserted inside the furnace tube, the outlet of which was located directly after the crucible to avoid the effect of precursors on the ruthenium vaporization rate.

The total flow rate through the facility was 5 l/min (NTP; NTP conditions 0 °C, 101325 Pa).

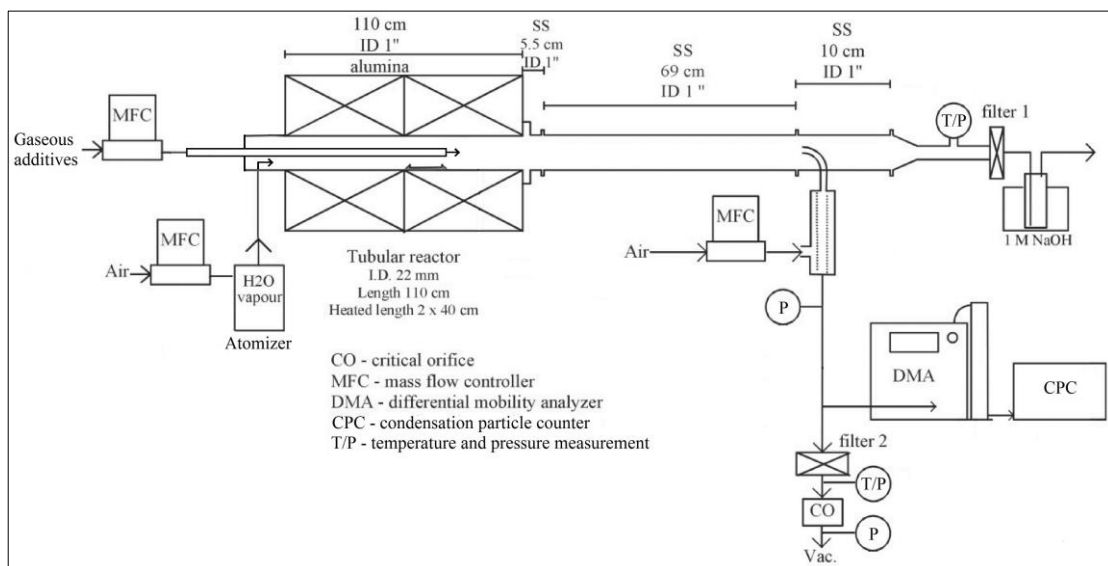


**Figure 4.15.** The basic set-up of the experimental facility for ruthenium tests[63].

After the gas flow passed through the outlet of the furnace, it was cooled in a stainless steel (SS; AISI 316L) tube. The aerosol products from the possible reaction of ruthenium oxides with the seed particles or the gaseous medium within the facility were filtered out at a point 106 cm downstream of the furnace. The filter used was 90 mm in diameter and it was made of Mitex® (pore size 5  $\mu\text{m}$ , Millipore). The temperature of the gas flow going through the filter was (30±2) °C. Downstream of the filter the gaseous ruthenium was trapped in a 1 M NaOH solution of Milli-Q water with two sequential liquid traps (400 ml of solution per trap) at ca. 25 °C. A NaOH solution was previously found to be an efficient trap for gaseous  $\text{RuO}_4$  [129], in which  $\text{RuO}_4$  is reduced into the form of ruthenate and perruthenate salts. The flow rate through the filter and traps was 4 l/min (NTP).

Aerosol gas-phase sampling was done at a point 74 cm downstream of the furnace using a J-shaped probe (inner diameter 4.6 mm) pointing upstream in the flow. The sample flow (1 l/min, NTP) was diluted and quenched to (25±2) °C with a porous tube diluter in order to minimize losses. The dilution ratio was 11±0.1. The formed particles were collected on a carbon/nickel grid (400 mesh, Agar Scientific) directly from the gas phase by directing a flow of 0.3 l/min [NTP] through the grid. The sampling flow rate was controlled using a critical orifice connected to a vacuum pump.

Particles were also collected on an analysis filter (pore size 5 µm, diameter 47 mm, Mitex®, Millipore). The sampling flow rate (2 l/min, NTP) through the analysis filter was also controlled with a critical orifice.

All gases fed into the facility were controlled with mass flow controllers (Brooks S5851). Pressure (Druck pressure meter, model DPI 145) and temperature (K-type thermocouple with a tip diameter of 1.5 mm) measurements were conducted upstream of the aerosol filter and at locations downstream of both the diluter and the analysis filter.

#### 4.5.3. Experimental procedures and matrix

The experiments were started by placing a crucible filled with RuO<sub>2</sub> powder (99.9%, Sigma-Aldrich), (1 g or 2 g depending on the experiment) into the furnace and then heating up the system (heating rate of 10 degrees per minute) under a nitrogen atmosphere. The gas flow through the facility was started when the set-point of the experiment (1300/1500/1700 K) was reached. The duration of the experiments was from 20 to 60 minutes. Particulate and gaseous reaction products in the experiments were collected on a filter and trapped in a 1M NaOH solution, respectively. At the same time, particles in the gas phase were analysed online and additional samples of the particles were collected for analyses to be conducted later. After the experiment the gas flow was stopped and the facility was cooled down (cooling rate of 10 degrees per minute) before the collected samples were removed.

The experimental matrix with the details of the experiments is presented in Table 4.1. Experiments with air atmosphere were reference experiments, in which RuO<sub>2</sub> powder was oxidized and transported. The release and transport results for vaporized ruthenium oxides were then compared with the other experiments.

The release rates of ruthenium from the crucible in the furnace were determined by weighing the mass of the crucible containing RuO<sub>2</sub> before and after the experiments. The mass of released RuO<sub>2</sub> was converted to the corresponding mass of metallic ruthenium for the evaluation of results.

In experiments with nitrogen oxides and HNO<sub>3</sub> an experimental setup with an inner tube was used. A flow of N<sub>2</sub>O, NO<sub>2</sub> or HNO<sub>3</sub> gases (2.5±0.1 l/min, NTP) was fed through the inner furnace tube. NO<sub>2</sub> and N<sub>2</sub>O were diluted with N<sub>2</sub> to obtain a desired concentration of precursor in the gas. As HNO<sub>3</sub> was fed with an additional atomizer (located at that time before the inlet of inner furnace tube, not shown in Figure 8), a carrier gas of nitrogen was used to transport HNO<sub>3</sub> droplets (solution of HNO<sub>3</sub> and Milli-Q water) via the heated line (120 °C) into the inlet of the inner furnace tube. After the outlet of the inner tube the precursors were mixed with the ruthenium volatile oxides in the gas stream, thus the overall flow rate at the outlet of the furnace was again 5 l/min, NTP.

The effect of seed CsI particles on the transport of ruthenium was investigated as follows. Air (flow rate of 5 l/min, NTP) was used to transport the droplets containing a 4% w/w CsI solution in the atomizer to the furnace by the main alumina tube. Water evaporated from the droplets inside the heated furnace and solid particles were formed. A low concentration of steam was therefore generated into the airflow.

The steam concentration in all experiments was dependant on the flow rate through the atomizer.

Ruthenium in the sodium hydroxide liquid traps was quantitatively precipitated with injection of EtOH (96%, Sigma-Aldrich). Samples were then centrifuged and precipitates of ruthenium were filtered from the solution. The filters used for trapping aerosols in the gas stream at the sampling point of the facility were used as they were, without additional manipulation. Both precipitates from the sodium hydroxide traps and aerosol filters were afterwards used for neutron activation and consequent quantification of transported elements.

**Table 4.1.** Experimental matrix for ruthenium transport experiments

T [K]	Gas	Flow rate over the crucible [l/min]	Precursor <sup>a</sup>	Additive precursor conc.	Humidity <sup>b</sup> [ppmV]	Other
1300±12	Air	5/2.5	RuO <sub>2</sub>	-	2.14E+04± 2.1E3	Atomizer with water only
1500±12						
1700±12						
1500±12	Air	5/2.5	RuO <sub>2</sub>	-	<60	-
1300±12	Air+NO <sub>2</sub>	2.5	RuO <sub>2</sub> +NO <sub>2</sub>	NO <sub>2</sub> 50 ppmV	2.14E+04± 2.1E3	Atomizer with water only
1500±12						
1700±12						
1300±12	Air+N <sub>2</sub> O	2.5	RuO <sub>2+</sub> N <sub>2</sub> O	N <sub>2</sub> O 50 ppmV	2.14E+04± 2.1E3	Atomizer with water only
1500±12						
1700±12						
1300±12	Air+HNO <sub>3</sub>	2.5	RuO <sub>2+</sub> HNO <sub>3</sub>	HNO <sub>3</sub> 5 ppmV	2.14E+04± 2.1E3	Atomizer with HNO <sub>3</sub> solution
1500±12						
1700±12						
1300±12	Air+CsI	5	RuO <sub>2+</sub> CsI	CsI 0.4 mg/l air	2.14E+04± 2.1E3	Atomizer with CsI 4% (w/w) solution
1500±12						
1700±12						

<sup>a</sup> The mass of RuO<sub>2</sub> powder in the crucible was 1 g for temperatures 1300 K and 1500 K, and 2 g for temperature 1700 K.

<sup>b</sup> The humidity in the gas flow came from the water-based precursor solution of the atomizer.

Chemical speciation of the transported aerosols was determined using a variety of techniques including X-ray photoelectron spectroscopy (XPS), X-ray diffraction (XRD), Scanning Electron Microscopy (SEM), and Transition Electron Microscopy (TEM). Speciation of the gaseous compounds trapped in the liquid sodium hydroxide traps was performed with UV/VIS spectrometry. Quantification of both transported gaseous and aerosol fractions was done by neutron activation connected to measurements by gamma spectrometry or, in the case of cesium and iodine, with ICP-MS.

#### 4.5.4. Results and discussion

##### Ruthenium release

It was assumed that the release rate of ruthenium from the crucible was constant during the course of each experiment, as has been shown previously [KAR07]. In addition, ruthenium was assumed to be released only when air was introduced into the gas flow, i.e. when the furnace was heated to the set-point temperature (1300 K-1700 K). The ruthenium release rate results are presented in Figure 4.16.

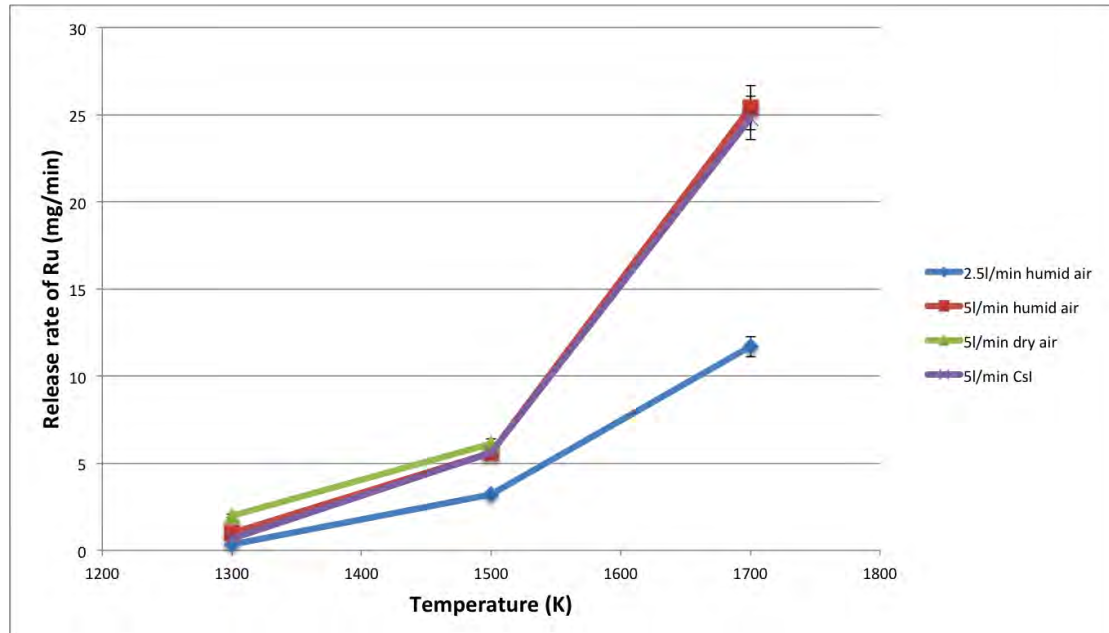


**Figure 4.16.** Dependence on temperature of ruthenium release rates from the crucible. The results are given as 2 standard deviations. Points for flow of 5 l/min in the humid air at 1300 K and 1700 K are taken from Kärkelä et al. [KAR07].

As can be seen from Figure 4.16 the release rates were fairly similar when the sample temperature and airflow over the crucible were kept constant. Increase of temperature led to significant increase of ruthenium release rate from RuO<sub>2</sub> powder. When the airflow over the sample was decreased to 2.5 l/min the release rate of ruthenium from the crucible was decreased to approximately half when compared to 5 l/min. Humidity in the atmosphere or CsI aerosols did not seem to have a significant effect on the release rate of ruthenium from the crucible.

#### Ruthenium transport

The amount of ruthenium transported as aerosol particles on the filter and as gaseous RuO<sub>4</sub> to the liquid traps of 1 M NaOH solution was quantified with the use of instrumental neutron activation analysis. In the experiments with CsI aerosols in the airflow, liquid traps were also analysed using ICP-MS in order to evaluate the content of cesium and iodine in the traps. Based on these measurements the quantities of ruthenium in the form of aerosols and gas could be determined. Effects of different precursors, temperatures and flow rates are discussed in the following sections.

#### The effect of temperature on ruthenium transport in air

The masses of ruthenium transported in gaseous and aerosol form in an air atmosphere under different temperatures and humidity are summarized in Table 4.2.

From the results it can be concluded that both increased humidity and increased temperature significantly increased the transport of ruthenium through the facility. The

increased transport due to humidity in the atmosphere mainly took place in the form of RuO<sub>2</sub> aerosol, with a decreased RuO<sub>4</sub> fraction when compared to dry air conditions. The proposed explanation is that steam passivizes the surfaces of the outlet tube, which is made of stainless steel, and thus decreases the catalytic decomposition of RuO<sub>3</sub> to RuO<sub>2</sub> and the deposition of RuO<sub>2</sub> taking place on the surface when the temperature decreases to below 1000 K. Therefore, the gas phase formation of RuO<sub>2</sub> particles is increased and the transport of particles is enhanced. The temperature had similar effects on the increase of RuO<sub>2</sub> and the decrease of the RuO<sub>4</sub> transported fraction. An explanation of this behaviour is that according to the thermodynamic calculations a higher fraction of RuO<sub>3</sub> is released from the RuO<sub>2</sub> in the crucible with increased temperature. Additionally, at 1700 K the non-negligible volatilization of RuO<sub>2</sub> itself and consequent condensation when the temperature decreases contribute to the transport of ruthenium in the form of aerosols.

**Table 4.2.** The fractions of ruthenium transported as RuO<sub>2</sub> aerosol particles and RuO<sub>4</sub> gas through the model primary circuit, as well as the fraction of ruthenium deposited inside the circuit. All values are given as % of the released Ru. The uncertainties are given as 1 standard deviation.

Exp. [#]	Total Ru transported (%)	RuO <sub>2</sub> trans- ported (%)	RuO <sub>4</sub> trans- ported (%)	Ru deposited (%)
1 1500 K dry 5 l/min	3.40±0.30	3.30±0.30	0.13±0.01	96.6±1.0
2 1300 K hu- mid 5 l/min <sup>a</sup>	11.6±1.2	6.5±0.7	5.2±0.5	88.4±1.3
3 1500 K hu- mid 5 l/min	21.3±2.1	21.2±2.1	0.20±0.02	78.7±2.8
4 1700 K hu- mid 5 l/min <sup>a</sup>	25.0±2.5	24.8±2.5	0.18±0.02	75.0±3.1
5 1300 K hu- mid 2.5 l/min	9.3±0.9	9.1±0.5	0.024±0.012	90.7±1.4
6 1500 K hu- mid 2.5 l/min	12.8±1.3	12.8±0.6	0.010±0.005	87.2±1.9
7 1700 K hu- mid 2.5 l/min	14.3±1.4	14.3±0.7	0.001±0.005	85.7±2.0

*a)* data taken from [KAR07].

The airflow seems to affect both the absolute amount of transported ruthenium and the RuO<sub>4</sub> transported fraction. This behaviour can be explained due to the longer residence time of the RuO<sub>4</sub> in the facility, therefore resulting in more time for the decomposition on the surfaces within the facility.

In all experiments the major part of the released ruthenium was deposited inside the facility, as can be seen in Table 4.2. The highest retention of ruthenium in the facility

was observed at the outlet of the furnace, where the temperature decreased rapidly. This behaviour was attributed to the decomposition of RuO<sub>3</sub> into solid ruthenium deposits. Similar effects were observed in the previous experiments with the same facility.

#### *The effect of temperature on ruthenium transport in air with 50ppmV NO<sub>2</sub>*

The results of the transported ruthenium in the form of aerosols and gaseous form under the humid air atmosphere with addition of 50 ppmV of NO<sub>2</sub> are presented in Figures 4.17 and 4.18. Introduction of NO<sub>2</sub> into the airflow strongly affected the resulting composition of transported ruthenium. As a result a higher transport of gaseous RuO<sub>4</sub> through the facility was observed when compared to the pure humid air atmosphere at temperatures of 1300 K and 1500 K.

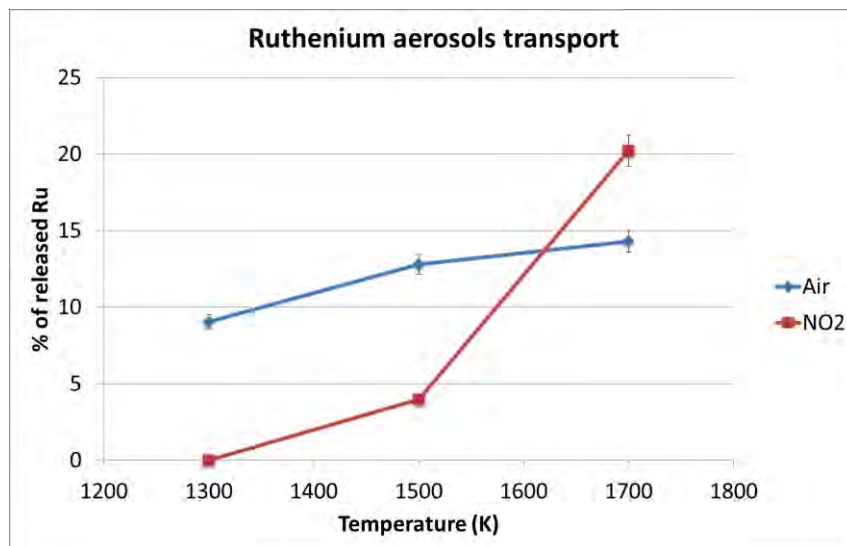


**Figure 4.17.** The fraction of ruthenium transported as RuO<sub>2</sub> aerosol particles through the model primary circuit. The values are given as % of the released ruthenium. The uncertainties are given as 2 standard deviations.

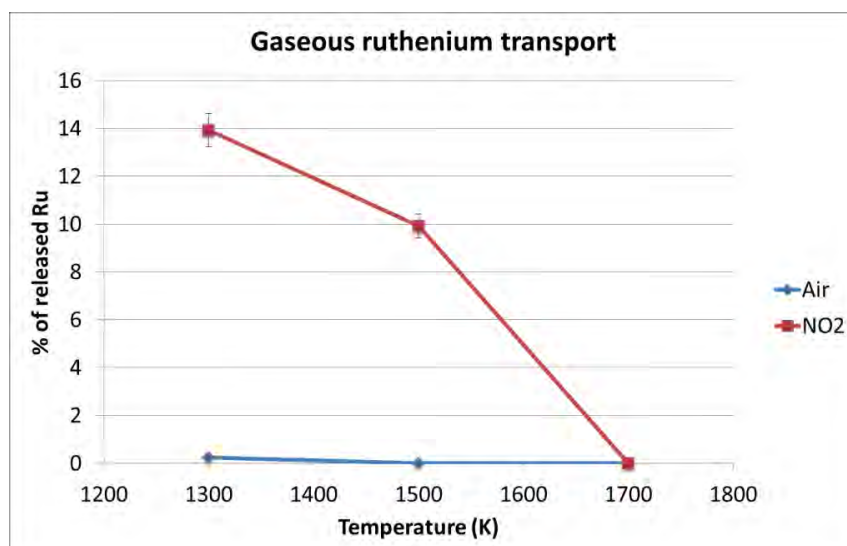
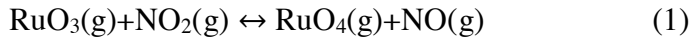


**Figure 4.18.** The fraction of ruthenium transported as RuO<sub>4</sub> gas through the model primary circuit. The values are given as % of the released ruthenium. The uncertainties are given as 2 standard deviations.

The increased gaseous fraction of transported ruthenium was attributed to reaction (1).



The temperature used during the experiments showed a strong effect on the form of transported ruthenium. A decreasing trend of transported gaseous fraction was observed from 1300 K to 1700 K. This behavior was attributed to the thermal decomposition of NO<sub>2</sub> according to reactions (29) and (30). A second reason is the decreasing equilibrium constant for the oxidation of RuO<sub>3</sub> over the temperature interval, as presented in Table 4.3 [HSC02].



**Table 4.3.** Equilibrium constants for the oxidation of RuO<sub>3</sub> by NO<sub>2</sub> to RuO<sub>4</sub> at different temperatures[HSC02].

Temperature	K <sub>eq</sub>
1300 K	28.55
1500 K	16.85
1700 K	11.3

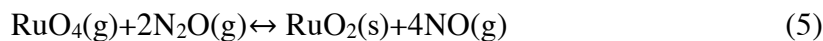
As a result of these two factors the ratios between the aerosol and gaseous fractions of transported ruthenium are lower than the thermodynamic equilibrium calculations predict.

As can be seen from Figures 4.17 and 4.18, the absolute amount of transported ruthenium was increased at temperatures of 1300 K and 1700 K when compared to the humid air atmosphere, with nearly 92% and 49% increase, respectively.

#### *The effect of temperature on ruthenium transport in air with 50 ppm V N<sub>2</sub>O*

The effect of N<sub>2</sub>O on the transport of ruthenium is presented in Figures 4.19 and 4.20.

The injection of N<sub>2</sub>O significantly increased the aerosol fraction of ruthenium transported through the facility when compared with the humid air experiment at 1500 K. This behavior was attributed to reactions (4) and (5) and the subsequent decomposition of RuO<sub>3</sub> into a RuO<sub>2</sub> solid at the outlet of the furnace, where the temperature decreased below 1000 K. The equilibrium constants for reactions (31) and (32) over the temperature interval used in the experiments are presented in Tables 4.4 and 4.5 [HSC02].



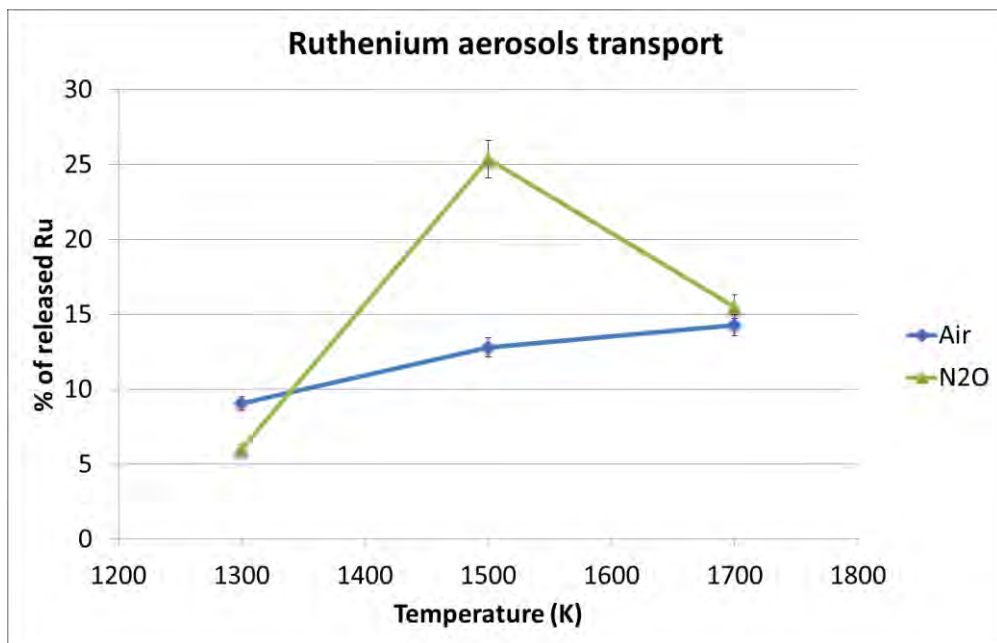


**Figure 4.19.** The fraction of ruthenium transported as  $\text{RuO}_2$  aerosol particles through the model primary circuit and the fraction of ruthenium deposited inside the circuit. The values are given as % of the released ruthenium. The uncertainties are given as 1 standard deviation.

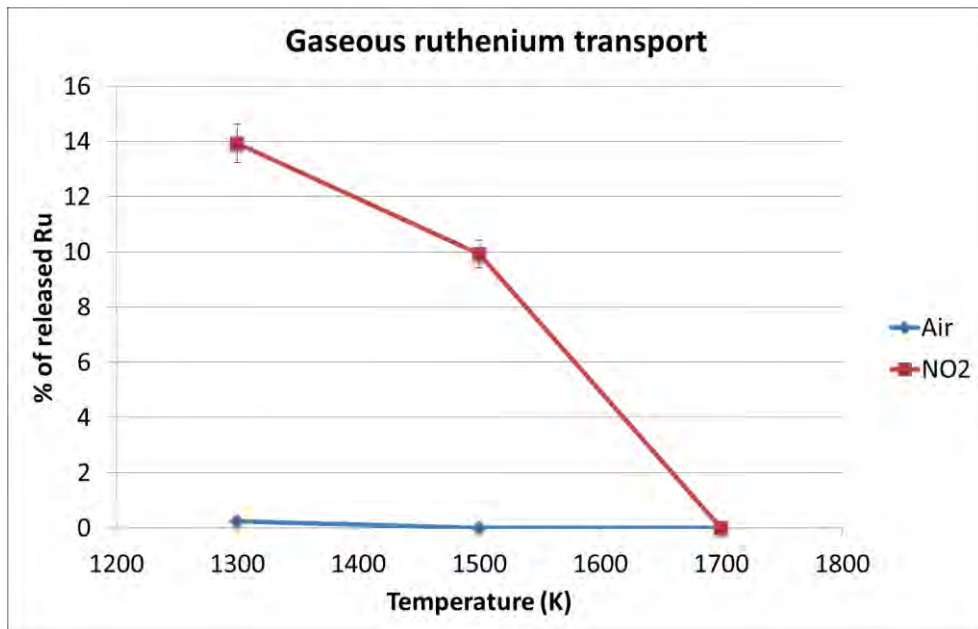


**Figure 4.20.** The fraction of ruthenium transported as  $\text{RuO}_4$  gas through the model primary circuit and the fraction of ruthenium deposited inside the circuit. The values are given as % of the released ruthenium. The uncertainties are given as 1 standard deviation.

**Table 4.4.** Equilibrium constants for the reduction of RuO<sub>4</sub> by N<sub>2</sub>O to RuO<sub>3</sub> at different temperatures. [HSC02]

Temperature	K <sub>eq</sub>
1300 K	19.03
1500 K	217.9
1700 K	137.6

**Table 4.5.** Equilibrium constants for the reduction of RuO<sub>4</sub> by N<sub>2</sub>O to RuO<sub>2</sub> at different temperatures. [HSC02]

Temperature	K <sub>eq</sub>
1300 K	1.48 E6
1500 K	4.79 E6
1700 K	1.21 E7

The overall transport of ruthenium through the facility was increased by a factor of 2 at 1500 K when compared to the humid air atmosphere. The opposite effect was detected at 1300 K when the overall transport was decreased by ca. 16%. A modest increase in ruthenium transport was observed at 1700 K.

*The effect of temperature on ruthenium transport in air with 5 ppmV HNO<sub>3</sub>*  
The results for ruthenium transport under the humid air atmosphere with 5 ppmV of HNO<sub>3</sub> are presented in Figures 4.21 and 4.22.

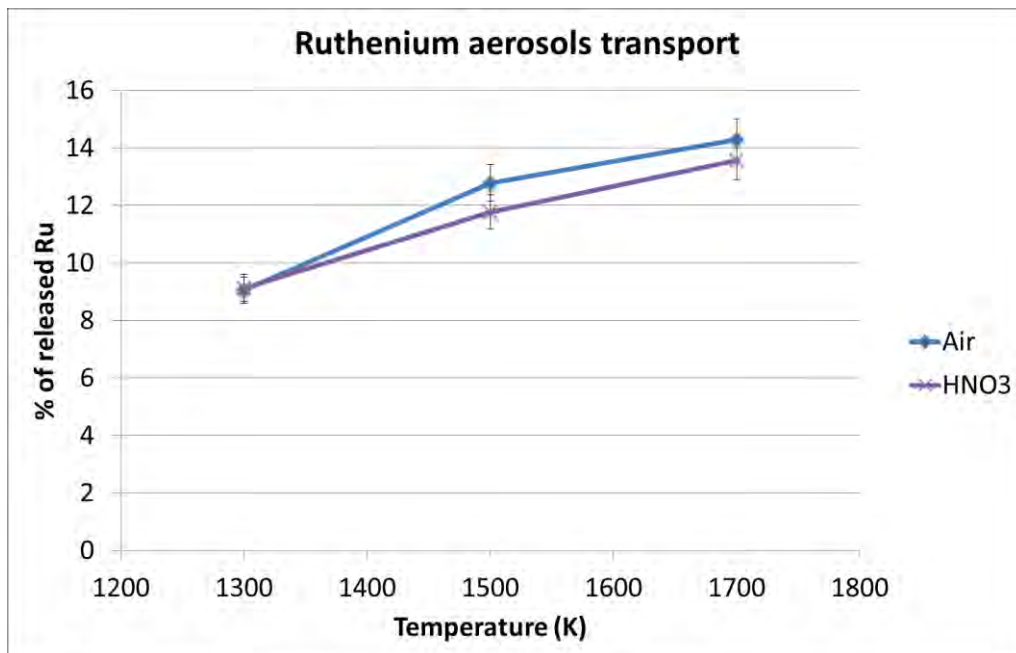


**Figure 4.21.** The fraction of ruthenium transported as RuO<sub>2</sub> aerosol particles through the model primary circuit and the fraction of ruthenium deposited inside the circuit. The values are given as % of the released ruthenium. The uncertainties are given as 1 standard deviation.

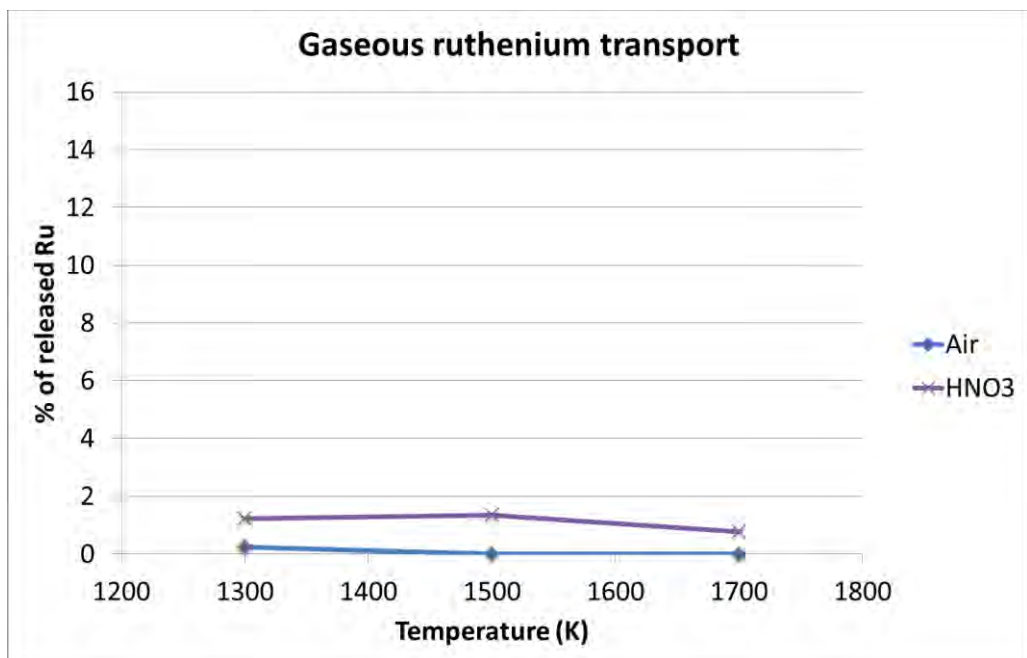


**Figure 4.22.** The fraction of ruthenium transported as RuO<sub>4</sub> gas through the model primary circuit and the fraction of ruthenium deposited inside the circuit. The values are given as % of the released ruthenium. The uncertainties are given as 1 standard deviation.

The introduction of HNO<sub>3</sub> feed into the airflow affected the composition of transported ruthenium, resulting in a higher transport of gaseous RuO<sub>4</sub> through the facility when compared to the pure humid air atmosphere at all experimental temperatures. The effect of nitric acid injection was not as prominent as could be expected from the thermodynamic calculations, as presented in Table 4.6 [HSC02].

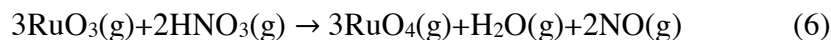


**Table 4.6.** Stability constants for the oxidation of RuO<sub>3</sub> by HNO<sub>3</sub> to RuO<sub>4</sub> at different temperatures [HSC02].

Temperature	K <sub>eq</sub>
1300 K	1.65 E11
1500 K	4.57 E10
1700 K	1.66 E10

An explanation for the decreased transport of gaseous ruthenium fraction, when compared to the thermodynamic calculations could be the thermal decomposition of HNO<sub>3</sub> to the lower nitrogen oxides, leading to the lower amount of precursor in the gas phase [ELL53, HAR62].

#### *The effect of temperature on ruthenium transport in air with a feed of CsI aerosols*

The results of transported ruthenium under the humid air atmosphere with the addition of CsI aerosols (ca. 0.8 mg/l air) into the airflow are presented in Figures 4.23 and 4.24.

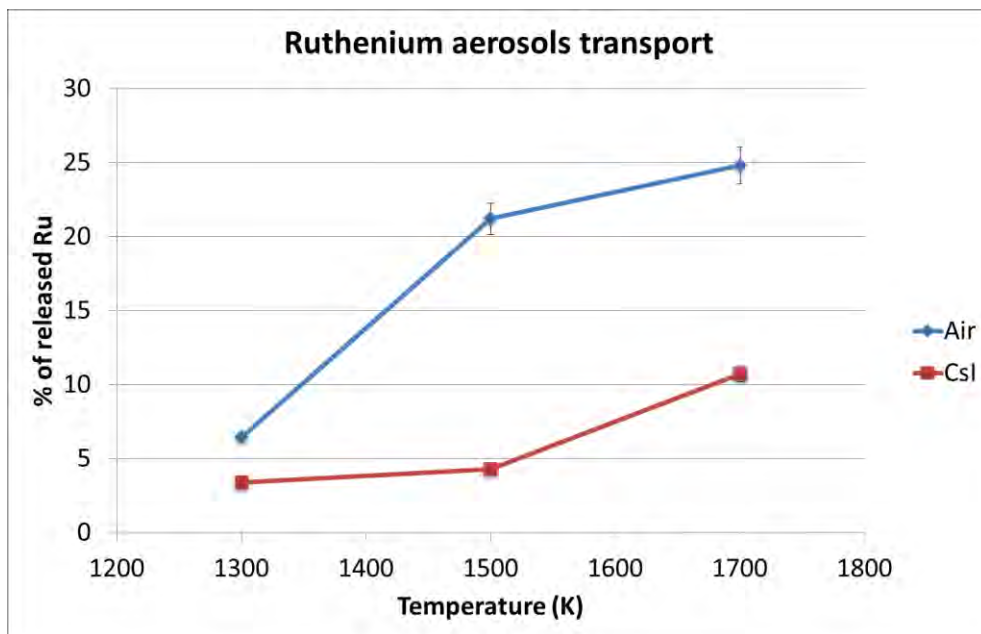


**Figure 4.23.** The fraction of ruthenium transported as  $\text{RuO}_2$  aerosol particles through the model primary circuit, as well as the fraction of ruthenium deposited inside the circuit. All values are given as % of the released Ru. The uncertainties are given as 1 standard deviation.

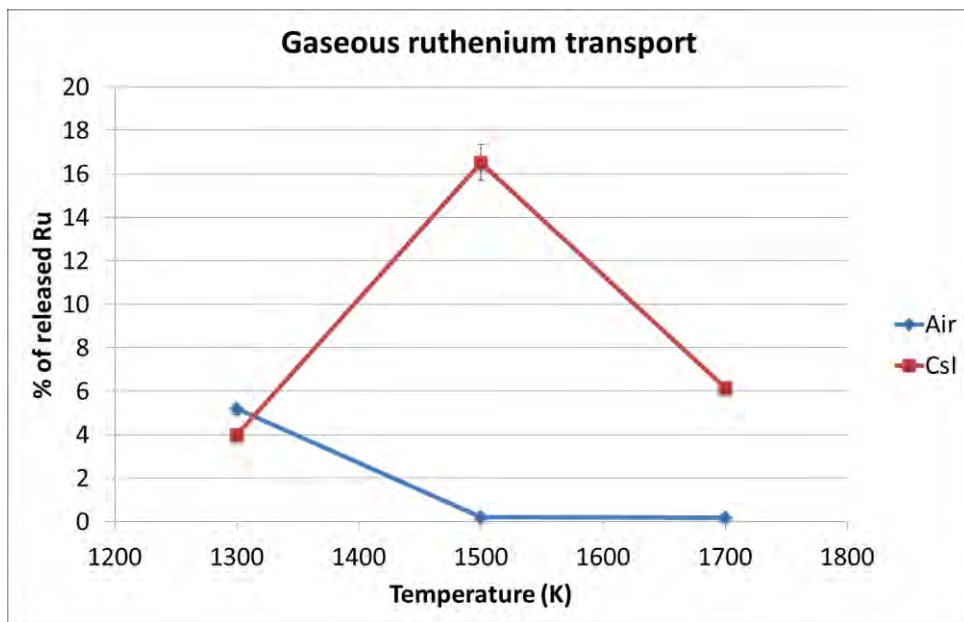


**Figure 4.23.** The fraction of ruthenium transported in gaseous form through the model primary circuit, as well as the fraction of ruthenium deposited inside the circuit. All values are given as % of the released Ru. The uncertainties are given as 1 standard deviation.

An introduction of CsI aerosols fed into the airflow led to the decrease of overall ruthenium transport through the facility at temperatures of 1300 K and 1700 K. During the experiment conducted at 1500 K the overall ruthenium transport was the same as in the pure humid air atmosphere. The fraction of transported gaseous ruthenium was increased significantly at temperatures of 1500 K and 1700 K. This effect was most prominent at 1500 K where about 16.5% of the transported ruthenium was in the form of a gas when compared to the 0.2% in humid air atmosphere at the same temperature.

*The transport of cesium and iodine in the experiments on ruthenium transport with CsI feed*

The amounts of cesium and iodine transported through the primary circuit simulating facility during the experiments conducted at temperatures of 1300 K-1700 K were quantified using NAA and ICP-MS. The results are summarized in Tables 4.7-4.9. The quantification of iodine collected on the main filter was not possible due to iodine evaporation during the neutron activation. Data is therefore available only for iodine collected in the liquid 1 M NaOH trap.

**Table 4.7.** Masses of cesium and iodine transported as aerosol particles and gas through the model primary circuit. The uncertainties are given as 1 standard deviation.

Exp	CsI in feed (mg)	CsI concentration (mg/l air)	Iodine as gas (mg)	Cs aerosol (mg)	Cs gas (mg)
1300 K CsI	126.9±3.1	0.81±0.02	1.1±0.005	0.25±0.01	1.2E-3±1.2E-5
1500 K CsI	123.4±3.1	0.79±0.02	1.7±0.008	0.42±0.02	9.2E-3±9.2E-5
1700 K CsI	120.1±3.1	0.77±0.02	2.8±0.01	0.45±0.02	1.0E-2±1.0E-4

**Table 4.8.** The fractions of cesium transported as aerosol particles and gas through the model primary circuit, as well as the fraction of cesium deposited inside the circuit. All values are given as % of the injected cesium in the form of CsI. The uncertainties are given as 1 standard deviation.

Exp.	Total Cs transported (%)	Cs aerosol transported (%)	Cs gas transported (%)	Cs deposited (%)
1300 K CsI	0.39±0.02	0.39±0.02	1.9E-3±1.9E-5	99.6±0.02
1500 K CsI	0.68±0.03	0.67±0.03	1.2E-2±1.2E-4	99.3±0.03
1700 K CsI	0.74±0.04	0.74±0.04	2.6E-3±2.6E-5	99.3±0.04

**Table 4.9.** The fractions of iodine transported as aerosol particles and gas through the model primary circuit, as well as the fraction of iodine deposited inside the circuit. All values are given as % of the injected iodine in the form of CsI. The uncertainties are given as 1 standard deviation.

Exp.	Total I transported (%)	I aerosol transported (%)	I gas transported (%)	I deposited (%)
1300 K CsI	1.72±0.01	-	1.72±0.01	98.28±0.01
1500 K CsI	2.76±0.01	-	2.76±0.01	97.24±0.01
1700 K CsI	4.75±0.02	-	4.75±0.02	95.26±0.02

As can be seen from Tables 4.7-4.9 iodine was partly volatilized from the feed of CsI and transferred in the form of gas to the liquid traps. The detected volatile fraction of cesium was very minor. As discussed further, some iodine was detected on the aerosol filter measured by XPS. The overall quantification of transported of iodine is therefore underestimated.

From the measured data it is obvious that the overall transport of both cesium and iodine through the facility was very small in all the performed experiments. The fraction of transported iodine increased when the temperature increased, whereas the increase of the transported cesium fraction was only minor.

#### 4.5.5. Characterization of the gaseous ruthenium fraction from all ruthenium transport experiments

Characterization of the gaseous ruthenium speciation was not possible due to the high temperatures inside the hot zone of the facility online. However, as the thermodynamic calculations and previously published results indicate, RuO<sub>4</sub> is the only gaseous ruthenium species that is relatively stable at temperatures lower than 1000 K. As it is known that RuO<sub>4</sub> forms ruthenate and perruthenate salts of sodium in solutions of NaOH, the liquid traps were examined by spectrophotometry in order to determine the formation of these compounds in the solutions. A representative UV-VIS spectrum of the liquid traps is presented in Figure 4.16.

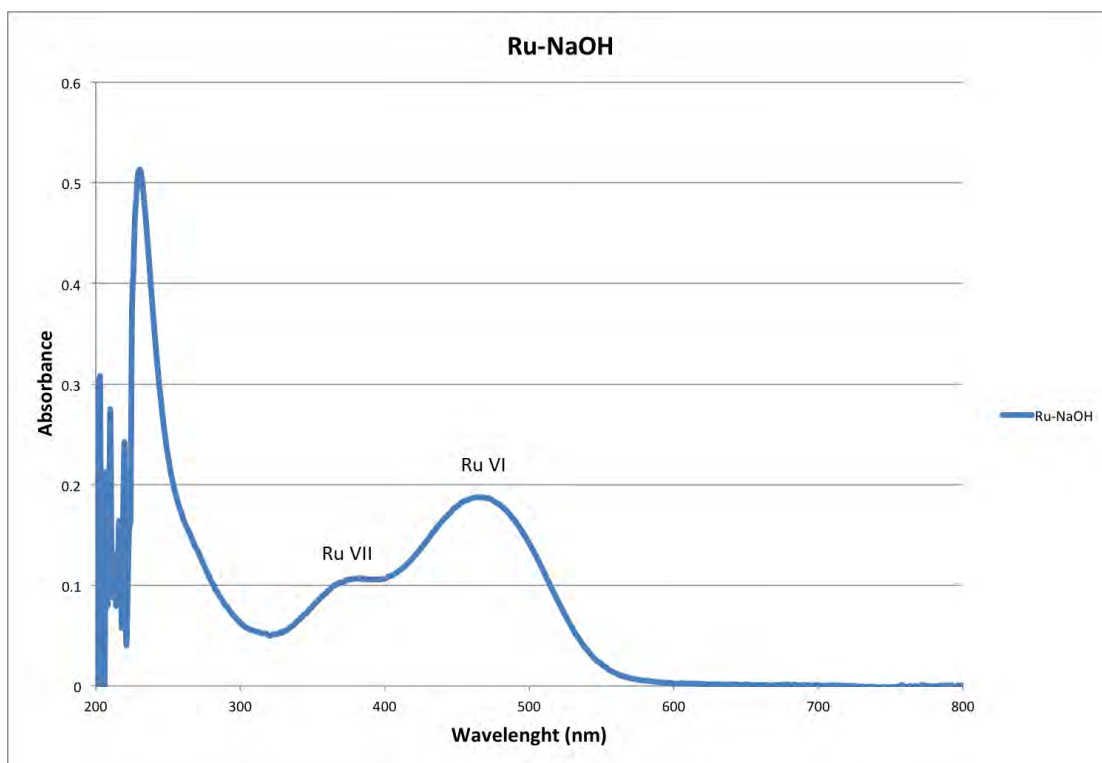


**Figure 4.24.** UV-VIS spectrum obtained from the measured 1 M NaOH liquid trap.

The two distinctive peaks originating from Ru<sup>VI+</sup> and Ru<sup>VII+</sup> could be identified in the obtained spectra from the experiments [CON52]. The spectra obtained from all the ruthenium transport experiments showed the same behavior. This, along with the data from the previous studies, was interpreted as a strong indication that the gaseous fraction of ruthenium collected in the 1 M NaOH traps was in the form of RuO<sub>4</sub>. However, it should be stated that if ruthenium in oxidation states (VI-VIII) formed volatile

oxyhalides with iodine and if those would be retained in the liquid traps, ruthenium absorption spectra would look very similar to spectra obtained during the experiments. Thus the possibility of gaseous ruthenium transport in the form of oxyhalides could not be disregarded in the experiments with CsI feed.

*SEM/EDX characterization of aerosols collected on the filters from ruthenium transport experiments*

The ruthenium particle samples collected during the experiments were analysed with a scanning electron microscope. The SEM micrographs of the particles collected from some of the experiments are presented in Figure 17. Depending on the reaction conditions, the morphology (particle size and shape) of ruthenium aerosol particles varied greatly between the samples. In experiments with humid air atmosphere the typical crystalline needle-shaped form of RuO<sub>2</sub> was clearly evident and was the predominant form of ruthenium in the samples.

The feed of NO<sub>2</sub> gas into the flow of Ru oxides seemed to have an effect on the shape and quantity of the ruthenium particles. A variety of different sized cuboid crystals were formed instead of needle shaped crystals. However, the concentration of the formed particles was very low due to the high formation of gaseous ruthenium and therefore only a few particles were observed on the grid for the analysis (see Figure 4.25b). In the other experiments the particle concentration was high inside the Ru transport facility and this led to an agglomeration of particles in the gas phase before these particles were collected on the grid, as can be seen in Figures 4.25a and 4.25c.

The Energy-dispersive X-ray spectroscopy (EDX) analysis of two spots on the sample from the experiment conducted in air verified that the particles that were formed contained ruthenium (Figure 18). The identified characteristic X-ray line energies for Ru were for example 2.558 keV (L<sub>α1</sub>) and 2.683 keV (L<sub>β1</sub>). In addition to Ru, signals of other elements were also observed at both analysis locations. Nickel originated from the grid and carbon from the foil, whereas the signal of aluminium was from the sample holder. Oxygen originated mainly from the oxidized Ru and the grid.

*XPS*

The chemical speciation of the particles transported through the facility that were collected directly from the gas phase on a quartz glass surface was analysed by XPS technique. As a result of the analysis the binding energies of ruthenium (3d5/2 peak), cesium (3d5/2 peak) and iodine (3d5/2 peak) (if used in the experiments) were obtained. The identification was based on the comparison between the identified binding energies of elements on the samples with the reference binding energy values found in the literature. The reference samples of commercial ruthenium dioxide powders, both anhydrous and hydrated (purity of 99.5%, Alfa Aesar), were analyzed and the obtained spectra were then compared with the spectra of ruthenium-containing samples. The reference values of the binding energies used in the evaluation of the data are presented in Table 4.10. As can be seen from Table 4.10, the binding energies are not only dependent on the oxidation state of ruthenium but also on its chemical environment, e.g. the hydration of RuO<sub>2</sub>. Thus, the comparison of all obtained spectra in the region of the Ru 3d5/2 peak gives better insight into the chemical characterization of the measured ruthenium compound.

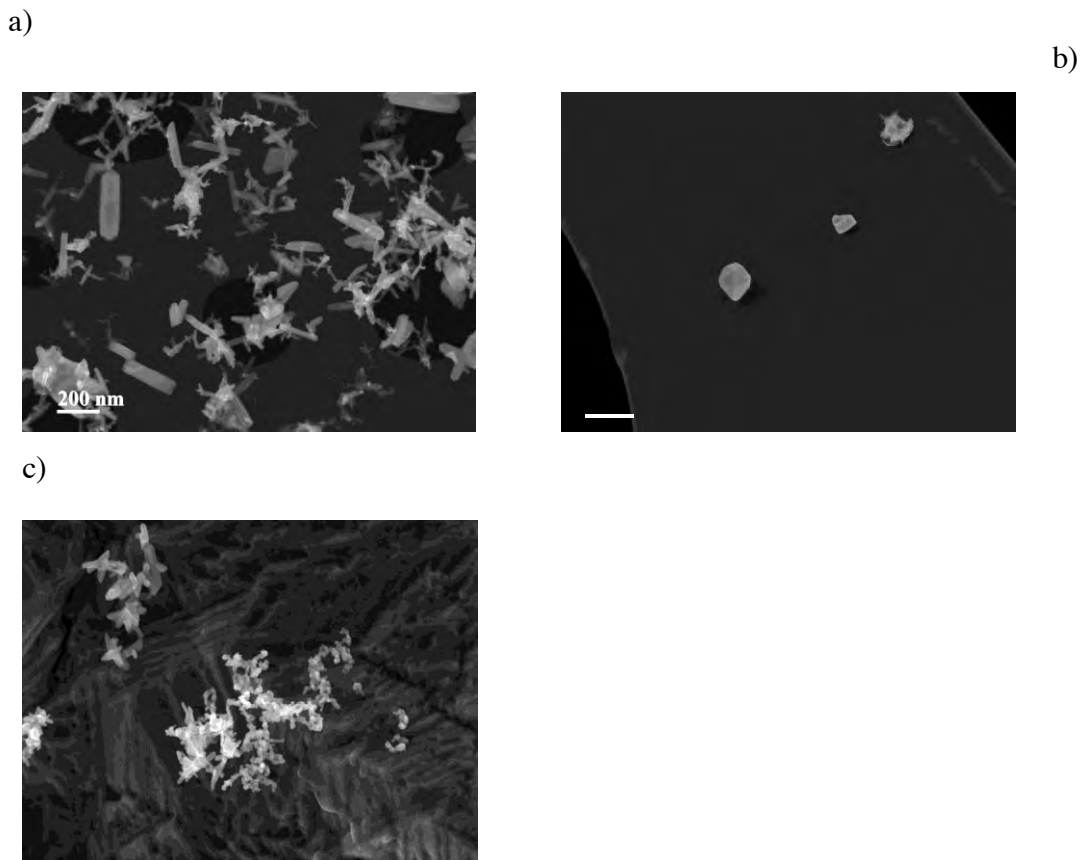


**Figure 4.25.** SEM micrographs of ruthenium particles on a nickel/carbon grid in experiments (a) with humid air, (b) with  $NO_2$  gas injection, and (c) with feed of CsI.

*XPS measurements of samples from experiments with air,  $N_2O$ ,  $NO_2$ , and  $HNO_3$  atmospheres*

The binding energies for the Ru 3d5/2 peak in all samples were within the region of 280.4 eV-280.5 eV, regardless of the atmosphere used, as can be seen in Figure 4.27. This provides a strong indication that the transported ruthenium aerosols were in the form of anhydrous  $RuO_2$  in all experimental conditions. The overall characteristics of the spectra are very similar to each other, which strengthens the assumption that all spectra originate from the same compound.

During the XPS measurements no nitrogen was detected in the collected samples. The possible formation of ruthenium nitrosyl compounds was therefore ruled out during the data evaluation process.

#### *XPS measurements of samples from experiments with CsI aerosols*

The results obtained from XPS analysis of aerosols collected during the experiment conducted under temperatures of 1300 K, 1500 K and 1700 K with CsI aerosol injection are presented in Table 4.11. As can be seen from Table 4.11, ruthenium in the aerosols was in the form of  $RuO_2$ . The binding energy of the Ru 3d5/2 peak was slightly higher than the reference binding energy for anhydrous  $RuO_2$  in all experiments. Additionally the hydration of  $RuO_2$  decreased with the increased temperature used in the experiments. Therefore it can be assumed that  $RuO_2$  was in a partially

hydrated form, where the amount of adsorbed moisture was lower than the stoichiometry of the  $\text{RuO}_2 \cdot 2.3\text{H}_2\text{O}$  used as a reference sample. The determined binding energies were also significantly lower than for the ruthenium in its perruthenate form.

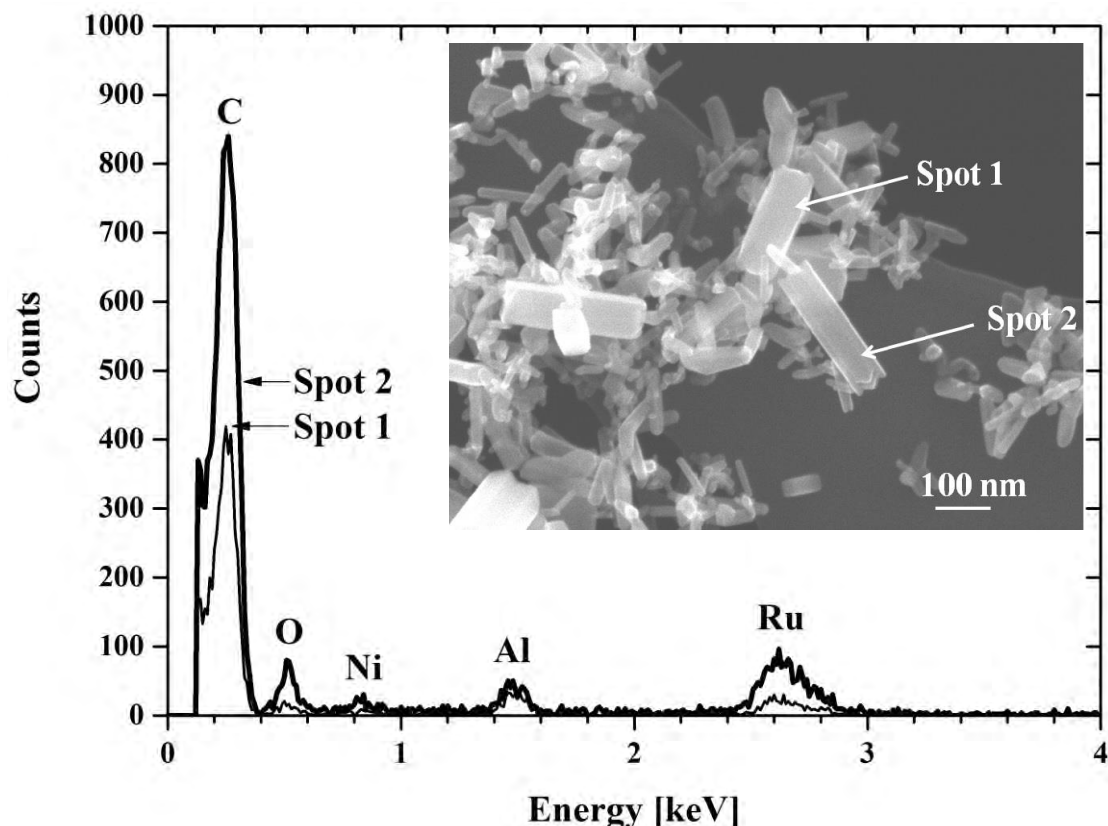


**Figure 4.26.** EDX spectra of spots #1 and #2 of Ru particles. The recorded true counts of spot #2 are multiplied by two.

The binding energies for the iodine species were dependent on the temperature. At a temperature of 1300 K both iodide (62%) (BE  $618.9 \pm 0.1$  eV) and periodate ( $\text{IO}_4^-$ ) (38%) (BE  $624 \pm 0.1$  eV) forms were detected (where the iodide form originated most probably from the CsI compound). At a temperature of 1500 K the iodine in the collected aerosols was found to be in 2 different oxidation states. The most dominant form was iodide ( $\text{I}^-$ ) (42%), with a determined binding energy for the  $\text{I}3\text{d }5/2$  peak of  $618.5 \pm 0.1$  eV (60%). The second identified form of iodine was iodate ( $\text{IO}_3^-$ ), with a binding energy of  $623.0 \pm 0.1$  eV (40%). At a temperature of 1700 K iodine was identified to be in 3 different chemical forms. The most prominent was the iodide form ( $\text{I}^-$ ) (60%) (BE  $618.4 \pm 0.1$  eV), followed by adsorbed elemental iodine ( $\text{I}_2$ ) (30%) (BE  $620.4 \pm 0.1$  eV), and iodate ( $\text{IO}_3^-$ ) (10%) (BE  $622.9 \pm 0.1$  eV). The content of iodine on the filter was very low in this sample (<0.5 mass %), thus analysis of iodine species partitioning was less reliable even after long acquisition times.

Cesium was detected only in one oxidation state with a binding energy for the  $\text{Cs }3\text{d}5/2$  peak of  $724.2$ - $724.0$  eV under all experimental conditions. This binding energy corresponds to the form of cesium as  $\text{Cs}^+$  ion.

*XRD measurements of samples from experiments with air,  $\text{N}_2\text{O}$ ,  $\text{NO}_2$ , and  $\text{HNO}_3$  atmospheres*

The results from the qualitative crystallographic X-ray diffraction analysis of the samples are shown in Figure 4.28. The recorded XRD spectra in experiments with

air, N<sub>2</sub>O, NO<sub>2</sub> and HNO<sub>3</sub> show the same diffraction pattern, which corresponds to the rutile structure of RuO<sub>2</sub>. This is in good agreement with the XPS analysis, leading to the conclusion that aerosols collected from the gas flow were in the form of anhydrous ruthenium dioxide.

**Table 4.10.** The reference binding energies (eV) for Ru 3d5/2, I 3d5/2, O 1s and Cs 3d5/2 peaks in various compounds.

Compound	Ru 3d5/2	I 3d5/2	Cs 3d5/2	O 1s
Ru metal	280.0[ZIM90]	-	-	-
RuO <sub>2</sub>	280.5[KAJ16]	-	-	-
RuO <sub>2</sub> ·2.3H <sub>2</sub> O	282.1[KAJ16]	-	-	-
BaRuO <sub>4</sub>	284.2[OHY80]	-	-	-
RuO <sub>4</sub>	283.3[ZIM90]	-	-	-
RuI <sub>3</sub>	281.5 <sup>a</sup>	619.0 <sup>a</sup>	-	-
CH <sub>3</sub> I	-	620.5[ZHO89]	-	-
CH <sub>2</sub> I <sub>2</sub>	-	620.6 [SOL93]	-	-
C <sub>2</sub> H <sub>5</sub> I		620.7[ZHO89b]	-	-
I <sub>2</sub>	-	620.2[WAG79] 619.9[SHE76]	-	-
I <sub>2</sub> O <sub>5</sub>	-	623.3[SHE76]	-	529.9[157]
HIO <sub>3</sub>	-	623.1[SHE76]	-	-
NaIO <sub>4</sub>	-	624[SHE76]	-	-
CsI	-	618.4[MOR73]	724.1[MOR73]	-
CsOH	-	-	724.15[WAG79]	530.6[WAG79]
OH <sup>-</sup>	-	-	-	≈530.5- 531.7[WAG79]
H <sub>2</sub> O	-	-	-	≈532.1- 533.3[WAG80]]

Values obtained from measurements with commercial RuI<sub>3</sub> (98% Sigma Aldrich). (b) Estimated value.

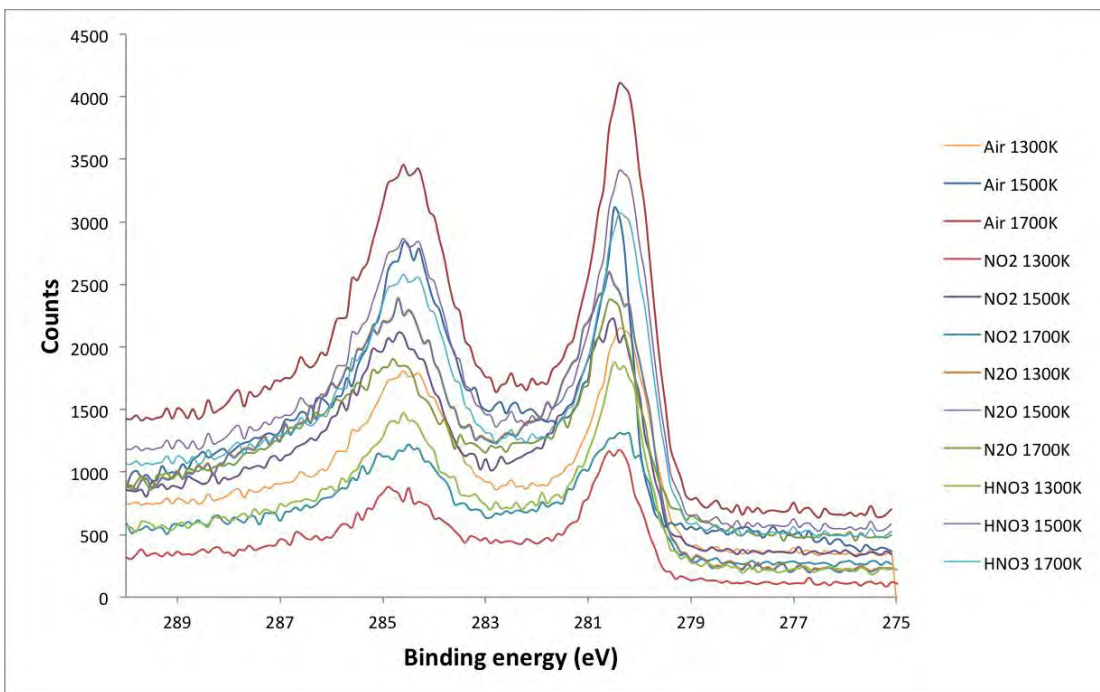


**Figure 4.27.** The XPS spectra obtained from the analysis of collected aerosols on filters. Spectra were scaled to fit the figure.

**Table 4.11.** Obtained binding energies and identified compounds from the collected aerosols from experiments with CsI aerosol injection.

Temperature	Peak	Ru 3d5/2	I 3d5/2	Cs 3d5/2
1300 K	<b>Binding energies</b>	281.3±0.1 624.0±0.1	618.9±0.1 624.0±0.1	724.2±0.1
1300 K	<b>Chemical state of element</b>	$RuO_2$	$I^-$ $IO_4^-$	$Cs^+$
1500 K	<b>Binding energies</b>	281.0±0.1 623.0±0.1	618.5±0.1 623.0±0.1	724.0±0.1
1500 K	<b>Chemical state of element</b>	$RuO_2$	$I^-$ $IO_3^-$	$Cs^+$
1700 K	<b>Binding energies</b>	280.8±0.1 620.4±0.1 622.9±0.1	618.4±0.1 620.4±0.1 622.9±0.1	724.0±0.1
1700 K	<b>Chemical state of element</b>	$RuO_2$	$I^-$ $I_2$ $IO_3^-$	$Cs^+$

#### 4.5.6. Conclusions

It was shown that the air-radiolysis products ( $\text{NO}_2$ ,  $\text{N}_2\text{O}$ ,  $\text{HNO}_3$ ) and aerosols ( $\text{CsI}$ ) formed during a severe nuclear accident have a significant effect on the transport of ruthenium through the primary circuit of a NPP. These effects were determined at different temperatures (1300 K, 1500 K, and 1700 K). It was shown that even the very low concentrations (50-5 ppmV) of air radiolysis products in a gas stream will affect the chemical composition of transported ruthenium and can decrease or increase the gaseous and aerosol fractions thereof. Additionally, these precursors will affect the absolute amount of ruthenium transported through the primary circuit of the power plant. By means of neutron activation analysis of collected ruthenium samples, these amounts could be quantified. The chemical compositions of the collected aerosol fractions were identified by means of SEM/EDX, XPS and XRD techniques. Additionally it was shown that there was a strong effect of temperature and air flow (2.5 l/min, 5 l/min) on both the release rates of ruthenium and also the amount and chemical composition of ruthenium transported through the primary circuit of a NPP. It was also shown that the transport of ruthenium does not correspond to the thermodynamic equilibrium calculations, and therefore chemical kinetics will play an important role during a severe nuclear accident.

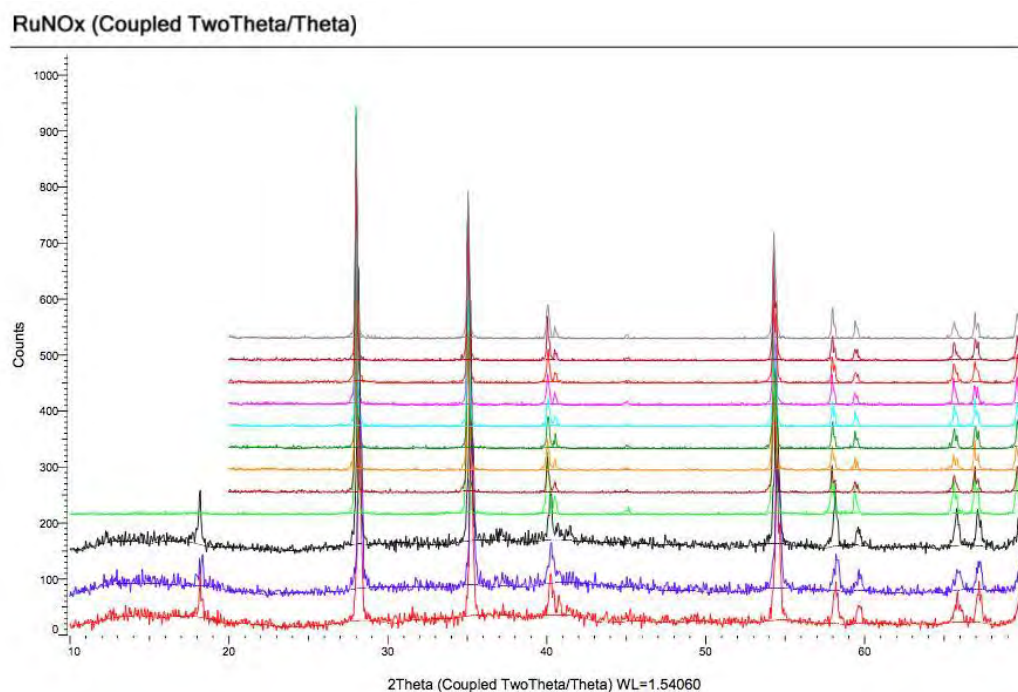


**Figure 4.28.** The obtained XRD spectra from the samples from experiments with air,  $\text{N}_2\text{O}$ ,  $\text{NO}_2$  and  $\text{HNO}_3$ . The height of the peaks was scaled in order to fit in the figure.

### 4.6 Tellurium, niobium and ruthenium interaction with iodine

#### 4.6.1. Introduction

During an accident when radionuclides are released from the fuel, chemical interactions between these radionuclides will take the place during the transport through the reactor coolant system (RCS). These interactions are currently poorly examined when compared to the release of radionuclides from fuel itself and their containment chemistry. It is known that volatility of particular elements during a nuclear accident is

strongly dependent on their chemical form. Thus, during transport through a RCS new and potentially more volatile chemical forms of radionuclides can be formed as a result of chemical interactions. It was shown previously that interaction of ruthenium with cesium-iodide increases the volatile fraction of ruthenium transported into the containment within two orders of magnitude when compared to the pure air atmosphere. This effect was attributed to the formation of volatile ruthenium oxy-iodides. Oxyhalides and halides were shown to significantly increase the volatility of noble metals, even at low temperatures, and thus their formation would significantly affect the source term during an accident within the nuclear power plant. A similar effect can be expected also with other metals, resulting in a higher release of radionuclides to the containment than predicted by the severe accident codes nowadays. Effects of the formation of halides can be demonstrated on tellurium and niobium, which were both released during the Fukushima accident where seawater containing sodium chloride was used for the emergency cooling of the fuel.

Tellurium in its metallic and dioxide forms has boiling points of 988°C and 1245°C, respectively [GRE97], in comparison to the boiling point of tellurium tetrachloride (380°C, sublimation point 200°C). Similar behaviour can be expected from the tellurium tetraiodide that has a melting point of 280°C [GRE97]. The effect of halides formation can also be seen on niobium. Metallic niobium has a boiling point of 4741°C [GRE97], whereas in the form of niobium pentachloride its boiling point is 247°C [GRE97].

It is therefore necessary to obtain deeper knowledge of the properties of halides and oxyhalides of metals that can be released from the nuclear fuel. Iodine is the most important halogen produced by fission during the operation of a nuclear power plant. The isotope I-131 is one of the main concerns in such an accident, as iodine is readily released from the fuel when the consistency of fuel elements is lost, and it will interact with other released fission products within the RCS. These interactions can possibly lead to the formation of new chemical species where several radionuclides will be transported in one compound to the containment.

The effect of air atmosphere and air with iodine vapour on the transport quantities and chemical forms of particular metals was investigated. This report shows the initial experiments carried out to determine if anything occurs at all when iodine is added to the oxidizing gas.

#### 4.6.2. Experimental

Tellurium, niobium and ruthenium in their metallic forms were used in separate experiments. Metal powder was placed in a ceramic crucible positioned inside the tubular furnace and heated to the temperature desired for the experiment under an inert atmosphere. At the desired temperature, a gas flow was initiated into the furnace to simulate oxidizing conditions during an accident. The release of metals was determined by measuring the lost fraction of metal from the ceramic crucible after the experiment. Furthermore, an aerosol filter was situated at the outlet to catch any aerosols of the elements transported by the gas flow. Sodium hydroxide and water traps were placed after the filter, the latter to trap any gaseous species.

An overview of the setup can be seen in Figure 4.1. However, some minor modifications were made, with the iodine introduced to the gas prior to entering the furnace. This was achieved by channelling the gas through a gas trap containing iodine. To ensure enough iodine throughout the experiment, the iodine was constantly heated

This was done by adding an excessive amount of solid iodine inside the gas trap and then placing the gas trap on a heating plate, allowing constant volatilization of iodine.

#### 4.6.3. Results

The results obtained in the furnace experiments are presented in Figures 4.21, 4.22 and 4.23. These show what the samples and filters looked like after the experiments. By comparing the results in Figure 4.21 to how these looked before the experiments, significant changes can be observed. Part [A] shows the crucible that contained the niobium (metallic powder of niobium is black/dark grey). It is now a white solid with a slight yellow tone to it. This indicates that something has happened to the source. Niobium(V) iodide solid has a characteristic yellow colour, which could mean that this could have formed. Alternatively, it could also be iodine, as it is also yellow. However, as iodine easily sublimes it should disappear given enough time. Yet, after several months the yellow colour remains. Observing the filter, it was also changed to yellow/black areas. This could be niobium(V) iodide (yellow parts). However, after roughly a week the deposition on the filter has disappeared, indicating iodine. However, as oxyhalides are very unstable it could possibly be some sort of niobium oxyhalide.



**Figure 4.21.** [A] shows the crucible where the niobium was located initially, before possible volatilization. [B] shows the filter located at room temperature at the outlet of the system. [C] shows the outlet, where the filter was located.



**Figure 4.22.** [A] shows the crucible where the tellurium was located initially, before possible volatilization. [B] shows the filter at room temperature located at the outlet of the system. [C] shows the inlet, close where the crucible was located.

The tellurium powder after exposure is shown in Figure 4.22, [A]. This has drastically changed from the “initial state” (black/grey powder). Small “drops” can be seen to have formed, seemingly with a white coating surrounding a grey mass. Moreover, the filter in [B] has turned brown, which neither metallic tellurium nor tellurium dioxide exhibits as a colour. The latter results indicate that something has occurred between tellurium and iodine under oxidizing conditions.

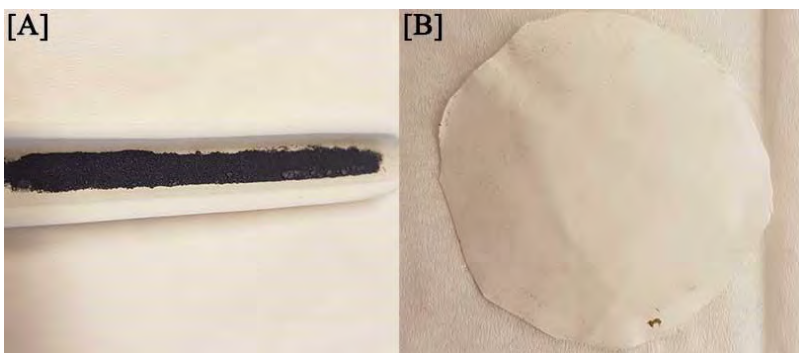


**Figure 4.23.** [A] shows the crucible where the ruthenium was located initially, before possible volatilization. [B] shows the filter at room temperature located at the outlet of the system. The colour spot on the bottom part of the filter comes from dirt on the outlet.

The ruthenium part (Figure 4.23) is still inconclusive and further experiments are required for a definite answer about whether there is oxyhalide formation of ruthenium.

As seen for the niobium experiments, the end product can be very unstable, which may interfere with the final analysis. As such, the current setup will require a slight adjustment to ensure that these compounds are trapped and remain stable long enough for proper analysis. This could be achieved by low temperatures or online measurements.

#### 4.6.4. Conclusions

For both the niobium and tellurium experiments positive indications of the interaction between these and iodine in oxidizing conditions have been produced. For ruthenium, no evidence was found during these experiments. However, further experiments to fully determine this is required, as previous, nonpublished experiments have indicated that something actually does happen as the filter was completely blackened. It is still unclear what this reaction is and it will require further analysis to determine the reaction routes.

These results indicate that under RCS conditions, tellurium and niobium will interact with iodine. This interaction consequently increases the source term of both of these, as the melting/boiling point of iodine compounds with tellurium and niobium is lower than when these are not in an iodine compound.

## 4.7 References

- [ALO91] Alonso A., Gonzalez C. Modelling the Chemical Behaviour of Tellurium Species in the Reactor Pressure Vessel and the Reactor Cooling System under Severe Accident Conditions. Luxembourg: Commission of the European Communities; 1991. no. EUR{13787}
- [BAG77] Bahl, M.K., Watson, R.L., Irgolic, K.J. X-ray photoemission studies of tellurium and some of its compounds. The Journal of Chemical Physics. 1977 Jun; 66 (12): 5526-5535
- [BOE97] Boer R., Cordfunke E.H.P. The chemical form of fission product tellurium during reactor accident conditions J. Nucl. Mater. 1997 Jan; 240:124-130

- [COL87] Collins J.L., Osborne M.F., Lorenz R.A. Fission Product Tellurium Release Behavior Under Severe Light Water Reactor Accident Conditions. *Nucl. Technol.* 1987 Apr; 77:18-31
- [GLA04] H. Glänneskog, Interactions of I<sub>2</sub> and CH<sub>3</sub>I with reactive metals under BWR severe-accident conditions. *Nuclear Engineering and Design*, 227(3), 323-329 (2004).
- [HOU12] Housiadas, C., Kissane, M. and Sehgal, R. Nuclear Safety in Light Water Reactors: Severe Accident Phenomenology. Oxford: Elsevier; 2012. 5, Fission Product Release and Transport; 425-517.
- [IAE15] International Atomic Energy Agency IAEA. The Fukushima Daiichi Accident. IAEA, International Atomic Energy Agency, 2015. isbn: 978-92-0-107015-9.
- [JOH88] Johnson I., Johnson C.E. Mass Spectrometry Studies of Fission Product Behavior I. Fission products released from irradiated LWR fuel. *J. Nucl. Mater.* 1988 Jun; 154:67-73
- [JOH18] John R. Rumble, ed., CRC Handbook of Chemistry and Physics, 98th Edition (Internet Version 2018), CRC Press/Taylor & Francis, Boca Raton, FL.
- [KAN15] Y. Kanai. “Geochemical behavior and activity ratios of Fukushima-derived radionuclides in aerosols at the Geological Survey of Japan, Tsukuba, Japan”. In: *Journal of Radioanalytical and Nuclear Chemistry* Vol. 303 (2015), pp. 1405–1408.
- [LEP14] Le Petit, G., Douyssset, G., Ducros, G., Gross, P., Achim, P., Monfort, M., Raymond, P., Pontillon, Y., Jutier, C., Blanchard, X., Taffary, T. and Moulin, C. “Analysis of Radionuclide Releases from the Fukushima Dai-Ichi Nuclear Power Plant Accident Part I”. In: *Pure and Applied Geophysics* (2014). Vol. 171, 629-644.
- [LEW08] Lewis B.J., Dickson R., Iglesias F.C., Ducros G., Kudo, T. Overview of experimental programs on core melt progression and fission product release behaviour. *J. Nucl. Mater.* 2008 Oct; 380:126-14
- [MAL70] Makinauskas, A.P., Gooch, J.W. and Redman, J.D. The Interaction of Tellurium Dioxide and Water Vapor. *Nuclear Applications & Technology*. 1970 Jan; 8:52-57
- [MCF96] McFarlane J. Fission Product Tellurium Chemistry from Fuel to Containment. 1996 Switzerland: Paul Scherrer Inst., Report no.PSI {97-02
- [MCP95] McPhail D.C. Thermodynamic properties of aqueous tellurium species between 25 and 350 °C. *Geochim. Cosmochim. Acta*. 1995; 5:851-866
- [MEI01] Meier D.A., Kaplan, M.M. Radioiodine Uptake and Thyroid Scintiscanning. *Endocrinol Metab. Clin. North Am.* 2001 Jun; 30:291-313
- [TAY96] Taylor A. Biochemistry of Tellurium. *Biol. Trace Elem. Res.* 1996 Apr; 55:231-239
- [GRE97] Greenwood, N.N. Earnshaw, A. Chemistry of the Elements. 2nd ed. elsevier, 1997. isbn: 978-0-7506-3365-9. Slutsatser och rekommendationer.

## 5. UPPFÖLJNING AV KÄRNKRAFTSOLYCKAN I FUKUSHIMA DAIICHI

Ett viktigt syfte med uppföljningen inom APRI är att undersöka om de insikter som utvecklats efter olyckan i Fukushima kan leda till ändrad strategi för den svenska haverihanteringen. Viktiga element i den svenska strategin är att kunna kyla en härdsmälta i inneslutningen genom att låta den falla i vatten och att skydda inneslutningens integritet genom tryckavlastning. Efter olyckan har dessa element fått ökad internationell acceptans och någon omvärdering av den svenska strategin grundad på nuvarande insikter är inte aktuell.

I rapporten från APRI-8 [1] behandlades förloppen i reaktorerna vid Fukushima Daiichi och möjliga tekniska orsaker. Den analysverksamhet som har bedrivits efter APRI-8 har inte lett till några avgörande ändrade slutsatser. Därmed anses de slutsatser om förloppen som drogs i APRI-8 fortfarande gälla.

Det kan konstateras att härdsmälter har ägt rum i tre reaktorer. Olyckan i Fukushima ger en unik möjlighet till att förbättra kunskapen om härdsmälter i BWR och våra möjligheter att kunna simulera härdsmältförlopp. Ambitionen är att genom analyser av sluttillstånden kunna få en klarare uppfattning om dominerande fenomen. Det finns frågor kring bildandet av härdsmältan och hur den har relokerats. Det är viktigt att spåra hur smältan har ansamlats i nedre plenum, hur den tog sig genom reaktortanken och hur den reagerade med vatten och betong i piedestalen.

Det har tills nu (februari 2018) inte varit möjligt att klarställa vart härdsmältorna finns. Morfologi och kemiska egenskaper har därför inte kunnat fastställas. Detta är frågeställningar som har prioriterats för att förbättra våra kunskaper.

I avsnitt 5.1 beskrivs nuvarande status för reaktorerna och de säkerhetsförbättringar som har genomförts och planeras, och även några frågeställningar med kvarstående betydande osäkerheter. En mer detaljerad beskrivning finns i [2]. I avsnitt 5.2 ges en översikt över arbetet som pågår för att klärlägga skador i inneslutningen och vart härdarna har tagit vägen. Detta gäller visuella undersökningar med robotteknik och identifikation av ledtrådar grundade på andra mätningar. En mer detaljerad beskrivning finns i [3].

I avsnitt 5.3 ges en översikt över vad som hände med bassängerna för använt bränsle. En fullständig överraskande explosion inträffade i Block 4. Denna ledde till obefogade farhågor om stora utsläpp och ett i det närmsta katastrofalt informationsläge. Även SSM:s respons beskrivs. Det kan i efterhand konstateras att bränslet i bassängerna inte hade väsentliga skador som härrörde från olyckan. En mer detaljerad beskrivning finns i [4].

### 5.1 Status för kärnkraftsreaktorerna i Fukushima Daiichi 1-3

Nuvarande situation (februari 2018) för kärnkraftsreaktorerna i Fukushima Daiichi 1-3 är att dessa kyls genom inpumping av ca  $200 \text{ m}^3/\text{dygn}$  vatten genom härdstril och i fallspalt. Då reaktortankar och inneslutningar är skadade rinner vattnet vidare till turbinbyggnaden varifrån det pumpas ut och behandlas. På grund av betydande inflöden av grundvatten till reaktorbyggnaderna har det utpumpade flödet tidvis varit dubbelt så stort som inflödet, och överskottet har fått lagras i ett ökande antal uppförda lagringstankar. I februari 2018 fanns ca 1,1 miljoner  $\text{m}^3$  ("1100 tankar á 1000  $\text{m}^3$ ") vatten lagrat på kraftverksområdet.

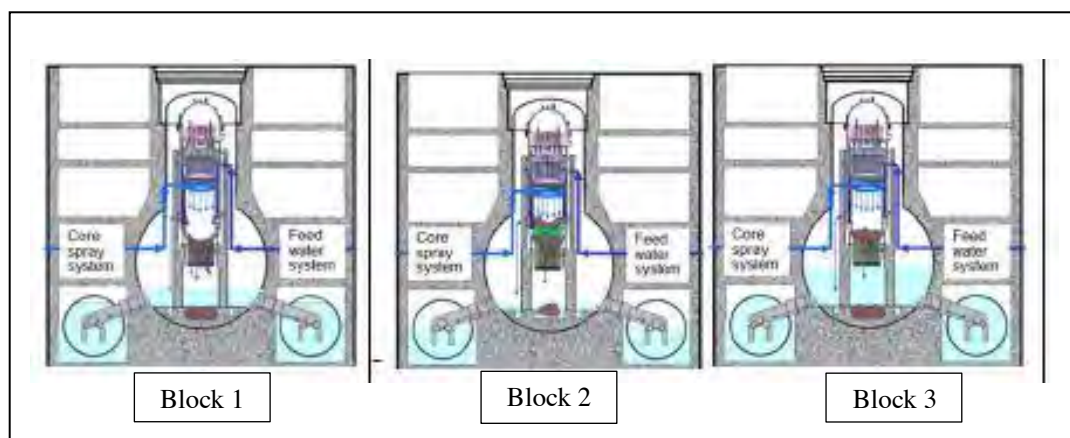
Läget för arbetet med att begränsa inträngning av grundvatten och begränsa spridning av kontaminerat vatten till grundvatten och havet har fått viss framgång. Man har frusit en vägg runt anläggningen som blivit operativ hösten 2017 för att begränsa såväl in- som utläckage. Olika observationer görs för att se om väggen har avsedd effekt.

Förberedelser pågår för att kunna flytta bränslet från bränslebassängerna. Ett antal områden har identifierats där det fortfarande finns väsentliga osäkerheter och frågeställningar om slutsatserna.

När det gäller säkerhetsförbättringar måste samtliga anläggningar visa att man uppfyller de nya kärnkraftsregler som trädde i kraft i juli 2013. Dessa regler innehåller långtgående krav på tålighet mot ytter händelser (jordbävning, tsunami), diversificerade system för insprutning och tryckkontroll under haveriförhållanden samt kapabilitet att hantera vätgas.

I januari 2018 hade 14 reaktorer (12 PWR och 2 BWR) fått godkännande av sina upgraderingsplaner av NRA (den japanska kärnkraftsmyndigheten), och av dessa har 5 hunnit återstarta, se länken <http://www.genanshin.jp/english/> för senaste status. Ytterligare 12 reaktorer (8 BWR och 4 PWR) har ansökt om godkännande av sina upgraderingsplaner. För de två ABWR (TEPCO:s Kashiwazaki-Kariwa 6/7) som har fått godkännande har en reviderad ansökan lämnats in i augusti 2017. Uppstart av dessa kommer att senareläggas några år. Trots att Kashiwazaki-Kariwa 6/7 har fått godkännande av myndigheten hösten 2017, avser TEPCO att införa ett nytt system för kyllning av inneslutningen för att reducera behovet för tryckavlastning som det är svårt att få acceptans för i den japanska befolkningen. Tryckavlastning skulle i dagsläget kräva godkännande av lokala myndigheter [5].

### 5.1.1. Nuvarande situation vid anläggningen i Fukushima



Figur 5.1 Översiktsbild över sluttillstånden hämtat från [11] (Härdarnas lägen är spekulatoria)

Mätdata från anläggningen finns i [6] - [8]. Det kan konstateras att värdena fluktuerar från dag till dag. I samtliga block sker inpumping av vatten genom stril över ursprungligt härdområde och genom matarvattensstutsarna i fallspalten. I Block 1 och 3 är torusen helt fyllt med vatten. I Block 2 är det samma vattennivå innanför och utanför torusen. Vattennivån i inneslutningen varierar något. I januari 2017 var nivån i Block 1 ungefär 1,9 m från botten, i Block 2 ungefär 0,3 m från botten och i Block 3 ungefär 6,4 m från botten. Skillnaderna beror på varierande skadeomfattning i inneslutningarna.

För Block 1 är temperaturerna i reaktortank och inneslutning runt 20 °C. Mängden inpumpat vatten är ca. 3 m<sup>3</sup>/timme. Temperaturerna varierar i reaktortank och inneslutning mellan 24 °C och 27 °C och det pumpas in ungefär 2.8 m<sup>3</sup>/timme i Block 2. I Block 3 är det ungefär 25°C i reaktortank och inneslutning och mängden inpumpat vatten är 2,8 m<sup>3</sup>/timme. Det pumpas således in drygt 200 m<sup>3</sup>/dygn till de tre reaktorerna. Vattnet som pumpas in har gått igenom en reningsprocess där framför allt klorider och Cs har tagits bort.

Man har satsat på att fryska en vägg runt anläggningen. Den sista delen av väggen mot väst (mot landsidan) började frysas i augusti 2017. Erfarenheterna så länge tycks peka på att väggen fungerar. Det har observerats en ökande nivåskillnad mellan insidan och utsidan av väggen. Temperaturer på grundvatten och i marken övervakas också.

I Block 1 har man tagit bort höljet kring reaktorn och har börjat förbereda ett vindskydd för att skydda omgivningen under arbetet med att ta bort skräpet i reaktorbyggnaden. Skräpet skannas för att planera för borttagningen utan att kontaminera omgivningen. Bortforslande av bränsle planeras att påbörja under 2023.

I Block 2 har man som förberedelse för att ta bort bränslet från bränslebassängen tagit upp ett hål i väggen i reaktorbyggnaden mot landsidan. Man kommer så småningom att ta bort hela övre delen av byggnaden för att underlätta hantering av bränslet. Arbetet med att ta bort bränslet planeras att påbörja 2023.

I Block 3 har skräpet i reaktorbyggnaden efter explosionen nu tagits bort. För att förbereda borttagande av bränslet i bränslebassängen har man installerat skenor som maskinen för hantering av bränslet kan manövreras längs. För närvarande installeras kupoltak över reaktorn. Kupoltaket installeras i sektioner och de första två har installerats. Bortforslingen av bränsle planeras att påbörjas 2018.

### 5.1.2. Säkerhetsförbättringar

Många erfarenheter har gjorts som har lett till nytt regelverk och ett stort antal säkerhetsförbättringar. I december 2017 hade 12 reaktorer fått godkännande av sina uppraderingsplaner och tillstånd av NRA att starta upp. Fem reaktorer har hunnit starta. Samtliga av dessa är PWR [5].

För BWR är TEPCO ledande i processen med att införa förbättringar i säkerhetssystemen. För BWR krävs bland annat att ett system för filtrerad tryckavlastning eller utrustning med motsvarande eller bättre prestanda installeras. Det finns bland den japanska befolkningen en stor misstänksamhet mot BWR och ett stort motstånd mot att medvetet släppa ut radioaktiva ämnen. Det pågår diskussioner om att det skulle behövas tillstånd från lokala myndigheter för att aktivera systemet och eventuellt en samordning med evakueringsplaner [9]. På grund av detta kommer TEPCO att installera ett nytt extra kylysystem för inneslutningen i Kashiwazaki-Kariwa [10].

I [1] konstaterades att en grundorsak till kärnkraftsolyckan är att man inte korrekt hade identifierat vilka händelser som kunde inträffa vid anläggningen vilket ledde till helt oförutsedda konsekvenser. Det var brister i utbildning och träning för att kunna ta hand om ett svårt havari.

Ett stort antal säkerhetsförbättringar har införts. Detta gäller givetvis skydd mot jordbävningar och tsunamis genom installation av väggar mot sjön, förstärkning och tätning av byggnader och säkerställning av vattenkällor när tsunami-vågen drar sig tillbaka.

Extra utrustning installerades i form av mobila system, förstärkning av reaktorns värmesänkor och skydd mot terroristanfall och flygplanskrascher.

För förstärkning av elsystemen installeras diversifierade, redundanta och distribuerade faciliteter som till exempel mobila fordon med gasturbiner och andra alternativa möjligheter för växelströmsförsörjning. Batterikapaciteten ökas och fördelas på olika ställen.

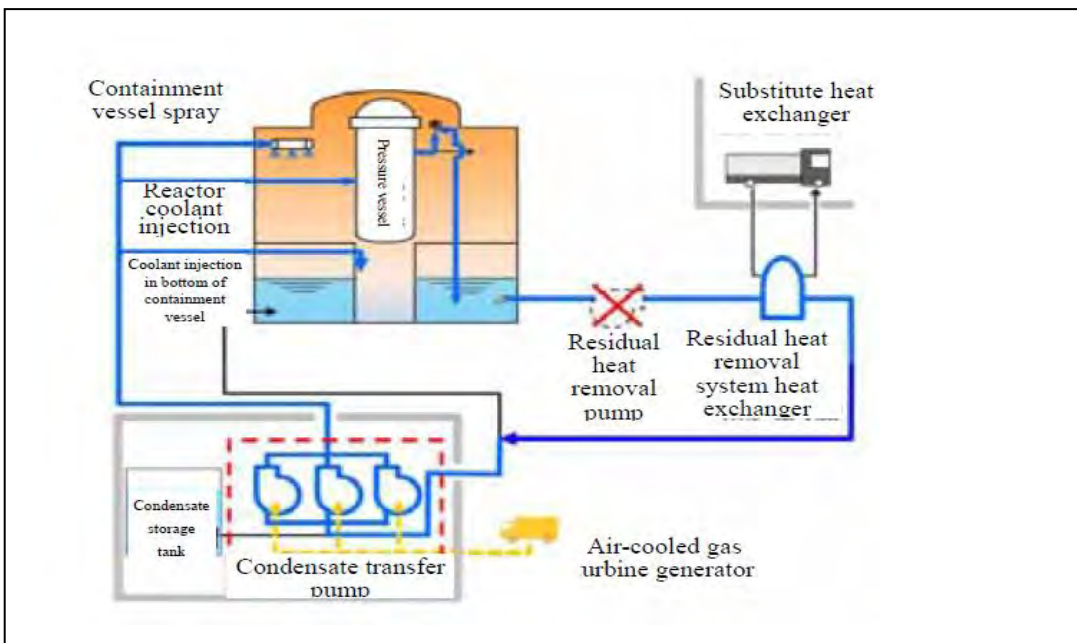
Bland de tekniska faktorerna som bidrog till härdsäkerheten verkar komponentskyddet ha spelat en väsentlig roll. Det fanns inbyggda trippvillkor som inte på ett enkelt sätt kunde hävas eller överridas. Detta innebar i flera fall att viktiga komponenter av betydelse för säkerheten inte var tillgängliga som förutsatt. Detta diskuteras vidare i avsnitt 5.1.3. Det gjordes vid flera tillfällen upprepade försök att få i gång kritisk utrusning. I Block 2 som var mest utsatt för el-bortfall och som därmed inte hade skydden och trippvillkoren aktiverade tog det längst tid innan härden smälte.

Strategin att använda brandutrustning för att förse reaktorerna med vatten medförde vissa problem. När inpumpningen kom igång kom bara en mindre del av vattnet dit det skulle. I stället fanns det alternativa flödesvägar på grund av felmonterade eller läckande ventiler. Enligt TEPCO är det troligt att man hade kunnat kyla härden om allt vatten hade gått dit det skulle. Ett annat problem med brandvattnet var att trycket inte var tillräckligt för att pumpa in vatten mot reaktortrycket. Man var således helt beroende av att avblåsningen genom säkerhetsventilerna fungerade. Detta diskuteras vidare i avsnitt 5.1.3.

Det var även problem med tryckavlastningen som endast kunde aktiveras med extra-ordinära åtgärder när trycket i inneslutningen väsentligt översteg konstruktionstrycket. I de nya säkerhetsbestämmelserna krävs att filtrerad tryckavlastning ska finnas. I TEPCO:s anläggning i Kashiwazaki-Kariwa hade man satsat på ett system med avblåsning från ”wetwell” som kan öppnas manuellt från en skyddad plats.

Även om den japanska myndigheten har varit positiv till de åtgärder som TEPCO föreslagit, har företaget dragit tillbaka sin ansökan om uppstart. TEPCO kommer att gå vidare med konstruktion och installation av ett nytt extra säkerhetssystem, se figur 5.2. Systemet tar vatten från kondensationsbassängen. Vattnet leds genom värmeväxlare som även kan förses med vatten från mobila system på sekundärsidan. Från ett bunkrat utrymme pumpas vattnet, eventuellt kompletterat med vatten från brandpumper eller mobila system, in till inneslutningen genom strilning i primärutrymmet, till reaktortanken och till piedestalen under reaktortanken. Från reaktortanken ska vatten kunna avbördas till kondensationsbassängen.

För de två aktuella TEPCO-reaktorerna av ABWR-typ, Blocken 6 och 7 i Kashiwazaki-Kariwa, godkände myndigheterna de föreslagna uppgraderingsplanerna. TEPCO drog tillbaka sin ansökan om uppstart och det planeras nu för uppstart i 2020. De andra företagen med BWR avvaktar TEPCO:s åtgärder.



Figur 5.2. Nytt kylsystem för inneslutningen i Kashiwazaki-Kariwa. (Hämtad från [10]).

TEPCO hävdar att systemet ger bättre skydd mot övertryckning av inneslutningen och därmed消除ar behovet för filtrerad tryckavlastning av inneslutningen.

### 5.1.3. Områden med återstående frågor eller stora osäkerheter

Ett omfattande analysarbete har gjorts för att förklara förloppen. TEPCO har tillsammans med andra analysgrupper arbetat med ett stort antal frågeställningar. De flesta av dessa har fått en något så när sluttgiltig förklaring. Det återstår dock en del frågor där resultaten inte helt kan bekräftas och en del olösta frågor. Analysrapporten nummer fyra [11] blir därför den sista i denna serie och slutsatserna nedan är för en del hämtade från denna.

Det framhålls som speciellt viktigt att förstå varför utrustning av säkerhetsmässig betydelse fick funktionsstörningar eller visade oväntad respons. Det kan också finnas fysikaliska fenomen av säkerhetsmässig betydelse som har påverkat förloppen. Ett huvudsyfte med analysarbetet är att komma fram till slutsatser om funktionen av existerande säkerhetssystem.

En frågeställning som återstår berör drift av tryckavlastningsventiler efter härdskadorna. Tryckavlastningsventilerna fungerar dels som säkerhetsventiler som aktiveras oberoende av operatörsingrepp; dels som ventiler för kontrollerad tryckavlastning. Den kontrollerade tryckavlastningen behöver tillgång till likström och kvävgastryck för att kunna användas. För kvävgassystemen fanns uppbackning i form av trycksatta ackumulatorer. I vissa fall fungerade inte dessa, ovisst dock av vilka orsaker. Brandpumpar och mobila system användes för att pumpa in vatten i blocken 1-3. Det behövdes att trycket i systemen var lågt vilket innebar att avlastningsventilerna behövde kunna öppnas. TEPCO efterlyser bättre kunskaper om funktionaliteten för säkerhetsventiler och avlastningsventiler under svåra haverier.

En annan frågeställning som återstår berör mängden inpumpat vatten. Det är oklart var det inpumpade vattnet verkligt hamnade. Detta har tidigare påpekades som ett problem för Block 1 [1] där det kunde visas att bara en mindre del (20-50%) av vattnet i verkligheten kom in till reaktorn. I stället upptäcktes läckagen och felvända ventiler

som gjorde att det inpumpade vattnet tog helt andra vägar. För Block 1 hittades till exempel inpumpat vatten i turbinkondensorn. Dessa erfarenheter ledde till omfattande prov och modifikationer i andra verk.

Mängderna som pumpades in baserades på flödesmätningar som gjordes på den använda utrustningen. Det visade sig snart att förväntad respons på till exempel tryck och nivå i många fall uteblev. Detta ledde till analyser som även omfattade de andra reaktorerna. Det visade sig att problemen kring omkoppling och bypass av flödesvägarna in till reaktorn i större eller mindre grad gällde samtliga reaktorer.

Ett gemensamt problem var nivåmätsystem med dp-mätning på referensben i reaktorerna som till exempel inledningsvis för Block 1 felaktigt indikerade hög nivå, vilket vilseledde operatörerna att tro att härdstenen delvis var kyld. Nivåmätningarna gav inte heller någon respons på olika åtgärder som till exempel intermittent tillförsel av vatten. Även om klarhet inte finns i alla detaljer kan det konkluderas att vattnet i referensbenet för samtliga reaktorer antingen hade förångats eller läckt ut och orsakat hög indikerad nivå. Det är även troligt att vattennivån hade sjunkit under nedre tryckuttag vilket gör att mätningarna frikopplas från den verkliga nivån.

En tredje frågeställning som återstår berör härdarnas relokering till nedre plenum. De analyser som har gjorts har som utgångspunkt fölloppet i TMI-2. Det är möjligt att en mer kontinuerlig relokering av smält material kan vara mer trolig för en BWR. Denna hypotes diskuteras närmare i avsnitt 5.2.11.

Baserat på experiment har TEPCO identifierat och analyserat 5 läckagevägar från härdstenen till nedre plenum. Dessa är genom inloppstrympningarna till bränslet, genom styrstavsledrören, genom instrumentledningar, genom brott på härduppställningsplattan och genom brott på härdhöljet. Båda hypoteserna för relokering har analysrats dock utan att säkra konklusioner kan dras.

En fjärde frågeställning som återstår berör ökning av dos runt reaktorn den 20 mars, 2011. Denna frågeställning är med eftersom det skapades speciell uppståndelse på grund av rekommendationen om att inte små barn skulle dricka kranvattnet. TEPCO:s analyser pekar på att det var en ändring av vindriktning som orsakade ökningen av uppmätt dos.

#### 5.1.4. Återstående frågor som berör Block 1

Driften av IC (Isolation Condensor) i **Block 1** är en fråga som inte har fått något riktigt svar. En bra beskrivning av säkerhetssystemen finns i [12].

Tsunamin ledde till fullständigt bortfall av el och innebar att signaler från reaktorn inte längre var tillgängliga. Det noterades att båda ventilerna utanför inneslutningen visade stängt. Detta är normalt eftersom ventilerna ska gå till stängt läge vid el-bortfall. Det är dock oklart om ventilerna verkligen stängde eftersom de behöver tillgång till el för att stänga. Senare undersökningar pekar på att ventilerna utanför inneslutningen helt eller delvis kan ha stängt.

Operatörerna gjorde upprepade försök att öppna ventilerna men drog slutsatserna att systemen inte fungerade. De kunde höra att det strömmade ut ånga och att flödet strax därefter avstannade. En huvudhypotes är att värmeöverföringen kan ha försämrats genom ackumulering av vätgas i tuberna på värmeväxlaren. Analyser visade dock att någon större mängd vätgas inte hade hunnit genereras åtminstone under de första försöken.

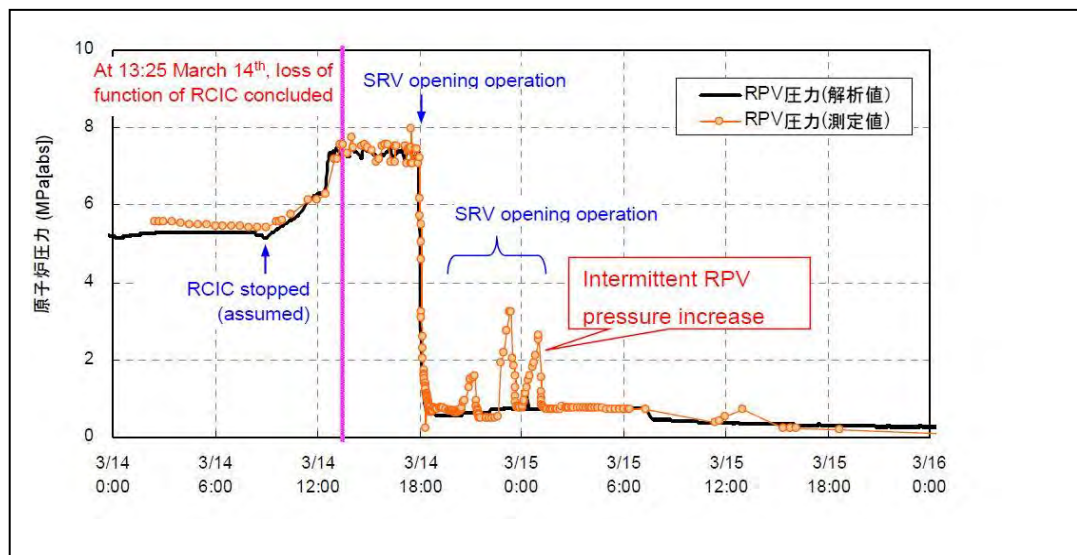
Förnyade analyser har gjorts med antaganden om att IC hade fungerat. Resultatet visade att driften av IC inte hade gjort någon större skillnad på förloppet. Visserligen hade tidpunkten för tankgenomsmältnings födröjts något med IC:n i drift, men temperaturerna i reaktorn skulle ha blivit högre. Det är sannolikt att förloppet redan hade kommit så långt när IC:n aktiverades att den inte fick nämnvärd betydelse för de vidare händelserna.

Vittnesmålen är ganska entydiga om att ändringen av ventilläget hade viss effekt eftersom man fick en reaktion på flödet ut från värmeväxlaren. Klart är dock att IC:n inte fungerade som värmesänka som den skulle. Det bedöms som om förloppet i Block 1 representerar en typisk respons på ett totalt elbortfall utan ingripanden från operatörerna.

En skillnad jämfört med Block 2 och 3 är att det i Block 1 uppmättes mycket höga stråldoser i komponentkylsystemet på olika nivåer i reaktorbyggnaden över lång tid. TEPCO:s analyser pekar på att det sannolikt har varit en genomsmältningsolycka i komponentkylsystemet i piedestalen under reaktorn.

### 5.1.5. Återstående frågor som berör Block 2

Under förloppet i **Block 2** observerades det kraftiga tryckspikar i reaktortanken efter trycknedtagningen som skedde ungefär klockan 18:14 mars, 2011. Tryckförloppet visas i figur 5.3. Klockan 13:25 kunde det konstateras att högtrycksinpumpningssystemet RCIC (Reactor Core Isolation Cooling) definitivt var borta och trycket var kring det nominella. Det uppskattas att härdavtäckningen började strax efter trycknedtagningen och att hela härden var avtäckt ungefär 18:55.



Figur 5.3 Tryckförloppet i reaktortanken i Block 2 (Bilden är hämtad från [11]).

Situationen har analyserats vilket pekar på följande scenario: När trycket hade sjunkit kunde vatten pumpas in från brandvattenspumparna. Tryckspikarna kan ha orsakats av ångproduktion på grund av hög vattennivå, genom interaktion med härdsämältan och genom metall-vattenreaktion. Vid varje tryckhöjning öppnades avlastningsventillerna vilket tog ned trycket. Vid det lägre trycket kunde inpumpningen återupptas och ge fart åt ökad värme- och ångproduktion.

En annan återstående fråga för Block 2 är sprängblecket i avblåsningsystemet för inneslutningen. Vid Block 2 behövde man tryckavlasta inneslutningen och då behövde ventilerna i ledningen vara öppna och sprängblecket i ledningen ha utlösats. Tryckavlastningen fick inte någon inverkan på inneslutningstrycket. Detta kan ha inneburit att sprängblecket inte hade löst ut och att den efterföljande reduktionen av trycket orsakades av läckage. Inneslutningstrycket översteg väsentligt sprängbleckets utlösningstryck. Det gjordes i efterhand flera försök att bestämma läget för sprängblecket utan att någon konklusion kunde nås.

Det kan konstateras att situationen under denna period (00:00-12:00 den 15 mars) var ganska oöverblickbar. Tryckmätningen i inneslutningen visade plötsligt noll övertryck och en explosion hördes. Detta tolkades som att det fanns en stor läcka på inneslutningen. Det är sannolikt att detta var en felmätning och att den explosion som hördes orsakades av att reaktorbyggnaden i Block 4 exploderade.

#### 5.1.6. Återstående frågor som berör Block 3

Under förloppet i **Block 3** från tsunamin till 11:36 12 mars 2011 då RCIC trippas var likström tillgänglig och RCIC reglerades på tryck och vattennivån i reaktortanken. Under perioden var trycket i reaktortanken högt och ånga avbördades genom säkerhetsventilerna till kondensationsbassängen. Också den ångdrivna RCIC avbördade ångan till kondensationsbassängen. Detta är normal drift av säkerhetssystemen under haverier.

Den tillförda ångan ledde till att trycket i inneslutningen ökade. Analyser visade att ökningstakten var högre än förväntat med ett antaget ångflöde som motsvarade resteffekten. En trolig förklaring är en lokal uppvärmning av ytvattnet i kondensationsbassängen runt utloppet från RCIC som sprider sig längs vattenytan. Det blir en stratifiering i kondensationsbassängen med högre temperatur nära ytan. Den säkerhetsmässiga betydelsen är en farhåga att trycknedsnagningsfunktionen för inneslutningen genom kondensation inte skulle fungera även när säkerhetssystemen fungerar som avsett.

En återstående fråga är att förklara varför RCIC slutade att fungera i Block 3. RCIC kan trippas antingen genom en elektrisk signal som stänger ångtillförseln eller genom mekaniskt stopp på grund av övervarvning. Operatörerna provade flera gånger att återställa trippvillkoren och återstarta RCIC utan att lyckas. Det var det elektriska stoppet av ångflödet som varje gång aktiverades. Analyser av data visade att det sannolikt var trippvillkoret på pumpens utloppstryck som orsakade stoppen.

Efter ungefär en timme startades högtrycksinpumpningen (HPCI) automatiskt. Då blev det problem med nivåmätningen i reaktortanken och trycket i reaktortanken sjönk snabbt vilket ledde till att drivtrycket för pumpen och HPCI avbröts manuellt den 13 mars klockan 02:42. Analyser pekar på att härdens börjar avtäckas ungefär vid denna tidpunkt. Efter detta började trycket i reaktortanken att stiga och stabiliseras på 7 MPa. Det gjordes upprepade försök att starta RCIC och HPCI utan att lyckas.

En efterföljande undersökning visade att under de återkommande försöken att starta RCIC kan et mekaniskt fel ha inträffat och lett till stängning av ångventilen till RCIC.

## 5.2 Status för reaktorhärdarna i Fukushima Daiichi 1-3

För närvarande (november 2017) har man inte visuellt kunnat säkert bestämma var härdarna i de tre reaktorerna har tagit vägen. Sådan information är givetvis mycket

viktigt för vår kunskap om härdsmältförlopp och att undersökningar av härdsmältorna kan göras.

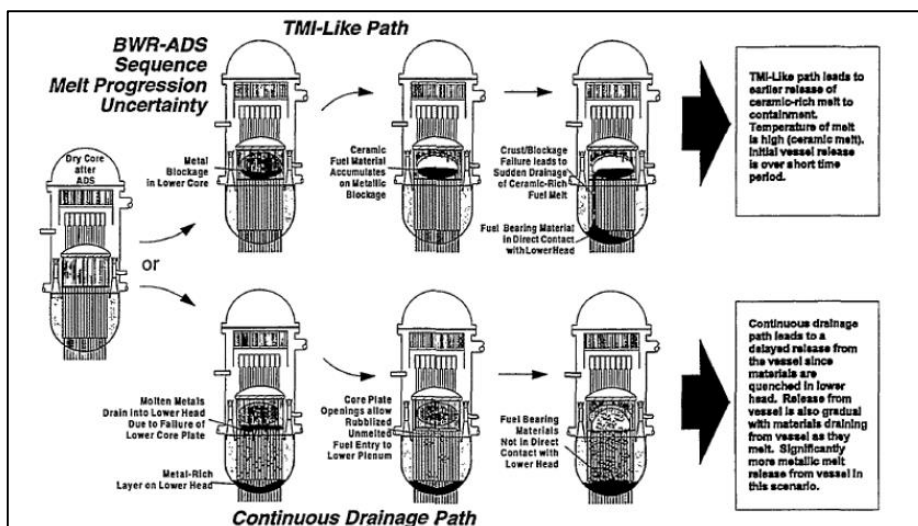
Det är klart att det finns individuella skillnader i förloppen för de olika blocken. Det var olikheter när det gäller driften av nödkylningssystemen. I Block 1 bedöms det vara ett mer renodlat totalt bortfall av el utan några ingripanden. I de andra två reaktorerna var det tidvis drift av olika säkerhetssystem.

Det har gjorts en hel del analyser för att identifiera ledtrådar när det gäller förlopp och lokalisering av härdsmältorna. I detta avsnitt ges en översikt över observationer som gjorts och som kan tjäna som ledtrådar när det gäller förlopp och lokalisering.

Viktiga referenser för denna sammanställning har varit [13] som är ett arbete av en arbetsgrupp från USA och Japan, och det bildmaterial som har gjorts tillgängligt av TEPCO. En viktig referens är också Attachment 4 i [11] där viktiga resultat har sammantällts. För den senaste uppföljningen har rapporteringen i form av Nucelar Safety Reform Plan Progress Reports varit av stor betydelse [9], [10] och [14].

### 5.2.1. Hypoteser om härdsmältningsförlopp

Det kan finnas orsaker till skillnader mellan härdsmältningsförlopp i BWR och PWR. Möjliga skillnader illustreras i figur 5.4. I det övre scenariot illustreras förloppet i TMI-2. Det smälta bränslet samlas i en degel i härdens. Relokering av smälten sker genom att krustan runt degeln brister och en större eller mindre del av degelns innehåll relokeras till nedre plenum under en relativt kort period.



Figur 5.4 Hypotetiska härdsmältningsförlopp (Bild hämtad från [15]).

Det bedöms (se t. ex [15]) att en kontinuerlig relokering av smälta material som visats i det undre förloppet i figur 5.4, kan vara mer trolig för en BWR. Denna bedömning baseras på att föreningar kan bildas med låg smältpunkt. Drivande för temperaturökningen i härdens är givetvis resteffekten och oxidationsprocesser. Styrstavarna beräknas smälta redan runt 1250 °C. Det som bidrar till degraderingen av materialen i härdens vid relativt låga temperaturer är reaktioner mellan borkarbid och rostfritt stål, oxidering av stål samt reaktioner mellan zirkonium och rostfritt stål. Dessa reaktioner leder sannolikt till tidig relokering av härdens.

Scenariot är att materialet från härdens snarare än att bilda en degel som i TMI-2, rinner ner till härduppställningsplattan och även ner till nedre plenum. Delar av det

smälta materialet fragmenteras och kyls i vattnet i nedre plenum [15]. Mängden material i nedre plenum fylls på genom kontinuerlig relokering av härdmaterial och vattnet förångas. Detta leder till att större mängder material hinner ackumuleras i nedre plenum innan härdfragmenten igen smälter och tar sig genom reaktortankbotten. Det är troligt att smälorna föll ner i vatten i piedestalerna och i varierande grad fragmenterades och kyldes där.

### 5.2.2. Observationer och ledtrådar

På samma sätt som TMI-2 undersöktes och gav viktiga ledtrådar när det gäller beteende av härdsmälta i en PWR, kan olyckan i Fukushima ge viktig information om vad som händer vid en härdsmälta i en BWR.

En viktig fråga är att ta reda på läckagevägar mellan reaktortank och inneslutning och från inneslutning till reaktorbyggnad. En återstående fråga för reaktortanken är till exempel påverkan på säkerhetsventiler och ångledningar från heta gaser efter upprepade tryckavlastningar. För reaktorinneslutningarna är det viktigt att titta efter genomföringarna för att se var det läcker. Metodiken som används för reaktorerna är att identifiera områden med hög lokal reaktivitet som tecken på läckage.

### 5.2.3. Temperaturerna i reaktor och inneslutning

Det finns temperaturmätningar på olika nivåer i reaktorn, se figur 5.5. Temperaturen mättes i övre delen av tanken kring reaktortankens flänsförband (A) och vid bälgtäningen av säkerhetsventilerna (B). Dessutom mättes temperaturen nära matarvattensmunstycket (C) och botten av reaktortanken (D). Temperaturen mättes även i inneslutningen (E).

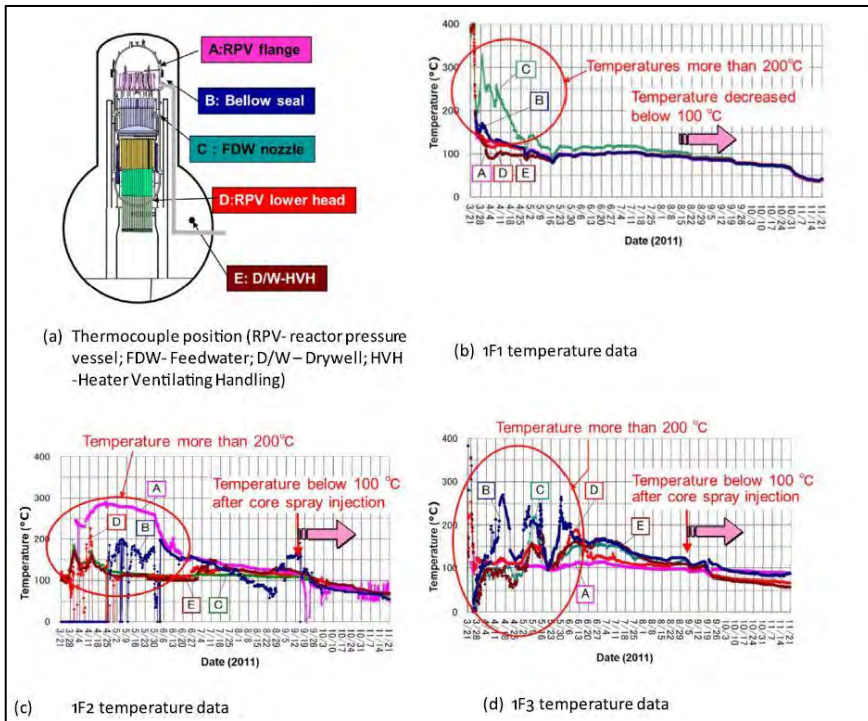
Temperaturmätningarna följdes upp i flera månader. Den första tiden efter havariet kyldes reaktorerna genom inpumpat vatten från brandpumpar och brandbilar. Detta var möjligt genom det befintliga restvärmekylsystemet (RHR) [16]. Systemet ansluter till cirkulationsledningen för jet-pumparna. I normala fall kan vatten pumpas in genom munstycket till jetpumpen och tas ut i fallspalten utanför diffusorn.

I tidperioden april-maj 2011 gjordes omkopplingar så att vatten kunde pumpas in genom det normala matarvattensystemet. Tanken var att få en mer stabil och effektiv kylning genom det befintliga systemet. Matarvattenstutsen ligger på en högre nivå i fallspalten och tanken var sannolikt att vattnet skulle kunna kyla en större del av reaktorn.

Temperaturerna i Block 1 visade viss överhettning till att börja med men föll snart till låga värden som indikerade god kylning. Det blev en tryckutjämning mellan primärsystem och inneslutning redan efter ungefär 10 timmar. Detta har tolkats som att ett brott på reaktortanken har skett vid denna tidpunkt. De låga temperaturerna i övre delen av reaktortanken indikerar en god kylning. Tolkningen är att en väsentlig del av härdens har lämnat reaktortanken och att det som är kvar går att kyla.

En intressant observation är att temperaturen i närheten av matarvattensstutsen visar överhettning fram till omkopplingen. Detta kan vara en indikation på att överhettat material kan ha tagit sig igenom väggen på moderatortanken och ut i fallspalten. TEPCO har analyserat fallet vilket skulle kunna vara tecken på ett mer TMI-2-likt förlopp.

När det gäller Block 2 och 3 så hade inte omkopplingen av kylvattnet någon effekt. Temperaturerna visade överhettning högt inuti reaktortanken och att kylningen fortfarande var otillräcklig. Detta har tolkats som att det finns en betydande del av härden kvar i reaktortanken utan tillräcklig kylning. Det har också tolkats som att det finns hål i botten av reaktortankarna där kylvattnet rinner ut i inneslutningen i stället för att kyla bränslet.



Figur 5.5 Temperaturförlloppen i reaktortankarna i Blocken 1-3 (Bilden är hämtad från [13])

Det finns även skillnader i temperaturmätningarna för Block 2 och 3. Detta kan ha orsakats av skillnader i förhållandet mellan mängden kylvatten som kommer in till härden och mängden kvarvarande bränsle. Det kan också ha orsakats av fördelningen av smälta inuti reaktortanken.

I september 2011 kunde man börja tillföra vatten genom strilning över härdarna i Block 2 och 3. Detta ledde till en mer effektiv kylning av härdresterna och etablering av underkylt tillstånd i reaktortankarna. I Block 1 gjordes omkopplingen till stril i december 2011. Detta fick ingen betydelse eftersom underkylda förhållanden redan existerade där.

Slutsatsen är att en betydande del av härden finns kvar i reaktortanken för Block 2 och 3 medan en större del av härden har fallit ner i inneslutningen i Block 1.

#### 5.2.4. Användning av myoner

Myon-teknologi används för att kvalitativt bestämma tätheten av material. Eftersom myoner har en svag interaktion med annat material tränger myonerna genom tjocka väggar av solid material. I princip är metodiken väl ägnad för att detektera områden med hög täthet. De bilder som har tagits fram är ganska otydliga och har ganska dålig upplösning. Metodiken beskrivs i [17]. Några resultat visas i [10].

Undersökningen i Block 1 som gjordes under 2015 pekade på att det inte var kvar material med hög densitet i härdområdet. Nedre delen av reaktortanken har dock inte

undersökts. Det kan antas att största delen av det smälta bränslet relokerades till inneslutningen.

Undersökningen av Block 2 som gjordes 2016 pekade på att det kan finnas material med hög täthet nära botten av reaktortanken. Detta tolkas som att det kan vara rester av härdsten som har fastnat där.

I Block 3 gjordes undersökningen sommaren 2017 [17]. Mängden material i härdområdet verkar ha reducerats väsentligt jämfört med utgångsläget. Det finns indikationer på att det kan finnas material med hög täthet nära botten av tanken. Detta kan tolkas så att några härdrester har stannat kvar i tanken.

#### 5.2.5. Visuella observationer och användning av robotar

I Block 1 pumpas vatten in genom matarvattensystemet och genom strilning över härdsten. Största delen av härdsmältan relokerades till nedre plenum och tog sig sedan vidare till piedestalen där det blev reaktioner mellan smälta och betong.

Läget nära botten av inneslutningen i Block 1 illustreras i figur 5.6. Undersökningen gjordes i oktober 2012. Det kunde då konstateras att vattennivån då var 2,8 m över golvet på primärutrymmet. Några härdrester kunde inte identifieras. Hela torusen är nu vattenfyld vilket illustreras i figur 5.6.

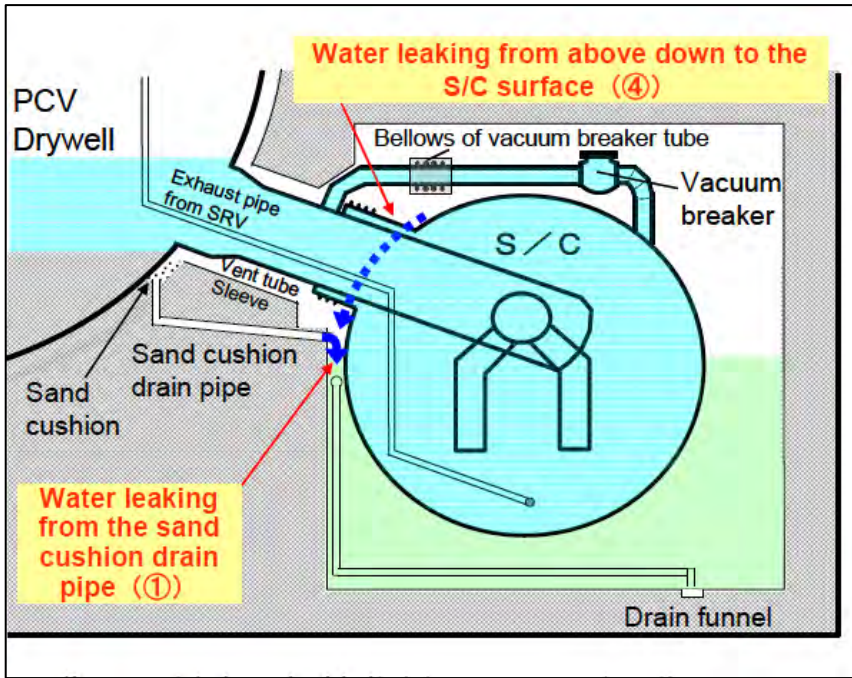
De flesta analyser pekar på att smälten borde ha varit utspridd på botten av piedestalen och varit kylbar där. Punktvisa undersökningar har inte kunnat bekräfta detta.

Området utanför torusen blev undersökt med båt. Det observerades en liten vattenström längs torusen sannolikt från bälgtätningen kring vakuumbrytarna mellan torusen och primärutrymmet (Se ring 4 i figur 5.6). Viktigare var att det observerades läckage i dräneringen från sandkudden, se figur 5.6. Eftersom denna ligger utanför inneslutningens tätplåt är detta en indikation på att smälten kan ha tagit sig igenom denna genom reaktioner mellan smälta och betong. Brott på tätplåten diskuteras även i [13] som inte utesluter att tätplåtens hållfasthet kan ha försämrats på grund av höga temperaturer i kombination med hög belastning på grund av det höga trycket i inneslutningen.

Undersökningar pågår med hjälp av robotar för att få en uppfattning om läget. I mars 2017 gjordes en kartläggning av strålningsnivån i vattnet utanför piedestalen.

Mätningarna under vatten visade att strålningsnivåerna ökade ju närmare golvet av inneslutningen man kom. Det var höga stråldoser nära öppningen av piedestalen. Observationer i närheten av tätplåten visade att det fanns material där med hög täthet. Ingen av dessa observationer motsäger slutsatserna att en stor del av härdstenen har lämnat reaktortanken och att överhettat material kan ha tagit sig ut till tätplåten. Det identifierades nedfallet skräp med hög densitet i vattnet utanför piedestalen.

I Block 2 gjordes visuella observationer [18]. I undersökningen som utfördes under januari och februari 2017 tog man sig in genom kanalen för utbyte av drivdon. Det visade sig att denna innehöll mycket skräp. En robot användes för att rensa bort skräpet för att sedan undersöka piedestalen. Extremt höga stråldoser uppmätttes just utanför väggen på piedestalen.



Figur 5.6. Läckagevägar i block 1 (Bilden är hämtad från [11], Attachment 4)

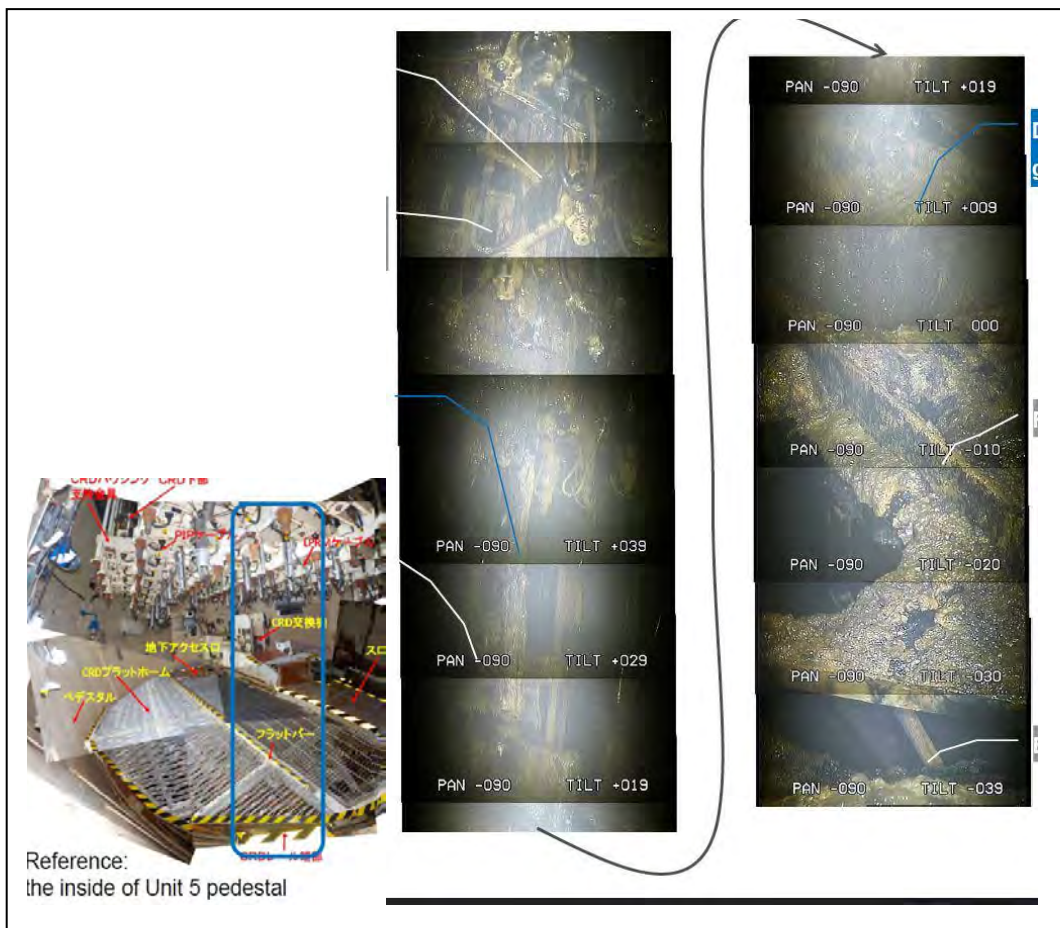
Det har observerats att en del av det övre grätingplanet i drivdonsgropen har deformerats, se nedre foton i figur 5.7. Som referens har en bild från en oskadad reaktor, Block 5, lagts in i bilden här. Området som har fotograferats är markerat med blått i bilden från Block 5. Undersökningen i Block 2 som planeras med den så kallade "scorpion" misslyckades eftersom den fastnade redan i kanalen för byte av drivdon.

I övre delen av bilden ses stöden för drivdonskåpor och kablar från LPRM-mätningar eller positionssystemet för styrstavarna. Det verkar som om härdrester har fastnat på TIP-systemet. I nedre delen av bilden kan den nedsunkna grätingen skönjas.

Slutsatsen är att det finns stora skador även på reaktortanken och att en väsentlig del av härdresterna kan ha tagit sig ut i inneslutningen. Detta verkar styrka de slutsatser som drogs i myon-undersökningen att en stor del av härdan har relokterats även i Block 2.

Bilder från bottensedimentet i piedestalen i Block 2 visas i Figur 5.8. Konsistensen av bottensedimentet är som sand eller lera. I fotot till höger kan en lyftbygel till en bränslepatron identifieras.

Under sommaren 2017 genomfördes undersökningar av botten av reaktortanken i Block 3 [20]. Eftersom vattennivån är hög i piedestalen gjordes undersökningen med en fjärrstyrd robot under vatten. Den var försedd med ljuskällor och kameror för att fotografera botten av reaktortanken.



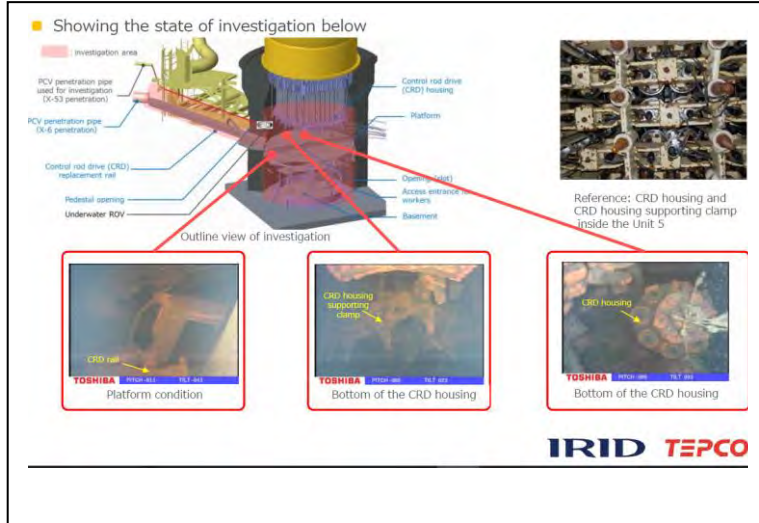
Figur 5.7 Vertikalt snitt från drivdonen ned till grätingplanet (Bilden är hämtad från [18])



Figur 5.8 Bilder från bottensediment i piedestalen i Block 2 (Bilden hämtad från [19]).

Exempel på bilder som togs visas i figur 5.9. Syftet med undersökningen var att börja klarlägga betingelserna innanför piedestalten. Motsvarande bild i en oskadad reaktor (Block 5) ses överst till höger i figur 5.9. Bilden visar att det är stora skador i reaktortankens botten. Det verkar som om stöden för kåporna runt några drivdon har lossnat och ramlat ner. Roboten rörde upp en del damm som gjorde bilderna otydliga. Det vore intressant att studera skadorna på till exempel övre grätingplanet i piedestalen men några sådana fotografier är ännu inte tillgängliga.

Undersökningen ledde fram till de första bilderna av påträffade härdrester [10]. Bilderna indikerar att en del av smältan har fallit ner och stelnat i piedestalen. Även om inte härdresterna ännu har analyserats ger dessa ett stöd för att större eller mindre delar av härdsmältan har tagit sig igenom botten av reaktortanken och ut i piedestalen där de har stelnat.



Figur 5.9 Bilder från undersökningen av botten av reaktortanken i Block 3 (Bild är hämtad från [10]).

### 5.2.6. Slutsatser

Det är klart att det finns individuella skillnader i förloppen för de olika blocken. Det var väsentliga skillnader när det gäller driften av nödkylningssystemen vilket medför osäkerheter när det gäller härdkylningen. Det finns begränsat med handfasta data att förlita sig på när det gäller själva förloppen. Förslag till vidare forskningsinsatser från OECD:s sida ges i [21]. Sammanfattningar ges i [15] och [22].

Vissa undersökningar är högprioriterade från både forsknings- och avvecklingssynpunkt. Detta gäller förloppen i reaktortanken, frågor kring bildandet av härdsmältan och hur den relokeras.

Av högprioriterade områden är beteendet av härdsmältan i inneslutningen och var härdsmältorna tog vägen. Det framhålls i [15] att observationer kring morfologin av härdsmältorna i inneslutningen är av stor betydelse. Det är troligt att smältorna föll i vatten i piedestalen och i varierande grad fragmenterades och kyldes där.

Det poängteras i [15] att en kartläggning av det som finns kvar av härden i olika positioner skulle vara av stort värde. Visuella observationer av skadorna på reaktortankbotten skulle kunna ge viktig information om genomsmältningsförloppet. Det skulle även vara av vikt att kartlägga skador på grund av höga gastemperaturer i reaktortanken.

Av områden med hög prioritet för forskningen på svåra haverier, men mindre betydelse för avvecklingen, tas även i [21] upp skrubbning i kondensationsbassängen, funktion av elektriska kablar och olika typer av genomföringar i inneslutningen.

### **5.3 Status för bränslebassängerna i Fukushima Daiichi**

Frågan kring vad som händer med bränslet i bränslebassängerna vid ett haveri är en återkommande fråga. Frågan fick avgörande betydelse för bedömningen av konsekvenser och insatser för att kunna ta hand om utsläppet i Fukushima. Bristfällig information om vad som hände i bränslebassängerna ledde till felaktiga beslut när det gäller uppskattning av utsläpp och vilka åtgärder som vidtogs för att kyla bränslet. Bristande instrumentering medförde att man under långa perioder var ovetande om vad som hände i bassängerna.

Man kan konstatera att gemensamt för samtliga block var att bränslebassängernas integritet inte förlorades. Det förlorades dock en del vatten på grund skvalpet vid jordbävningen och explosionerna. Mängden vatten minskade också på grund av förångning som orsakades av resteffekten i det använda bränslet.

Explosionen i Block 4 kom som en fullständig överraskning. Denna behandlas senare i detta avsnitt. När den amerikanska säkerhetsmyndigheten NRC gick ut med uppgiften om att en vätgasexplosion på grund av oxiderande bränsle hade ägt rum, befarades ett skräckscenario med bränslebrand i bränslebassängen och med mycket stora utsläpp som följd. NRC hävdade också att bassängen för använt bränsle var tom på vatten. På grund av detta uppstod en extrem oro och förvirring i media och bland berörda myndigheter och regeringstjänstemän. Från informationssynpunkt blev situationen i det närmsta katastrofalt.

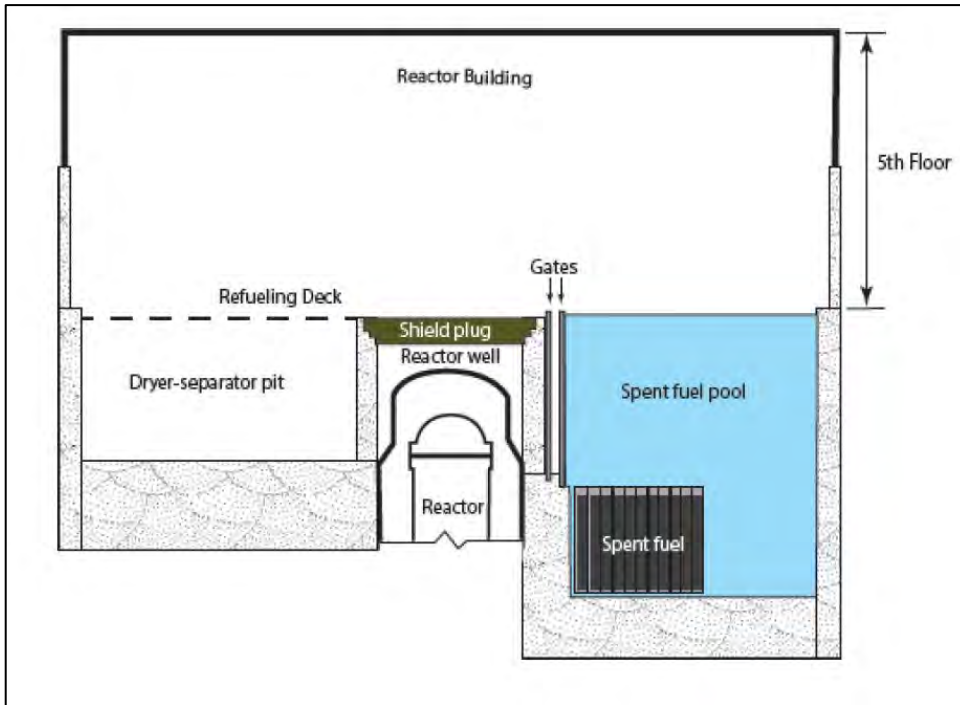
#### **5.3.1. Bränslebassängerna i Fukushima Daiichi före olyckan**

En principskiss av de geometriska förhållanden på femte våningen i de block som var i drift innan olyckan i Fukushima Daiichi visas i figur 5.10. Överkanten av det använda bränslet är lokaliseras ungefär 7 m under vattenytan i bränslebassängen. Under drift är det bara vatten i bränslebassängen. Under avställning är även volymen för lagring av ångseparatörer och ångtorkar och området kring reaktorn fyllt med vatten.

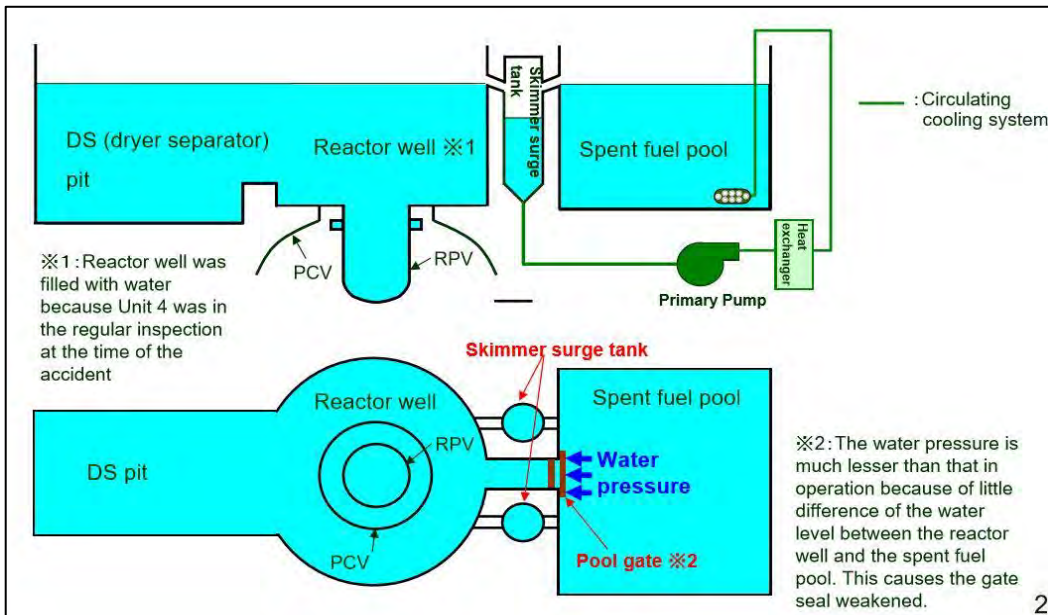
Bränslebassängerna är rektangulära i horisontell riktning. I Block 1 är dimensionen 12mx7.2m och i Blocken 2-4 12,2mx9,9m. Bränslebassängen och området över reaktorn är förbundet med en kanal med två portar (0,9 m breda och 6,4 m höga. Vid övertryck i bränslebassängen, vilket är det normala och visas i figur 5.10, hålls porten närmast bassängen tät genom vattentrycket. När portarna är stängda är bassängen och området kring reaktorn hydrauliskt isolerade från varandra.

Geometrin för Block 4 visas i figur 5.11. Skillnaden från blocken i drift är att locken på inneslutning och reaktortank är borttagna och att området kring reaktortanken och bassängen för förvaring av aktiva komponenter är vattenfylda. Dessa bassänger kommunicerar hydrauliskt genom en kanal.

Portarna till bränslebassängen är stängda men eftersom vattennivån nästan är den samma på båda sidorna blir tätningen försvagat. Ett läckage i tätningen, vilket var sannolik fram till 22 april bidrog till osäkerhet i beräkning av nivån i bränslebassängen. Detta diskuteras vidare i avsnitt 5.3.2.



Figur 5.10 Principskiss över femte våningen för de verk som var i drift vid olyckan (Bild hämtad från [23] (National Academies Press Open Book)



Figur 5.11. Den geometriska konfigurationen i block 4 (Bilden hämtad från [24])

Överloppstanken (Skimmer surge tank på bilden) spelade en viss roll under förloppet. Liknande överloppstankar finns på alla blocken. Slutsatsen drogs att när nivån i denna tank ökade så var detta en indikation på att bränslebassängen var full av vatten. Detta är givetvis korrekt med konfigurationen i Blocken 1 till 3. Med den situationen som fanns i Block 4, dvs. med vatten som sprutades ovanifrån, är inte denna slutsats självklar eftersom insprutat vatten även kunde flöda till överloppstanken från området kring reaktorn.

Stora insatser gjordes för att hålla bränslet i bränslebassängen täckt med vatten. För blocken 1-3 hade bränslet stått så länge i bassängen att konvektiv kylnings i luft sannolikt hade varit tillräcklig för att kyla dessa. Block 4 var avställd och bränslet från senaste härdladdning hade således stått 101 dygn i bränslebassängen. Detta bränsle stod för 82 % av restvärmens i bränslebassängen vid olyckan.

Temperaturen mättes 30 cm under den nominella vattennivån. När man tappade vatten från bassängerna mättes i stället väggtemperaturen. För att uppskatta nivåförloppen efter olyckan användes en förenklad beräkning av massa och energibalans där till exempel temperaturen i bassängen antogs vara uniform. Detta varade ungefär en månad efter olyckan då nivån kunde verifieras genom videokameror fästade på betongpumparna.

Gemensamt för samtliga block är att bränslebassängernas integritet inte förlorades. Bidragande till osäkerheten i nivån var uppskattningen av skvalpet vid jordbävning och explosioner. För Block 4 var det också osäkerhet kring mängden vatten som medverkade i förångningsprocessen.

### 5.3.2. Förloppen i bränslebassängerna för Blocken 1-3 och den gemensamma bassängen

Viktiga källor för att beskriva förloppen i bränslebassängerna vid Fukushima Daiichi är bilagorna (Attachment 9-2—9-5) som finns till TEPCO:s rapport [31] från olyckan och den utredning som publicerades av den amerikanska National Academies Press Open Book [23]. I den senare kunde oberoende erfarenheter av de egna bränslebassängerna vägas in.

Förlusten av växelspänning efter tsunamin medförde att bassängen inte kunde kylas eller påfyllas vatten för samtliga block. Det antogs allmänt att vattennivån var hög i bassängerna vilket baserades på att det fanns varierande vattennivåer i överströmningstanken. Det kan i efterhand konstateras att förloppen i bassängen för de reaktorerna som var i drift vid olyckan (Block 1-3) inte innebar några större säkerhetsrisker.

Innan jordbävningen innehöll bränslebassängen i **Block 1** 292 patroner med använt bränsle som utvecklade 0,18 MW restvärmee. Klockan 15:36 den 12 mars 2011 skadades reaktorbyggnaden av en vätgasexplosion och taket på byggnaden föll in. Taket fastnade dock delvis på en kran och nådde inte helt ned till bränslebassängen.

Med början den 31 mars 2011 användes betongpumpar för sprinkling av färskvatten över byggnaden. Inpumpningen med betongpumparna fortsatta intermittent fram till 28 maj då man kopplade sig på det befintliga rörsystemet för kylning av bränslebassängen. Ett förstärkt kylningsystem togs i bruk den 10 augusti 2011. Bränslet var väl täckt av vatten under hela förloppet och minimum beräknad nivå var drygt 4 m över bränslet. I slutet av maj 2011 var nivån återställd.

Den 11 mars 2011 fanns det 587 patroner med använt bränsle och 28 patroner med färskt bränsle i bassängen för **Block 2**. Effektutvecklingen var 0,62 MW. Vid explosionen i Block 2 blåstes några utblåsningsluckor ut i reaktorbyggnaden. Senare i förloppet observerades att vit dimma, som befarades komma från bränslebassängen, kom ut. Det kunde senare bekräftas att så inte var fallet. Det är sannolikt att dimman härrörde från kondenserande ångan som läckte från inneslutningen. Man använde ett existerande kylningsystem från en närliggande byggnad där sjövatten började pumpas in 20 mars 2011 från en brandbil. Som mest beräknades vattenförlusten till ungefär 1

m. Efter 29 mars 2011 började man pumpa in färskvatten. Den 31 maj kunde ett förstärkt alternativt kylysystem kopplas in och efter några dagar hade temperaturen i vattnet stabiliserats till kring 30 °C.

Då jordbävningen inträffade fanns det 514 patroner använt bränsle i bassängen i **Block 3**. Dessa alstrade 0.54 MW vid tiden för olyckan. Vid jordbävningen blev det en hel del skvalp som gjorde att nivån sjönk. Nivån sjönk ytterligare vid explosionen den 14 mars 2011 och det bedömdes att vattennivån i bränslebassängen hade sjunkit 2-3 m. Med hänsyn till osäkerheter kan nivån ha varit så låg som 3 m över bränslet.

Vätgasexplosionen inträffade den 14 mars 2011 klockan 11:01. Denna blåste ut reaktorbyggnaden och mycket skräp genom kollaps av stål och betongstrukturer och utrustning, föll ned på toppen av bassängen. Redan den 16 mars 2011 gjordes försök att dumpa vatten från helikopter. Från kvällen den 17 mars 2011 användes brandfordon för att sprinkla vatten. Fram till 25 mars 2011 användes även mobila vattenpumpar. Det var mest sjövatten som pumpades in. Vit dimma observerades från reaktorbyggnaden efter explosionen vilket befärdades komma från oxidation av bränsle eller kondenserad ånga från bränslebassängen. Det mest troliga är dock att denna härrör från inpumpat vatten som träffade toppen av inneslutningen.

Insatserna på Block 3 prioriterades och operatörerna försökte att tillföra vatten med hjälp av helikopter och brandfordonspumpar. och från 27 mars till 22 april 2011 använde man mobila betongpumpar för att pumpa in vatten. Man växlade till färskvatten 29 mars. Man kunde från 26 april pumpa in vatten på vanligt sätt. Ett förstärkt kylysystem kunde tas i bruk den 29 juni 2011. Bränslet i bränslebasängen har inte skadats. Skräpet över bränslebassängen har tagits bort och bränslet kommer att tas bort med början 2018.

Den gemensamma bassängen (som fungerar som ett mellanlager) som innehöll använt bränsle utvecklade en effekt på 1,13 MW då olyckan inträffade. Byggnaden var intakt och det kunde verifieras att bränslet var täckt med vatten.

### 5.3.3. Förlloppet i bränslebassängen för Block 4

Då jordbävningen inträffade fanns 1331 patroner använt bränsle i bassängen i **Block 4**. Det beräknas att dessa vid tiden för olyckan alstrade 2.26 MW. Av dessa hade 548 patroner tagits ut den 29 november 2010 och hade stått 101 dygn i bassängen. Dessa patroner alstrade 82 % av restvärmen i bränslebassängen. Vid jordbävningen och explosionen blev det en hel del skvalp som gjorde att nivån sjönk. Till att börja med prioriterades inte arbetet med Block 4.

Explosionen i Block 4 som inträffade den 15 mars 2011 klockan 06:10 orsakade en extrem oro och förvirring i media och bland berörda myndigheter och regeringstjänstemän. Explosionen var en av de mest överraskande händelserna under olyckan. Det var känt att blocket var nere för revision och byte av moderatortank och att allt bränsle hade flyttats till bränslebassängen. Ingen kamera fångade händelsen och det var därför svårt att i efterhand rekonstruera förlloppet. Explosionen förstörde taket och slog ut väggarna på de två översta våningarna. Explosionen gjorde att fokus ändrades. Spekulationer kring orsaken till explosionerna ledde till felaktiga utgångspunkter för vidare åtgärder och obefogade farhågor.

Flera gjorde bedömningen att bränslebassängen var tom på vatten med bara bränsle kvar. Ordförande för NRC, Gregory Jaczko, rapporterade till kongressen den 16 mars

2011 att en vätgasexplosion hade inträffat på grund av avtäckning av bränslet i bassängen [23]. Med skadad reaktorbyggnad och utan vatten i bränslebassängen befådes ett mardrömslikt scenario med överhettnings av bränslet och med bränslebrand och mycket stora utsläpp.

Det kan noteras att det redan den 16 mars 2011 gjordes observationer från de helikopter som släppte kylvatten över Block 3, att det fanns vatten i bränslebassängen i Block 4. Några direkta mätningar av vattennivån gjordes först tre veckor senare.

I avsaknad av bättre förklaring på vad som orsakade explosionen, fick observationerna inte något genomslag och även den japanska myndigheten och regeringstjänstemän delade bedömningen att ett mycket stort utsläpp var på gång. Man kom dock med olika bud om zoner med begränsat tillträde runt reaktorn vilket var förvirrande för press och allmänhet. Det framgår av senare dokument [26] att det amerikanska utsläppsscenarioet baserades på beräkningar med antagande om 100 % utsläpp från bränslet i bassängen i Block 4.

Uppgiften om att det var vätgasproduktion från bränslet i bränslebassängen kom att dominera informationen i dagarna som följde. Det kan i efterhand konstateras att en sådan process skulle innehålla att bränslet i bassängen hade oxiderats i en ångatmosfär. Oxidation i luft, vilket skulle vara fallet, skulle inte ge någon vätgas. NRC:s slutsats var således felaktig.

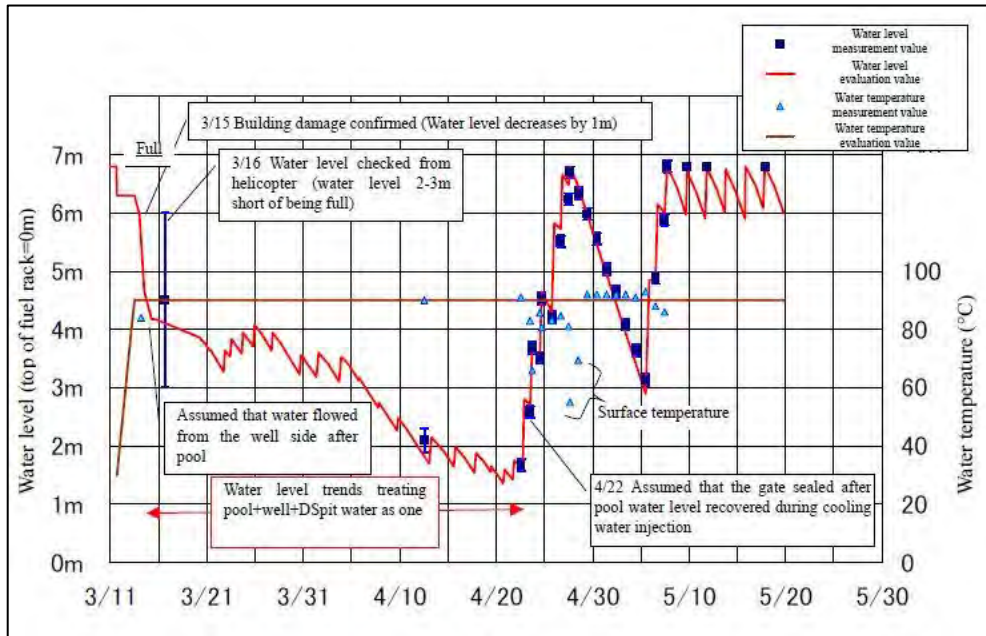
Det var problem med hypotesen om en vätgasexplosion på grund av oxiderande bränsle i bassängen. Efter några dagar kom TEPCO med en hypotes om att vätgasen kom från Block 3 genom avgasningssystemet som ledde till skorstenen som var gemensam för Block 3 och 4. Hypotesen om överströmning från Block 3 anses numera vara styrkt.

Det återstår dock en fråga. Det gick 19 timmar mellan explosionen i Block 3 och Block 4. Under denna tid skedde givetvis ingen överströmning och koncentrationen av vätgas i Block 4 bör ha minskat. Att ha en brännbar blandning av vätgas och luft utan antändning under så lång tid verkar mindre troligt. Det är mer troligt att det finns en källa som genererar vätgas även i Block 4. Analyser visar att det inte är uteslutet att radiolys i bränslebassängen kan ha bidragit till mängden vätgas.

På SSM den 16 mars 2011 spekulerades om vad som kunde ha lett till explosionen. På kvällen näddes SSM av meddelandet från NRC genom nyhetsmedia efter att Jaczko hade avlagt sin rapport till kongressen. SSM tog nyheten på stort allvar och gjorde bedömningen att ett mardrömsscenario med ett mycket stort utsläpp från oxiderande bränsle i bränslebassängen var möjlig. SSM noterade att oxidation i luft skulle ge mycket högre effektutveckling än i ånga; dock skulle bildande av vätgas under sådana förhållanden vara mer begränsad. SSM hade även tillgång till väderdata som visade att luften över Fukushima något dygn senare kunde nå Tokyo. Detta ledde till beslut om att skicka jod-tabletter till svenska ambassaden i Tokyo; i första hand till svenskar på kortare vistelse där.

En mycket viktig fråga för SSM, och andra, var hur mycket rutenium som kunde frigöras från bränslet. Vid oxidation i luft kan stora mängder rutenium frigöras vilket har studerats i samband med så kallad ”air ingress” scenario i PWR. SSM försökte under Fukushima-olyckan uppskatta frigörelse av ruteniumoxid baserat på experimentella data. Uppskattningen var svår på grund av bristande information om tillståndet i bassängen men det gjordes en bedömning som senare användes. Det

blev en rekommendation att inte vistas närmare Fukushima än 80 km. Det senare var ungefär samma avstånd som NRC hade kommit fram till.



Figur 5.12: Nivåförfloppet i Block 4 (Bild hämtat från [25] Attachment 9-5)

I figur 5.12 visas beräknad och uppmätt nivå i bränslebassängen. Till att börja med sjönk nivån på grund av skvalp efter jordbävningen. Skvalpet bedömdes ge en nivåsänkning på ungefär 0,5 m. Nivån bedömdes sjunka ytterligare 1 m på grund av explosionen. Efteråt var det avdunstningen på grund av restvärmens som dominérade. Uppmätt temperatur i bassängen steg till ungefär 88 °C. Vid denna temperatur försas hela restvärmens i bassängen bort genom avdunstning.

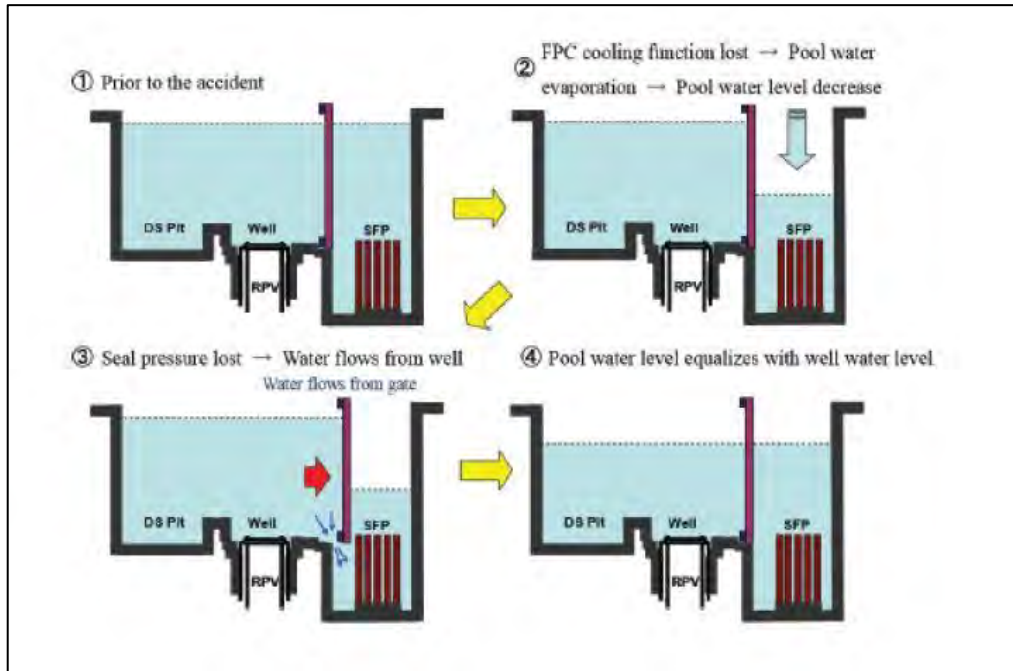
Den 20 mars 2011 påbörjades sprinkling med färskvatten från brandfordon. Den 22 mars 2011 påbörjades sprinkling med sjövatten med betongpumpar. Under perioden från mitten av mars till mitten av april då mätningar kunde göras, bedömdes att bränslebassängen var fylld med vatten eftersom nivån i överströmningstanken fluktuerade.

Denna bedömning var felaktig och orsakades troligen av att en del av det insprinklade vattnet direkt hamnade i överströmningstanken. En nivåmätning som hade installerats på en betongpump användes för att mäta vattennivån för första gången den 12 april 2011. Då var nivån 2,1 m över bränslet.

Man lyckades inte att pumpa in vatten i tillräcklig omfattning vilket innebar att vattennivån sjönk till 1,5 m över bränslet vilket observerades runt den 20 april 2011. Under den här tiden läckte portarna mellan bränslebassängen och området runt reaktorn vilket ledde till en överströmning som kan ha bidragit till att vattennivån inte sjönk under bränslets övre kant. Mellan den 22 april och 27 april 2011 var portarna täta och man kunde fylla på vatten.

Från den 16 juni 2011 kyldes bassängen med det installerade systemet för kylning av bränslebassängen. Ett troligt förlopp illustreras i figur 5.13. Innan olyckan var det öppet mellan komponentbassängen och området över reaktorn [1], se figur 5.13. Kanalen mellan området kring reaktorn och bränslebassängen var stängd och förångning

av vatten i bränslebassängen får nivån att sjunka [2]. Det bildas således en tryckskillnad med lägre tryck i bränslebassängen och läckage [3] och därefter nivåutjämning i bassängerna vid en lägre nivå. Den 22 april var nivån som lägst, ungefär 1,5 m över bränslets övre kant. Därefter kunde tätheten av portarna säkerställas och bränslebassängen kunde fyllas upp [4].



Figur 5.13: Förfloppet i bränslebassängen i Block 4 (Hämtad från [25] Attachment 9-5)

Överföringen av bränsle till den gemensamma bassängen slutfördes den 22 december 2014. Inga skador på bränslet som härrör från olyckan har identifierats.

#### 5.3.4. Viktiga resultat

Referens [27] ger en översikt över status för forskningen och speciellt vilken kunskap som har utvecklats vad gäller förfloppen i bränslebassänger. Speciellt har det fokuserats på antändning av och utbredning av en bränslebrand, se [28] - [30]. I ref. [31] finns en diskussion av vad som kan hända i bränslebassängen vid en jordbävning.

Generellt är det så att bränsle som är täckt av vatten i bränslebassängen är väl kylt. I fall att vatten inte kan fyllas på kommer nivån att sjunka på grund av förångning vilket är ett relativt långt utdragit förflopp. Vid en sådan avtäckning kan den konvektiva kylningen med luft vara otillräcklig för bränsle som nyss har tagits ut ur reaktortanken.

Internationella forskningsprojekt har genomförts med mätning av tid till antändning i olika konfigurationer. En slutsats som dragits av NRC [29] är att för bränsle som har tagits ut mindre än 30 dygn innan händelsen med härdavtäckning, behövs kylning med vatten, antingen genom påfyllnad eller genom sprinkling. Vid längre tider kan förfloppet påverkas genom att omfördela bränslet så att bränsle med hög resteffekt står i en omgivning av bränsle med lägre effekt. I USA har en regel införts [32] om att en omfördelning av bränsle bör ske inom 60 dygn. Luftkyllning är inte tillräcklig för visst bränsle även efter 60 dygn så den tekniska bakgrunden för regeln är något oklar.

I Block 4 hade bränslet inte omfördelats och bränsle med hög effekt hade lagrats i en begränsad del av bränslebassängen. De insatser som gjordes för att undvika avtäckning av bränslet i Block 4 kan därför ha varit motiverade. För Blocken 1-3 var den utvecklade effekten så låg att konvektiv kylning med luft hade varit tillräcklig.

En översikt över vad som kan förväntas under ett förlopp med avtäckning av bränsle med relativt hög effekt ges i [32]. I avsaknad av kylning kommer bränslet att värmas upp. Kemiska processer mellan zirkonium och omgivande gas påverkar förlloppet. Det intressanta temperaturspannet är mellan 500 °C och 1400 °C. De exoterma kemiska processerna beskrivs närmare i Appendix B i [21] och kan summeras enligt följande:

- *Oxidering av zirkonium i luft:*  $Zr + O_2 \rightarrow ZrO_2$  (1094.8 kJ/mol Zr) (3.1)
- *Oxidering av zirkonium i ånga:*  $Zr + 2H_2O \rightarrow ZrO_2 + 2H_2$  (529.1 kJ/mol Zr) (3.2)
- *Bildande av zirkonium nitrid:*  $Zr + \frac{1}{2}N_2 \rightarrow ZrN$  (365.4 kJ/mol Zr) (3.3)
- *Oxidation av zirkonium nitrid:*  $ZrN + O_2 \rightarrow ZrO_2 + \frac{1}{2}N_2$  (729.4.4 kJ/mol Zr) (3.4)

Den angivna energiutvecklingen för processerna är vid ungefär 1200 °C.

Vid höga temperaturer reagerar zirkonium med syre och bildar zirkoniumdioxid under stor värmeutveckling enligt ekv. 3.1. En färsk metallyta oxideras snabbt. Eftersom oxidskiktet växer kontrolleras fenomenet av diffusionen av syre genom oxidskiktet och oxidationshastigheten minskar. En motsvarande process med diffusion av ånga sker vid oxidation i en ångatmosfär enligt ekv. 3.2, och ett nästan identiskt oxidskikt bildas.

Vid kapslingstemperaturer under 1050 °C blir det en fasövergång i zirkoniumdioxiden som ökar oxidskiktets volym. Detta leder till uppsprickning av oxidskiktet och exponerar hela tiden färsk metallyta till gasen vilket i sin tur ökar oxidationen. Fenomenet betecknas som "breakaway". För att uppnå en realistisk simulering av oxidationen måste breakaway inkluderas. Vid temperaturer över 1100 °C försvinner denna effekt. Den fysikaliska förklaringen till fenomenet "breakaway" är inte helt klarlagt och det finns flera hypoteser. Forskningen på området fokuseras på att klaralägga vilka parametrar som påverkar fenomenet.

Förekomsten av kväve leder till bildande av zirkonium nitrid enligt ekv. 3.3. En tänkbar orsak är att oxidationen lokalt leder till brist på syre och därmed en anrikning av kväve. Detta leder till en kraftig ökning av breakaway. Vid 800 °C och 900 °C ökar breakaway med en storleksordning när det finns kväve tillgänglig. Vid oxidationen av zirkonium nitrid enligt ekv. 3.4 behöver nytt syre tillföras. Volymen ökar med 46 % vilket gör att nitridskiktet lätt krackelerar.

Experimenten i Sandia med antändning av en bränslebrand pekar på följande scenario vid en överhettning [29]. Antändningen sker nära utloppet av bränsleknippet och sprider sig transversellt till närliggande bränslepatroner. Den primära oxidationen (Ekv 3.1) sker i timskala och reaktionen med zirkonium konsumrar allt syre och en väsentlig del av kvävet bildar zirkonium nitrid (Ekv 3.3). Under en längre fas som kan vara i flera dygn oxideras zirkonium nitrid.

### 5.3.5. Slutsatser

I Fukushima fanns brister i instrumentering som gjorde att det var svårt att bilda sig en uppfattning om det verkliga läget.

När det gäller bortfallet av elektrisk kraft har man olika metoder värderats för att förse bassängerna med vatten. Till exempel för Kashiwazaki-Kariwa har bränslebassängerna, i tillägg till det vanliga kylsystemet som har förstärkts, försetts med dysor som kan sprinkla vatten [33]. Nivåmätningen har förbättrats för att täcka in hela bassängen.

För amerikanska verk har portarna mellan bränslebassängen och området kring reaktorn identifierats som svaga punkter. Det har upprepade gånger varit nära kylmedelsförlust från bränslebassängen på grund av defekter i portarna på likadant sätt som inträffade i Fukushima.

I OECD/NEA:s rapport [27] konstateras att inga olyckor med stora utsläpp har förekommit från bränslebassänger. Det konstateras att de viktigaste fenomenen som förekommer i samband med kylningsavbrott i bränslebassängen är kända. Förslag till vidare forskningsinsatser från OECD:s sida ges i [21]. I detta graderas säkerhetsintresset för ytterligare forskning kring fenomen i bränslebassängen som lågt.

Den analysverksamhet som har bedrivits efter APRI-8 har inte lett till några avgörande ändrade slutsatser. Därmed anses de slutsatser om förfloppen som drogs i APRI-8 fortfarande gälla d.v.s. att inga avgörande okända fenomen har identifierats som skulle påverka den svenska strategin för havarihantering och utförandet av de konsekvenslindrande systemen.

## 5.4 Referenser

- [1] Slutrapport APRI-8. SSM Report 2015:27.
- [2] APRI-9 - Status för reaktorerna i Fukushima Daiichi 1-3, Rapport 2018-1 OddSan Consulting, Februari 2018.
- [3] APRI-9 - Sluttillstånden för härdarna i Fukushima Daiichi 1-3, Rapport 2018-2 OddSan Consulting, Februari 2018,
- [4] APRI-9 – Bränslebassängen i Fukushima Daiichi. Rapport 2018-3. OddSan Consulting, Februari 2018
- [5] Nuclear World Association – Nuclear Power in Japan (December 2017) <http://www.world-nuclear.org/information-library/country-profiles/countries-g-n/japan-nuclear-power.aspx>
- [6] Temperatures measured inside the Unit 1 Primary Containment Vessel at [http://www.tepco.co.jp/en/nu/fukushima-np/f1/plantdata/unit1/pcv\\_index-e.html](http://www.tepco.co.jp/en/nu/fukushima-np/f1/plantdata/unit1/pcv_index-e.html)
- [7] Temperatures measured inside the Unit 2 Primary Containment Vessel at Fukushima Daiichi Nuclear Power Station [http://www.tepco.co.jp/en/nu/fukushima-np/f1/plant-data/unit2/pcv\\_index-e.html](http://www.tepco.co.jp/en/nu/fukushima-np/f1/plant-data/unit2/pcv_index-e.html)
- [8] Temperatures measured inside the Unit 3 Primary Containment Vessel at Fukushima Daiichi Nuclear Power Station [http://www.tepco.co.jp/en/nu/fukushima-np/f1/plant-data/unit3/pcv\\_index-e.html](http://www.tepco.co.jp/en/nu/fukushima-np/f1/plant-data/unit3/pcv_index-e.html)
- [9] Nuclear Safety Reform Plan FY2017Q1 Progress Report, August 4, 2017 [https://www4.tepco.co.jp/en/press/corp-com/release/betu17\\_e/images/170804e0102.pdf](https://www4.tepco.co.jp/en/press/corp-com/release/betu17_e/images/170804e0102.pdf)
- [10] Nuclear Safety Reform Plan FY2017Q2 Progress Report, November 1, 2017 <https://www4.tepco.co.jp/press/release/2017/pdf2/171101j0102.pdf>

- [11] TEPCO: Evaluation of the situation of cores and containment vessels of Fukushima Daiichi Nuclear Power Station Units- 1 to 3 and examination into unresolved issues in the accident progression. Progress Report No 4. December 17, 2015.
- [12] A Report by The American Nuclear Society Special Committee on Fukushima 2012 [http://fukushima.ans.org/inc/Fukushima\\_Appendix\\_F.pdf](http://fukushima.ans.org/inc/Fukushima_Appendix_F.pdf)
- [13] Rempe, J. et al. Safety Insights from forensic evaluations at Daiichi. Nuclear Materials and Energy 10 (2017) pp 18-34.
- [14] Nuclear Safety Reform Plan FY2016Q4 Progress Report, May 10, 2017 [http://www.tepco.co.jp/en/press/corp-com/release/betu17\\_e/images/170510e0102.pdf](http://www.tepco.co.jp/en/press/corp-com/release/betu17_e/images/170510e0102.pdf)
- [15] Lee, R. Thoughts on Fukushima Forensic BWR Accident Analysis. Technical Meeting On Post-Fukushima Research And Development Strategies and Priorities, IAEA Headquarters Vienna, Austria December 15-18, 2015 U.S. Nuclear Regulatory Commission.[https://www.iaea.org/NuclearPower/Downloadable/Meetings/2015/2015-12-15-12-18-NPTDS/2C-5\\_R.Lee.pdf](https://www.iaea.org/NuclearPower/Downloadable/Meetings/2015/2015-12-15-12-18-NPTDS/2C-5_R.Lee.pdf)
- [16] World Nuclear Association Fukushima: Background on Reactors (2012) <http://www.world-nuclear.org/information-library/safety-and-security/safety-of-plants/appendices/fukushima-reactor-background.aspx>
- [17] Locating Fuel Debris inside the Unit 3 Reactor Using a Muon Measurement Technology at Fukushima Daiichi Nuclear Power Station [https://www4.tepco.co.jp/en/nu/fukushima-np/handouts/2017/images/handouts\\_170928\\_01-e.pdf](https://www4.tepco.co.jp/en/nu/fukushima-np/handouts/2017/images/handouts_170928_01-e.pdf). September 28, 2017.
- [18] Pre-investigation results of the area inside the pedestal for the Unit 2 Primary Containment Vessel Investigation at Fukushima Daiichi Nuclear Power Station (examination results of digital images)[http://www.tepco.co.jp/en/nu/fukushima-np/handouts/2017/images/handouts\\_170202\\_01-e.pdf](http://www.tepco.co.jp/en/nu/fukushima-np/handouts/2017/images/handouts_170202_01-e.pdf). February 2, 2017
- [19] Fukushima Daiichi Nuclear Power Station Unit 2 Primary Containment Vessel Internal Investigation Results, February 1 2018. [http://www.tepco.co.jp/en/nu/fukushima-np/handouts/2018/images/handouts\\_180119\\_01-e.pdf](http://www.tepco.co.jp/en/nu/fukushima-np/handouts/2018/images/handouts_180119_01-e.pdf).
- [20] Progress of Unit 3 PCV Internal Investigation (Preliminary Report of July 19 Investigation. [http://www.tepco.co.jp/en/nu/fukushima-np/handouts/2017/images/handouts\\_170719\\_01-e.pdf](http://www.tepco.co.jp/en/nu/fukushima-np/handouts/2017/images/handouts_170719_01-e.pdf), July 19, 2017
- [21] Safety Research Opportunities Post-Fukushima Initial Report of the Senior Expert Group NEA/CSNI/R(2016)19 February 2017. <http://www.oecd-nea.org/nsd/docs/2016/csni-r2016-19.pdf>
- [22] Funaki, K, Status of CSNI Senior Expert Group (SEG) on Safety Research Opportunities Post Fukushima (SAREF), 19th CSNI/WGAMA meeting, September 2016
- [23] Lessons Learned from the Fukushima Nuclear Accident for Improving Safety and Security of US Nuclear Plants: Phase 2 (2016). Chapter 2. Lessons Learned for Spent Fuel Storage. The National Academies Press Open Book. <https://www.nap.edu/read/21874/chapter/5>
- [24] The skimmer surge tank drawdown at the Unit 4 spent fuel pool. [http://www.tepco.co.jp/en/nu/fukushima-np/roadmap/images/m120123\\_02-e.pdf](http://www.tepco.co.jp/en/nu/fukushima-np/roadmap/images/m120123_02-e.pdf) January 23 2012.
- [25] Fukushima Nuclear Accident Analysis Report, June 20, 2012.Tokyo Electric Power Company
- [26] Brev till Senator Jim Webb från Gregory Jaczko “Information regarding the assumptions used in recommending a 50-mile evacuation for U.S. citizens following the Fukushima Daiichi nuclear facility events” June 17, 2011. <https://www.nrc.gov/reading-rm/doc-collections/congress-docs/correspondence/2011/webb-06-17-2011.pdf>
- [27] Status Report on Spent Fuel Pools under Loss-of-Cooling and Loss-of-Coolant Accident. NEA/CSNI/R(2015)2 [www.oecd-nea.org/nsd/docs/2015/csni-r2015-2.pdf](http://www.oecd-nea.org/nsd/docs/2015/csni-r2015-2.pdf)
- [28] NUREG/CR-7215 Spent Fuel Pool Project Phase II: Pre-ignition and Ignition Testing of a Single Commercial 17 x17 Pressurized Water Reactor Spent Fuel Assembly under Complete Loss of Coolant Accident Conditions, April 2016

- [29] NUREG/CR-7216 Spent Fuel Pool Project Phase I: Pre-ignition and Ignition Testing of a 1 x 4 Commercial 17 x17 Pressurized Water Reactor Spent Fuel Assemblies under Complete Loss of Coolant Accident Conditions, April 2016
- [30] NUREG/CR-7143 Characterization of Thermal-Hydraulic and Ignition Phenomena in Prototypic, Full-Length Boiling Water Reactor Spent Fuel Pool Assemblies After a Postulated Complete Loss-of-Coolant Accident. March 2013
- [31] NUREG-2161 Consequence Study of a Beyond-Design-Basis Earthquake Affecting the Spent Fuel Pool for a U.S. Mark I Boiling Water Reactor. September 2014
- [32] Lessons Learned from the Fukushima Nuclear Accident for Improving Safety and Security of US Nuclear Plants: Phase 2 (2016). Chapter 6. Loss-of-Coolant Events in Spent Fuel Pools The National Academies Press Open Book. <https://www.nap.edu/read/21874/chapter/9>.
- [33] Kenji Tateiwa: Spent Fuel and Spent Fuel Storage Facilities at Fukushima Daiichi TEPCO January 2015 [http://dels.nas.edu/resources/static-assets/nrsb/miscellaneous/09\\_TATEIWA.pdf](http://dels.nas.edu/resources/static-assets/nrsb/miscellaneous/09_TATEIWA.pdf).

## 6. SAMMANFATTNING, SLUTSATSER OCH REKOMMENDATIONER

### 6.1 Sammanfattning av projektet

APRI-9 har följt den internationella forskningen och utvärderat resultaten. Det fortsatta stödet till KTH har gett ökad grundläggande kunskap om möjligheten att kyla den smälta härdens i reaktortanken och om processer i samband med kylbarheten i inneslutningen samt vid ångexplosioner. Stödet till Chalmers har gett ökad grundläggande kunskap om haverikemi, främst rutenium och tellurs uppförande i inneslutningen efter ett haveri.

#### 6.1.1. Internationella forskningsprojekt

Deltagande i CSARP ger tillgång till en mängd information om olika fenomen av betydelse för händelseförlopp vid svåra haverier som kommer fram från internationell forskning. Informationsutbytet sker huvudsakligen vid en årlig konferens. Deltagandet ger också tillgång till beräkningskoder utfärdade av NRC, varav MELCOR används i flera projekt.

OECD-projektet STEM syftar till att förbättra kunskapen om komplexa fenomen som påverkar den s.k. källtermen vid en radiologisk olycka, dvs. de radioaktiva ämnena som förväntas släppas ut till omgivningen i samband ett haveri. Projektets huvudsakliga fokus ligger på förståelse för fenomen kopplade till radioaktiv jod och dess interaktion med andra ämnen, samt också transportfenomen kopplade till rutenium som är en annan viktig fissionsprodukt. Det studeras åldringseffekter på målade ytor, radiolytiskt och kemiskt inducerat sönderfall av jodoxider, radiolytisk oxidation av jodaerosoler i multikomponentblandning och transport av rutenium från primärsystemet.

OECD-projektet THAI3 pågår med försök inom flera områden:

- Kartläggning hur PAR-enheternas uppstartsbehov och prestanda påverkas av motströmsflöde, samt hur prestandan påverkas av PAR-enhetens skorstenshöjd.
- Undersöka hur förbränningensförloppet för vätgas påverkas av strömningsförhållanden under naturlig konvektion och vätgaskoncentrationsgradienter.
- Kartläggning av hur fissionsprodukter (aerosoler och jod) kan återföras till inneslutningsatmosfären från en kondensationsbassäng/sump vid förhöjda temperaturer eller vid kokning.
- Undersökning av frigörelse av fördeponerade aerosoler och olika former av jod från ytor i samband med vätgasdeflagration.

OECD-projektet BIP 3 syftar till studier av olika aspekter av jodkemin. Studier av åldringseffekter på målade ytor visar att färsk färgytor ger den största produktionen av metyljodid vid gammabestrålning. Denna förmåga minskar med provets ålder. Dock är förändringen måttlig.

Lakning av organiska föreningar från målade ytor har studerats. Resultaten kan tolkas som att åldring förstör den polymera färgstrukturen, vilket leder till en fragmentering som underlättar urlakning. Detta kan förklara hur åldring påverkar ytans förmåga till bildning av organiska jodföreningar, som t.ex. metyljodid.

Vid försök med åldringseffekter på målade ytor är trenden att adsorptionshastigheten är oberoende av hur proverna har åldrats (på naturlig väg, genom värmepåverkan eller genom gammabestrålning), men att åldring gör att adsorptionshastigheten sjunker något.

Försöken inom OECD-projekten STEM-2, THAI-3 och BIP-3 ger goda förutsättningar att förbättra beräkningskoder för fissionsprodukters beteende, genom en ökad förståelse för olika komplexa fenomen och processer och hur de påverkar innehållet i de radioaktiva utsläpp som förväntas vid ett haveri.

### 6.1.2. ROAAM-projektet

Utvecklingen av ROAAM+ -metodiken har resulterat i att ett ramverk har utvecklats med en uppsättning beräkningsverktyg. I dessa ingår olika beräkningsmodeller i form av både full- och surrogatmodeller för härdnedsmältnings-, genomsmältnings- och reaktortankens, smältstrålens flöde, ablation av reaktortanken, ångexplosioner och kylbarhet. Syftet är att identifiera stora bidrag till osäkerheter i riskbedömningsarna. Omfattande analyser för att kvantifiera risker i samband ångexplosion och icke-kylbar härdsmälta har utförts. Det har visats att den största källan till osäkerhet är hur genomsmältnings- och reaktortankens sker. Resultaten tyder på att risken för inneslutningsbrott på grund av ångexplosion eller icke-kylbar härdsmälta är mycket liten om genomsmältningen sker genom ett hål i tanken som är mindre än 10 cm i diameter.

Utvecklingen av ROAAM+ metodiken under APRI 9 har bland annat innehållt:

- En omfattande studie av härdsmälteförlopp och nedrinning till nedre plenum i reaktortanken har gjorts. Målet var att studera egenskaperna hos härdgrus i tankens nedre plenum och hur genomsmältnings- och reaktortankens sker. Olika versioner av MELCOR-koden har använts.
- En metodik med kopplad termo-mekanisk analys med programmen PECM/FLUENT (CFD-analys) och ANSYS (FEM-analys) har utvecklats och tillämpats. Analysen simulerar strömningsförlopp och värmeöverföring i härdsmälten, samt elastisk och plastisk (termisk krypning) deformation och kollaps av reaktortank.
- En uppsättning modeller har utvecklats för att studera potentiella begränsande mekanismer vid tankgenomsmältningen bl.a. pluggning och ablation.
- Ett omfattande forskningsprogram har genomförts för att studera fenomen som kan påverka bildandet av en icke-kylbar bådd av härdgrus. Spridning av partikelformigt härdgrus och nivån på grusbädden har undersökts experimentellt och en uppsättning analytiska modeller har utvecklats och validerats. DECOSIM-koden har utvecklades vidare för att studera fenomen i porösa högar av härdgrus på inneslutningens golv.
- Agglomeration av härdgrus är för närvarande den största faktorn som kan leda till bildandet av icke-kylbar bådd av härdgrus. Full- och surrogatmodeller har utvecklats för att kvantifiera fenomenet agglomeration och effekterna av dessa fenomen på kylbarheten. DECOSIM-simuleringarna tyder på att kylbarheten kan försämras väsentligt när agglomererade partiklar når  $> 20 \sim 50\%$  (beroende på partikelstorleken) vilket motsvarar stråldiametrar på  $> 100$  mm. Ytterligare modellutveckling och validering är nödvändig för att minska och kvantifiera fenomenologisk osäkerhet i detta sammanhang.
- Surrogatmodellen för ångexplosioner har utvecklats med hjälp av en databas genererad med TEXAS-V som betraktas som en FM - Full Model. Totalt har

455000 simuleringsar av pre-mixing/explosionsförlopp har genomförts för en typisk BWR-reaktor.

Resultaten från ROAAM+ har visats kunna användas för att förfina och förbättra PSA-analyser på flera sätt. Studier med en storskalig PSA-modell visar att integration av ROAAM+ -resultatet med PSA-modellen inte bara är möjlig utan kan också leda till en ändring av den beräknade frekvensen för inneslutningsbrott.

### 6.1.3. MISTEE-projektet

MISTEE-HT experimentutrustningen har upgraderats så att ångexplosioner med högtemperarturmälta kan studeras. Följande material med hög temperatur har undersöks:

- Aluminiumoxid (Smälttemperatur 2050°C) för att studera energiutvecklingen vid ångexplosioner.
- Metalliskt zirkonium (Smälttemperatur 1870°C) för att studera oxidation vid smältans växelverkan med vatten.
- CeO<sub>2</sub>-ZrO<sub>2</sub> (Smälttemperatur 2400°C) för att identifiera potentiella simulantmaterial för studium av hur en smälta av corium växelverkar med vatten.
- En preliminär test med ZrO<sub>2</sub>-smälta (Smälttemperatur 2715°C) har gjorts. Man lyckades att smälta materialet, men det kvarstår utvecklingsarbete för att kunna släppa smältdroppen på önskat sätt.

Maximal temperatur i ugnen i den upgraderade MISTEE-utrustningen är 2800°C. Fortsatt utveckling av denna utrustning kommer att ge möjligheter att studera viktiga fenomen i samband med fragmentering av härdsmälta och ångexplosioner.

### 6.1.4. Tellurkemi vid svåra haverier

Forskningen av fissionsprodukten tellur vid svåra kärnkraftshaverier har givit kunskaper om tellurs aerosolkemi. Mer specifikt har studier gjorts av hur tellur i aerosol-form beter sig vid kontakt med olika ytor som finns i reaktorinneslutningen, vilket påverkar flyktigheten hos tellur-föreningarna. Vidare har studier gjorts av tänkbar påverkan på fissionsprodukter vid kyling med havsvatten. Det finns antydningar om att frigjord mängd av vissa fissionsprodukter, bl.a. tellur, kan öka vid kontakt med havsvatten..

### 6.1.5. Ruteniumkemi vid svåra haverier

Ruteniumstudierna inkluderade effekter av temperatur, radiolysprodukter i luft och cesiumjodidaerosoler på de kemiska formerna av rutenium som kan transporteras i reaktorinneslutningen vid ett svårt reaktorhaveri. Det noterades att temperaturen hade en mycket stor effekt på både utsläpp och transport av rutenium. Radiolysprodukter i luft såsom dem innehållande kväveoxider och salpetersyra påverkade både mängden och den kemiska formen av det rörliga ruteniumet. Cesiumjodiden visade sig ha en stor inverkan på mobiliteten av rutenium i primärkretsen.

Med dessa data finns det nu en bättre möjlighet att kunna förutse och skapa barriärer för utsläpp av rutenium vid svårare reaktorhaverier

### 6.1.6. Oxyhalider

För att utvärdera en potentiell effekt av fissionsprodukten jod på andra fissionsprodukter, har studier gjorts av ett luftflöde där jod fått interagera med niobium, rutenium

och tellur vid höga temperaturer. Försöken tyder på möjlig interaktion, där termodynamiska beräkningar indikerar oxyhalider som en tänkbar reaktionsprodukt. Oxyhalider kan vara betydelsefulla för transporten av fissionssprodukter från primärsystemet till inneslutningen.

#### 6.1.7. Uppföljning av kärnkraftsolyckan i Fukushima Daiichi

Ett viktigt syfte med uppföljningen av kärnkraftsolyckan i Fukushima är att undersöka om de insikter som utvecklats efter olyckan i Fukushima kan leda till ändrad strategi för den svenska haverihanteringen. I rapporten från APRI-8 [1] behandlades förloppen i reaktorerna vid Fukushima Daiichi och möjliga tekniska orsaker. Den analysverksamhet som har bedrivits efter APRI-8 har inte lett till några avgörande ändrade slutsatser. Därmed anses de slutsatser om förloppen som drogs i APRI-8 fortfarande gälla d.v.s. att inga avgörande okända fenomen har identifierats som skulle påverka den svenska strategin för haverihantering och utformningen av de konsekvenslindrande systemen.

### 6.2 Slutsatser

Från projektet APRI-9 kan följande slutsatser dras:

- Deltagande i CSARP har ökat kunskapen om svåra haverier genom utbyte av forskningsresultat och givit tillgång till haverianalskoden MELCOR.
- Deltagande i STEM, THAI och BIP -projekten har givit ökade kunskaper om fissionssprodukters beteende i inneslutningen under ett haveri.
- Uppföljning av Fukushimahändelsen har inte uppdagat några nya fenomen som skulle påverka den svenska strategin för haverihantering.
- Genom tillförsel av medel till KTH och Chalmers från SSM och industrin har kontinuiteten avseende forskning om svåra haverier kunnat säkras.
- Tillämpningen av ROAAM och utvecklingen av ROAAM+ vid KTH har bidragit till en ökad förståelse och ökade möjligheter att analysera fenomenen och förloppen under ett svårt haveri.
- Utvecklingen av ROAAM+ har också förbättrat möjligheten att beskriva och kvantifiera beroenden mellan haverifenomenen.
- ROAAM+ har gett kunskap om vilka experiment som behöver prioriteras.
- Forskningen på Chalmers har resulterat i ökade kunskaper om tellurs och ruteniums kemi i haverisammanhang.

### 6.3 Rekommendationer

Följande rekommendationer lämnas inför fortsättningen av APRI-projektet:

- Fortsatt deltagande i internationella projekt som CSARP, STEM, THAI-3, och BIP-3.
- Fortsatt uppföljning av kärnkraftshaveriet i Fukushima.
- Fortsatt utveckling av ROAAM+-metodiken.
- Fortsatta studier av de olika fenomenens inbördes beroende.
- Fortsatta studier av haveriförloppet i reaktortanken.
- Fortsatta studier av smältans kylbarhet i reaktortankens botten.
- Fortsatta studier av förlopp vid tankgenomsmälting.
- Fortsatta studier av smältans kylbarhet i reaktorinneslutningen.

- Fortsatta studier av de mekanismer som styr ångexplosioner.
- Fortsatta studier av haverikemi i inneslutningen av andra fissionsprodukter än jod som till exempel tellur, rutenium, molybden.

## 7. FÖRKORTNINGSLISTA

AECL	Atomic Energy of Canada Limited
ANL	Argonne National Laboratory
ANN	Artificial Neural Network
APRI	Accident Phenomena of Risk Importance
ASTEC	Accident Source Term Evaluation Code
BIP	Behavior of Iodine
BWR	boiling water reactor
CCFP	Conditional Containment failure Probability
CCI	Core-Concrete Interaction
CFD	computational fluid dynamics
CHF	critical heat flux
CRGT	control rod guide tube
CSARP	Cooperative Severe Accident Research Program
DCH	Direct Containment Heating
DECOSIM	code for debris bed coolability simulation
DEFOR	debris bed formation
DEM	discrete element method
DHF	dryout heat flux
LIVE	Late In-Vessel Phase Experiments
LWR	light water reactor
EC	European Commission
ECM	effective convectivity model
EDF	Electricité de France
EOP	Emergency Operating Procedures
ERMSAR	European Review Meetings on Severe Accident Research
EXAFS	Extended X-ray Absorption Fine Structure analysis
FCI	fuel coolant interaction
FM	Full Model
FP	framework programme
FPT	Fission Product Test
HPCI	High Pressure Coolant Injection
IC	Isolation Condenser
IGT	instrumentation guide tube
INCO	in-vessel coolability
IRSN	Institut de Radioprotection et de Sécurité Nucléaire
ISTP	International Source Term Project
IVR	in-vessel retention
KROTOS	a small-scale test facility for FCI (steam explosion) study at CEA
KTH	Royal Institute of Technology
LOCA	loss of coolant accident
LP	Lumped Parameter (beräkningsprogram med punktvis beskrivning av fysikaliska storheter)
LWR	Light Water Reactor
MCCI	Melt Corium Concrete Interaction
MET	Melt Eruption Test
MELCOR	code for integral simulation of severe accident developed by USNRC
MISTEE	micro interactions of steam explosion energetics
MSWI	melt structure water interactions
NCG	non-condensable gas
NPP	nuclear power plant
NRC	Nuclear Regulatory Commission
NROI	Nordic Research on Radiolytic Oxidation of Iodine
OECD	Organisation for Economic Co-operation and Development

PDS	Particulate debris spreading
PECM	phase-change ECM
POMEKO	porous media coolability
PSA	probabilistic safety analysis
PWR	pressurized water reactor
RCIC	Reactor Core Isolation Cooling
RHR	Residual Heat Removal
ROAAM	risk oriented accident analysis methodology
RPV	reactor pressure vessel
RTF	Radioiodine Test Facility
RUSET	Ruthenium Separate Effect Test
SAID	severe accident information distillation
SA	severe accident
SAM	severe accident management
SARNET	severe accident research network of excellence
SBO	station blackout
SEE	steam explosion energetics
SEM	Scanning electron microscopy
SERENA	Steam Explosion REsolution for Nuclear Applications
SIMECO	simulation of melt coolability
SM	Surrogate Model
SSWICS	Small-Scale Water Ingression and Crust Strength
TGA	Thermo Gravimetric Analysis
TROI	a medium-scale test facility for FCI (steam explosion) study at
VAPEX	code for FCI simulation developed in Russia
XPS	X-ray Photoelectron Spectroscopy
XRD	Glancing angle X-ray Diffraction Spectroscopy





2018:16

Strålsäkerhetsmyndigheten har ett samlat ansvar för att samhället är strålsäkert. Vi arbetar för att uppnå strålsäkerhet inom en rad områden: kärnkraft, sjukvård samt kommersiella produkter och tjänster. Dessutom arbetar vi med skydd mot naturlig strålning och för att höja strålsäkerheten internationellt.

Myndigheten verkar pådrivande och förebyggande för att skydda människor och miljö från oönskade effekter av strålning, nu och i framtiden. Vi ger ut föreskrifter och kontrollerar genom tillsyn att de efterlevs, vi stödjer forskning, utbildar, informerar och ger råd. Verksamheter med strålning kräver i många fall tillstånd från myndigheten. Vi har krisberedskap dygnet runt för att kunna begränsa effekterna av olyckor med strålning och av siktlig spridning av radioaktiva ämnen. Vi deltar i internationella samarbeten för att öka strålsäkerheten och finansierar projekt som syftar till att höja strålsäkerheten i vissa östeuropeiska länder.

Strålsäkerhetsmyndigheten sorterar under Miljödepartementet. Hos oss arbetar drygt 300 personer med kompetens inom teknik, naturvetenskap, beteendevetenskap, juridik, ekonomi och kommunikation. Myndigheten är certifierad inom kvalitet, miljö och arbetsmiljö.

Strålsäkerhetsmyndigheten  
Swedish Radiation Safety Authority

SE-17116 Stockholm  
Solna strandväg 96

Tel: +46 8 799 40 00  
Fax: +46 8 799 40 10

E-mail: [registrator@ssm.se](mailto:registrator@ssm.se)  
Web: [stralsakerhetsmyndigheten.se](http://stralsakerhetsmyndigheten.se)